



Computational Modelling of Functionally-Identified Retinal Ganglion Cells using a Multi-Objective Optimisation Approach

Author:

Guo, Tianruo

Publication Date:

2014

DOI:

<https://doi.org/10.26190/unsworks/18309>

License:

<https://creativecommons.org/licenses/by-nc-nd/3.0/au/>

Link to license to see what you are allowed to do with this resource.

Downloaded from <http://hdl.handle.net/1959.4/54772> in <https://unsworks.unsw.edu.au> on 2024-04-30

Computational Modelling of Functionally-Identified Retinal Ganglion Cells using a Multi-Objective Optimisation Approach

By

Tianruo Guo



A dissertation submitted in fulfillment of the requirements

for the degree of

Doctorate of Philosophy

in

Biomedical Engineering

at

The Graduate School of Biomedical Engineering

The University of New South Wales

Sydney, Australia

August 2014

Acknowledgements

Firstly, I am heartily thankful to my supervisor, A/Prof. Socrates Dokos, a real mentor, researcher and philosopher. Socrates led me to the research world of large-scale optimisation and neuronal modelling. His continuous encouragement, guidance and assistance from the initial to the final stages of this work, enabled me to develop a better understanding of the subject, start enjoying the research, and finally decide to spend the rest of my life on these interesting and challenging studies. Compared to his other students, Socrates spent much more time on me to watch my studies and English. In the last five years, he can almost understand Mandarin Chinese because of me! His permanent patience, unconditional kindness and rigorous academic attitude have my uttermost gratitude and respect. Without his guidance, help and pioneering work, this thesis would not be even possible.

I am also grateful to my co-supervisor, Prof. Nigel H. Lovell, a wise man, a trustworthy man and a very cool boss. Nigel offered me a PhD scholarship for the last several years, provided me many opportunities to present my work to the research community and shared his invaluable academic experience with me. I enjoyed his special sense of humour, and working style and excellent personality. I always look forward to my weekly discussions with Nigel: waiting for his unique response to my cute English accent, his “evil” smile and endless jokes (through I do not quite understand most of them). I would also like to thank Nigel for kicking away so many pretty girls that were “annoying” me during my working hours, making me more productive and more professional. It is such a great honour and enjoyable experience to work just five meters away from his sight every day.

I owe sincere and earnest thankfulness to Dr. David Tsai, Prof. Gregg J. Suaning and Prof. John W. Morley (he is also a rock star) for their benevolent support, professional comments and encouragement during my study. Also, special thanks go to Dr Ross A Odell, who had to tolerate my boring jokes every day. They are all honourable researchers and nice men. I learned more than knowledge from them.

I would like to take this opportunity to express my sincere gratitude to my parents, Mr. Yan Guo and Mrs. Na Li in Hulunbuir, China, for their countless love and support for me. I thank my younger brother, Mr. Sang Yi, who took care of me during my studies.

Finally, I offer my regards and blessings to my colleagues and friends in GSBME, Dr. Siwei Bai, Dr. Amr Al Abed, Dr Hongbo Xie, Mr Adrian Bradd, dear Xiaoying, Mrs Jane Li and Mr Shany Nitzan, who generously shared their experimental, programming experience and invaluable friendship with me during my study. I am enjoyed staying with you so much. I can definitely have finished this thesis one year ago without all of you!

To my lovely younger brother, Pi Sang

Abstract

Retinal neuroprostheses aim to restore functional visual percepts to patients suffering from retinal degenerative diseases such as retinitis pigmentosa (RP) and age-related macular degeneration (AMD). In such patients, it is desirable to reconstruct a useful sense of artificial vision by selectively activating different neuron populations in a planned sequence and spatial pattern. However, current retinal neuroprostheses have limited ability in targeting different retinal neuron types. Improvements in the field of prosthetic vision are highly dependent on better understanding the fundamental mechanisms underlying retinal ganglion cell (RGC) electrical stimulation, and how these can be quantitatively controlled through artificial stimulation. The aim of this thesis is to develop accurate computational models of functionally-distinct RGCs to assist in the further understanding of biophysical mechanisms underlying RGC activation, so that more sophisticated stimulation schemes can be developed.

Morphologically-realistic and functionally-accurate ON and OFF RGC models were developed by integrating multiple experimental information and biophysical principles, allowing the contribution of various morphological and intrinsic RGC properties in shaping RGC response patterns to be isolated. The multiple data used to optimise model parameters consisted of patch-clamp whole cell recordings of RGC spiking activity in the presence of multiple intracellular current injections, as well as associated action potential (AP) phase plots.

In addition, the optimised RGC models were used to gain insights into the mechanisms underlying selective RGC responses to 2 kHz electrical stimulation. By adjusting the extracellular stimulus amplitude across a wide range of values, the models were able to reproduce the distinct patterns of excitation observed experimentally, suggesting the utility of this approach in developing stimulation strategies.

The RGC modelling approach developed in this thesis will facilitate testing of a wide range of stimulus waveforms that aims for selective or differential activation of targeted RGC types, resulting in a dramatic improvement in the quality of prosthetic vision.

Abbreviations

In alphabetical order:

1-D	one-dimensional
2-D	two-dimensional
3-D	three-dimensional
AC	amacrine cell
AH	axon hillock
AIS	axonal initial segment
AMD	age-related macular degeneration
AP	action potential
BC	bipolar cell
CNS	central nervous system
DS	directional selective
EPSP	excitatory postsynaptic potential
FM	Fohlmeister and Miller
FSL	first spike latency
GA	genetic algorithm
GB	gradient-based algorithm
GCL	ganglion cell layer
HC	horizontal cell
HFS	high frequency stimulation
HH	Hodgkin-Huxley
INL	inner nuclear layer
IPL	inner plexiform layer
ISI	inter-spike interval
ODE	ordinary differential equation
ONL	outer nuclear layer
OPL	outer plexiform layer
PDE	partial differential equation
PPS	pulses per second

PR	photoreceptor
RGC	retinal ganglion cell
RP	retinitis pigmentosa
RPE	retinal pigment epithelium
SA	sag amplitude
SAN	peripheral sinoatrial node
SN	spike number
SOCB	sodium channel band

CONTENTS

ACKNOWLEDGEMENTS	I
ABSTRACT	III
ABBREVIATIONS.....	IV
CHAPTER 1 INTRODUCTION.....	2
1.1 MOTIVATION	2
1.2 THESIS AIMS	3
1.3 THESIS LAYOUT.....	4
CHAPTER 2 BACKGROUND	5
2.1 RETINAL ARCHITECTURE.....	5
2.1.1. <i>Rod and Cone Photoreceptors</i>	6
2.1.2. <i>Horizontal Cells</i>	7
2.1.3. <i>Bipolar Cells</i>	8
2.1.4. <i>Amacrine Cells</i>	8
2.1.5. <i>Retinal Ganglion Cells</i>	9
2.2 ACTIVATING RETINAL NEURONS USING ARTIFICIAL ELECTRICAL STIMULATION	12
2.2.1. <i>Visual Prostheses and Retinal Implants</i>	12
2.2.2. <i>Selective Activation of Retinal Neurons</i>	13
2.3 QUANTITATIVE DESCRIPTIONS OF NEURONAL MEMBRANE POTENTIAL	17
CHAPTER 3 REVIEW OF EXISTING COMPUTATIONAL MODELS OF RETINAL NEURONS AND PARAMETER ESTIMATION TECHNIQUES FOR EXCITABLE CELL MODELS	19
3.1 COMPUTATIONAL MODELS OF RETINAL NEURONS	19
3.1.1. <i>Single-Compartment Models</i>	25
3.1.2. <i>Morphologically-Realistic Models</i>	29
3.1.3. <i>Block-Compartment Models</i>	32
3.1.4. <i>Continuum Models</i>	34
3.1.5. <i>Block-Structured Models of Retinal Function</i>	36
3.1.6. <i>Discrete-Neuronal Network Models</i>	37
3.1.7. <i>Outlook on Retinal Neuron Modelling</i>	42
3.2 PARAMETER ESTIMATION OF EXCITABLE CELL MODELS.....	43
3.2.1. <i>Gradient-Based Algorithms</i>	45
3.2.2. <i>Evolutionary-Based Algorithms</i>	47
3.2.3. <i>Objective Function</i>	49
3.2.4. <i>Multi-Objective Optimisation</i>	52
3.3 OVERVIEW	56
CHAPTER 4 METHODOLOGY.....	59
4.1 IONIC MODELLING OF RETINAL GANGLION CELLS.....	59
4.1.1 <i>Single-Compartment RGC model</i>	59
4.1.2 <i>Morphologically-Realistic Cable Model of Intracellular RGC Stimulation</i>	60
4.1.3 <i>Morphologically-Realistic Model of Extracellular RGC Stimulation</i>	62
4.2 MULTI-OBJECTIVE PARAMETER OPTIMISATION.....	64

4.2.1	<i>Curvilinear Gradient Optimisation Method</i>	64
4.2.2	<i>Parameter Upper and Lower Limits</i>	68
4.2.3	<i>Multiple-Objective Optimisation</i>	69
4.2.4	<i>Multiple Objective Function</i>	70
4.3	WHOLE-CELL PATCH CLAMP DATA FOR MODEL OPTIMISATION AND PREDICTION	73
4.3.1	<i>Whole-Cell Current Clamp Recordings in Response to Intracellular Somatic Injections.</i>	73
4.3.2	<i>Cell-Attached Patch Clamp Recordings during 2 kHz Epiretinal Stimulation</i>	75
CHAPTER 5 A SINGLE-COMPARTMENT RGC MODEL		77
5.1	SIMULATING RGC NORMAL AND REBOUND EXCITATION	78
5.2	THE CONTRIBUTION OF J_H IN SHAPING REBOUND ACTIVITIES	84
5.3	DISCUSSION	88
CHAPTER 6 MORPHOLOGICALLY-REALISTIC RGC MODELLING		91
6.1	RGC MORPHOLOGY RECONSTRUCTION	93
6.2	CELL-SPECIFIC RGC MODELLING WITH SHARED KINETIC PARAMETERS	95
6.3	ACCURATE RECONSTRUCTION OF RGC ELECTRICAL ACTIVITIES WITH MULTI-OBJECTIVE OPTIMISATION 102	
6.3.1	<i>Morphologically and Functionally-Accurate ON and OFF RGC Model</i>	103
6.3.2	<i>RGC Dendritic Activation</i>	111
6.3.3	<i>Role of J_h and J_{CaT} in RGC Spiking</i>	112
6.4	INFLUENCE OF CELL MORPHOLOGY ON RGC FIRING PATTERNS	116
6.4.1	<i>Morphologically-Specific Responses of ON and OFF RGCs</i>	116
6.4.2	<i>Influence of Dendritic Bifurcations on Action Potential Propagation</i>	118
6.4.3	<i>Influence of Active Dendritic Density on RGC Firing Patterns</i>	121
6.5	DISCUSSION	123
6.5.1	<i>Accurate RGC Electrical Activity Reconstruction</i>	123
6.5.2	<i>Cell-Specific Ionic Channel Expression</i>	124
6.5.3	<i>Contribution of J_h and J_{CaT} to RGC Function</i>	125
CHAPTER 7 DIFFERENTIAL RGC RESPONSES TO HIGH-FREQUENCY EXTRACELLULAR STIMULATION		127
7.1	RESPONSE TO CONSTANT AMPLITUDE STIMULATION	128
7.1.1	<i>Possible Mechanisms Underlying the Non-Monotonic Extracellular Response</i>	131
7.1.2	<i>Effect of Electrode Location and Stimulus Frequency on Extracellular Stimulus-Response Profile</i>	134
7.2	RESPONSE TO AMPLITUDE-MODULATED STIMULATION	136
7.3	THRESHOLD MAPS	138
7.4	INFLUENCE OF RGC MORPHOLOGY ON STIMULUS-RESPONSE PROFILE	141
7.5	DISCUSSION	148
7.5.1	<i>Selective Activation and Possible Mechanisms</i>	148
7.5.2	<i>The Site of AP Initiation in RGCs</i>	151
7.5.3	<i>Continuous Spectrum of Spiking Patterns with Morphological Variations</i>	151
CHAPTER 8 CONCLUSIONS		153
8.1	THESIS CONTRIBUTIONS	153
8.1.1	<i>A generic neuron model optimisation approach</i>	153
8.1.2	<i>Accurate ON and OFF RGC simulations</i>	154
8.1.3	<i>Selective activation of ON and OFF RGC types</i>	154
8.2	FUTURE WORK	155

PUBLICATIONS ARISING FROM THIS THESIS.....	156
BIBLIOGRAPHY.....	157

Part I Background and Methods

Chapter 1 Introduction

1.1 Motivation

The remarkable performance of the mammalian retina arises from its compact and functional architecture. Visual information is initially transduced into electrical signals by photoreceptors located in the outer layers of the retina, with the resultant signals projecting to horizontal, bipolar, amacrine, and ultimately, retinal ganglion cells (RGCs): the latter located in the innermost layer of the retina. Normal retinal function can be compromised as a result of neural degenerative diseases such as retinitis pigmentosa (RP) and age-related macular degeneration (AMD). In many such conditions, the photoreceptors, horizontal cells and a large population of bipolar cells are lost, while most neurons in the inner retina such as amacrine cells and RGCs are still believed to be functional (Marc et al., 2003). The presence of intact RGCs in these disease conditions suggests the possibility of restoring visual percepts with artificial electrical stimulation. However, current retinal implants have limited ability in selectively targeting different retinal neuron types, due in considerable part to our incomplete knowledge of mechanisms underlying selective RGC activation.

A comprehensive description of RGCs has not yet been made due to their large diversity in both functional and morphological properties. At present, there is only a limited knowledge of cell-specific ion channel kinetics and distributions in identified RGC types. More importantly, the roles of cell-specific RGC biophysical properties in shaping their differential responses to identical inputs, have not been analysed.

In addition, existing RGC computational models reported in the literature have largely ignored the cellular morphology and membrane channel distributions/kinetics in each cellular region. In addition, their ability to simultaneously reconstruct multiple experimental data under a large range of conditions is still unclear, limiting their utility in clinical applications such as stimulus strategy design for retinal neuroprostheses.

Therefore, a realistic modelling approach incorporating cell-specific morphological information and ionic channel expression is required to improve our understanding of how functionally-distinct retinal neuron types respond to electrical stimulation, and how their unique

morphological and biophysical properties influence this behaviour. To adjust model parameters in order to reconstruct multiple experimental datasets, an unsupervised and computationally-efficient multi-objective optimisation toolbox for retinal neuron optimisation is also desirable.

1.2 Thesis Aims

This thesis was motivated by the need to improve our understanding of biophysical mechanisms underlying RGC activity during electrical stimulation to allow improved stimulation schemes to be developed in the future.

The aims of this thesis were:

- a) to develop a computationally-efficient multi-objective parameter optimisation technique, for RGC ionic models to fit multiple action potential datasets recorded in different RGC classes.
- b) to develop, with the above approach, biophysically- and morphologically-accurate RGC models capable of reproducing multiple action potential data for a large range of intracellular current stimuli.
- c) to investigate the effects of cellular morphology and intrinsic properties on responses of functionally-distinct RGCs using above models, to improve our existing understanding of RGC activation mechanisms.
- d) to further investigate RGC response to high-frequency extracellular stimulation in the above models; in particular, to examine how to optimise stimulus waveforms and parameters to differentially target individual RGC classes.

1.3 Thesis Layout

This thesis describes the development of computational models to simulate the electrical activity of ON and OFF RGCs in response to extracellular and intracellular electrical stimulation. The thesis chapters are structured as follows:

Chapter 2 provides an overview of retinal anatomy/electrophysiology, necessary background on artificial stimulation of the retina, and mathematical concepts related to ionic modelling of excitable tissues.

Chapter 3 gives a critical review of existing modelling approaches for retinal neurons, as well as current optimisation methodologies in excitable cell modelling.

Chapter 4 details the development of single- and multiple-compartment computational RGC models. In addition, a multi-objective parameter optimisation method is presented. Finally, *in vitro* recording approaches under intra- and extracellular stimulation conditions are also briefly described.

Chapter 5 presents a generic single-compartment RGC ionic model, enabling simultaneous reconstruction of multiple RGC spiking activities under a range of depolarising and hyperpolarising intracellular current injections.

Chapter 6 presents biophysically-accurate ON and OFF RGC models incorporating detailed cell morphologies with optimised ionic channel expressions in various cellular regions. The contribution of dendritic morphology and regional ionic channel expressions to RGC response patterns is also explored.

Chapter 7 explores the predictive power of the optimised ON and OFF RGC models by testing their behaviour in response to 2 kHz extracellular electrical stimulation. The models are also used to gain insights into the possible mechanisms underlying selective RGC responses to electrical stimulation.

Chapter 8 summarises the main contributions and conclusions of this thesis, and proposes some directions for future development.

Chapter 2 Background

2.1 Retinal Architecture

Very few neural circuits are comparable to the complexity and structured layout of the retinal system. For one, the retina has a clear and regularly-organised architecture, and every functional retinal layer can be physically identified: this is in contrast to the seemingly overwhelming complex structure of the brain. Furthermore, input and output relationships in many retinal neurons and layers have been well-characterised (Masland, 2012, Roska and Meister, 2014). Finally, this “one-directional” signal-processing system can be represented as an isolated system without considering efferent feedback from the brain.

The retina is an elaborate architecture of neurons interconnected through gap junctions and synapses (see the schematic drawing in Figure 2.1). At the outer retina, a network of rod and cone photoreceptors convert the incident light to neural activities. These signals then pass through ~11 types of bipolar cells before arriving at the output neurons located in the inner retina: the RGCs. The ~12 types of RGCs then transmit the signals to the brain via the optic nerve. In addition to this vertical excitatory pathway, the retina also contains two lateral inhibitory pathways. In the outer retina, horizontal cells provide inhibitory feedback to the photoreceptors and inhibitory feed-forward input to the bipolar cells. In a similar scheme, amacrine cells in the inner retina provide inhibition to the bipolar cells and RGCs (Masland, 2001, Wassle, 2004).

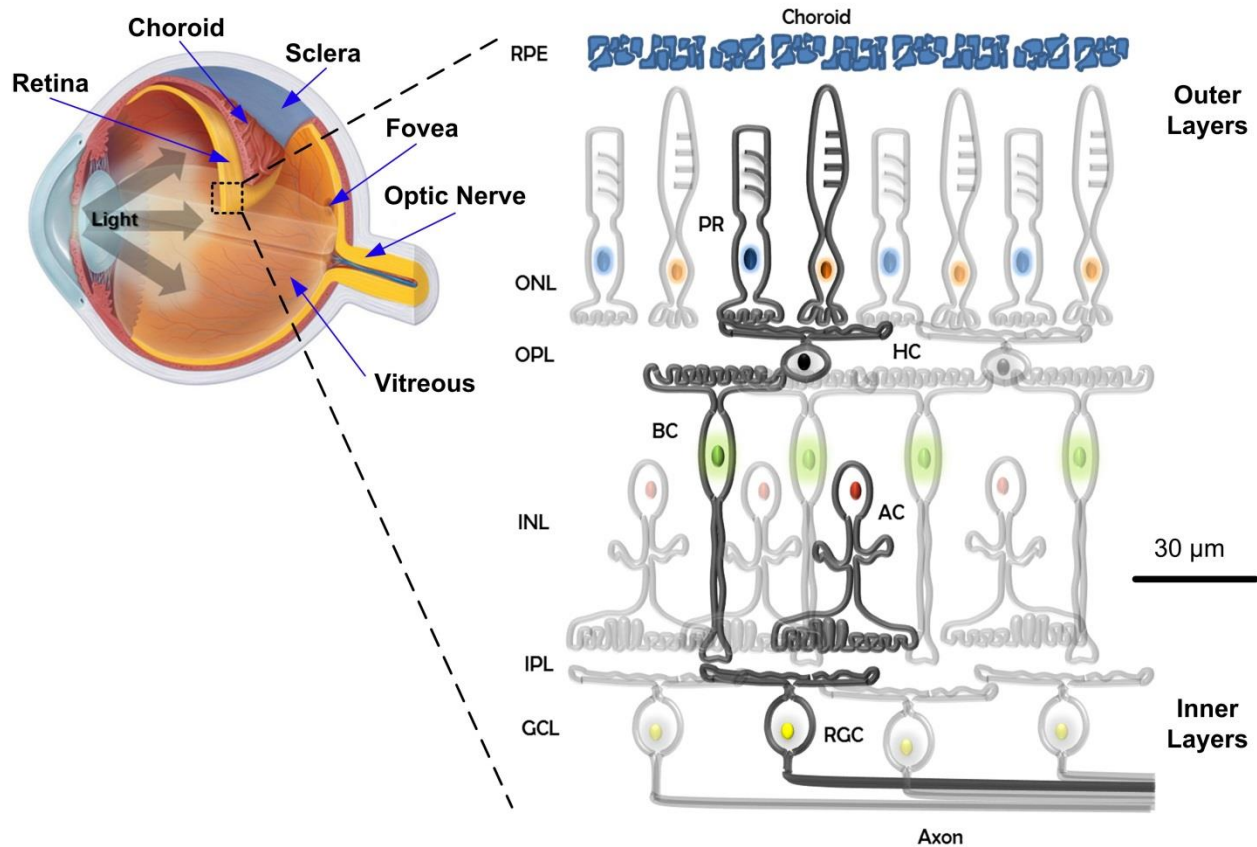


Figure 2.1 Schematic diagram of a retinal cross section. Light enters the retina from the inner layers, with resulting neural signals travelling from the outer to the inner layers. RGC cell bodies make up the ganglion cell layer (GCL). The cell bodies of horizontal (HC), bipolar (BC) and amacrine (AC) cells make up the inner nuclear layer (INL), and cone and rod photoreceptors (PRs) make up the outer nuclear layer (ONL).

2.1.1. Rod and Cone Photoreceptors

Each photoreceptor is made up of several segments: the outer segment, inner segment, cell body and synaptic terminal. The outer segment is located farthest away from incoming light; however, it is the photosensitive portion containing the visual pigment rhodopsin. Based on the shape of the outer segment, vertebrate photoreceptors can be classified into two types: rods, which have a relatively long and cylindrical outer segment, and cones, whose outer segment is shorter and tapered (Steinberg et al., 1980).

Rods provide a graded response up to dim levels of light, and become saturated under day-light (Masland, 2012). These cells are notably absent from the fovea but their density increases towards the periphery of the retina. As there is a high convergence in rod pathways, i.e. the

outputs of thousands of rods ultimately converge on single RGCs (Sterling et al., 1988), spatial resolution in dim light conditions is relatively poor. In addition, retinal rods are incapable of differentiating colours, since they all contain the same visual pigment.

Cones respond best under photopic or bright light conditions, as they are less sensitive but respond faster than rods. Because single RGCs collect information from only a small number of cones, the convergence in cone pathways is notably smaller than in rod pathways. Therefore, the resolution of fine spatial detail is possible, especially in central vision where cones are more densely packed; moving away from the fovea the density of cones drops rapidly. Unlike rods which come in only one variety, cones can be classified into three classes in humans and some other primates: long-wavelength (L), middle-wavelength (M), and short-wavelength (S), which are also respectively referred to as red, green and blue cones (Kuchenbecker et al., 2008, Hofer et al., 2005). As a result of their trichromatic nature, any colour in the visible spectrum, i.e. wavelengths from about 390 to 700 nm, can be matched by a particular combination of the three primary colours, which differentially stimulate the three different populations of cones (Starr et al., 2010).

2.1.2. Horizontal Cells

Horizontal cells are interneurons in the retinal pathway, synaptically active in the outer plexiform layer (OPL), with cell bodies in the distal edge of inner nuclear layer (INL) (Nolte, 2009). They spread laterally and are interconnected with photoreceptors, bipolar cells and other horizontal cells, and thus form a dense network across the whole OPL, modulating photoreceptor output gain through feedback. There are two main types of horizontal cells, *HI* and *HII*, in most mammalian retinas (Kolb, 1974). These horizontal cell types are connected by gap junctions. *HI* is the classic type of horizontal cell in the primate retina, demonstrating larger dendritic trees with radiating dendrites contacting cone photoreceptors. They also have long and thick axons that transverse laterally through the OPL, terminating at rod photoreceptors. *HII* cells have a more spidery and intricate dendritic tree, and in contrast to *HI* cells, have a shorter axon that synapses with cone cells. It has been suggested that there is a colour-specific wiring mechanism for these different cell types (Ahnelt and Kolb, 1994b, Ahnelt and Kolb, 1994a): *HI* cells are primarily connected to M and L cones, whereas *HII* cells are mainly in contact with S cones.

2.1.3. Bipolar Cells

The cell bodies of bipolar cells are distributed in the INL (see Figure 2.1). There are several varieties of different cell types based on their morphological difference (Connaughton et al., 2004, Wassle and Boycott, 1991, Euler and Wassle, 1995). Functionally, however, they are either ON- or OFF-types. As a result, the diversity in morphology results from other factors, such as pre- and post-synaptic connections. Some bipolar cells are in contact with only rods, some only with cones, and others receive mixed inputs (Boycott and Wassle, 1991, Li and DeVries, 2006). As for cone bipolar cells, some are post-synaptic to only a specific type of cone cell, whereas others receive integrated information from multiple cone types. Following the receipt of an optical signal by the retinal photoreceptors, a specific type of neurotransmitter – glutamate – is released from the synapses of photoreceptors (Ayoub and Copenhagen, 1991). Glutamate then triggers the light response in bipolar cells. Depending on the response to this stimulus, bipolar cells can be categorised into two types: ON-cells, which are hyperpolarised in the presence of glutamate, and OFF-cells, which are depolarised by the same neurotransmitter. This dichotomy in light response results from the differential expression of glutamate receptors: ON bipolar cells express a metabotropic receptor (mGluR), whereas OFF bipolar cells express an ionotropic glutamate receptor (iGluR).

2.1.4. Amacrine Cells

Amacrine cells are interneurons synaptically active in the inner plexiform layer (IPL), with their cell bodies in the proximal layer of the INL. They interact at the second synaptic level of the photoreceptor-bipolar cell-RGC pathway, and serve to modulate retinal activity. With at least 22 types discovered, amacrine cells represent the largest diverse population of cells in the retina (Kolb et al., 1981, MacNeil and Masland, 1998). Based on dendritic field diameter measurements, (Kolb et al., 1981), amacrine cells may be considered to fall within one of four groups: narrow-field (30-150 μm), small-field (150-300 μm), medium-field (300-500 μm) and wide-field (>500 μm). Further classification can be made by adding the cell stratification, including which of the five strata in the IPL the dendrites project to, and whether or not projections extend to multiple strata.

In the vertebrate retina, most amacrine cells are inhibitory interneurons, releasing inhibitory neurotransmitters such as γ -aminobutyric acid (GABA) and glycine. Amacrine cells frequently make reciprocal synapses with bipolar cells, and therefore they play a crucial role in the integration and modulation of visual messages presented to the RGC.

2.1.5. Retinal Ganglion Cells

RGCs form the final stage of the visual pathway in the vertebrate retina (Nolte, 2009). They serve to collect the visual information pre-processed by vertical and lateral pathways, before delivering it to the visual cortex via the optic nerve (which is formed by the RGC axons). RGCs are larger than most preceding interneurons in the retina, and they also have larger axons capable of rapidly conveying neuronal signals to the visual processing centres in the brain.

RGCs in the vertebrate retina exhibit a large variety based on their dendritic morphology, cell body and dendritic tree size, as well as stratification level. Figure 2.2 shows the currently identified RGC types in the retinas of a rat (Wong et al., 2012) and a cat (O'Brien et al., 2002). Different RGCs are preferentially activated to detect different features of the visual scene. For example, the large cells with open radiating dendritic branching patterns capable of processing fast and transient impulse trains, are related to motion detection, whereas small bushy RGCs primarily process small stationary, fine details of the visual scene.

Initially discovered by Hartline (1938), it is now established that RGCs present three different patterns of light response. ON cells respond to the onset of light stimuli with a transient burst of impulses, and with a sustained burst throughout the course of stimulation until the stimulus is absent. OFF cells, however, stay silent during light stimulation until the stimulus is switched off. Thereafter, they respond with a sustained impulse discharge. Finally, ON-OFF cells only respond with transient discharge bursts at both the onset and offset of light stimuli. These cells have been identified with distinct stratification patterns in the IPL (Nelson et al., 1978, Peichl et al., 1981, Amthor et al., 1989). Briefly, ON cell dendrites are close to the ganglion cell bodies, connecting with the axon terminals of ON type bipolar cells. The dendrites of OFF cells are typically close to the amacrine cell bodies, connecting with the axon terminals of OFF type bipolar cells, and ON-OFF dendritic trees typically arbourise in both zones of the IPL, presenting a “bistratified”

appearance (Rockhill et al., 2002, Sivyer and Vaney, 2010, Moritoh et al., 2013, Sun et al., 2002).

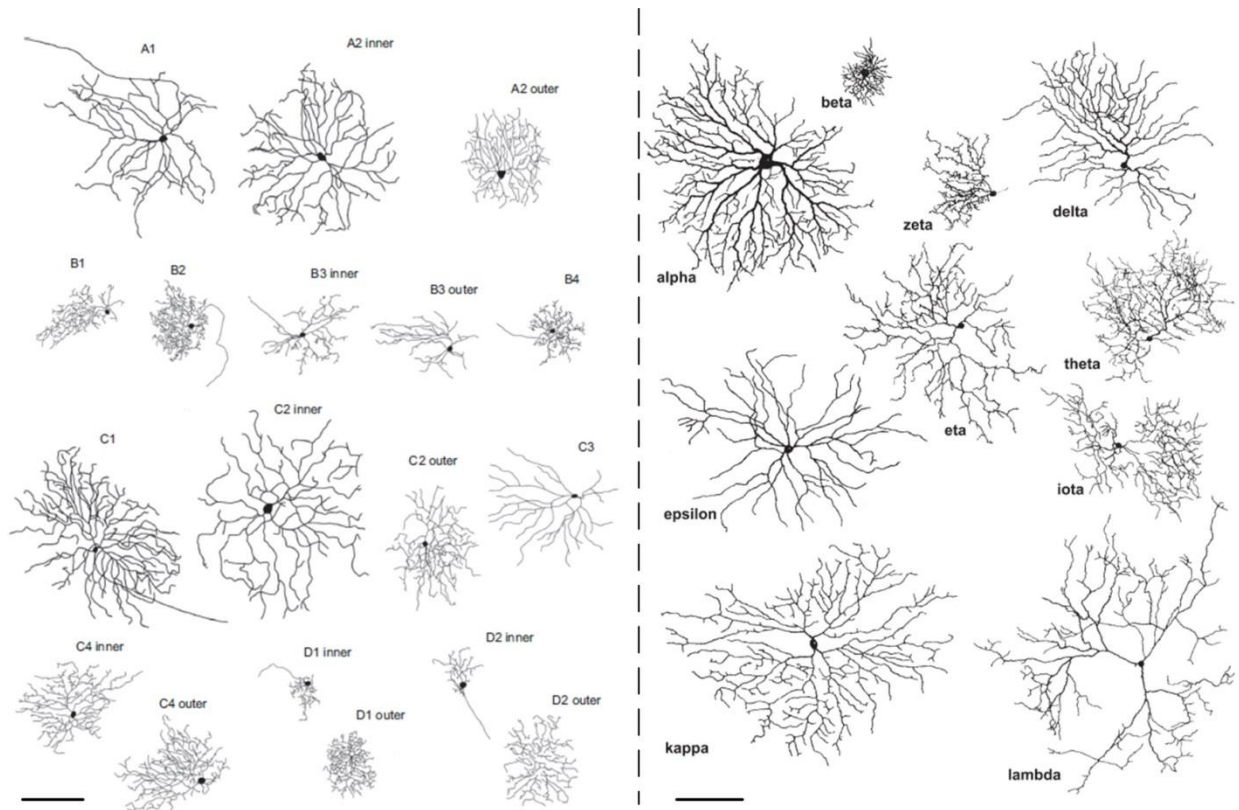


Figure 2.2 Current identified RGC types in the retina of rat (left) and cat (right). Scale bar: 100 μm . Adapted from Wong et al. (2012) and O'Brien et al. (2002)

Hartline (1938) also introduced the definition of “receptive field” in order to investigate the spatial properties of RGCs. This term refers to the spatial region in which a stimulus is capable of firing the neuron. One of the characteristics of an RGC receptive field is “antagonistic surround” or “centre surround”. These terms describe the organisation of the receptive field, whereby two concentric regions antagonise one another (Kuffler, 1953). In the case of an ON-centre cell, a light stimulus near the centre evokes a burst of impulses at the stimulus onset, and a light stimulus at the periphery evokes impulses at the offset. As for an OFF-centre cell, light stimuli have a converse effect. When both the centre and periphery are stimulated simultaneously, the two regions antagonise each other: since the sensitivity to stimulation diminishes radially from the centre, oftentimes only the centre response is observed. Therefore, a large contrast between the light and dark phases is necessary in order to ensure maximal response.

Other than their morphological and stratification diversity, different RGC types also demonstrate

distinct intrinsic properties (Wong et al., 2012, O'Brien et al., 2002). With further advances in *in vitro* experimental techniques, known ionic mechanisms of RGCs continues to be updated with the identification of new ionic channel types (Miller et al., 2002, Tabata and Ishida, 1996, Lee and Ishida, 2007, Margolis and Detwiler, 2007, Henderson and Miller, 2003). The properties of these new currents and their regional distributions in different neuron types may significantly contribute to their overall response. However, there is still limited knowledge on differences in ion channel expression among the identified RGC types. More importantly, the contribution of this diversity to their unique responses to visual inputs is still unclear. This thesis presents a novel computational framework for developing RGC models, integrating multiple experimental information and biophysical principles to provide a quantitative understanding of activation processes in the different RGC types.

2.2 Activating Retinal Neurons Using Artificial Electrical Stimulation

2.2.1. Visual Prostheses and Retinal Implants

Visual prostheses are neurostimulators which electrically activate neurons along the visual pathway, in the hope of creating a sensation of vision in blind individuals. By differentially activating retinal neurons in a desired sequence and spatial pattern, phosphenes can be elicited sequentially at specific sites; if sequential stimuli are applied sufficiently fast, the phosphene map may lead to a perceptible reconstruction of visual information presented to the patients. Research in this field has largely converged towards electrical neurostimulation of the retina, the optic nerve, or the visual cortex (Guenther et al., 2012). We are particularly interested in retinal stimulation, as it provides significant advantages over cortical prostheses which require inter-cranial neurosurgery, and individual mapping of stimulation sites in the cortex (Dowling, 2005, Weiland et al., 2005).

One of the major concerns in terms of retinal implant design of a retinal implant is its size and placement, since it cannot be too large to interrupt eye movements, which help in acquiring, fixating and tracking visual stimuli. Therefore, a split system design has been proposed by our research group at UNSW (Jung et al., 2013), where only a part of the implant, typically the electrode array, is placed inside the eyeball, with the rest remaining extraorbitally. Based on the location of the electrodes in the eye, retinal implants can broadly be divided into three major groups: 1) epiretinal, 2) subretinal and 3) suprachoroidal.

1. Epiretinal implants have their electrode array located in the vitreous (see Figure 2.1) of the eye, and therefore have the advantage of being near or in direct contact with the RGCs (Ahuja et al., 2011, de Balthasar et al., 2008, Klauke et al., 2011). As a result of being close to the target tissue layer, stimulus thresholds necessary to activate RGCs are significantly lower compared to other retinal implants. However, the challenge with epiretinal implants is their fixation, which requires a retinal tack or other fastening means, which may in turn result in mechanical damage to the surrounding tissue or even higher thresholds due to the electrodes not closely positioned adjacent to the epiretinal surface (Gerding, 2007, Hesse et al., 2000).

2. Subretinal implants have their electrodes placed between the retinal pigment epithelium (RPE, see Figure 2.1) and the photoreceptor layer (Wilke et al., 2011, Zrenner et al., 2011). Some of these utilise microphotodiode arrays to act as a replacement for degenerated photoreceptors by converting optical information into an electrically equivalent signal. These devices thus take advantage of the remaining functional retinal pathway (Zrenner et al., 2011, Volker et al., 2004), and do not require an external camera or external image processing unit. However, implant fixation is also not very easy, and may cause detachment of the retina (Sachs and Gabel, 2004). Furthermore, the implant may result in transport blockage between the choroid and retina, as retinal nutrients and waste are normally distributed and uptaken by the choroid.
3. Suprachoroidal implants have their electrodes inserted between the sclera and the choroid (Zhou et al., 2008, Wong et al., 2009, Shivdasani et al., 2010, Fujikado et al., 2007, Matteucci et al., 2013). The insertion and placement of the electrode array at this location is relatively easy, which in turn suggests minimally invasive surgery and less risk of damage to the retina. However, since the electrodes are further away from the target cells, higher stimuli are required, and since the current density is also reduced further from the electrodes, the size of the receptive field of each electrode increases, which may potentially limit visual acuity (Dowling, 2005, Weiland et al., 2005).

2.2.2. Selective Activation of Retinal Neurons

It is anticipated that improvements in the quality of prosthetic vision will mainly arise from more sophisticated stimulation strategies, possibly enabling selective activation of specific types of ganglion cells. Such strategies would enable neuronal activity elicited by artificial stimulation to be closer to physiological spiking patterns seen in response to natural visual inputs.

Selective activation or differential activation in this context refers to the mean targeted activation of one neuron type in preference to another neuron type not targeted for stimulation. In the normal retina, different RGC classes demonstrate unique light-response properties to natural visual inputs (e.g. increase or decrease of light intensity, adaptation, and sensitivity to multiple image object motion). *In vitro* experimental studies also suggested that the characteristic response patterns in identified RGC types are formed by their unique intrinsic and morphological

properties (O'Brien et al., 2002, Wong et al., 2012, Margolis et al., 2010, Margolis and Detwiler, 2007). In these studies, morphologically- or functionally-distinct RGC types indicated differential responses to somatic current injections, without the influence of network inputs by applying synaptic blockers. Therefore, it is reasonable to expect that these cells also show noticeable differences in their intrinsic response to extracellular electrical stimulation.

However, existing visual prosthetic devices have limited or indeed no ability to selectively stimulate retinal neurons in clinical settings due to the relatively large area of retinal tissue activated by the electrodes, as well as the limited knowledge of mechanisms underlying neuronal activation. Multiple experimental studies have reported the difficulty in targeting different retinal neurons using artificial electrical stimulation (Sekirnjak et al., 2008, Margalit and Thoreson, 2006, Tsai et al., 2009, Freeman et al., 2011), while some studies have suggested the possibility of preferentially activating individual RGC types using particular stimulus configurations (Jensen and Rizzo, 2005, Jensen and Rizzo, 2006).

Typically, there exist two types of artificial activation. One is direct activation, in which the RGCs are activated directly and elicit a single spike (or two spikes occasionally) for each stimulus pulse (Jensen et al., 2005, Sekirnjak et al., 2006, Ahuja et al., 2008). This can be achieved by both epiretinal and subretinal stimulation (Stett et al., 2000, Tsai et al., 2009), and the region with the lowest RGC threshold is reported to be near the proximal axon (Sekirnjak et al., 2008, Fried et al., 2009). Studies aimed at selective activation of direct responses in RGCs have shown some success. Results have raised the possibility that such types of selective activation are optimal for small-diameter electrodes (Jensen et al., 2005). However, such selective activation may be possible only over a relatively small range of stimulus amplitudes (Freeman et al., 2011). In addition, such stimulation may induce the incidental activation of passing axons, which would reduce the ability to elicit spatially-localised percepts.

The other type of artificial activation is indirect activation. In this case, neurons presynaptic to RGCs generate responses, which elicit an indirect spiking response in the RGCs due to synaptic activation. The types of neurons activated may be different between healthy and degenerate retina: in the healthy retina, either bipolar cells or photoreceptors can be the target of indirect stimulation, whereas in the degenerative retina where photoreceptors are largely absent, the

indirect response likely initiates from activation of bipolar cells (Jensen and Rizzo, 2008). Since passing axons would likely be activated by direct activation, selective indirect activation of RGCs may be more desirable. Nevertheless, studies in epiretinal stimulation have shown that it is difficult to selectively elicit an indirect response using pulsatile stimuli without eliciting direct responses (Jensen et al., 2005). In terms of subretinal stimulation, the threshold for direct versus indirect activation may be indistinguishable in healthy retina (Tsai et al., 2009). In the degenerate retina, the threshold for indirect activation increases relative to healthy retina (Jensen and Rizzo, 2008), whereas the threshold for direct activation is not affected by degeneration (Sekirnjak et al., 2009). It is thus speculated that the ability to selectively activate the indirect response is reduced in the degenerate retina.

Selective activation of either ON or OFF type RGCs has also been investigated. It has been reported that for direct activation, ON and OFF cells may share similar activation thresholds, for both subretinal (Tsai et al., 2009) and epiretinal (Sekirnjak et al., 2008) stimulation. This will clearly limit the quality of visual perception afforded by a prosthetic device, since ON and OFF RGCs representing the same image “pixel” will be activated by the electrical stimulation (Freeman et al., 2011). For indirect activation however, the OFF-cell threshold in the healthy retina is lower than ON cells (Jensen and Rizzo, 2006). However, since this difference may be influenced by photoreceptor activation, it may not be evidenced in the degenerate retina.

In the aforementioned studies of selective activation, pulsatile stimuli were conventionally used. In more recent studies, more complex stimulus waveforms have been investigated to determine if they provide better selectivity (Langille et al., 2008, Freeman et al., 2010b, Foutz and McIntyre, 2010). For example, it has been found that low-frequency sinusoidal waveforms resulted in robust indirect activation of RGCs with little or no direct effect. When the stimulus frequency was increased to ~100 Hz, the direct response became stronger but the synaptic response was hardly influenced (Freeman et al., 2010a). A more recent *in vitro* study first suggested the possibility of employing 2 kHz high-frequency stimulation (HFS) to maximise the difference in responses between ON and OFF RGC types (Twyford et al., 2014), underlying the possibility of HFS to selectively activate different retinal neuron types. HFS has been explored in cochlear prosthetics (Litvak et al., 2001, Litvak et al., 2003). It has also been used to induce selective conduction block in peripheral axon fibres (Joseph and Butera, 2011), revealing its potential for

visual prosthetic stimulation. However, in the Twyford et al. (2014) study, the size and location of the stimulus electrodes were far smaller and closer to the target neurons than those that would be used in practical retinal prosthetic devices: For example, Twyford et al. used 40 μm disc electrodes compared to $\sim 200\text{-}400$ μm for practical electrodes in a therapeutic device. Moreover, the height of the stimulating electrode was accurately fixed 25 μm above the inner limiting membrane, which is difficult to achieve in clinical applications. Therefore, the utility of this HFS approach as a practical visual stimulation strategy still needs to be investigated. In this thesis, computational RGC models are utilised to better understand the possible mechanisms underlying differential RGC responses to 2 kHz HFS, shedding light on future stimulation strategies to improve the quality of prosthetic vision.

2.3 Quantitative Descriptions of Neuronal Membrane Potential

The ionic models developed in this thesis are described by Hodgkin-Huxley-type formulations. Excitable neuronal membranes are composed of micromolecular complexes of proteins and phospholipids (Rouser et al., 1968). This structure can be described by a capacitor (phospholipids) in parallel with several conductive elements (ionic channels assembled by proteins), with the relationship between transmembrane potential and ionic currents described by the standard space-clamped ordinary differential equation (ODE):

$$dV_m/dt = -(i_L + \sum_{j=1}^N i_j)/C_m \quad (2.1)$$

where i_j denotes the j th time-dependent ionic current, N is the total number of such time-dependent currents present, and i_L is a background or leakage current.

The quantitative description of membrane potential was first provided by Sir Alan L. Hodgkin and Sir Andrew F. Huxley for the giant axon of the squid (Hodgkin and Huxley, 1952). In their work, membrane conductance g_j terms are given by the product of a maximum membrane conductance for each ion type (\bar{g}_j) with voltage and time-dependent gating variables $x(V_m, t)$ representing the fraction of open channels:

$$g_j(V_m, t) = \bar{g}_j \cdot \prod_{k=1}^M x_k(V_m, t)^{n_k} \quad (2.2)$$

where M is the total number of gating variables for the j th ionic current. Each gating variable is represented by a first order differential equation:

$$dx(V_m, t)/dt = \alpha(V_m)(1 - x) - \beta(V_m)x \quad (2.3)$$

where $\alpha(V_m)$ and $\beta(V_m)$ are the opening and closing rates of the corresponding gating variable respectively, all being empirical functions of the membrane potential V_m .

From Ohm's law, the general form of each ionic current is given by:

$$i_j(V_m, t) = g_j(V_m, t) \cdot (V_m - V_{rev,j}) \quad (2.4)$$

where V_m is the membrane potential, $V_{rev,j}$ is the Nernst equilibrium potential described by:

$$V_{rev,j} = -\frac{RT}{zF} \ln \frac{C_I}{C_O} \quad (2.5)$$

where R , T and F are the gas constant, absolute temperature and Faraday's constant, respectively. z is the valence of the corresponding ion carried by the channel, and C_I and C_O are the respective ion concentrations in the intra- and extracellular spaces. $V_m - V_{rev,j}$ represents the electrochemical driving force of each ionic channel.

Since ionic mechanisms underlying various excitable cell types are similar, the Hodgkin-Huxley model and its extensions have been widely utilised in cardiac, muscle, brain and retinal neuron modelling studies, with the inclusion of detailed ionic mechanisms, morphological information and network interactions (see Chapter 3). Although more detailed modelling approaches (e.g. Markov schemes) have been found to provide better approximations of single channel microscopic structure and kinetics (Fink and Noble, 2009), Hodgkin-Huxley schemes are still recognised as standard in most excitable cell modelling studies. Details of their wide application in retinal neuron modelling are reviewed in Chapter 3.

Chapter 3 Review of Existing Computational Models of Retinal Neurons and Parameter Estimation Techniques for Excitable Cell Models

3.1 Computational Models of Retinal Neurons

Existing anatomical and neurophysiological knowledge of retinal function has allowed computational models to reproduce retinal responses to either visual or artificial electric stimuli at various levels of complexity. These models, in turn, have improved our understanding of the retina, particularly in how intrinsic biophysical and anatomical properties at the cellular level, and integration of synaptic inputs at the network scale, contribute to retinal function (see Figure 3.1 and Table 3.1). Indeed, over recent decades computational models have been important for understanding the response dynamics and computations of single retinal neurons and their functional contributions in larger neural networks (see Table 3.2)

Despite these major advances, a large amount of retinal function remains to be understood. For instance, experimental studies increasingly indicate that the functions of many retinal neuronal types are more intricate than originally thought (Zhang et al., 2012, Hosoya et al., 2005, Freed, 2001, Fried et al., 2002, Masland, 2012, Gollisch and Meister, 2010). Similarly, at the clinical frontier, the mechanisms underlying the large diversity in retinal neuronal responses to artificial electrical stimulation are still being investigated (Twyford et al., 2014, Freeman et al., 2011, Felsen and Dan, 2005, Tsai et al., 2009).

On a micro scale, retinal neurons extract their preferred visual information, process this information - often with the help of other neurons, then transfer the results to downstream neurons. A single neuron can be represented by either a single-compartment model, a morphologically-realistic model, or via a block-compartment approach, depending on the aims, complexities and physiological assumptions on which the model is based, as well as the computational resources available to process a particular model formulation. Such models integrate electrophysiological current/voltage-clamp recordings and biophysical principles into a mechanistic understanding of individual neuronal properties, and have the capacity to reconstruct ionic mechanisms hidden in the data, as well as utilising new experimental information to improve existing model structures.

On a larger scale, visual information is arrayed across large inhomogeneous populations of neurons within each retinal layer. One approach of representing such a neuronal network involves bringing together individual neurons, each being a complete model capable of stand-alone execution, and connecting them together using computational representations of synapses. As such, these models are mechanistically detailed, but computationally expensive to run.

Alternatively, functional block-structured models could also be used to construct large-scale models of the retina. Unlike the aforementioned approach, these models aim to capture only the input-output relationship of the neuron/network by treating the constituent neurons as black boxes (Dokos, 2014). By omitting neuronal morphological details, and often the associated ionic biophysics too, these approaches have the advantage of computational efficiency. These large-scale tissue- or network-based models have been used to investigate how each retinal neuron contributes to a particular sub-circuit or to the entire retinal tissue, and how they work together to collectively encode visual input. Irrespective of the modelling techniques, they offer improved understanding of the growing amount of experimentally-recorded retinal responses to light or electrical stimuli, and can be used to make testable predictions. For clinical applications, some of these models also provide valuable insights into the development of effective stimulation strategies for visual prostheses (Luo and da Cruz, 2014). In this review section, an overview is given of the current state-of-the-art of computational models of the neural retina, across different scales, discussing their advantages, limitations and future potential.

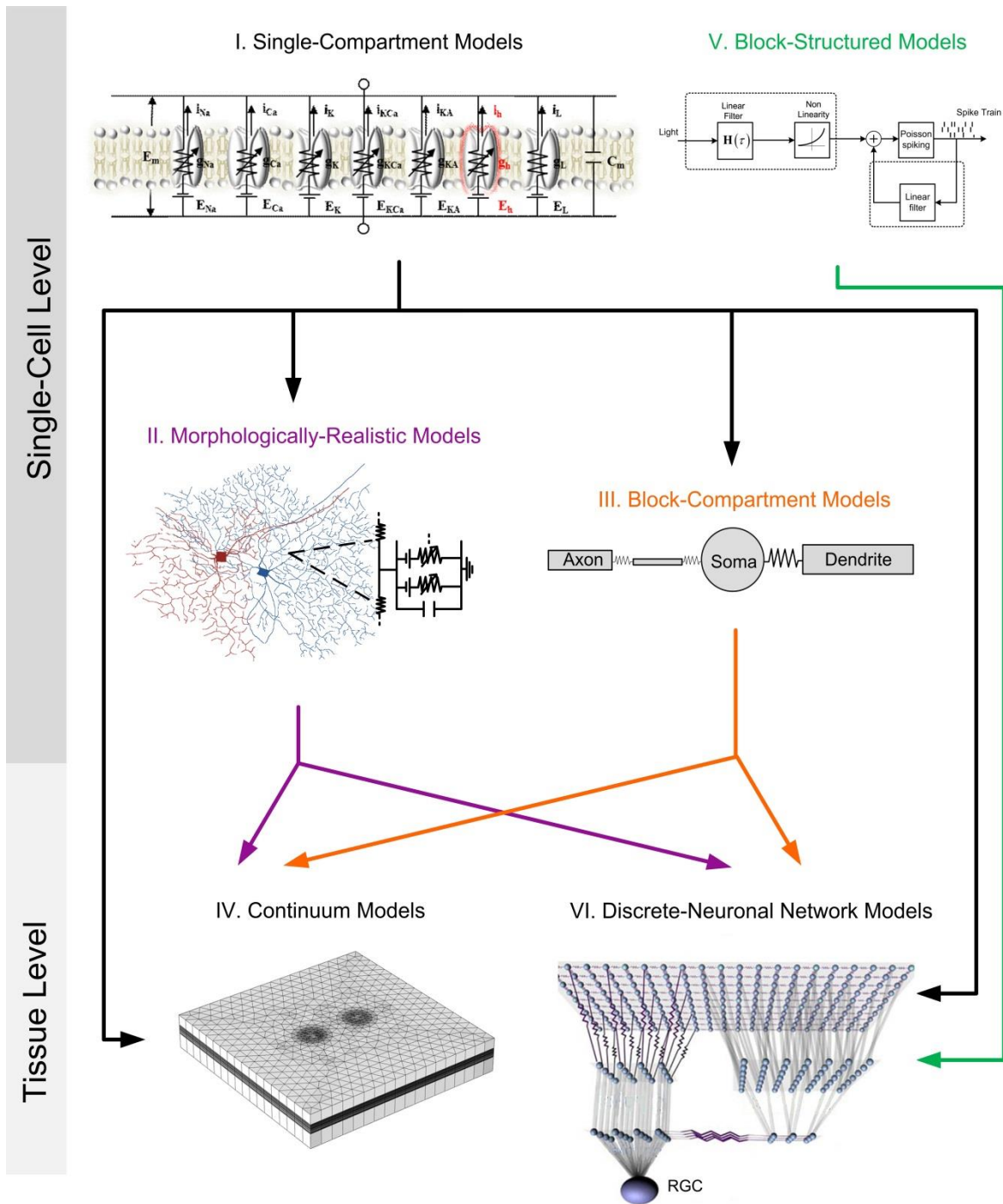


Figure 3.1 Six types of computational models typically used in retinal neuron modelling. I. Single-compartment models, II. Morphologically-realistic models, III. Block-compartment models, IV. Continuum models, V. Block-structured models and VI. Discrete-neuronal network models, adapted from (Publio et al., 2009).

Model type	Published computational retinal neuron models
I.	(Vallerga et al., 1980, Usui et al., 1996a, Steffen et al., 2003, Shirahata, 2011, Shirahata, 2008, Publio et al., 2006, Ogura et al., 2003, Kourennyi et al., 2004, Kamiyama et al., 1996, Kameneva et al., 2011, Fohlmeister and Miller, 1997a, Boinagrov et al., 2010, Baylor et al., 1974, Aoyama et al., 2005, Fohlmeister et al., 1990)
II.	(Velte and Miller, 1997, Velte and Miller, 1995, Tukker et al., 2004, Tsai et al., 2012, Sheasby and Fohlmeister, 1999, Schachter et al., 2010, Resatz and Rattay, 2004, Rattay et al., 2003, Rattay and Resatz, 2004, Publio et al., 2012, Miller et al., 2006, Maturana et al., 2013, Jeng et al., 2011, Greenberg et al., 1999, Fohlmeister and Miller, 1997b, Fohlmeister et al., 2010, Borg-Graham, 2001, van Rossum et al., 2003)
III.	(Werginz et al., 2014, Abbas et al., 2013, Abramian et al., 2011, Carras et al., 1992, Al Abed et al., 2013b, Smith, 1995, Mennerick et al., 1997, Poznanski, 1992, Enciso et al., 2010, Schiefer and Grill, 2006, Taylor et al., 1995, Tukker et al., 2004, Usui et al., 1996b, Fohlmeister and Miller, 1997b)
IV.	(Yin et al., 2011, Yin et al., 2010, Yin et al., 2013, Joarder et al., 2011, Dokos et al., 2005, Al Abed et al., 2012, Al Abed et al., 2013b, Abramian et al., 2011, Abramian et al., 2014)
V.	(Wohrer and Kornprobst, 2009, Victor, 1988, Victor, 1987, van Hateren and Snippe, 2007, Teeters et al., 1997, Shah and Levine, 1996b, Shah and Levine, 1996a, Robson and Frishman, 1996, Robson and Frishman, 1995, Lamb and Pugh, 1992, Keat et al., 2001, Juusola et al., 1995, Hood et al., 1993, Hennig and Worgotter, 2007, Hennig et al., 2002, Hamer et al., 2005, Curlander and Marmarelis, 1987, Cai et al., 2007, Borst et al., 2005, Bomash et al., 2013, Berry et al., 1999, Pillow et al., 2005, Pillow et al., 2008)
VI.	(Wohrer and Kornprobst, 2009, Wang et al., 2011, Usui et al., 1983, Usui et al., 1996b, Teeters et al., 1997, Smith and Vardi, 1995, Smith, 1995, Shah and Levine, 1996b, Shah and Levine, 1996a, Saglam et al., 2009, Robson and Frishman, 1996, Rekeczky et al., 2001, Publio et al., 2009, Publio et al., 2012, Hosoya et al., 2005, Hennig and Worgotter, 2007, Hennig et al., 2002, Haderer and Kuhn, 1987, Freed et al., 1992, Curlander and Marmarelis, 1987, Cottaris et al., 2005, Baccus et al., 2008, Aoyama et al., 2005, Rattay and Resatz, 2004, Rattay et al., 2003, Resatz and Rattay, 2004, Bomash et al., 2013, Arguello et al., 2013, Pillow et al., 2008)

Table 3.1 Existing computational models of retinal neurons categorised by type. Model types correspond to those shown in Figure 3.1. Depending on the study aim, a single-compartment neuron model can be extended to any biophysical model type (II, III, IV, VI), by adding new assumptions such as anatomical structure, synaptic or inter-neuron coupling information. Conductance-based models (i.e. types I, II and III) can be used as individual neuron elements in both continuum models and discrete-network models. Block-structured models are often used in building retinal networks or localised sub-circuits. Large-scale network models can capture the essential function of photoreceptors, bipolar cells and RGCs, as well as the contribution of retinal heterogeneity in visual information processing.

Task	Stimulation	Type	Model used	Biological System	Reference
AP initiation in response to electrical stimulation	Epiretinal electrical stimulation	III	(Fohlmeister and Miller, 1997a)	Rabbit RGC	(Schiefer and Grill, 2006)
AP initiation in response to electrical stimulation	Epiretinal electrical stimulation	II	(Fohlmeister and Miller, 1997a)	Rabbit RGC	(Jeng et al., 2011)
AP initiation in response to electrical stimulation	Epiretinal electrical stimulation	III	(Fohlmeister and Miller, 1997a)	Tiger salamander RGC	(Werginz et al., 2014)
AP initiation in response to electrical stimulation	Somatic injection	III	(Hodgkin and Huxley, 1952)	Mudpuppy RGC	(Carras et al., 1992)
Axonal excitation in response to electrical stimulation	Epiretinal electrical stimulation	IV	(Fohlmeister and Miller, 1997a)	Rabbit RGC axon	(Abramian et al., 2011)
Synaptic signal integration	Dendritic injection	II	(Fohlmeister et al., 1990)	Rabbit starburst amacrine cell	(Velte and Miller, 1997)
Influence of dendritic morphology	Light stimulation	III	(Poznanski, 1992)	Rabbit starburst amacrine cell	(Poznanski, 1992)
Mechanisms of direction sensitivity	Light stimulation	VI	(Enciso et al., 2010)	Rabbit starburst amacrine cell	(Enciso et al., 2010)
Influence of dendritic varicosities	Somatic/dendritic injection	II	(Fohlmeister et al., 1990)	Tiger salamander amacrine cell:	(Miller et al., 2006)
Synaptic signal amplification	Dendritic injection	II	(Fohlmeister and Miller, 1997a)	Rabbit direction selective RGC	(Schachter et al., 2010)
Presynaptic signal processing	Dendritic injection	VI	(Borg-Graham, 2001)	Turtle direction selective RGC	(Borg-Graham, 2001)
Contribution of active dendrites and networks	Dendritic injection	VI	(Fohlmeister and Miller, 1997a)	Tiger salamander RGC	(Publio et al., 2012)
Bipolar-RGC interaction	Dendritic injection	VI	(Enroth-Cugell and Freeman, 1987)	Cat ON alpha RGC	(Freed et al., 1992)
Influence of dendritic field size	Somatic/dendritic injection	II	(Fohlmeister et al., 1990)	Mudpuppy RG C	(Velte and Miller, 1995)
Influence of cell morphology, dendritic active conductance	Somatic/ dendritic injection	II	(Fohlmeister and Miller, 1997b)	Tiger salamander RGC	(Fohlmeister and Miller, 1997b)
Influence of J_h on damped oscillation activity	Light stimulation	I	(Kamiyama et al., 1996, Torre et al., 1990)	Bullfrogs rod photoreceptor:	(Ogura et al., 2003)
Contribution of J_{NaT} , J_{NaP} on spontaneous activity	Somatic injection	I	(Steffen et al., 2003)	Mouse dopaminergic amacrine cell:	(Shirahata, 2011, Steffen et al., 2003)
Contribution of J_{Ca} and networks on receptive-field properties	Light stimulation	I, VI	(Aoyama et al., 2000)	Goldfish horizontal cell:	(Aoyama et al., 2005)
Contribution of J_{KCa} in shaping spiking activity	Somatic injection	I	(Fohlmeister and Miller, 1997a)	Tiger salamander RGC	(Fohlmeister and Miller, 1997a)
Contribution of J_h , J_{CaT} and J_{NaP}	Somatic injection	I	(Fohlmeister and Miller, 1997a)	Mouse ON and OFF RGC	(Kameneva et al., 2011)
Contribution of J_h	Light stimulation	VI	(Publio et al., 2006)	Mammalian rod photoreceptor	(Publio et al., 2009)
Contribution of J_h in directional summation	Light stimulation	II	(Abbas et al., 2013)	Rat ON RGC	(Abbas et al., 2013)
Contribution of dendritic morphology in shaping spiking activity	Somatic injection	II	(Fohlmeister and Miller, 1997b)	Tiger salamander RGC	(Sheasby and Fohlmeister, 1999)
Influence of electrode size and	Somatic injection,	II	(Fohlmeister and	Mouse and monkey	(Tsai et al.,

location and cell morphology	Epiretinal electrical stimulation		Miller, 1997b)	RGC	2012)
Contribution of morphology in shaping spiking activity	Somatic injection	II	(Fohlmeister and Miller, 1997b)	Mouse ON and OFF RGC	(Maturana et al., 2013)
Influence of hexagonally arranged bipolar electrodes	Epiretinal electrical stimulation	IV	(Fohlmeister and Miller, 1997b)	Rabbit RGC	(Abramian et al., 2011)
Influence of bipolar electrode configuration	Epiretinal electrical stimulation	IV	(Fohlmeister and Miller, 1997b)	Rabbit retina	(Dokos et al., 2005, Joarder et al., 2011, Abramian et al., 2014)
Influence of electrode location and stimulus configuration	Epiretinal/subretinal / suprachoroidal electrical stimulation	IV	(Fohlmeister and Miller, 1997b)	Rabbit RGC	(Joarder et al., 2011)
Influence of quasi-monopolar electrical stimulation	Epiretinal electrical stimulation	IV	(Fohlmeister and Miller, 1997b)	Rabbit RGC	(Abramian et al., 2014)
Influence of electrode location and soma size	Epiretinal electrical stimulation	II	(Fohlmeister and Miller, 1997b, Hodgkin and Huxley, 1952)	Mudpuppy retina:	(Greenberg et al., 1999)
Influence of length and resistance of the electrode	Epiretinal electrical stimulation	VI	(Fohlmeister and Miller, 1997a)	Tiger salamander RGC:	(Rattay and Resatz, 2004)
Influence of electrode location	Epiretinal electrical stimulation	VI	(Fohlmeister and Miller, 1997a)	Tiger salamander RGC:	(Resatz and Rattay, 2004)
Strength–duration relationship	Epiretinal electrical stimulation	III	(Fohlmeister and Miller, 1997b, Hodgkin and Huxley, 1952)	Tiger salamander RGC	(Boinagrov et al., 2010)
Influence of synaptic noise	Somatic/dendritic injection	II	(van Rossum et al., 2003)	Cat beta RGC	(van Rossum et al., 2003)
Influence of retinal networks	Epiretinal electrical stimulation	VI	(Teeters et al., 1997)	Primate retina:	(Cottaris et al., 2005)
Mechanisms of motion extrapolation	Light stimulation	V	(Berry et al., 1999)	Tiger salamander and rabbit RGC:	(Berry et al., 1999)
Influence of eye moment	Light stimulation	V, VI	(Hennig and Worgotter, 2007)	Cat RGC:	(Hennig and Worgotter, 2007)
Mechanisms of motion detection	Light stimulation	V, VI	(Borst et al., 2005)	Fly visual system:	(Borst et al., 2005)
Mechanisms of adaptation	Light stimulation	V, VI	(Hosoya et al., 2005)	Tiger salamander/ rabbit retina:	(Hosoya et al., 2005)
Mechanisms of motion detection	Light stimulation	V, VI	(Baccus et al., 2008)	Tiger salamander retina	(Baccus et al., 2008)

Table 3.2 Examples of task-specific applications of various retinal neuron model levels.

3.1.1. Single-Compartment Models

Single-compartment models, also known as “point models”, (see Figure 3.1, type I) have been used to simulate nearly all retinal neuron types, including photoreceptors (Kamiyama et al., 1996, Publico et al., 2006, Kourennyi et al., 2004), horizontal cells (Aoyama et al., 2005, Usui et al., 1996b, Shirahata, 2008), bipolar cells (Usui et al., 1996a), amacrine cells (Steffen et al., 2003, Shirahata, 2011) and a range of RGC types (Fohlmeister and Miller, 1997a, Fohlmeister et al., 1990, Kameneva et al., 2011). These models approximate the structure of the neural excitable membrane using a capacitance to mimic the membrane phospholipid bilayer, in parallel with several conductances to represent transmembrane channels composed of proteins. The relationship between the transmembrane potential and membrane currents is described by the following ODE:

$$J_m = C_m \frac{dV_m}{dt} + J_{ion} + J_{stim} = 0 \quad (3.1)$$

where J_m denotes total membrane current density (in current per unit membrane area), V_m represents membrane potential, C_m is the membrane capacitance per unit area and J_{ion} represents the total ionic current density (Aidley, 1979). A single-compartment model assumes no net current across the cell membrane ($J_m = 0$), since all current flowing through the ionic channels charges the membrane capacitance. This is also known as the space-clamped condition. Furthermore, the neuron may be activated by an intracellular stimulus current (J_{stim}) delivered into the cell, to mimic experimental intracellular current injection during intracellular recordings.

Since ionic mechanisms of retinal neurons are more complex than those of the classic Hodgkin-Huxley model of the squid giant axon (Hodgkin and Huxley, 1952), most modelling studies extend this classical description to replicate known ionic mechanisms in various retinal neurons. Among the first ionic models developed for the retina were those for the RGCs. Their all-or-none spiking behaviour is similar to the classical description and thus easily modelled by modifying existing Hodgkin-Huxley-type formulations.

A landmark in RGC modelling was the Fohlmeister-Miller (FM) formulation (Fohlmeister et al., 1990, Fohlmeister and Miller, 1997b, Fohlmeister and Miller, 1997a), based on voltage clamp studies in tiger salamander. It contains five intrinsic ion currents underlying RGC spiking:

$$\frac{dV_m}{dt} = -\frac{1}{C_m}(J_{Na} + J_{KA} + J_K + J_{Ca} + J_{KCa} + J_L) \quad (3.2)$$

where J_{Na} denotes the voltage-gated sodium current, J_K the delayed-rectifying potassium current, J_{KA} the A-type potassium current, J_{Ca} the L-type calcium current and J_{KCa} the calcium gated potassium current. J_L is the leakage current.

The FM model also incorporated intracellular calcium ($[Ca^{2+}]_i$) dynamics responsible for temporal spiking properties.

$$\frac{d[Ca^{2+}]_i}{dt} = -\left(\frac{3J_{Ca}}{2Fr}\right) - \frac{[Ca^{2+}]_i - [Ca^{2+}]_{res}}{\tau_{Ca}} \quad (3.3)$$

where F denotes Faraday's constant, r is the depth of the shell beneath the membrane for the inward calcium current, τ_{Ca} is the time constant for the sarcolemmal calcium pump, and $[Ca^{2+}]_{res}$ denotes the resting cytosolic calcium concentration. Prior to this study, experimental knowledge of detailed ion channel kinetics or their neuronal compartment distribution was rarely used in retinal neural modelling.

Utilising more detailed Na^+ and K^+ gating kinetics, the FM model demonstrates many advantages over the original Hodgkin–Huxley formulation in terms of impulse encoding flexibility (Fohlmeister, 2009), revealing its ability to reconstruct a large range of neuronal spiking behaviours.

An important extension of the FM formulation was the Kameneva et al. (2011) model, incorporating three additional ionic currents hypothesized to play a role in generating RGC post-offset activation, burst firing, and sub-threshold oscillations. Eq. (3.3) was updated to,

$$\frac{dV_m}{dt} = -\frac{1}{C_m}(\sum J_{FM} + J_h + J_{CaT} + J_{NaP}) \quad (3.4)$$

where $\sum J_{FM}$ represents the original FM currents, J_h is the hyperpolarization-activated current based on the data from rat subiculum neurons (van Welie et al., 2006), J_{CaT} is the low-threshold activated calcium current based on rat thalamocortical relay neurons (Wang et al., 1991), and J_{NaP} is the persistent sodium current based on cat cortical pyramidal neurons (Traub et al., 2003).

With these additional ionic mechanisms, the Kameneva et al. (2011) model could account for various different experimental recordings from ON and OFF RGCs in a qualitative manner.

Moreover, the single-compartment FM model was also validated in higher dimensional simulations with detailed anatomical information or network interactions. Figure 3.2 illustrates most applications and extensions based on FM formulations over the last two decades. Its morphological-, tissue- and network-based extensions are further discussed in the following sections.

Despite the reported functional significance of all five ionic currents in the FM model, relatively simpler ionic models have still been used to study specific RGC response properties when accurate impulse generation was not required (Carras et al., 1992, Al Abed et al., 2013b, Boinagrov et al., 2010), as well as for other retinal neurons (e.g. photoreceptors or bipolar cells) (Taylor et al., 1995, Aoyama et al., 2005).

The advantage of simplicity in single-compartment models are also their weakness. Certain disparities between the single-compartment FM model and known biological RGC behaviour cannot be reconciled by optimising model parameters alone (Fohlmeister and Miller, 1997a). Having additional neuronal compartments that differ in size, kinetics and ion channel densities is able to produce more realistic spike generation and propagation (Carras et al., 1992). Recent brain cell studies suggest that single-compartment models cannot capture subtle response characteristics, such as fast action potential (AP) depolarisation, without incorporating representations of axons and dendrites, and the propagation of current along these neurites (McCormick et al., 2007, Mainen and Sejnowski, 1996, Herz et al., 2006). Therefore, rather than simply incorporating intrinsic properties at a single point, spatial anatomical information and ionic channel distributions are also required for accurate neuronal modelling.

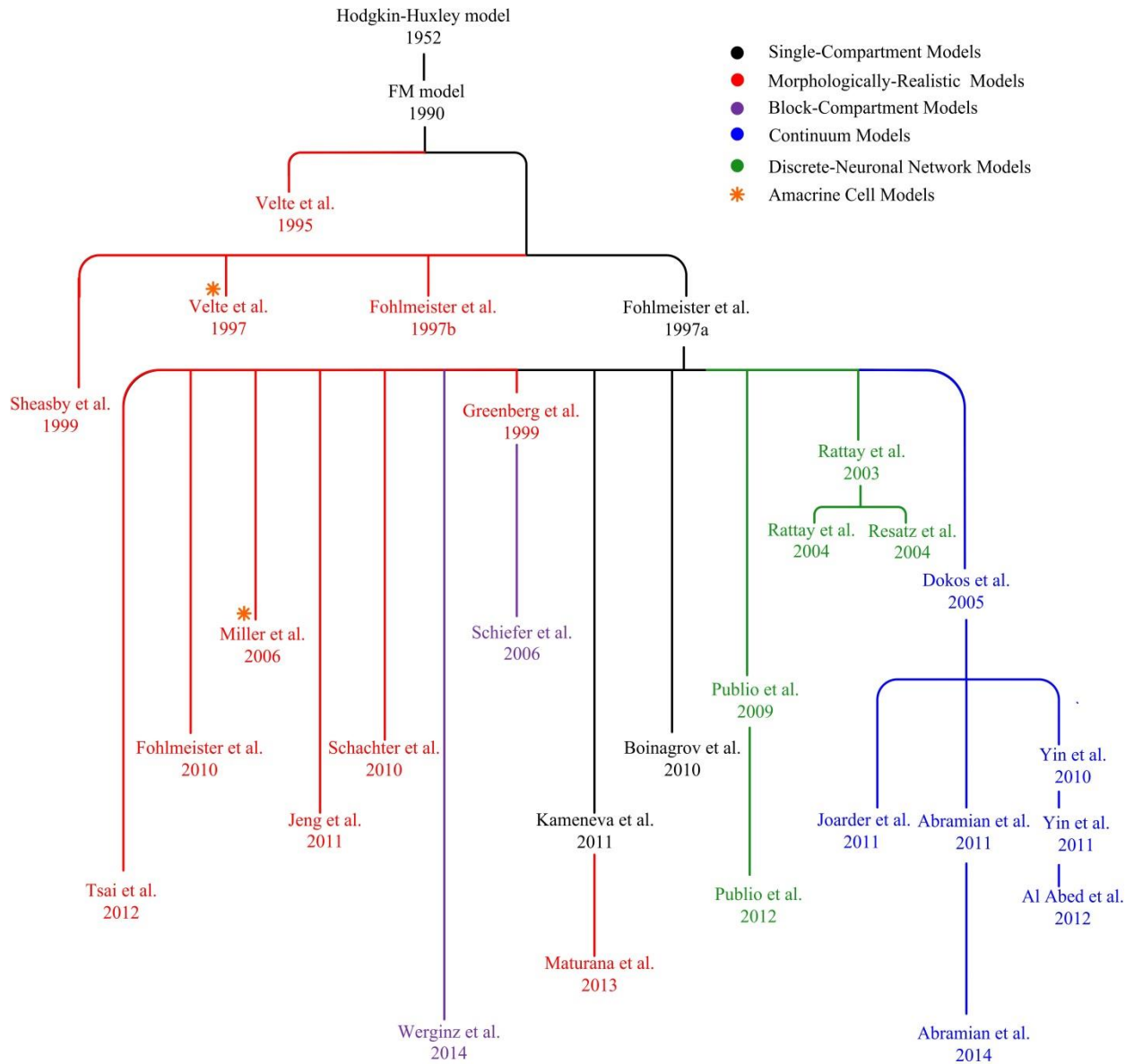


Figure 3.2. Fohlmeister-Miller (FM) model family. The FM model and its extensions have been successfully used for RGC or amacrine cell model formulations. Existing FM type models are widely applied in morphologically-realistic modelling (red) to study the effect of non-uniform channel distribution or regional interaction. Single-compartment FM models (black) focus on studying the contribution of each active conductance and integrating new identified ionic currents into an existing model framework. The FM model is also widely used as individual RGC elements in continuum tissue-based (blue) and retinal circuit models (green), by incorporating retinal layers and network interactions.

3.1.2. Morphologically-Realistic Models

Morphologically realistic neuronal models (see Figure 3.1, type II) are based on detailed anatomical representations of physical components of biological neurons, including soma, axon initial segment (AIS), axon hillock (AH), the distal axon and dendrites. Such models are ideal for studying how cell morphologies and non-uniform distributions of ionic channels contribute to neuronal response dynamics and function. Such models provide a good approximation of biological neuronal behaviour and have been largely used to build structurally “complex” retinal neurons such as amacrine cells and RGCs. They can sometimes include more than 1000 morphological segments to ensure accurate spatial resolution (Fohlmeister et al., 2010).

In morphological cable models, membrane potential is both space and time-dependent, necessitating the modification of eq. (3.1) as follows:

$$I_m = \frac{\partial}{\partial s} \left(\sigma_i \frac{\partial V_m}{\partial s} \right) = \beta \left(C_m \frac{\partial V_m}{\partial t} + J_{ion} + J_{stim} \right) \quad (3.5)$$

where I_m is the volumetric current density (in current per unit volume), s is the arc-length distance along the neuron, σ_i is the intracellular conductivity, β is the local surface to volume ratio ($\beta=2/r$ for a circular cross-section neural region of radius r).

In practice, eq. (3.5) is approximated by separating the neuron into multiple discrete regions, each region associated with its own ionic properties, being connected with neighbouring compartments by axial conductors. The more compartments used, the closer the model tends toward the biological neuron.

An advantage of this type of formulation is that it can also simulate cell responses to extracellular electrical stimulation, as opposed to only intracellular stimulation in the single-compartment model (a single-compartment model assumes no net current across the cell membrane). In this situation, membrane potential is calculated by taking the difference between intracellular potential V_i and extracellular potential V_e :

$$V_m = V_i - V_e \quad (3.6)$$

where V_i is derived from,

$$\frac{\partial}{\partial s} (\sigma_i \frac{\partial V_i}{\partial s}) = \beta \left(C_m \frac{\partial V_m}{\partial t} + J_{ion} \right) \quad (3.7)$$

and the extracellular voltage distribution can be simulated by either a monopolar point source (Greenberg et al., 1999, Jeng et al., 2011) or a disk electrode (Greenberg et al., 1999, Tsai et al., 2012, Jeng et al., 2011) respectively modelled as:

$$V_e = \rho_e I / 4\pi r \quad (3.8)$$

$$\text{or} \quad V_e = \frac{2IR_s}{\pi} \arcsin\left(\frac{2R}{\sqrt{(a-R)^2+z^2}+\sqrt{(a+R)^2+z^2}}\right) \quad (3.9)$$

where ρ_e denotes the resistivity of the retinal extracellular solution, I is the extracellular stimulus current, r is the distance between the stimulating electrode and the point at which the voltage is being computed, a and z are the radial and axial distance respectively from the centre of the disk for $z \neq 0$, R is the radius of the disk, and R_s is the electrode transfer resistance. Note that eqs. (3.8) and (3.9) are applicable to infinite and semi-infinite homogeneous media, respectively.

In some cases, the extracellular voltage distribution is coupled to the local membrane potential (Abramian et al., 2011), and given by

$$\frac{\partial}{\partial s} (-\sigma_e \frac{\partial V_e}{\partial s}) = \beta \left(C_m \frac{\partial V_m}{\partial t} + J_{ion} \right) \quad (3.10)$$

where σ_e denotes the extracellular conductivity.

Neuronal morphology can influence the flow of intracellular currents between neighbouring compartments through the local cell membrane and by intracellular conductance. As a result, morphology can also contribute to the unique spiking behaviour of different RGC types (Sheasby and Fohlmeister, 1999). Although RGC dendritic morphologies and stratifications have been examined extensively, their contribution to RGC spiking patterns is not well understood, owing to the difficulty of isolating and manipulating such properties in experimental preparations. However, the morphologically-realistic modelling approach can quantitatively control a variety of cellular properties, including morphology, and isolate their contributions in shaping firing patterns.

Notable examples of morphologically-realistic retinal neuron models include: a) the Fohlmeister and Miller (1997b) model, the first morphologically-detailed RGC formulation, able to closely

reconstruct action potential shapes and spiking properties; b) the Sheasby and Fohlmeister (1999) realistic RGC encoder, which was used to explore the effect of regional ionic channel distributions along the cellular morphology; c) the Schachter et al. (2010) model, able to reproduce the mechanisms of active dendritic processing of synaptic inputs in direction-sensitive RGCs; and d) the Jeng et al. (2011) sodium channel band model that enabled the determination of factors underlying RGC AP initiation site in response to electrical stimulation.

These morphologically-detailed modelling approaches offer important information on how channel distributions influence RGC firing patterns, and how the interaction between different cell regions influences neural coding. The recent morphologically-realistic model by Abbas et al. (2013) suggested that dendritic ionic channels provide RGCs with the ability to code “looming” motion. Another recent study by Maturana et al. (2013) focused on how physical properties of RGCs contribute to their specific spiking response patterns in response to electrical stimulation.

Experimental findings have also suggested that RGC dendrites exhibit regenerative spikes, as opposed to being simply passive neurites (Velte and Masland, 1999, Oesch et al., 2005, Sivyer and Williams, 2013). The detailed dendritic structure of morphologically-realistic models can provide the framework for investigating dendritic signal processing, since their physical properties can be precisely controlled in these models. In summary, the realistic neuron modelling approach provides a promising tool for studying soma-dendritic interactions, assisting in interpreting experimental studies in dendritic patch-clamp recordings, fluorescent imaging and immunocytochemical channel localisation techniques.

Other than their application to RGCs, morphologically-realistic models have also been applied to amacrine cells. These cells also demonstrate a large diversity in functional properties (Vigh et al., 2000, Yang et al., 1991). A morphologically-realistic starburst amacrine cell model was developed to study the mechanisms underlying local dendritic processing (Fohlmeister et al., 1990). By testing different artificial morphologies, another amacrine modelling study by Tukker et al. (2004) suggested that directional sensitivity mainly depends on a sufficient number of synaptic inputs at the distal dendrites rather than the dendritic morphology itself. Another amacrine modelling study by Miller et al. (2006) suggested that various amacrine cell spiking properties could be reproduced by a RGC model with minimal parameter adjustment, revealing the close ionic relationships between specific amacrine cells and RGCs.

Although certain morphologically-realistic retinal neuron models have also been used in formulating accurate models of local circuits or the whole-tissue retina, to study neuronal interactions during electrical stimulation (Greenberg et al., 1999, Resatz and Rattay, 2004, Rattay et al., 2003, Rattay and Resatz, 2004), their huge computational demand has resulted in their restricted use for population-based simulations, especially in large-scale network modelling.

3.1.3. Block-Compartment Models

An alternative modelling strategy, block-compartment modelling (see Figure 3.1, type III), is typically only used to represent a small number of neuronal regions. This is a compromise between computational efficiency and biological realism. These models can be considered a simplified version of the morphologically-realistic approach, extracting the most essential anatomical information to provide high computational efficiency with minimal neural structure.

The simplest model in this genre is a two-compartment system coupled by a linear conductance, representing a soma and dendritic or axonal compartment. In this way, eq. (3.5) can be updated as follows:

$$\begin{aligned}\frac{G_c}{p}(V_x - V_s) &= C_m \frac{dV_s}{dt} + J_{ion,s} \\ \frac{G_c}{1-p}(V_s - V_x) &= C_m \frac{dV_x}{dt} + J_{ion,x}\end{aligned}\tag{3.11}$$

where V_s and V_x represent the membrane potential in the soma and connected compartment respectively, G_c is the coupling conductance between compartments, p is the percentage of the cell membrane area taken up by the soma, $J_{ion,s}$ and $J_{ion,x}$ are the membrane ion currents of the soma and connected compartment respectively.

This morphology-reduction process depends largely on the motivation of specific studies, as well as the ionic mechanisms involved. Previous findings have suggested that reasonably realistic RGC spiking patterns, comparable to experimental recordings and simulations from morphologically-realistic models, can be obtained using only four neuronal compartments (dendrites, soma, thin segment and axon) (Fohlmeister and Miller, 1997b). A single unbranched dendritic compartment, which allowed region-specific activation of individual channel subtypes,

was shown to be sufficient to elicit summation of excitatory postsynaptic potentials (EPSPs) in RGCs (Abbas et al., 2013). In addition, a simplified axonal activation model was able to successfully predict RGC experimental threshold profiles, as well as the initial activation location in response to electrical stimulation (Abramian et al., 2011).

In another model investigating the origin of AP initiation in RGCs, the dendrites were reduced to unbranched cables of uniform diameter (Carras et al., 1992). Another such simplified RGC-structure model was used to investigate how epiretinal electrical stimulation could result in the production of punctate phosphenes, as opposed to diffuse or streaked perceptions that would be consistent with the recruitment of axons from distant RGCs (Schiefer and Grill, 2006). In a more recent tissue-based retinal model, each point in the RGC layer was represented by an active soma and a passive dendritic compartment, with synaptic input into dendrites included to approximate the underlying neural structure (Al Abed et al., 2013b).

Apart from RGC models, equivalent cable representations have also been used to simulate starburst amacrine cells (Poznanski, 1992, Enciso et al., 2010, Tukker et al., 2004). These models incorporated various levels of simplified cylindrical dendritic structures, and were helpful in elucidating the influence of morphological structure on the mechanisms underlying directional sensitivity in starburst amacrine cell networks.

Block-compartment models have also been applied to morphologically-simple neurons such as photoreceptors (Taylor et al., 1995), bipolar cells (Mennerick et al., 1997), and horizontal cells (Usui et al., 1996b, Smith, 1995) (see Table 3.3). Most of these retinal neuron types do not demonstrate a significant morphological diversity, and only require a relatively simple physical structure such as a cylindrical soma connected to an axon terminal.

One question that must be answered in block-compartment models: is to what extent can retinal neurons be simplified without compromising realistic cell behaviour? A general principle is that models should be at the simplest level required to reproduce desired behaviour of a physical system. This also raises another question: to what extent does neural morphology contribute to its response? Since there is no generally clear simplification approach in block-compartment neural modelling, an alternative approach comprises iterative morphometric simplification, wherein the reducing process is stopped when the model fails to reproduce biological cell responses.

Although the influence of systematic morphologic perturbations in neuronal behaviour has been reported in several brain cell studies (van Elburg and van Ooyen, 2010, Mainen and Sejnowski, 1996), no similar approach has been used yet in retinal neuron modelling. A morphometric simulator was developed recently to study how dendritic intersections, branching points and terminal tips contribute to correct classification of RGC images (Ristanovic et al., 2009). One could conceive, for example, the integration of such a morphometric generator into a modelling framework, to create a platform for exploring the ramifications of RGC morphological variations (Wong et al., 2012, O'Brien et al., 2002, Rockhill et al., 2002).

3.1.4. Continuum Models

Continuum models (see Figure 3.1, type IV) have been used to simulate the response of bulk retinal tissue activation in an averaged spatial sense, without explicit representation of the constituent neurons. Continuum bidomain (i.e. intra- and extracellular domain) formulations have proven useful in cardiac (Roth and Wikswo, 1994, Henriquez, 1993) and neural tissue simulations (Altman and Plonsey, 1990, Martinek et al., 2008). These models are able to simulate bulk active or passive current flow across neuronal membranes into the extracellular space, perturbing the extracellular potential, as has been observed experimentally dating back several decades (Brindley, 1956). This advantage allows the continuum bidomain approach to be an ideal tool for simulating the spatial extent of retinal activation due to extracellular electrical stimulation (see Table 3.2), as well as investigate the influence of electrode configuration, position and stimulus parameters on retinal tissue responses.

In continuum retinal models, the dynamics of both extracellular and intracellular potentials are considered:

$$I_m = \nabla \cdot (-\sigma_e \nabla V_e) = \nabla \cdot (\sigma_i \nabla V_i) = \beta \left(C_m \frac{\partial V_m}{\partial t} + J_{ion} \right) \quad (3.12)$$

where $V_m = V_i - V_e$. Some formulations adopt a “pseudo-bidomain” approach (Yin et al., 2010), by tying the intracellular potential to a remote resting potential,

$$I_m = \nabla \cdot (-\sigma_e \nabla V_e) = g_r (V_r - V_i) \quad (3.13)$$

where V_r is the intracellular potential of a “remote” neural compartment, and g_r is an intracellular conductance tying the intracellular potential to this remote compartment. The effect of the latter parameter is to prevent the intracellular potential from floating freely with changing extracellular potential, due to an applied extracellular stimulus.

The first such model of retinal electric simulation was the Dokos et al. (2005) model, comprising a vitreous and an active RGC layer. It represented a “genuine bidomain” formulation (see eq. (3.9)), and was used to simulate the retinal response to a bipolar electrode configuration using various stimulus waveforms. This model was then extended by adding further retinal layers, including a passive inner plexiform layer, nuclear layer, subretinal space, retinal pigment epithelium and choroid (Joarder et al., 2011). A similar model was also used to investigate the threshold of neuronal activation and the spatial extent of activation, thus providing valuable information regarding stimulus thresholds and localization of activation (Abramian et al., 2011). A more recent retinal model also by Abramian et al. (2014) was used to investigate multi-electrode array stimulation. This model examined the advantages of so-called “quasi-monopolar” stimulation compared to bipolar or monopolar stimulation, combining the low thresholds of monopolar stimulations with the focal spatial activation of hexapolar configurations (Matteucci et al., 2013).

Continuum models can be also be further extended by adding network effects, as in the retinal model of Yin et al. (2010) which included excitatory input from bipolar cells and inhibitory input from wide-field amacrine cells. This model was subsequently refined by adding a dendritic compartment and synaptic currents to account for presynaptic influences on RGC activation (Al Abed et al., 2013b). A further model utilising micro-circuitry of the ON cone pathway was formulated to investigate the network response to large and small spots of light (Yin et al., 2011).

These retinal models can potentially be used in studying the spatial activation profile of electrical stimulation. They provide a promising modelling framework which could be easily extended by incorporating newly identified ionic currents and synaptic connections.

3.1.5. Block-Structured Models of Retinal Function

Apart from the aforementioned biophysically-detailed models, a black-box approach may be used to represent the retinal network. The goal of these models is to capture statistical relationships between light stimuli and cell firing rates without describing detailed neural structure, biophysics, and network connectivity. A popular approach for implementing these block-structured models, also known as “cascaded models”, (see Figure 3.1, type V) involves representing the retina as a series of linear and nonlinear temporal filter elements (Pillow et al., 2005, Pillow et al., 2008). These models can closely reproduce responses of the retina to simple laboratory light stimuli using only a few free parameters. Block-structured models do not attempt to accurately reconstruct biophysical aspects of real retinal neurons. However, they can provide enough overall functional characteristics to cover both the computational aspects of individual retinal neurons, as well as the collective capabilities of large-scale neural networks. They are thus very popular in modelling local neural circuits (Curlander and Marmarelis, 1987) or the whole retinal network (Teeters et al., 1997, Wohrer and Kornprobst, 2009) (see section 3.1.6).

Block-structured models have been largely used to simulate behavioural characteristics of outer retinal neurons, the cones (van Hateren and Snippe, 2007, Shah and Levine, 1996a, Shah and Levine, 1996b) and rods (Hamer et al., 2005, Lamb and Pugh, 1992) (see Table 3.3). Despite their high degree of simplicity, these phenomenological models have been successfully applied to investigate specific physiological mechanisms, including those underlying normal and abnormal rod-receptor activity affected by retinodegenerative disease (Hood et al., 1993), as well as nonlinear synaptic dynamics between photoreceptors and downstream neurons (Juusola et al., 1995).

In block-structured models, the specific neural spiking behaviours are reproduced by their unique transfer functions, characterising linear and non-linear spatial summation mechanisms in various types of RGCs in cat retina (Victor, 1988, Victor, 1987). A generic spike-train simulator was also able to accurately reconstruct spiking responses in a large range of functionally-identified RGCs from different species (Keat et al., 2001).

These functional models have also been popular for studying retinal motion detection and anticipation (see Table 3.2). In one study, motion extrapolation in many species was reproduced by block structures representing the spatially extended receptive field, the biphasic temporal

response and a nonlinear contrast-gain control (Berry et al., 1999). Another block-structured model of object motion sensitive circuitry was able to predict the neuronal response at each stage of the circuit (Baccus et al., 2008), revealing the contribution of specific retinal interneurons in global motion detection.

As mentioned above, there have been numerous successful examples of block-structured models in defining various retinal pathways, receptive fields and stimulus-response transfer functions. However, the mechanisms underlying visual information processing may be far more complex than a series of temporal filters. Functional computation in a real retinal neuron is also closely related to its physical structure, ionic channel expressions and synaptic interactions. In this regard, block-structured models are not ideal for relating high-level response characteristics of neurons, or of a neural network, to the underlying mechanisms from which these characteristics arise. Block-structured models also cannot easily simulate cellular responses to extracellular or intracellular electrical stimulation, limiting their utility in modelling retinal activation by artificial electric stimulation, as in the case of visual prostheses.

3.1.6. Discrete-Neuronal Network Models

The retinal network can also be simulated by grouping discrete retinal neuron elements, based on techniques described in Sections 3.1.1 or 3.1.2 for instance, with excitatory and inhibitory synaptic interactions. In addition to neural properties and stimulus parameters, these discrete-neuronal network models (see Figure 3.1, type VI) also take into consideration the influence of feed-forward and feedback connections among neurons, as well as the physical architecture of the retina.

A discrete-neuronal network model can represent either the entire retinal structure (Wohrer and Kornprobst, 2009) or a retinal subsystem, including the cone-rod network (Smith et al., 1986), the rod-bipolar network (Robson and Frishman, 1996), the cone-horizontal cell circuit (Smith, 1995), the horizontal cell layer (Usui et al., 1996b), the rod pathway (Publio et al., 2009), the cone-pathway (Arguello et al., 2013, Cottaris et al., 2005, Teeters et al., 1997), the amacrine network (Smith and Vardi, 1995), bipolar-RGC interactions (Rattay et al., 2003) and the RGC layer (Publio et al., 2012) (see Figure 3.3).

Most discrete-neuronal network models do not focus on physiological accuracy in individual neurons, but on the functional output of the retina on a large scale. They are generally constructed using non-biophysical neuron formulations such as cascaded models. This allows the models to include a large number of cells with multiple visual pathways rather than specific local micro-circuits, while remaining computationally tractable. As such, they can be very effective for investigating complex neural networks containing a large number of cells of different types. For example, one large-scale retinal model, comprising up to 10^5 neuron elements, was able to achieve both accurate physiological behaviour, as well as reasonable computational efficiency (Wohrer and Kornprobst, 2009). Another study examined the contribution of different cell subclasses in a large RGC population, facilitating the development of testable population-based hypotheses (Bomash et al., 2013). In addition, these functional network models have also been used to provide a comprehensive description of electroretinogram (ERG) generation using only local rod-bipolar circuits (Robson and Frishman, 1996). They can also qualitatively explain various types of adaptation during visual information processing (Hosoya et al., 2005).

Some discrete-neuronal network models also incorporate detailed descriptions of retinal connectivity in successive neural layers, with these connections modelled by conductance-based formulations with a full set of cellular and synaptic parameters. For example, the model of Cottaris et al. (2005) was developed by including both ON and OFF cone pathways with nine types of retinal neuron. The model was able to characterise the spatio-temporal activation of the retinal network during epiretinal electric stimulation, demonstrating the potential contribution of this artificial stimulus mode in shaping visual input to the cortex. Another detailed network model by Hennig et al. (2002) was used to test the influence of various retinal cell classes and sub-circuits on unique response patterns in each identified RGC type. Although conductance-based formulations used in these models were not based on detailed ionic mechanisms in individual neurons, they were still able to achieve a high degree of accuracy in neural outputs at different levels of the retinal circuit (Rekeczky et al., 2001).

It is important to note that detailed single-cell ionic models or morphologically-realistic models are not typically used in discrete-neuronal network modelling, for computational efficiency reasons, except for studies focusing on local micro-circuit stimulation. Examples of the latter include: 1) ionic models of rod/cone photoreceptors, bipolar cells, amacrine cells and RGCs in an

accurate network retinal description (Publio et al., 2009); 2) a modified Hodgkin-Huxley model to represent single neurons in an amacrine cell network (Smith and Vardi, 1995); 3) a morphological RGC model in a local bipolar-RGC circuit (Resatz and Rattay, 2004, Rattay and Resatz, 2004); and 4) a recent model of the RGC layer represented by morphologically-realistic models with dendro-dendritic gap junctions (Publio et al., 2012).

Model type Neuron type	I	II	III	V
Rod photoreceptor (RR)	(Kamiyama et al., 1996, Kourennyi et al., 2004, Ogura et al., 2003, Publio et al., 2006)	N/A	(Taylor et al., 1995)	(Hood et al., 1993, Hamer et al., 2005, Lamb and Pugh, 1992)
Cone photoreceptor (CR)	(Baylor et al., 1974, Kourennyi et al., 2004, Vallego et al., 1980, Publio et al., 2009)	N/A	(Smith, 1995, Taylor et al., 1995)	(van Hateren and Snippe, 2007, Teeters et al., 1997, Shah and Levine, 1996a, Shah and Levine, 1996b)
Horizontal cell (HC)	(Usui et al., 1983, Aoyama et al., 2005, Shirahata, 2008, Aoyama et al., 2000)	N/A	(Usui et al., 1996b, Smith, 1995)	N/A
Bipolar cell (BC)	(Publio et al., 2009, Usui et al., 1996a)	N/A	(Mennerick et al., 1997)	(Robson and Frishman, 1996, Robson and Frishman, 1995)
Amacrine cell (AC)	(Publio et al., 2009, Shirahata, 2011, Steffen et al., 2003, Smith and Vardi, 1995)	(Velte and Miller, 1997, Miller et al., 2006)	(Enciso et al., 2010, Poznanski, 1992, Tukker et al., 2004)	(Saglam et al., 2009)
Retinal ganglion cell (RGC)	(Fohlmeister et al., 1990, Fohlmeister and Miller, 1997a, Kameneva et al., 2011, Publio et al., 2009)	(Velte and Miller, 1995, Publio et al., 2012, Rattay and Resatz, 2004, Rattay et al., 2003, Maturana et al., 2013, Tsai et al., 2012, Sheasby and Fohlmeister, 1999, Schachter et al., 2010, Jeng et al., 2011, Greenberg et al., 1999, Fohlmeister et al., 2010, Velte and Miller, 1997, Resatz and Rattay, 2004, Fohlmeister and Miller, 1997b, van Rossum et al., 2003)	(Abramian et al., 2011, Carras et al., 1992, Al Abed et al., 2013b, Abbas et al., 2013, Fohlmeister and Miller, 1997b, Werginz et al., 2014)	(Cai et al., 2007, Keat et al., 2001, Victor, 1987, Victor, 1988, Hosoya et al., 2005, Pillow et al., 2005)

Table 3.3 Computational models of different retinal neuron and model types. I. single-compartment model, II. morphologically-realistic model, III. Block-compartment model and V. block-structured model (IV. Continuum models and VI. Discrete-neuronal network models are not included in this table). RR, CR, HC and BC models are largely limited to the single-compartment and block-compartment levels due to their relatively simple morphology. Morphologically-complex neurons such as ACs and particularly RGCs are represented across all model types. Block-structured formulations can reproduce the functional input/output relationship between light stimulus inputs and cell responses in nearly every retinal neuron type without considering the detailed biophysical structure of the neuron.

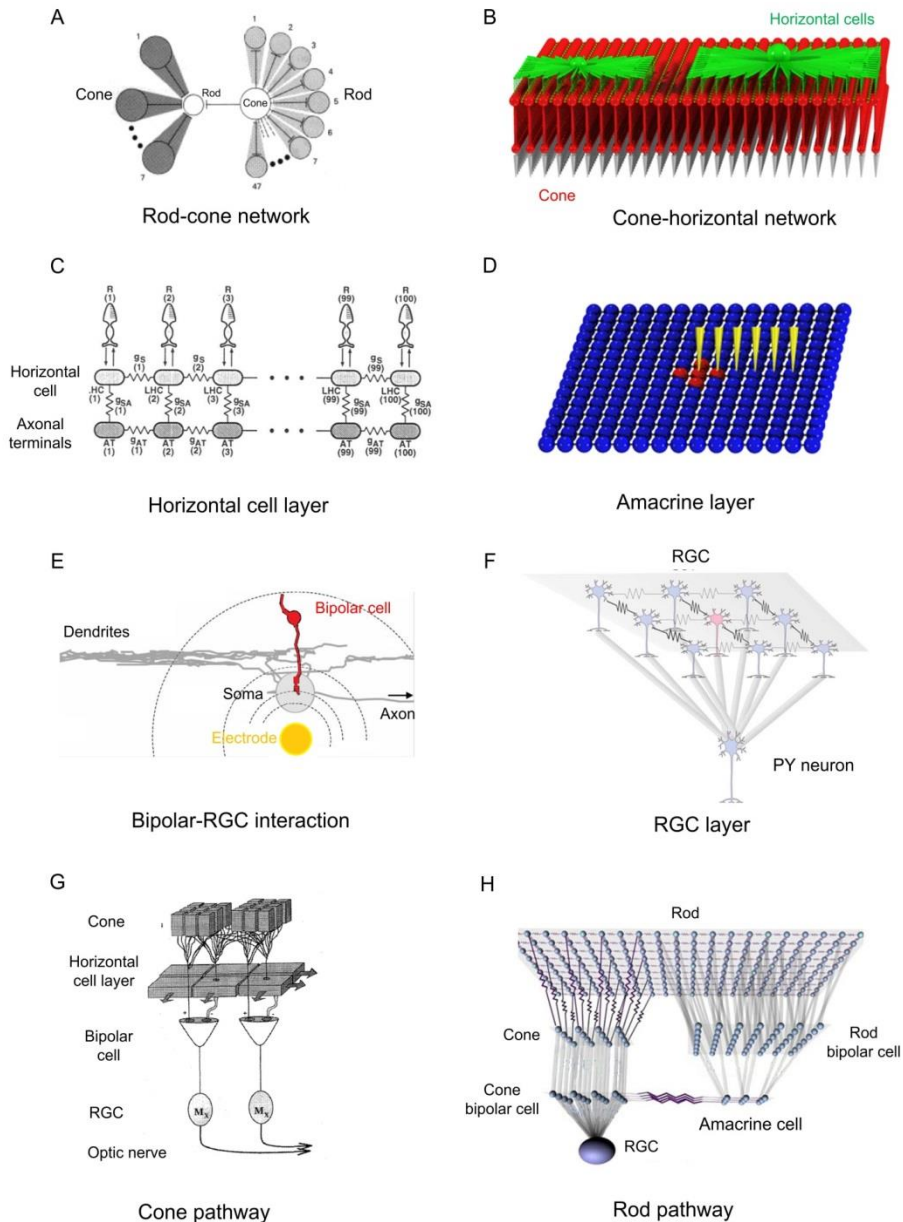


Figure 3.3. Examples of types of retinal network models. A: Cone-rod network, based on Rallian static cable equations (Rall, 1959). 48 rods converge on each cone and each cone connects to 8 other cones via gap junctions. Each rod or cone model is represented by a spherical soma and a cylindrical axonal segment. Rod-cone basal processes and cone-cone basal processes are modelled by cable segments with different terminating gap junction conductances (Smith et al., 1986). B: Cone-horizontal circuit, consisting of a 26×26 cone (red) array and two different types of horizontal cells (green). Both cones and horizontal cells are approximated using block-compartment models. Each horizontal cell is in contact with multiple cones through their dendritic terminals (Smith, 1995). C: 1-D horizontal cell layer, consisting of 100 horizontal cell elements with a Hodgkin-Huxley-type somatic compartment and a linear RC axonal compartment. Different gap junction values are employed between neighbouring somas and those between axonal terminals (Usui et al., 1996b). D: Amacrine network, reconstructed using a 15×15 array of Hodgkin-Huxley-type spherical isopotential somas with presynaptic terminals and synapses (Smith and Vardi, 1995). E: Local bipolar-RGC circuit, coupled by a morphologically-detailed RGC and bipolar cell models (Rattay et al., 2003). F: RGC layer, reconstructed using a 3×3 array of morphologically-detailed RGC models, with dendrodendritic gap junctions between neighbouring cells. Each RGC reproduces an excitatory chemical synapse with a pyramidal (PY) cell from the lateral geniculate nucleus (LGN) of the thalamus (Publio et al., 2012). G: Cone-pathway circuit (Shah and Levine, 1996a), reconstructed with a series of block-structured models. There is approximately one RGC output for every nine cones. H: Rod pathway circuit, built using connected single-compartment ionic models of rod/cone photoreceptors, bipolar cells, amacrine cells and RGCs coupled with electrical and chemical synapses (Publio et al., 2009).

3.1.7. Outlook on Retinal Neuron Modelling

Among all retinal neuron types, the mechanisms underlying morphologically complex neurons such as amacrine cells or RGCs are still unclear (for a review see Masland (2012)). There are more than thirteen identified amacrine cell types and twelve RGC types in the mammalian retina. A definitive description of these cells has not yet been made due to their rich diversity in both intrinsic electrophysiological and morphological properties. Limited experimental information on ion channel kinetics and regional distributions in identified cell types also makes cell-specific model parameter optimisation a difficult task. Prior models of these neurons (see Table 3.3) have been limited to identification of individual RGC types without regard to the diversity of cellular morphology and membrane channel distributions/kinetics in each cellular region. This is despite the fact that the correlation between neuronal function and inherent biophysical properties is highly significant, as suggested by experimental studies (O'Brien et al., 2002, Wong et al., 2012). On the other hand, there are still many debates about the functional classification and mechanisms of horizontal cells and bipolar cells, despite their far less morphological diversity. New knowledge about these “pre-processing” neurons continues to be discovered (Herrmann et al., 2011, Klaassen et al., 2011, Jackman et al., 2011, Freed, 2000, Dreosti et al., 2011). Therefore, further model validation based on newly found experimental evidence is still required to quantitatively identify and define these cells.

At the single cell level, the composition of ion channels in retinal neuron models continues to be refined. The initial FM model with five active membrane currents appears to be oversimplified, with the identification of further ionic channels in retinal neurons (Miller et al., 2002, Tabata and Ishida, 1996, Lee and Ishida, 2007). Ionic channel formulations are generally based on voltage-clamp experimental data. The properties of these new currents and their regional distributions in different neuron types may significantly contribute to the overall neural response. With the likely discovery of more ionic mechanisms in retinal neurons, there still remains substantial room for improvement of the single-cell models.

In whole-retina models, the functional significance of cell morphology has not been systematically studied, unlike their reported importance in brain neuron network modelling (Traub et al., 2005). Why do retinal neurons present a large range of morphological diversity? It appears that morphological factors play some role in mediating neuronal function. Cell-specific morphological information will therefore play an increasing role in the development of future tissue or network-based models of retinal function.

3.2 Parameter Estimation of Excitable Cell Models

Modelling neuronal electrical activities is perhaps more challenging than other excitable tissues, due to the large diversity of AP shapes and spiking properties. Most neuronal models are formulated using a system of ODEs or PDEs containing a number of model parameters. The number of parameters can range from 3-5 in simple phenomenological models to more than 100 in a biophysically-detailed conductance-based model.

Despite the significant improvement of experimental techniques including dendritic patch-clamp, fluorescent imaging and immunocytochemical channel localisation techniques, there is still considerable lack of knowledge on differences in ion channel expressions among many identified neuron types, due to their large diversity in both physical and physiological properties. For example, there are more than twelve identified RGC types in the mammalian retina, but limited experimental information has been found on their cell-specific ion channel kinetics and distributions. In addition, certain model parameters are impossible to be measured directly in experiments due to the limited knowledge of the micro-structure of the cell membrane and transmembrane channels. For instance, the patch-clamp technique can provide single channel conductance but not the total number of ion channels in a whole cell membrane. General kinetics such as time/space constants and steady-state gating values can be determined by voltage-clamp recording, but detailed kinetic parameters are still undeterminable with current recording techniques. The number of these unknown parameters rises with the increasing complexity of model formulations.

Therefore, model parameter values need to be numerically estimated by minimising the difference between experimental data and model outputs. Although hand-tuning of parameters is still being used in recent modelling studies (Gold et al., 2007), automated parameter estimation approaches are essentially required in neuronal model development, especially when the number of parameters is large and detailed information on the physiological characteristics of the target neuron is not available.

In practice, the size and complexity of the parameter search space grows dramatically with an increase in the number of free parameters. A higher degree of complexity in parameter interactions or co-dependencies also results from the presence of additional voltage and calcium-dependent dynamics in a model. In addition, the varying morphological properties and regional ionic channel distributions adds considerable complexity to overall model structure, making optimisation of model parameters even more difficult. Over the last few

decades, many parameter optimisation strategies based on different theories and motives, have been proposed to solve the aforementioned problems.

A parameter optimisation strategy, regardless of the principle it is based on, can be summarised using two components: 1) a numerical algorithm used to quickly search the best solution in a given parameter space; 2) an objective function that best represents the differences between the behaviour of the model and the real biological system. In this review section, we will begin by reviewing optimisation studies in developing computational neuronal models based on two algorithm classes: gradient-based and evolutionary-based methods. We will then discuss the significance and limitations of these applications using different objective functions: point-point time-series matching, phase-plane matching, and a variety of feature-based match functions. Other than optimisation algorithms, some recent alternative methods for parameter estimation in neuronal modelling will also be discussed.

3.2.1. Gradient-Based Algorithms

In non-linear least squares problems, a strict convex quadratic model is often used to locally approximate the objective function (also see Section 3.2.3 and 3.2.4).

$$Q(\Delta\mathbf{p}) = \sum_{i=1}^m r_i^2(\mathbf{p}) = Q_0 + \Delta\mathbf{p}^T \cdot \mathbf{G} + \frac{1}{2} \Delta\mathbf{p}^T \cdot \mathbf{H} \cdot \Delta\mathbf{p} \quad (3.14)$$

where $r_i(\mathbf{p})$ is the i th nonlinear residual equation of the system, \mathbf{p} is the unknown parameter vector, $\Delta\mathbf{p}$ is the parameter modification vector, \mathbf{G} is the gradient vector and \mathbf{H} is the Hessian square matrix. The detailed derivation of eq. (3.14) is provided in Section 4.2 of Chapter 4. All optimisation methods based on the above quadratic form assume that parameter convergence to the local objective minimum can be iteratively obtained, even though the objective function is not perfectly quadratic.

A gradient-based (GB) algorithm tries to find the most efficient downhill path from an arbitrary initial point. These methods can be summarised by two main components: 1) choice of parameter step direction; 2) choice of step size (Beveridge and Schechter, 1970). Many significant improvements have been made to more efficiently estimate the above two components.

Most existing gradient methods are based on two fundamental algorithms – Newton’s method and the steepest descent method. The Newton step (parameter increment vector $\Delta\mathbf{p}$) can be obtained by setting the gradient of eq. (3.14) to zero, to obtain:

$$\Delta\mathbf{p} = -\mathbf{H}^{-1}\mathbf{G} \quad (3.15)$$

Usually the Hessian matrix can be approximated from the Jacobian matrix $\mathbf{J} = (\partial Q(\mathbf{p})/\partial \mathbf{p})$ using $\mathbf{H} \approx 2\mathbf{J}^T\mathbf{J}$, to avoid calculating the second derivative matrix, which is highly computational demanding. The minimum can be achieved by taking a single Newton step if the objective surface is perfectly quadratic, which satisfies eq. (3.14). However, the Newton step will be undefined when $\mathbf{J}^T\mathbf{J}$ is singular. Such a problem arises especially when large-scale parameter optimisations are performed. More importantly, the objective function is often non-quadratic in practical problems.

In the steepest descent method, the objective function eq. (3.14) is iteratively minimised along the direction of the local gradient, according to:

$$\Delta\mathbf{p} = -\gamma\mathbf{G} \quad (3.16)$$

where γ is a non-negative factor governing the downhill direction step. The searching direction is updated at each iteration based on the previous local gradient. For a poorly conditioned convex objective (the surface contains long-thin “valleys”), the steepest descent algorithm may increasingly undergo a time-consuming “zigzag” searching pattern until the minimum is found.

Many extensions to gradient-based methods, employing a series of quasi-Newton methods (Pal, 2009), have been proposed to iteratively improve the estimate of the inverse of the Hessian matrix H^{-1} , because its analytical calculation is almost impossible in most practical problems. Extensions such as the Levenberg-Marquadt method (Marquardt, 1963) and curvilinear gradient method (Dokos and Lovell, 2003) have been proposed to combine the traditional Newton and steepest descent approaches. That is, the minimum search starts with the steepest descent direction and terminates at the full Newton step (details of the curvilinear gradient method are given in Chapter 4).

The advantage of the curvilinear gradient routine becomes more apparent for large-scale optimisation problems, when quasi-Newton routines fail to estimate the nearly singular Hessian, and the Levenberg-Marquadt method degenerates to the pure steepest decent routine (Dokos and Lovell, 2003, Dokos and Lovell, 2004). The curvilinear gradient routine has been largely used in modelling studies of cardiac electrophysiology and been extended to retinal neuron modelling more recently. Notable examples include: 1) fitting a biophysically-detailed myocyte model to multiple AP waveforms recorded experimentally from central and peripheral sinoatrial node (SAN) tissue (Lovell et al., 2004), 2) fitting a generic ionic model to *in vitro* AP waveforms from central/peripheral SAN as well as right and left atrial myocytes under different electrical stimulus protocols and pharmacological conditions (Guo et al., 2013) and 3) fitting a tissue-based model to *in vitro* AP waveforms from central/peripheral SAN and right atrial myocytes (Al Abed et al., 2013a). All of these studies were large-scale optimisation problems with some 60-170 estimated parameters. However, they also found that large numbers of parameters result in over-determined systems for which unique identification cannot always be achieved.

Another improvement employs a hybrid of the gradient-based method and other optimisation methods. For example, a hybrid method was used to optimise a 22-parameter Markov-type hERG channel gating model (Szekely et al., 2011). In this study, a genetic method (see next section) was combined with the curvilinear gradient method to effectively select optimal

initial parameter sets, thus avoiding exhaustive searches in large parameter space. In another study involving multi-compartment neuron model optimisation (Huys et al., 2006), a gradient-based algorithm was used to estimate the local neuronal properties, whereas the global channel distributions, inter-compartment resistances and synaptic input for the whole cell morphology were inferred by a linear regression approach.

Other than optimising conductance-based neuronal models, the gradient-based method was also used to optimise a cascade encoding model to reproduce multiple spiking responses recorded *in vivo* (Paninski et al., 2004).

Despite their extensive use in excitable cell model optimisation, the gradient-based algorithm has an inherent disadvantage: namely, the “gradient” by itself is a local property. Although some improvements including an iterative reweighting strategy (Dokos and Lovell, 2004) and a hybrid approach (Szekely et al., 2011) have been described to “escape” the local minimum, these methods still suffer from local minima problems when being applied in practice. Therefore, gradient-free methods such as the evolutionary method, simplex method, random searching method as well as some hybrid strategies are also popular in neuron modelling (see Table 3.4).

3.2.2. Evolutionary-Based Algorithms

Evolutionary-based algorithms use stochastic searching to simulate natural phenomena or social behaviours of biological species (Elbeltagi et al., 2005). Unlike gradient-based methods, evolutionary-based algorithms do not require local derivative information or even any knowledge about the system.

A landmark example of the evolutionary-based method in neuronal model optimisation is the genetic method (Goldberg, 1989). Many other evolutionary-based algorithms, such as the memetic algorithm (Moscato, 1989) and covariance matrix adaptation evolution strategy (Bush et al., 2005), follow a similar optimising strategy to the genetic method. In the genetic method, parameter optimisation begins with multiple initial parameter sets which are considered as interbreeding individuals in the population. Individuals with good fitness values are critically selected as “parents”, and then the “children” are updated by recombination of the current generation (reproduction) as well as random modifications (mutation). The existing population will keep on being substituted by the naturally-selected

advanced individuals until some terminating condition is achieved. Algorithm parameters such as population size, generation number, crossover rate and mutation rate are user-defined.

Since their first reporting, genetic methods have proven their ability and generic nature in studies of myocyte modelling (Syed et al., 2005, Dastgheib et al., 2009), single-compartment models (Vanier and Bower, 1999), block-compartment models (Keren et al., 2005), morphologically-realistic neuronal modelling (Keren et al., 2009), as well as single ionic channel kinetic models (Gurkiewicz and Korngreen, 2007). In some morphologically-realistic model studies, the genetic method was also combined with other methods such as parameter peeling procedures and linear regression to improve parameter identifiability (Keren et al., 2009, Huys et al., 2006).

The evolutionary-based algorithm has also been compared with the gradient-based method in terms of performance for excitable cell model optimisation. In one study of cardiac myocyte modelling, both methods were applied to estimate ionic conductance values to simulate 1-D ventricular re-entry waveforms. Results showed that the maximum and mean deviation of estimated parameters from their default values using the genetic method is significantly less than those using the curvilinear gradient method, revealing improved identifiability achieved by the genetic method over the gradient-based method (Dastgheib et al., 2009). In contrast, another study of neuron modelling found that a significant number of iterations were required when more parameters were involved using evolutionary-based algorithms, revealing their disadvantage for large-scale problems (Vanier and Bower, 1999). Indeed, the applicability of the evolutionary method for large-scale problems is still not evident. In most of the optimisation studies in Table 3.4, only maximum conductance parameters (normally less than 20 parameters) were optimised, and all of the kinetic parameters were assumed to be “well-known”. In fact, optimised kinetics is also important, since the kinetic parameters from the literature were defined based on a particular experimental data (Willms et al., 1999, Guo et al., 2013, Murphey et al., 1995, Tabak et al., 2000). Although the kinetic parameters in some well-defined biophysically-detailed models (McCormick and Huguenard, 1992, Fohlmeister and Miller, 1997a) were validated using multiple experimental voltage-clamp data, whether they are capable of reproducing additional datasets based on different conditions or neuron types, is still unclear.

As an alternative approach, database search methods generate a huge database of all possible neuronal activities, by independently varying parameters using a single-cell neuron model

based on *in vitro* experimental evidence (Goldman et al., 2001, Prinz et al., 2003a, Gunay et al., 2008). Some of these databases can include more than 1.7 million neuronal responses (Prinz et al., 2003a). Rather than a single point in parameter space, this approach can generate a global map of the activity states of a neuron as a function of corresponding parameters, thus revealing a clear linear or nonlinear dependency between each parameter. However, the “global” identification is limited to certain model parameters (normally 5-9 maximum conductance parameters). Moreover, preliminary knowledge of the physiological range of these parameters is required to generate the database, which limits its utility in large-scale parameter optimisation problems.

As well as the methods mentioned above, random or pseudo-random searching algorithms such as simulated annealing (Vanier and Bower, 1999, Nowotny et al., 2008), stochastic searching (Foster et al., 1993, Vanier and Bower, 1999, Hayes et al., 2005), and exhaustive searching (Gunay et al., 2008), have also been used in neuron model optimisation. Similarly, their applicability to large-scale problems is still not proven.

Based on algorithm performance in existing optimisation studies, there exists no generic global optimisation method. In fact, the same neuronal model can usually be optimised using a range of routines (Vanier and Bower, 1999, Tabak et al., 2000, Mitra et al., 2012, Dastgheib et al., 2009).

3.2.3. Objective Function

A searching algorithm is a method for locating the best solution in a given search space, but the definition of “best solution” and the shape of the “searching surface” are given by the objective function (also known as error function, cost function or fitness function). The most frequently-used objective functions in excitable cell modelling can be categorised into time-series sum of squares error, phase-plane sum of squares error, and a variety of feature-based match functions.

I. Time-series sum of squares error function

The most straightforward objective function is defined by the sum of squares of the point-by-point error between the model and data:

$$\sigma_{TSPP} = \sqrt{\frac{1}{M} \sum_{i=1}^M (f_i(\mathbf{p}) - d_i)^2} \quad (3.17)$$

where $f_i(\mathbf{p})$ is the model output as a function of parameter vector \mathbf{p} corresponding to the i th data point d_i , and M is the number of data points in the dataset.

One problem of this time-series point-by-point (TSPP) match function is its high sensitivity to spike timing shift between the model and data, limiting its utility in neuron model optimisation, since most neuron-generated AP durations are less than ~ 2 ms. However, this objective function has been widely used in cardiac myocyte AP fitting (Guo et al., 2013, Dokos and Lovell, 2004, Al Abed et al., 2013a, Syed et al., 2005), voltage-clamp data fitting (Gurkiewicz and Korngreen, 2007, Szekely et al., 2011) and a variety of “non-spiking” data fitting (Daguanno et al., 1986, Vanier and Bower, 1999).

II. 2-D phase-plane sum of squares error function

Another approach is to compare the 2-D phase plot (also termed phase-plane) determined by the relationship between membrane potential and its derivative (V_m vs. dV_m/dt). For instance, the phase-plane trajectory density (PPTD) method is formulated as follows:

$$\sigma_{PPTD} = \sqrt{\frac{1}{M} \sum_{i=1}^M (d_i - f_i(\mathbf{p}))^2} \quad (3.18)$$

where d_i and $f_i(\mathbf{p})$ denote the number of points in the $V_m - dV_m/dt$ sequences for data and model respectively, and M denotes the total number of data and model points. Recent neuron studies suggest that neuronal AP features, best visualized using an AP phase plot, can indirectly reflect the interactions between different neuronal compartments and indicate important information such as ionic channel distribution in multiple functional cellular regions (McCormick et al., 2007, Mainen and Sejnowski, 1996, Herz et al., 2006, Fohlmeister and Miller, 1997b).

Compared to the time-series least squares error approach, the phase-plane least squares match demonstrates much less sensitivity to spike time shifts, and has been independently used in cerebellar purkinje neuron model optimisation (Achard and De Schutter, 2006). However, the advantage of the phase-plane objective function is also its disadvantage, since accurate

reconstruction of spike timing information is important in neuron studies such as the study of neuron types in visual systems. Therefore, the phase-plane objective approach is often combined with other criteria to evaluate model performance (Druckmann et al., 2007, Keren et al., 2005, Hayes et al., 2005).

III. Feature-based match functions

Various “feature-based” objective functions have also been shown to improve the match between neuron model and data. Rather than comparing all data points in experimental profiles, these approaches extract only essential information of interest (features) directly from the training data. This information includes spiking rate (Druckmann et al., 2007, Gunay et al., 2008), spiking latency (Druckmann et al., 2007), inter-spike interval (ISI) (Lovell et al., 2004, Bhalla and Bower, 1993, Keren et al., 2005), AP overshoot (Druckmann et al., 2007, Lovell et al., 2004), after-hyperpolarization potential (Druckmann et al., 2007, Lovell et al., 2004), sag amplitude (Gunay et al., 2008), AP width (Druckmann et al., 2007, Lovell et al., 2004, Gunay et al., 2008), AP amplitude (Druckmann et al., 2007, Gunay et al., 2008) and AP threshold (Gunay et al., 2008).

Apart from providing a single scalar value directly extracted from given experimental profiles, this approach can also be used to modify time-series spiking datasets using a user-defined “transfer function”. For example, a “staircase” function to represent the spiking-timing relationship was proven successful in optimising a phenomenological neural model to produce complex spike-timing behaviours in pyramidal cells. An accommodation index function, defined by the normalised average of the difference in consecutive ISIs, was used to disregard possible transient spiking behaviours recorded in basket cells (Druckmann et al., 2008, Druckmann et al., 2007). Moreover, in order to solve the spiking-time shifting problem, one study using a pyramidal neuron model converted the voltage time-series into the frequency domain via a fast Fourier transform (Bush et al., 2005, Murphey et al., 1995). Another modelling study in the ganglia of *Aplysia* summed the individual traces over time in order to broaden the peaks in the objective function (Hayes et al., 2005).

With these feature-based objective functions, a model can be designed to focus on the specific behaviour of interest in turn providing more effective training sets for the model.

3.2.4. Multi-Objective Optimisation

Typically, a single dataset is not sufficient to optimise a model defined by multiple ODEs and parameters. Given enough degrees of freedom, a powerful searching algorithm may be able to find a set of parameters to accurately fit a model to a specific dataset. However, such a model will typically fail to predict new data, particularly if the model is highly non-linear and involves many parameters. Therefore, multi-objective optimisation is to be preferred when developing excitable cell models.

In this context, multi-objective can be interpreted as 1) multiple datasets of the same quantity, e.g. multiple voltage- or current-clamp datasets corresponding to different stimulation conditions (Vanier and Bower, 1999, Gurkiewicz and Korngreen, 2007); 2) different properties obtained from the same experimental profile, e.g. time and frequency domain representations of membrane potential (White et al., 1992, Tabak et al., 2000); 3) data features recorded from multiple profiles, e.g. spiking number, latency and interval patterns obtained from spiking responses to multiple stimuli (Lovell et al., 2004); 4) the combination of the previous three items for a high-level accurate neuron reconstruction (Druckmann et al., 2008, Keren et al., 2005, Hayes et al., 2005).

A multi-objective sum of squares cost function can be defined by the weighted sum:

$$\sigma^2 = \sum_{k=1}^N W_k \cdot \sigma_k^2 \quad (3.19)$$

where $\sigma_k(\mathbf{p})$ is the RMS error in the k th objective record, and W_k is a user-defined weight function whose value may be adjusted depending on the relative importance of each objective, and N is the total number of objectives required to be simultaneously minimised. Some studies normalised each $\sigma_k(\mathbf{p})$ value to allow them to equally contribute to the cost function.

Optimising a neuron model using multi-objectives is extremely difficult due to the highly nonlinear behaviour of neurons. Adding more objectives will have a significant impact on the parameter search surface in terms of the locations and density of the local minima distributions. In general, the search space may become more “noisy” with more local optima and ridges which negatively affect optimisation performance. This is even worse for the gradient-based optimisation method, since more computational resources are required due to the larger size of the Jacobian matrix (Bush et al., 2005).

However, its benefits to model validation are more obvious. When fitting simultaneously to multiple datasets (or objectives), model behaviours tend to be well defined because extra

physiological information is incorporated into the optimisation. Many studies indicate that multi-objective optimisation can improve the predictive power of different model types (Mitra et al., 2012, Nowotny et al., 2008, Achard and De Schutter, 2006, Al Abed et al., 2013a, Rauch et al., 2003).

In addition, adding a well-chosen objective can also improve the parameter identifiability. For example, extracellular and intracellular measurements at known locations have been shown to be useful for constraining passive model parameters such as intracellular resistivity and membrane capacitance (Gold et al., 2007). Another study suggested that unique parameter solutions are possible if the membrane potential datasets are available in all compartments of a neuron, since model conductivity parameters can be calculated by a linear regression without resorting to a search of the parameter space in this situation. (Huys et al., 2006). In practice, however, performing multiple membrane potential measurements on the same cell is difficult *in vitro*, and currently impossible *in vivo*.

As an alternative approach, fitting to a membrane potential dataset in response to random, pseudo-random and EPSP-like current injections, may provide a better representation of realistic neuronal inputs than step function-like injections, providing more useful information for model training (Jolivet et al., 2004, Mitra et al., 2012, Dokos and Lovell, 2004, Paninski et al., 2004, Foster et al., 1993). This approach can also be considered equivalent to multi-objective optimisation, since the model is optimised to adapt to multiple neuronal sub-threshold and spiking properties induced by more informative and independent inputs.

Optimisation Method	Objective function	Training dataset(s)	No. of free parameters	Model level	Model description	Biological System	Reference
GB	time-series point-by-point match	1 artificial * V_m 1 <i>in vitro</i> V_m	9	M-C	Rall (1977) model	neuronal passive properties	(Daguanno et al., 1986)
GB	time-series point-by-point match frequency-domain match	12 artificial V_m	4	M-C	White et al. (1992) model	neuronal passive properties	(White et al., 1992)
GB	time-series point-by-point match multiple spiking pattern match	5 <i>in vitro</i> V_m	8	M-C	Bhalla and Bower (1993) model	olfactory bulb neuron	(Bhalla and Bower, 1993)
SS	time-series point-by-point match frequency-domain match	<i>in vitro</i> V_m in response to EPSC-like input	4	S-C	Connor et al. (1977) model	brain stem neuron	(Foster et al., 1993)
GB	time-series point-by-point match frequency-domain match	4 <i>in vitro</i> V_m (voltage-clamp)	11	M-C	Murphey et al. (1995) model	spinal neuron	(Murphey et al., 1995)
GA/GB/SA/SS	spiking-timing match	6 artificial V_m	8	S-C	McCormick and Huguenard (1992) model	thalamocortical relay neuron	(Vanier and Bower, 1999)
GA/GB/SA/SS	time-series point-by-point match	5 artificial V_m	15	M-C	Vanier and Bower (1999) model	neuronal passive dendrites	(Vanier and Bower, 1999)
GA/GB/SA/SS	time-series point-by-point match	6 <i>in vitro</i> V_m	23	M-C	Koch and Segev (1997) model	L2 superficial pyramidal neuron	(Vanier and Bower, 1999)
GB/NM	time-series point-by-point match frequency-domain match	5 artificial V_m	11	M-C	Tabak et al. (2000) model	generic neuron	(Tabak et al., 2000)
DS	N/A	N/A	5	S-C	Liu et al. (1998) model	stomatogastric ganglion	(Goldman et al., 2001)
DS	N/A	N/A	8	S-C	Prinz et al. (2003b) model	stomatogastric ganglion	(Prinz et al., 2003a)
SS	frequency-domain match	5 <i>in vitro</i> V_m	5	I-F	Rauch et al. (2003) model	L5 pyramidal neuron	(Rauch et al., 2003)
GB	time-series point-by-point match	2 <i>in vitro</i> V_m	170	S-C	Lovell et al. (2004) model	Sinoatrial myocyte	(Lovell et al., 2004)
GB	time-series point-by-point match	artificial V_m in response to random input	63	S-C	Beeler and Reuter (1977) model	Ventricular myocyte	(Dokos and Lovell, 2004)
NM	averaged V_m match	artificial V_m in response to random input	4	I-F	Jolivet et al. (2004) model	cortical neuron	(Jolivet et al., 2004)
RB+GB	spiking density match	artificial V_m in response to random input	5	I-F	Paninski et al. (2004) model	generic neuron	(Paninski et al., 2004)
GA	time-series point-by-point match phase-plane match ISI match function	4 <i>in vitro</i> V_m	19	M-C	Mainen et al. (1995) model	L5 pyramidal neuron	(Keren et al., 2005)
SS	time-series point-by-point match phase-plane match cumulative voltage integral match	2 <i>in vitro</i> V_m	10	S-C	Hayes et al. (2005) model	ganglia of <i>Aplysia</i> neuron	(Hayes et al., 2005)

Continued on next page

Optimisation Method	Objective function	Training datasets	No. of free parameters	Model level	Model description	Biological System	Reference
GA	time-series point-by-point match	4 <i>in vitro</i> V_m	9	S-C	Nygren et al. (1998) model	atrial myocyte	(Syed et al., 2005)
RB/CMA-ES	frequency-domain match	8 artificial V_m	10	M-C	Pinsky and Rinzel (1995) model	CA3 pyramidal neuron	(Bush et al., 2005)
RB+GB	time-series point-by-point match	artificial V_m in response to random input	10	M-C	Dayan and Abbott (2001) model	generic neuron	(Huys et al., 2006)
GA	phase-plane match	21 artificial V_m	24	M-C	Deschutter and Bower (1994) model	cerebellar purkinje cell	(Achard and De Schutter, 2006)
GA	time-series point-by-point match	27 <i>in vitro</i> V_m (voltage-clamp)	20	S-C	Baranauskas and Martina (2006) model	single ionic channel	(Gurkiewicz and Korngreen, 2007)
HT	time-series point-by-point match	2 <i>in vitro</i> V_m	14	M-C	Gold et al. (2006) model	CA1 pyramidal neuron	(Gold et al., 2007)
GA	multiple spiking feature-based match	2 <i>in vitro</i> V_m	12	M-C	Druckmann et al. (2007) model	basket cell interneuron	(Druckmann et al., 2007)
ES+DS	multiple spiking feature-based match	4 artificial V_m	9	M-C	Gunay et al. (2008) model	globus pallidus neuron	(Gunay et al., 2008)
GA	phase-plane match	1 artificial V_m	12	M-C	Druckmann et al. (2007) model	basket cell interneuron	(Druckmann et al., 2008)
SA	multiple spiking feature-based match	1 <i>in vitro</i> V_m					
	spiking-timing match	11 <i>in vitro</i> V_m	20	M-C	Nowotny et al. (2008) model	lateral pyloric neuron	(Nowotny et al., 2008)
	averaged V_m match						
GA	time-series point-by-point match	2 <i>in vitro</i> V_m	19	M-C	Mainen et al. (1995) model	L5 pyramidal neuron	(Keren et al., 2009)
GA/GB	time-series point-by-point match	1 artificial V_m	6	M-C	Luo and Rudy (1991) model	ventricular myocyte	(Dastgheib et al., 2009)
GA+GB	time-series point-by-point match	1 <i>in vitro</i> I_{hERG}	22	S-C	Lu et al. (2001) model	cardiac hERG channel gating	(Szekely et al., 2011)
RB+GB	time-series point-by-point match	<i>in vitro</i> V_m in response to random input	12	I-F	Mensi et al. (2012) model	cortical neuron	(Mensi et al., 2012)
	spiking-timing match						
GB/NM	spiking-timing match	<i>in vitro</i> V_m in response to random input	5	I-F	Yamauchi et al. (2011) model	L5 pyramidal neuron	(Mitra et al., 2012)
GB	time-series point-by-point match	2 <i>in vitro</i> V_m	86	S-C	Guo et al. (2013) model	atrial myocyte	(Guo et al., 2013)
GB	time-series point-by-point match	3 <i>in vitro</i> V_m datasets	86	M-C	Guo et al. (2013) model	atrial myocyte	(Al Abed et al., 2013a)

Table 3.4 Existing parameter estimation approaches in excitable cell modelling. GA: genetic algorithm. GB: gradient-based algorithm. SA: simulated annealing algorithm. SS: stochastic searching algorithm. NM: Nelder-Mead simplex algorithm. RB: regression-based approach. HT: hand turning approach. CMA-ES: covariance matrix adaptation evolution strategy. ES: exhaustive search algorithm. * Artificial: model-generated.

3.3 Overview

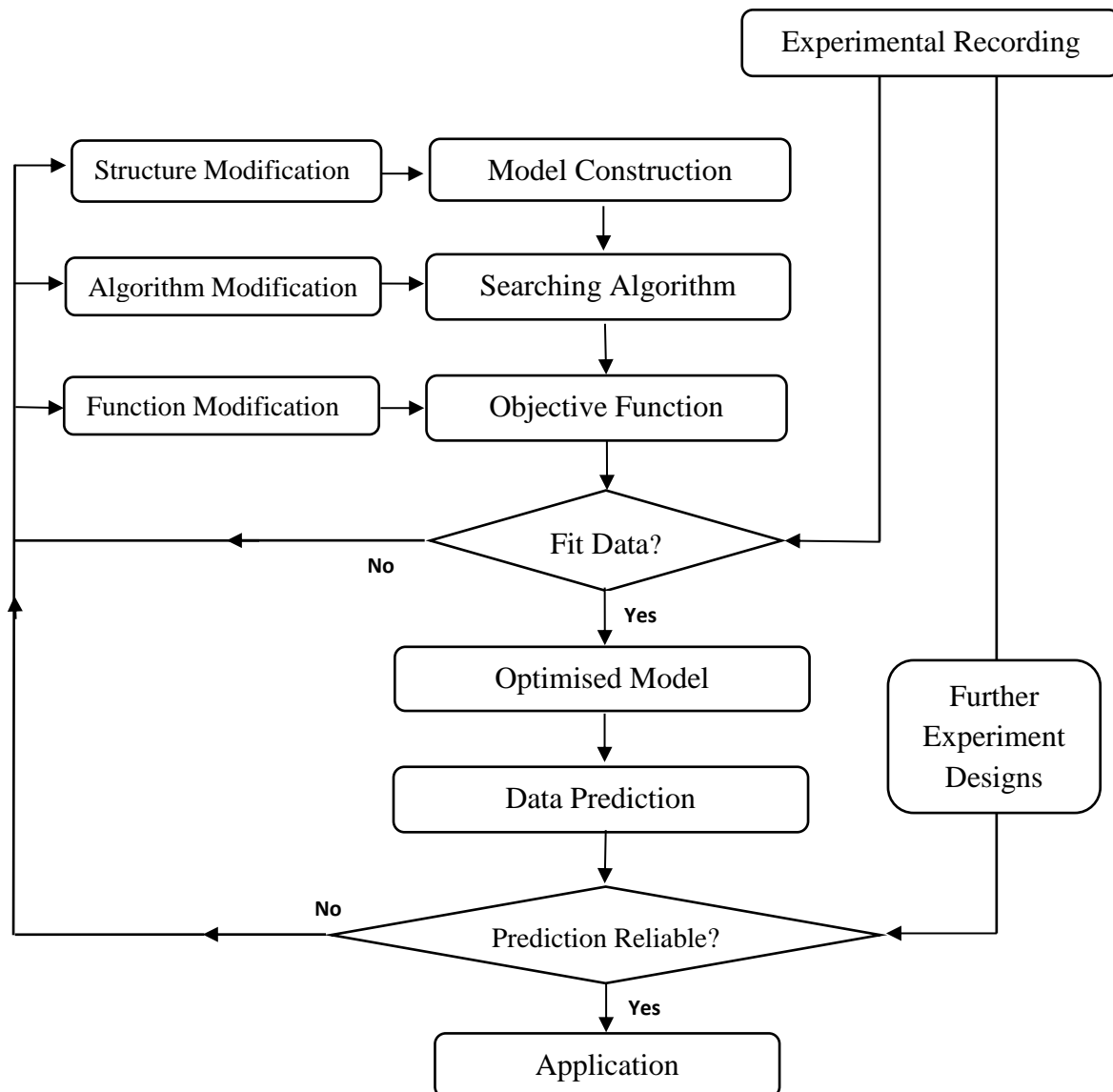


Figure 3.4 The iterative model validation process, with interaction between experiment and modelling, can be described as a closed-loop process. In addition to simulating existing data, a computational model can also quantitatively predict other experimental data to help optimise further experimental designs. By iteratively comparing the model-predicted results with corresponding experimental data, the reliability and robustness of a model (both its structure and parameter values) can be critically assessed. The initial non-optimised model will be continuously improved by necessary modification of the model structure, until its predicted outcome reasonably matches the updated experimental data. On the other hand, the corresponding experimental design may benefit from hidden knowledge that only the model could provide.

This review chapter discussed current neuronal modelling strategies and corresponding model optimisation approaches reported in the literature. As shown in Figure 3.4, a computational model is numerically optimised to integrate the experimental information and biophysical principles into a systematic, quantitative understanding of the underlying electrophysiology:

in turn, it may be capable of predicting biological information hidden in the data, as well as utilising available information to develop therapeutic techniques and to improve existing knowledge. The predicted results may help refine experimental designs to obtain appropriate data, which in turn may modify the model structure (e.g. by continually incorporating additional ionic currents into the model) or parameters (e.g. by limiting or relaxing constraints on certain model parameters to reproduce new experimental information). A positive coupling between simulation and experiment can be achieved by iteratively comparing model-predicted results and subsequent experimental data.

A model's value is confirmed by two main factors: identifiability and predictability. A biophysically-detailed neuronal model is designed to accurately represent the biological mechanisms of the target neuron, with each estimated parameter possessing a corresponding physiological significance (no matter if it can be measured using current techniques or not). In this situation, a set of uniquely identified model parameters can be obtained.

In practice, however, there are often multiple neuronal model parameter combinations sharing nearly identical fitting quality. Even gradient-free methods and well-defined multi-objective functions cannot guarantee the uniqueness of solutions (Gunay et al., 2008, Guo et al., 2013, Sarkar and Sobie, 2010). Non-uniqueness can exist even when only few parameters are optimised (Vanier and Bower, 1999).

One reason is that biophysically-detailed models are normally formulated by many non-linear ODEs with a large number of parameters. Limited knowledge of the detailed mechanisms underlying ion channel behaviour in the target neurons makes it challenging to constrain model parameters to a physiologically-relevant range. Many studies have suggested that fitting a Hodgkin-Huxley-type model can become plagued with local minima if prior physiological knowledge is not available (Achard and De Schutter, 2006, Druckmann et al., 2008). Furthermore, a perfect match between model and experimental data is extremely difficult to achieve due to machine precision, round-off errors, physiological variation, data noise or artifacts (Tabak et al., 2000). Therefore, as soon as the match between model and data is visually acceptable, there is no other predictor to demonstrate if this is the best minimum to be found.

It should also be noted that in principle, no one model can be guaranteed or claimed to characterise the actual system, since models are constructed based on limited biological knowledge. The history of biophysical modelling of excitable cells is approximately seventy

years old, since Sir Alan L. Hodgkin and Andrew F. Huxley published their famous model of the squid giant axon in 1952. It is impossible to completely simulate all known behaviours of these systems solely according to our limited knowledge of these complex systems. Therefore, all current models are developed to reconstruct only the partial rather than complete system. A numerical optimisation routine is exclusively a searching tool for locating the best solution defined by the objective functions, but not a strategy of constructing the perfect model. It cannot improve the model if the model fails to closely represent realistic biological behaviour.

On the other hand, a computational model in some sense can be considered a phenomenological generator providing considerable abstraction of the target biological system. The power of a model can be determined not by its performance on the training data, but by its ability to perform well under unseen physiological situations. With well-defined objective functions and effective numerical searching methods, many neuronal models have demonstrated their predictive power in regards to extra data, which was not used for model training: this reveals their high flexibility to reproduce even more complex electrophysiological activity. Since a perfect model which can accurately simulate all physiological mechanisms does not exist, the standard of a good model will then depend on the aims of a particular study. The validating process in Figure 3.4 will be terminated once the simulation results are consistent with the required physiological information. The resulting model can then be applied to theoretical or clinical problems, such as neural prosthetics or drug development.

Finally, a review of existing optimisation studies showed that these were largely limited to CNS neurons and cardiac myocyte models (see Table 3.4). Most existing retinal neuron model studies to date have been based on published parameter values or manual approaches to update model parameters (Fohlmeister and Miller, 1997a, Kameneva et al., 2011, Fohlmeister and Miller, 1997b, Velte and Miller, 1997). The ability of existing retinal neuron models to simultaneously reproduce multiple experimental data under a large range of diverse experimental conditions is still unclear. Most of the retinal model parameters need to be adjusted and optimised in order to reproduce additional behaviours, as well as datasets not included in the original model formulation. Thus, an unsupervised multi-objective optimisation toolbox for realistic retinal neuron modelling will be a major contribution to this area.

Chapter 4 Methodology

4.1 Ionic Modelling of Retinal Ganglion cells

In this thesis, single-compartment ionic models were simulated and analysed in Matlab 2010 (Mathworks Inc, Nattick, MA). Multi-compartment ionic models were performed and analysed in NEURON 7.2 (Hines and Carnevale, 1997) and Matlab 2010.

4.1.1 Single-Compartment RGC model

The single-compartment model in this thesis was formulated according to:

$$\frac{dV_m}{dt} = -\frac{1}{C_m}(J_{Na} + J_{KA} + J_K + J_{Ca} + J_{KCa} + J_h + J_L) + \frac{I_s}{A_c} \quad (4.1)$$

where V_m denotes the membrane potential, I_s represents the intracellular stimulus current (in amperes) and A_c denotes the cell membrane area. Membrane capacitance (C_m) per unit membrane area was set to $1 \mu\text{F}\cdot\text{cm}^{-2}$. A total of six time-dependent ionic currents were implemented: the voltage-gated sodium (J_{Na}) current, the delayed-rectifying potassium (I_K) current, the A-type potassium (J_{KA}) current, the L-type calcium (J_{Ca}) current, the calcium gated potassium (J_{KCa}) current, the hyperpolarising-activated (J_h) current, as well as one time-independent leakage current (J_L) (see also Figure 4.1). In particular, the J_h current was added to simulate RGC responses to hyperpolarising current somatic injections. All membrane ionic currents given in terms of J refer to membrane current densities, that is, membrane current divided by cell membrane area.

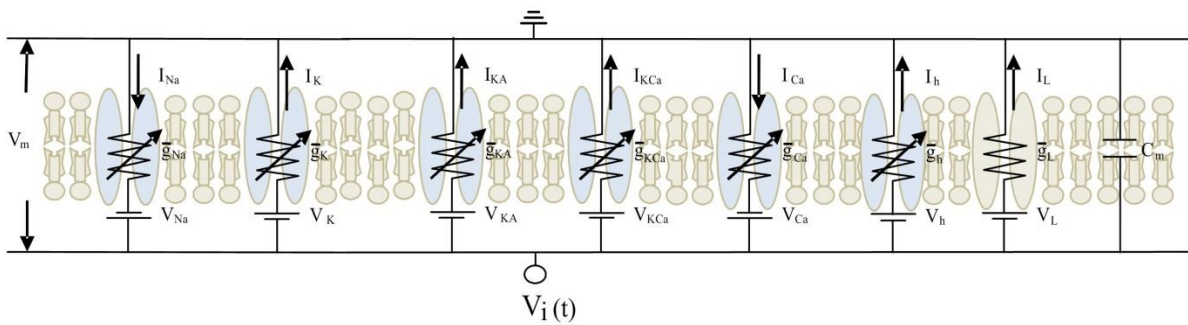


Figure 4.1 A equivalent circuit of RGC cell membrane. The capacitor branch (C_m) represents the lipid bilayer. Conduction parallel branches formed by membrane-spanning protein pores denote various time-dependent ionic channel types and the time-independent background (i.e. leakage) current. Each conduction branch includes a series potential to model the corresponding equilibrium potential. Total membrane current consists of six ionic currents and one leakage current. In the single-compartment model, extracellular potential is fixed to zero. Membrane potential is equal to the intracellular potential.

The formulations of all membrane currents are described by:

$$\begin{aligned}
J_{Na} &= \bar{g}_{Na} m^3 h (V_m - V_{Na}) \\
J_{Ca} &= \bar{g}_{Ca} c^3 (V_m - V_{Ca}) \\
J_K &= \bar{g}_K n^4 (V_m - V_K) \\
J_{KCa} &= \bar{g}_{KCa} (V_m - V_{KCa}) \\
J_{KA} &= \bar{g}_{KA} A^3 h_A (V_m - V_{KA}) \\
J_h &= \bar{g}_h y^2 (V_m - V_h) \\
J_L &= \bar{g}_L (V_m - V_L)
\end{aligned} \tag{4.2}$$

where m , h , c , A , h_A , y are gating variables, satisfying first order ordinary differential equations (ODEs):

$$dx/dt = \alpha_x(1 - x) - \beta_x x \tag{4.3}$$

where x is the gating variable, α_x , β_x are the opening and closing rates respectively, with initial values given by:

$$x_0 = \alpha_x / (\alpha_x + \beta_x) |_{V_m=V_0} \tag{4.4}$$

where V_0 is the initial (i.e. resting) value of V_m . The detailed ionic current formulations and rate parameters are given in Chapter 5.

4.1.2 Morphologically-Realistic Cable Model of Intracellular RGC Stimulation

In morphological models, membrane potential is both space and time-dependent, with the neuron approximated by separating into multiple discrete cables. Each neural region is associated with its own ionic properties and is connected with neighbouring compartments by axial resistances (see Figure 4.2). In the particular cellular region, the local membrane current i_m (in amperes per unit length) can be calculated by,

$$i_m = \frac{1}{r_i} \frac{\partial^2 V_i(t,s)}{\partial s^2} = i_c + i_{ion} \tag{4.5}$$

where s is the arc-length distance along the neuron, r_i is the local intracellular axial resistance (in ohms per unit length), V_i is the intracellular membrane potential, and i_c and i_{ion} are respectively the local membrane capacitance current (in amperes per unit length) and total ionic current (in amperes per unit length). For the detailed derivation of eq. (4.5), refer to Naundorf et al. (2006)

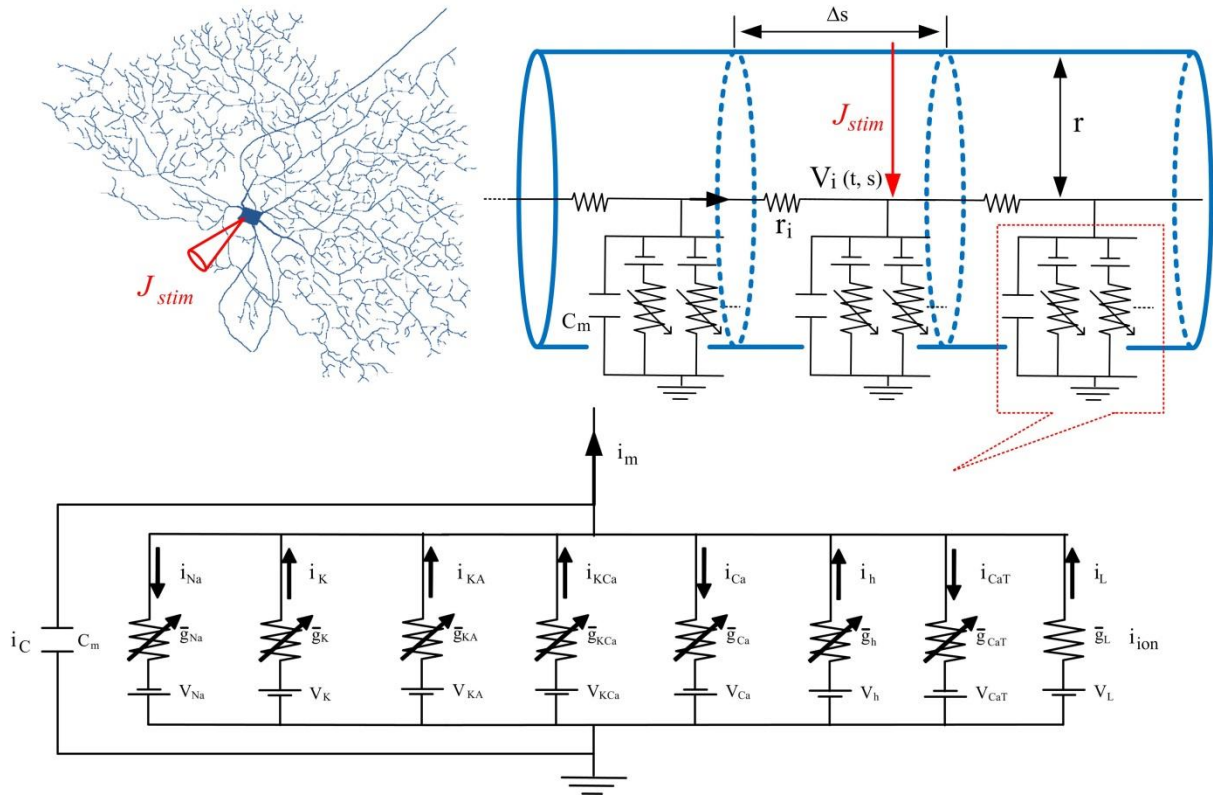


Figure 4.2 Top left: RGC morphology with somatic stimulation electrode. Top right: Equivalent circuits of local cell membrane. r_i is the intracellular axial resistance per unit length, i_C is the membrane capacitance current per unit length, i_{ion} is the total ionic current per unit length, and i_m is the membrane current per unit length. Extracellular potential V_e is fixed to zero (ground).

For the whole neuron, total membrane current density J_m (in current per unit membrane area) and intracellular resistivity R_i (in resistance times unit length) can be calculated using the radius of the cylindrical neural region r , the local membrane current i_m and intracellular resistance r_i :

$$J_m = i_m / 2\pi r$$

$$R_i = \pi r^2 r_i \quad (4.6)$$

Eq. (4.5) can be updated to:

$$J_m = \frac{r}{2R_i} \frac{\partial^2 V_i}{\partial s^2} = J_C + J_{ion} - J_{stim} \quad (4.7)$$

where total membrane capacitance current density $J_C = C_m \frac{\partial V_i}{\partial t}$, total ionic current density $J_{ion} = J_{Na} + J_K + J_{KA} + J_{KCa} + J_{Ca} + J_h + J_{CaT} + J_L$, and J_{stim} is the stimulus current injection per unit area. Rearranging eq. (4.7) to

$$\sigma_i \frac{\partial^2 V_m}{\partial s^2} = \beta \left(C_m \frac{\partial V_m}{\partial t} + J_{Na} + J_{KA} + J_K + J_{Ca} + J_{KCa} + J_h + J_{CaT} + J_L - J_{stim} \right) \quad (4.8)$$

where σ_i is the intracellular conductivity ($\sigma_i=1/R_i$) and β is the local surface to volume ratio ($\beta=2/r$). In the intracellular monodomain model, $V_m = V_i$ since V_e is assumed to be zero. Most of the ionic currents (except J_h and J_{CaT}) are defined according to eq. (4.2)

For J_h and J_{CaT} , their formulation is described by:

$$\begin{aligned} J_h &= \bar{g}_h \gamma (V_m - V_h) \\ J_{CaT} &= \bar{g}_{CaT} m_T^3 h_T (V_m - V_{Ca}) \end{aligned} \quad (4.9)$$

It should be noticed the power of gating variable in J_h equations was reduced to the first power in order to better represent J_h in the experimental voltage-clamp behaviours and current-voltage (I-V) relationship (see Figure 6.9 in section 6.3.3) in the multi-compartment models.

The gating variable dynamics used for J_{CaT} are:

$$\begin{aligned} m_T: \quad dm_T/dt &= m_T(1 - \alpha_{mT}) - \beta_{mT}\alpha_{mT} \\ h_T: \quad dh_T/dt &= \alpha_{hT}(1 - h_T - d_T) - \beta_{hT}h_T \\ d_T: \quad d(d_T)/dt &= \alpha_{dT}(1 - h_T - d_T) - \beta_{dT}d_T \end{aligned} \quad (4.10)$$

where the inactivation process for I_{CaT} was modelled with two transition gates, h_T and d_T (Wang et al., 1991, Kameneva et al., 2011, Maturana et al., 2013). Initial values were given by:

$$\begin{aligned} m_{T,0} &= \alpha_{mT}/(\alpha_{mT} + \beta_{mT})|_{V_m=V_0} \\ h_{T,0} &= \alpha_{dT}\beta_{hT}/(\alpha_{dT}\beta_{hT} + \beta_{dT}\alpha_{hT} + \beta_{dT}\beta_{hT})|_{V_m=V_0} \\ d_{T,0} &= \alpha_{dT}\beta_{hT}/(\alpha_{hT}\beta_{dT} + \beta_{hT}\alpha_{dT} + \beta_{hT}\beta_{dT})|_{V_m=V_0} \end{aligned} \quad (4.11)$$

where V_0 is the initial (i.e. resting) value of V_m . The detailed ionic current formulations and kinetic parameter values of each rate are described in Chapter 6.

4.1.3 Morphologically-Realistic Model of Extracellular RGC Stimulation

In the extracellular stimulation model, the neuron is excited by the extracellular voltage gradient (see Figure 4.3). In this case, membrane potential is calculated by:

$$V_m = V_i - V_e \quad (4.12)$$

where V_i was given by:

$$\sigma_i \frac{\partial^2 V_i}{\partial s^2} = \beta \left(C_m \frac{\partial V_m}{\partial t} + J_{Na} + J_{KA} + J_K + J_{Ca} + J_{KCa} + J_h + J_{CaT} + J_L \right) \quad (4.13)$$

and the extracellular voltage distribution was given by a disk electrode source (Greenberg et al., 1999, Tsai et al., 2012, Jeng et al., 2011):

$$V_e = \frac{2IR_s}{\pi} \arcsin\left(\frac{2R}{\sqrt{(a-R)^2+z^2} + \sqrt{(a+R)^2+z^2}}\right) \quad (4.14)$$

where I is the extracellular stimulus current, a and z are the radial and axial distance respectively from the center of the disk for $z \neq 0$, R is the radius of the disk, and R_s is the electrode transfer resistance. It should be noted that multiple neuronal active compartments may be simultaneously excited by the extracellular stimulation.

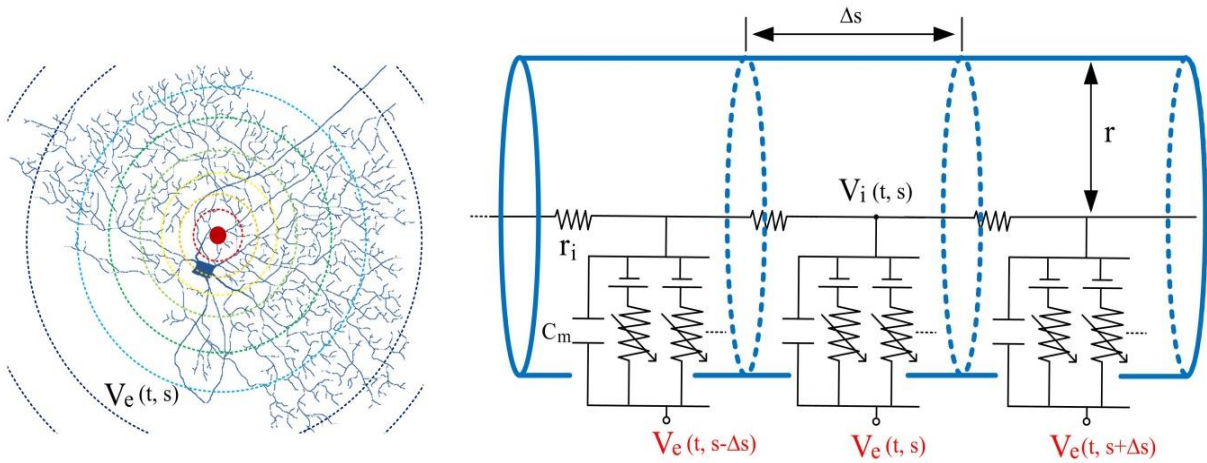


Figure 4.3 Left: RGC morphology with extracellular stimulation electrode (red dot). Right: Equivalent circuits of local neural membrane. $V_e(t, s)$ denotes the extracellular potential at a specific neural location. In the extracellular stimulation model, the cell is excited by the extracellular voltage gradient rather than intracellular current injection. The membrane potential is determined from the difference between intracellular potential V_i and extracellular potential V_e ,

4.2 Multi-Objective Parameter Optimisation

In this thesis, parameter optimisation involved the systematic modification of parameter values of a RGC model in order to minimise the disparity between multiple model outputs and experimental data. A custom curvilinear gradient-based optimisation method, combining the advantages of both Newton and steepest descent methods, was coded and implemented on a standard desktop PC using Matlab.

4.2.1 Curvilinear Gradient Optimisation Method

Assume we wish to fit a vector of $m \times 1$ data points \mathbf{d} by an ODE system $\mathbf{f}(\mathbf{p})$, a function of $n \times 1$ parameter vector \mathbf{p} . We can define a $m \times 1$ residual function \mathbf{r} according to:

$$\mathbf{r}(\mathbf{p}) = \mathbf{f}(\mathbf{p}) - \mathbf{d} \quad (4.15)$$

This residual function can be approximated by:

$$\mathbf{r}(\Delta\mathbf{p}) = \mathbf{r}_0 + (\partial\mathbf{f}(\mathbf{p})/\partial\mathbf{p}) \Delta\mathbf{p} \quad (4.16)$$

where $\Delta\mathbf{p}$ is an $n \times 1$ parameter step vector, and \mathbf{r}_0 is the $m \times 1$ residual vector at the current parameter position \mathbf{p} , for which $\Delta\mathbf{p} = 0$. A least squares objective function can be calculated from:

$$\begin{aligned} Q(\Delta\mathbf{p}) &= \mathbf{r}(\Delta\mathbf{p})^T \mathbf{r}(\Delta\mathbf{p}) \\ &= [\mathbf{r}_0 + (\partial\mathbf{f}(\mathbf{p})/\partial\mathbf{p})\Delta\mathbf{p}]^T [\mathbf{r}_0 + (\partial\mathbf{f}(\mathbf{p})/\partial\mathbf{p})\Delta\mathbf{p}] \\ &= \mathbf{r}_0^T \mathbf{r}_0 + 2 \Delta\mathbf{p}^T \mathbf{J}^T \mathbf{r}_0 + \Delta\mathbf{p}^T \mathbf{J}^T \mathbf{J} \Delta\mathbf{p} \\ &= Q_0 + \Delta\mathbf{p}^T \mathbf{G} + \frac{1}{2} \Delta\mathbf{p}^T \mathbf{H} \Delta\mathbf{p} \end{aligned} \quad (4.17)$$

where \mathbf{J} is the $m \times n$ Jacobian matrix ($\mathbf{J} = (\partial\mathbf{f}(\mathbf{p})/\partial\mathbf{p})$) or

$$\mathbf{J} = \begin{bmatrix} \partial f_1(p_j)/\partial p_1 & \partial f_1(p_j)/\partial p_2 & \cdots & \partial f_1(p_j)/\partial p_n \\ \partial f_2(p_j)/\partial p_1 & \partial f_2(p_j)/\partial p_2 & \cdots & \partial f_2(p_j)/\partial p_n \\ \vdots & \vdots & \ddots & \vdots \\ \partial f_m(p_j)/\partial p_1 & \partial f_m(p_j)/\partial p_2 & \cdots & \partial f_m(p_j)/\partial p_n \end{bmatrix}$$

and $Q_0 = \mathbf{r}_0^T \mathbf{r}_0$.

The $n \times 1$ gradient vector \mathbf{G} is given by:

$$\mathbf{G} = \nabla Q = 2 \mathbf{J}^T \mathbf{r}_0 \quad (4.18)$$

Furthermore, it can readily be shown that

$$\nabla Q(\Delta \mathbf{p}) = \mathbf{G} + \mathbf{H} \Delta \mathbf{p} \quad (4.19)$$

where \mathbf{H} is the $n \times n$ Hessian matrix ($\mathbf{H} = 2 \mathbf{J}^T \mathbf{J}$).

Parameterising the curvilinear search trajectory $\Delta \mathbf{p} = \mathbf{L}(\theta)$, $\theta \in (0, +\infty)$, we wish to find the θ value, θ^* , which minimises $\mathbf{f}(\mathbf{p})$ along the curve $\mathbf{L}(\theta)$, representing the curvilinear trajectory of steepest slope. To determine this trajectory, we solve

$$\frac{d(\mathbf{L}(\theta))}{d\theta} + \mathbf{H} \mathbf{L}(\theta) = -\mathbf{G} \quad (4.20)$$

These equations state that the derivative of the trajectory \mathbf{L} with respect to parameter θ is in the negative direction of the local objective gradient (i.e. is aligned in the direction of steepest slope). To solve this equation, let $\mathbf{L}(\theta) = \mathbf{u}(\theta)e^{-\int \mathbf{H}d\theta}$

$$\frac{d\mathbf{u}(\theta)}{d(\theta)} e^{-\int \mathbf{H}d\theta} - \mathbf{H} \mathbf{u}(\theta) e^{-\int \mathbf{H}d\theta} + \mathbf{H} \cdot \mathbf{u}(\theta) e^{-\int \mathbf{H}d\theta} = -\mathbf{G}$$

$$\frac{d\mathbf{u}(\theta)}{d(\theta)} = -\mathbf{G} e^{\int \mathbf{H}d\theta}$$

$$\mathbf{u}(\theta) = -\int \mathbf{G} e^{\int \mathbf{H}d\theta} d\theta + C_0$$

$$\begin{aligned} \mathbf{L}(\theta) &= e^{-\int \mathbf{H}d\theta} \left(-\int \mathbf{G} e^{\int \mathbf{H}d\theta} d\theta + C_0 \right) \\ &= -\mathbf{H}^{-1} \mathbf{G} + C_0 e^{-\mathbf{H}\theta} \end{aligned} \quad (4.21)$$

When $\theta = 0$, $\mathbf{L}(\theta) = 0$. Hence,

$$C_0 = \mathbf{H}^{-1} \cdot \mathbf{G}$$

$$\begin{aligned} \mathbf{L}(\theta) &= -\mathbf{H}^{-1} \mathbf{G} + e^{-\mathbf{H}\theta} \mathbf{H}^{-1} \mathbf{G} \\ &= (e^{-\mathbf{H}\theta} - \mathbf{I}) \mathbf{H}^{-1} \mathbf{G} \quad \theta \in (0, +\infty), \end{aligned} \quad (4.22)$$

In our optimisation procedure, we search for the value of θ that minimises $\mathbf{f}(\mathbf{p})$ along the curve $(e^{-\mathbf{H}\theta} - \mathbf{I}) \mathbf{H}^{-1} \mathbf{G}$

We see that the trajectory will reach a final point given by:

$$\lim_{\theta \rightarrow \infty} (e^{-\mathbf{H}\theta} - \mathbf{I}) \mathbf{H}^{-1} \mathbf{G} = -\mathbf{H}^{-1} \mathbf{G} \quad (\text{Full Newton step})$$

Also,
$$\lim_{\theta \rightarrow 0} \frac{d[(e^{-\mathbf{H}\theta} - \mathbf{I}) \mathbf{H}^{-1} \mathbf{G}]}{d\theta}$$

$$\begin{aligned}
&= \lim_{\theta \rightarrow 0} (-\mathbf{H} e^{-\mathbf{H}\theta} \mathbf{H}^{-1} \mathbf{G}) \\
&= -\mathbf{G} \quad (\text{Steepest descent direction}) \quad (4.23)
\end{aligned}$$

According to the above equations, the curvilinear trajectory includes the advantages of both the Newton and steepest descent methods, i.e. the trajectory follows a curve which begins with the steepest descent direction and terminates at the full Newton step.

The eigenvalues of $(e^{-\mathbf{H}\theta} - \mathbf{I}) \mathbf{H}^{-1}$ are given by the diagonal entries of $n \times n$ diagonal matrix

$$\boldsymbol{\varepsilon} = \begin{bmatrix} (e^{-\lambda_1\theta} - 1)/\lambda_1 & 0 & \dots & 0 \\ 0 & (e^{-\lambda_2\theta} - 1)/\lambda_2 & \dots & 0 \\ & \vdots & \ddots & \vdots \\ 0 & 0 & \dots & (e^{-\lambda_n\theta} - 1)/\lambda_n \end{bmatrix} \quad (4.24)$$

where λ_j is the j th eigenvalue of \mathbf{H} , $j \in [1, n]$

Using this matrix, the curvilinear trajectory $\mathbf{L}(\theta)$ can be well defined by spectral decomposition, a computationally effective approach to calculate the exponential of a real symmetric matrix:

$$\mathbf{L}(\theta) = \mathbf{V} \boldsymbol{\varepsilon} \mathbf{V}^{-1} \mathbf{G} \quad (4.25)$$

where \mathbf{V} is the orthogonal, eigenvector matrix of \mathbf{H} . From eq. (4.24) and (4.25), it should be noted that matrix inversion is not required during the whole process.

Since \mathbf{H} is a positive semi-definite matrix, $\lambda_j \in [0, +\infty)$. Furthermore, the eigenvalues of $(e^{-\mathbf{H}\theta} - \mathbf{I}) \cdot \mathbf{H}^{-1}$ are well-behaved in the limit the eigenvalues of \mathbf{H} approach zero:

$$\begin{aligned}
\frac{e^{-\lambda_j\theta} - 1}{\lambda_j} &= \lim_{\lambda_j \rightarrow 0} \frac{d(e^{-\lambda_j\theta} - 1)/d\lambda_j}{d\lambda_j/d\lambda_j} \\
&= \lim_{\lambda_j \rightarrow 0} (\theta e^{-\lambda_j\theta}) \\
&= -\theta \quad (\lambda_j = 0) \quad (4.26)
\end{aligned}$$

i.e. $\mathbf{L}(\theta)$ is always well-behaved, even if \mathbf{H} is singular ($\lambda_j = 0$)

To avoid the searching terminating in a local minimum without further downhill directions, an iterative re-weighting approach was used in conjunction with the curvilinear method.

Given an $m \times 1$ initial weight vector \mathbf{W} , we form the weighted residual:

$$\mathbf{r}(\mathbf{p}) = \mathbf{W} [f(\mathbf{p}) - \mathbf{d}] \quad (4.27)$$

When a local minimum is reached, the initial weight is updated:

$$W_j^{(1)} : \text{User-defined}$$

$$W_j^{(k+1)} = \frac{|r_j^{(k)}|}{|r_j^{(k)}| + \text{mean}|\mathbf{r}^{(k)}|}, \quad k = \{1,2,3\}, \quad j \in [1, m] \quad (4.28)$$

where $W_j^{(1)}$ is the j th element of the initial weight vector, whose values may depend on the dataset to be fit: normally $W_j^{(1)} = 1$. However, considerations have to be given in particular cases: we may place a higher initial weight on regions of data we are more interested in. On the other hand, a lower or even zero weight may be put on noisy regions (e.g. due to stimulus artifacts). $W_j^{(k+1)}$ is the j th element of the weight vector after the k th reweighting, $r_j^{(k)}$ is the j th element of the residual vector $\mathbf{r}^{(k)}$ at the k th reweighting. The weight vector is reset to its default initial value after k iterations of reweighting, to calculate the original objective. By iteratively ‘‘smoothing’’ the searching surface, this reweighting strategy will assist in finding an alternative path to the global minimum, navigating around any local minima with respect to the original residual weight (Dokos and Lovell, 2004).

After the weight function has been reset to its initial value, each unconstrained parameter is randomly perturbed according to:

$$\hat{\mathbf{P}}_{\text{new}} = \hat{\mathbf{P}}_0 + \boldsymbol{\delta} \quad (4.29)$$

where $\hat{\mathbf{P}}_0$ is the $n \times 1$ current unconstrained parameter vector, after it has been transformed by eq. (4.30), $\hat{\mathbf{P}}_{\text{new}}$ is the $n \times 1$ randomly perturbed vector, perturbed by a $n \times 1$ normally-distributed random vector $\boldsymbol{\delta}$, with each element having a mean of 0 and standard deviation SD ($SD = 0.01$). If the objective cost is significantly increased as a result of this perturbation ($Q_{\text{new}} \geq 6Q_0$) indicating we are far from the global optimum, SD will be halved. When the objective cost has slightly increased ($Q_{\text{new}} \geq 1.5Q_0$), suggesting the searching is still trapped in the previous local minimum, then SD will be scaled up 1.5 times. The improved parameters ($Q_{\text{new}} < Q_0$) will be saved as the current optimised set. The randomly perturbed parameter set is then used as the initial point from which to begin a new curvilinear gradient search.

4.2.2 Parameter Upper and Lower Limits

Estimated parameter values should have their values constrained to within a reasonable physiological range to ensure their reliability. In our case, most of the Hodgkin-Huxley type parameters were assigned to fixed upper and lower value limits. These limits based on experience and published experimental and modelling studies from the literature (Wang et al., 1991, Kameneva et al., 2011, Maturana et al., 2013, Fohlmeister et al., 2010, Fohlmeister and Miller, 1997b, Jeng et al., 2011, Tsai et al., 2012). Particularly, kinetic parameters were constrained to within $\pm 100\%$ of their default values in the original FM formulations. All maximum conductance parameters were constrained to lie with 0~10-fold of their default values (Fohlmeister and Miller, 1997b).

The curvilinear gradient method represents an unconstrained minimisation method. The constrained parameters described above can be transformed into unconstrained parameters using an appropriate transforming function. For any parameter p_i which is limited to the closed interval $[Lower_i, Upper_i]$, We use the transformations:

$$p_i = Lower_i + (Upper_i - Lower_i)\sin^2(\hat{P}_i)$$

and
$$\hat{P}_i = \arcsin[\sqrt{(p_i - Lower_i)/(Upper_i - Lower_i)}] \quad (4.30)$$

where \hat{P}_i is the unconstrained parameter corresponding to p_i . Thus any unconstrained parameter $\hat{P}_i \in (-\infty, +\infty)$ can follow $p_i \in [Lower_i, Upper_i]$, and the limits do not have to be explicitly enforced during the optimisation.

4.2.3 Multiple-Objective Optimisation

When optimising a model to fit multiple datasets (objectives) simultaneously, the residual in eq. (4.15) was formed by appending together the residuals of the corresponding individual datasets. The calculation of the Jacobian matrix \mathbf{J} was then updated. Three cases can be considered:

1. Multiple data (R datasets) fitted using the assumption that each dataset shares the same parameter values \mathbf{p} . This will be the case, for example, when optimizing to fit multiple AP data recorded from the same cell in response to different somatic current injections. For this case, \mathbf{J} will be a block matrix:

$$\mathbf{J} = \begin{bmatrix} \mathbf{J}_{\mathbf{p},1} \\ \mathbf{J}_{\mathbf{p},2} \\ \vdots \\ \mathbf{J}_{\mathbf{p},R} \end{bmatrix} \quad (4.31)$$

where $\mathbf{J}_{\mathbf{p},j} = (\partial \mathbf{f}_j / \partial \mathbf{p})$, R is the number of data records and \mathbf{f}_j is the j th model simulation. If m is the total number of data points across all records, and n is the number of optimised model parameters, then \mathbf{J} will be of size $m \times n$.

2. Multiple data (R datasets) fitted using the assumption that each model uses a unique set of parameters to fit each experimental dataset. Data-specific parameters \mathbf{x}_1 to \mathbf{x}_R , each of size $n \times 1$, are used for datasets 1 to R . This process is equivalent to performing multiple single dataset optimisations independently. In this case, the form of \mathbf{J} will be of size $m \times nR$, given by:

$$\mathbf{J} = \begin{bmatrix} \mathbf{J}_{\mathbf{x},1} & 0 & \cdots & 0 \\ 0 & \mathbf{J}_{\mathbf{x},2} & \cdots & 0 \\ \vdots & \vdots & \ddots & \vdots \\ 0 & 0 & \cdots & \mathbf{J}_{\mathbf{x},R} \end{bmatrix} \quad (4.32)$$

where $\mathbf{J}_{\mathbf{x},j} = (\partial \mathbf{f}_j(\mathbf{x}) / \partial \mathbf{x}_j)$.

3. Multiple data (R datasets) fitted using a combination of both shared and data-specific parameters. For S data-specific parameters (i.e. S parameters unique to each dataset), \mathbf{J} will be of size $m \times [n + (R-1) \times S]$ and given by:

$$\mathbf{J} = \begin{bmatrix} \mathbf{J}_{\mathbf{p},1} & \mathbf{J}_{\mathbf{x},1} & 0 & \cdots & 0 \\ \mathbf{J}_{\mathbf{p},2} & 0 & \mathbf{J}_{\mathbf{x},2} & & 0 \\ \vdots & \vdots & \vdots & \ddots & \vdots \\ \mathbf{J}_{\mathbf{p},R} & 0 & 0 & \cdots & \mathbf{J}_{\mathbf{x},R} \end{bmatrix} \quad (4.33)$$

Eqs. (4.31) - (4.33) suggest that more computational resources are required for parameter optimisation with multiple datasets due to the larger size of the Jacobian matrix, as well as the fact that more local minima are likely to be present in the objective parameter search space.

4.2.4 Multiple Objective Function

A multi-objective cost function consisting of three main components was implemented in this thesis:

1. Time series sum of squares error

When fitting time-series voltage recordings in response to multiple somatic current injections, the objective cost function can be represented by the sum of squares of the point-by-point error between the model outputs and data:

$$\sigma_1 = \sqrt{\frac{1}{MR} \sum_{k=1}^R \sum_{i=1}^M (f_i(\mathbf{p}) - d_{i,k})^2} \quad (4.34)$$

where $f_i(\mathbf{p})$ is the model output as a function of parameter vector \mathbf{p} corresponding to the i th data point $d_{i,k}$, and M is the number of data points in each dataset record. R is the number of datasets.

2. The 2-D phase-plane sum of squares error

The second cost function quantifies the error in the phase plot. A custom normalised 2-D RMS was defined by

$$\sigma_2 = \sqrt{\sum_{j=1}^N \min_i \frac{D_{i,j}^2}{N-1}} \quad (4.35)$$

where $\min_i D_{i,j}$ represents the minimal normalised distance (D_j) from one phase plot to another at the j th point, N is the number of data points in one phase plot, and

$$D_j = \min_i \sqrt{(V_{1,i} - V_{2,j})^2 + \left(\frac{V_{1,i}}{dt} - \frac{V_{2,j}}{dt}\right)^2} \quad (4.36)$$

where $V_{1,i}$ and $V_{2,j}$ are normalised voltage values at the i th model and the j th data point respectively.

3. The spiking pattern objective function

Other than the time-series AP datasets and AP phase plots, the objective functions used in this thesis also included important firing features such as total spike number, post-onset first spike latency (FSL), rebound or post-offset FSL, average ISI and ‘‘sag’’ amplitude. The third type of objective function implemented is described by:

$$\sigma_3 = \sqrt{\frac{1}{SR} \sum_{k=1}^R \sum_{i=1}^S (f_i(\mathbf{p}) - o_{i,k})^2} \quad (4.37)$$

where $f_{i,k}(\mathbf{p})$ is the model output corresponding to the k th feature observation $o_{i,k}$ in response to the i th current injection, and S is the number of current stimulations. R is the number of features.

The three components were combined in a weighted linear sum:

$$\sigma^2 = \sum_{j=1}^3 W_j \cdot \sigma_j^2 \quad (4.38)$$

where W_j is a user-defined weight function whose value may be adjusted depending on the relative importance of each dataset to the objective cost σ . In our case, the W_j were chosen empirically such that the first component (time-series voltage trains) accounted for about 40% of the initial objective value, the second (phase plots) approximately 30%, and the third component (spiking patterns) the remaining 30%.

TABLE 4.1
Spiking property definition and measurement method

spiking property	Definition and measurement method
total spike number (or SN)	The number of full APs elicited during a depolarising (post onset) or after a hyperpolarising (post offset) current injection
post onset FSL	time difference between stimulus offset and half-maximum amplitude of first induced AP
rebound FSL (or post offset FSL)	time difference between stimulus offset and half-maximum amplitude of the first induced AP
average ISI (or ASI)	mean inter-spike interval measured using full APs elicited during a depolarising (post onset) or after a hyperpolarising (post offset) current injection
hyperpolarisation-induced sag amplitude (or SagA)	the voltage difference between steady-state and maximum hyperpolarization membrane potential during a hyperpolarizing current injection

Table 4.1 The definition and measurement method of spiking properties quantifying model performances

4.3 Whole-Cell Patch Clamp Data for Model Optimisation and Prediction

This section briefly describes the standard whole-cell patch clamp techniques used for recording RGC spiking in this thesis. All of this patch clamp experimental data used in model optimisation (Chapters 5 and 6) was obtained by Dr. David Tsai in the Graduate School of Biomedical Engineering, UNSW, using whole-cell current clamp methods (Tsai et al., 2011). The extracellular stimulation data for validating model predictive ability (see Chapter 7) was obtained by Dr. Perry Twyford from the VA Boston Healthcare System, using cell-attached patch clamp methods (Twyford et al., 2014).

4.3.1 Whole-Cell Current Clamp Recordings in Response to Intracellular Somatic Injections.

New Zealand white rabbits weighing 2.0 ~ 3.0 kg were anesthetized with Ketamine (70 mg/kg) + Xylazine (10 mg/kg). After enucleating an eye, the animal was euthanized with sodium pentobarbital. The eye was hemisected, the anterior portion discarded and the vitreous cleared. Small pieces of the inferior retina, with the sclera attached, were dissected and kept in Ames' medium equilibrated with 95% O₂/5% CO₂, supplemented with 1% Penicillin/Streptomycin at room temperature in darkness. Before electrophysiological recordings, a small piece of the retina was separated from the pigment epithelium and sclera and transferred RGC-side up into an imaging chamber. The retina was perfused with equilibrated Ames medium at ~ 5 mL/min and heated to 34 ~ 35 °C throughout the recording period. RGCs in the whole-mount retina were visualized and targeted for recording with near-infrared (IR) illumination. All procedures were approved and monitored by the University of New South Wales Animal Care and Ethics Committee.

Whole-cell current clamp recordings were performed in rabbit RGCs using glass electrodes filled with (mM): 116 KMgSO₄, 10 KCl, 0.008 CaCl₂, 0.7 EGTA, 1 MgCl₂, 10 HEPES, 4 ATP-Na₂, 0.5 GTP-Na₃, 0.075 Alexa Fluor 488, and 10 Neurobiotin-Cl, pH 7.2. Electrode resistances ranged from 3.0 ~ 5.0 MΩ. Series tip resistance was compensated accordingly on the amplifier (MultiClamp 700B, Molecular Devices). All data were low-pass filtered at 10 kHz and digitized at 50 kHz on a computer running pClamp 10 (Molecular Devices). All data were analyzed in pClamp 10 and Matlab R2010a. RGC excitatory (AMPA/kainate, NMDA and mGluR6) and inhibitory (GABA_A/c and glycine) synaptic inputs were blocked. All blockers were supplied by Tocris Bioscience and Sigma Aldrich.

Functionally-intact RGCs were identified by their electrophysiology, morphology and stratifications. Details of cell identification are described further in chapter 6. Voltage responses from each RGC were recorded during depolarising and hyperpolarising somatic current injections with 500 ms duration and stimulus amplitudes of -120 to 210 pA in 30 pA steps.

Figure 4.4 illustrates a portion of the current clamp data recorded in different identified cells. Typically, OFF cells are more excitable than ON cells. Particularly during hyperpolarising stimuli, OFF cells showed obvious depolarising “sag” during the hyperpolarising stimulus period (indicated by arrows in B and C), and a rebound excitation after hyperpolarisation. These responses were absent in ON cells. In addition, each RGC type exhibited different spike timing, frequency adaptation and firing variations in response to the various stimulus amplitudes.

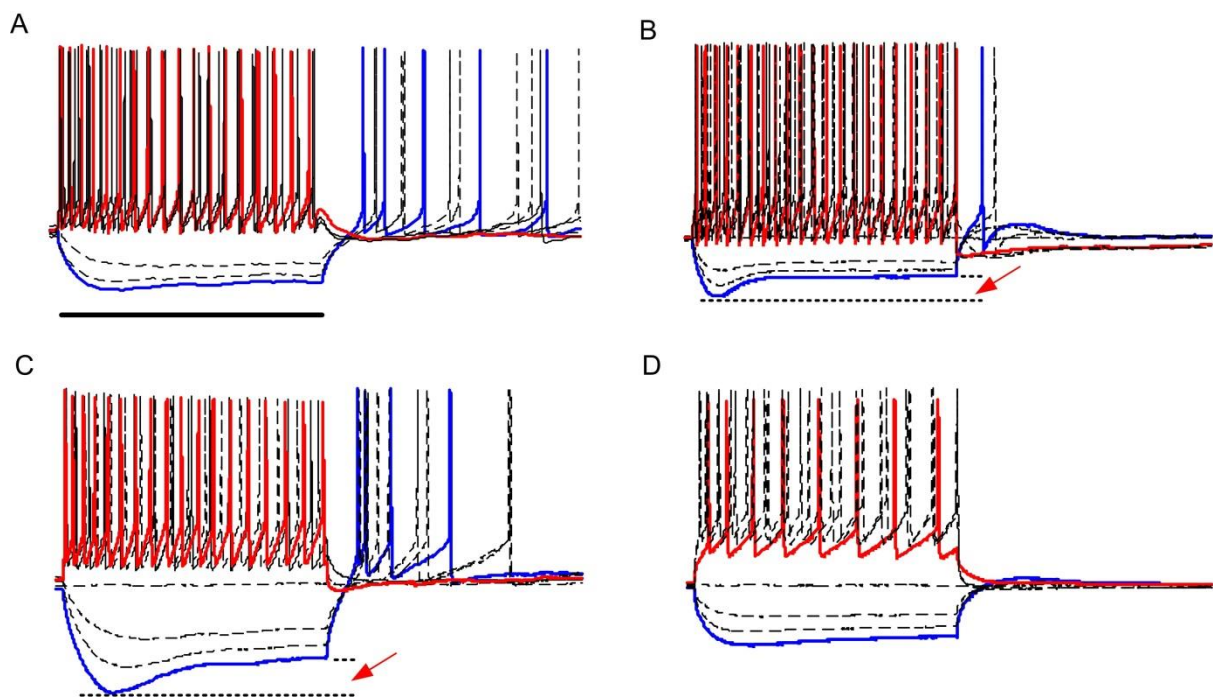


Figure 4.4 Whole-cell current clamp recordings in A) OFF beta RGC, B) OFF Parasol RGC, C) OFF RGC, D) ON RGC, in response to multiple depolarising (red) and hyperpolarising (blue) somatic current injections. In later chapters of this thesis, these cell types are sometimes referred to simply as ON or OFF. All of these biological cell-specific response properties were used for optimising RGC models in Chapters 5 and 6. Horizontal bar: stimulus interval (500 ms).

4.3.2 Cell-Attached Patch Clamp Recordings during 2 kHz Epiretinal Stimulation

In this set of experiments, the care and use of animals followed all federal and institutional guidelines, and all protocols were approved by the Institutional Animal Care and Use Committees of the Boston VA Healthcare System and/or the Subcommittee of Research Animal Care of the Massachusetts General Hospital. Cell-attached patch clamp recordings were performed in the New Zealand white female rabbit (~2.5 kg) RGCs, and electrical stimulation was applied epiretinally via a 10 k Ω platinum–iridium electrode (MicroProbes). The exposed electrode tip was conical with an approximate height of 125 μm and base diameter of 15 μm , giving a surface area of 5900 μm^2 , which was comparable to the area of a 40 μm radius disc electrode. The height of the stimulating electrode remained fixed at 25 μm above the inner limiting membrane. A synaptic blocker CNQX (6-cyano-7-nitroquinoxaline-2,3-dione, 50 μM) and AP-7 (DL-2-amino-7-phosphonoheptanoic acid, 100 μM) was used in cell-attached recordings, and the synaptic blockage was confirmed by the absence of light elicited responses. The electrical artefact produced by the stimulus in the data was removed via a custom notch filter. All processing was performed in Matlab R2010a (Mathworks).

The stimulation consisted of biphasic constant-current pulses (cathodal first) delivered at rates of 2 kHz. Cathodal and anodal phase durations were 100 μs each. Cathodal-anodal interpulse interval (IPI) was 160 μs , and anodal-cathodal IPI was set to be 140 μs . Two main types of stimulation were used: 1) constant amplitude stimulation, 2) an amplitude modulated “diamond”, to distinguish between different RGC classes. Details of the stimulation strategy are further described in Chapter 7.

Part II Results and Discussion

Chapter 5 A Single-Compartment RGC Model

In this chapter, a conductance-based single-compartment RGC model was modified to reconstruct multiple membrane potential datasets recorded from rabbit RGCs. The model included a hyperpolarisation activated current (J_h) to reconstruct the “rebound excitations” under hyperpolarising stimulation conditions.

Rebound excitation, also termed post-inhibitory rebound, has been studied in a number of neuron types (Mitra and Miller, 2007b, Kepler et al., 1992, Van Hook and Berson, 2010). Recently published modelling work has also given more attention to the mechanisms underlying rebound excitation in different types of neurons (Kepler et al., 1992, Kameneva et al., 2011, Buchholtz et al., 1992, Engbers et al., 2011, McCormick and Huguenard, 1992). To our knowledge, only a limited number of existing RGC models can effectively reproduce such phenomena (Kameneva et al., 2011). At the same time, the contribution of J_h to neuronal excitability during hyperpolarising stimulation has been reported in many *in vitro* studies (Rateau and Ropert, 2006, Moosmang et al., 2001, Momin et al., 2008, Stradleigh et al., 2011).

The optimised model presented in this chapter was able to reproduce the mechanisms underlying both normal and rebound action potentials. The significance of the modified model structure and the inherent limitation of current modelling approaches are also discussed in detail

5.1 Simulating RGC Normal and Rebound Excitation

A generic rabbit RGC ionic model, based on the Fohlmeister and Miller (FM) formulation (1997) (Fohlmeister and Miller, 1997a), was optimised to simultaneously reproduce multiple RGC electrophysiological behaviours. An additional ionic current, the hyperpolarisation-activated current (J_h), activated in response to hyperpolarising current injection, was present in the model to simulate rebound spiking following a hyperpolarising stimulus.

The single-compartment model can be described by,

$$\frac{dV_m}{dt} = -\frac{1}{C_m} (J_{ion} + J_h - \frac{I_{stim}}{A_c}) \quad (5.1)$$

Where V_m denotes the membrane potential, C_m is membrane capacitance per unit area, J_{ion} denotes the total ionic current per unit area in the original FM model, I_{stim} represents the intracellular stimulus current and A_c denotes the cell membrane area. Systematic differences between experimental data and original FM model outputs (Figure 5.1 middle) indicated that additional ionic currents activated by hyperpolarisation were necessary for reproducing rebound excitation. As a result, J_h was added to the model to simulate RGC responses to hyperpolarising current somatic injections. A total of six time-dependent ionic currents and one leakage current were included in the new model structure.

The modified RGC model was optimised to simultaneously fit two trains of voltage responses stimulated by both depolarising and hyperpolarising intracellular current injections (120 and -120 pA). All maximum conductance and kinetic parameters were optimised. Optimised parameters across these two datasets were specified to share the same values, since any AP waveshape variation would be due to differences in the injected current alone. All optimised model parameters and rate equations are shown in Table 5.1.

From the results shown in Figure 5.1, the optimised model that included J_h (right panel) closely matched the experimental data (left panel), including the slow depolarising “sag” on hyperpolarisation below the resting membrane potential and the rebound spiking activity after the termination of hyperpolarising stimuli. However, in the original FM model, a negative current injection caused the membrane to hyperpolarise along an approximately exponential time course governed by the passive membrane time constant. When the current step was terminated, the membrane voltage smoothly decayed back to its original resting potential (Figure 5.1A, middle panel). In addition, the optimised model was able to closely reproduce the corresponding spike frequency and FSL variation due to stimulus amplitude (Figure 5.1B,

left panel). The error between both models and experimental data in the right panel of Figure 5.1B indicated a substantially improved model accuracy over the original FM model in terms of the four spiking properties. Finally, we found that the optimised model could also effectively predict datasets which were not used in the optimisation process by altering the stimulus amplitude (i.e. -60 and 60 pA).

Figure 5.2B illustrates the reconstructed model ionic current waveforms in response to the hyperpolarising stimulus. Even though the amplitude of J_h was relatively small (only ~1% of the total membrane sodium currents), it still played an important role in shaping RGC spiking to hyperpolarising current injections.

Certain disagreement between model and experimental data could not be eliminated by optimising the model parameters. This included the “kink” at the foot of the action potential upstroke, defined as the sudden onset of upstroke depolarisation, as labelled by the red arrows in Figure 5.3, also known as initial segment-soma dendritic (IS-SD) break in the 2-D phase plot (see Figure 5.3). These differences were due to the inherent limitation of using a single-compartment model (see discussion).

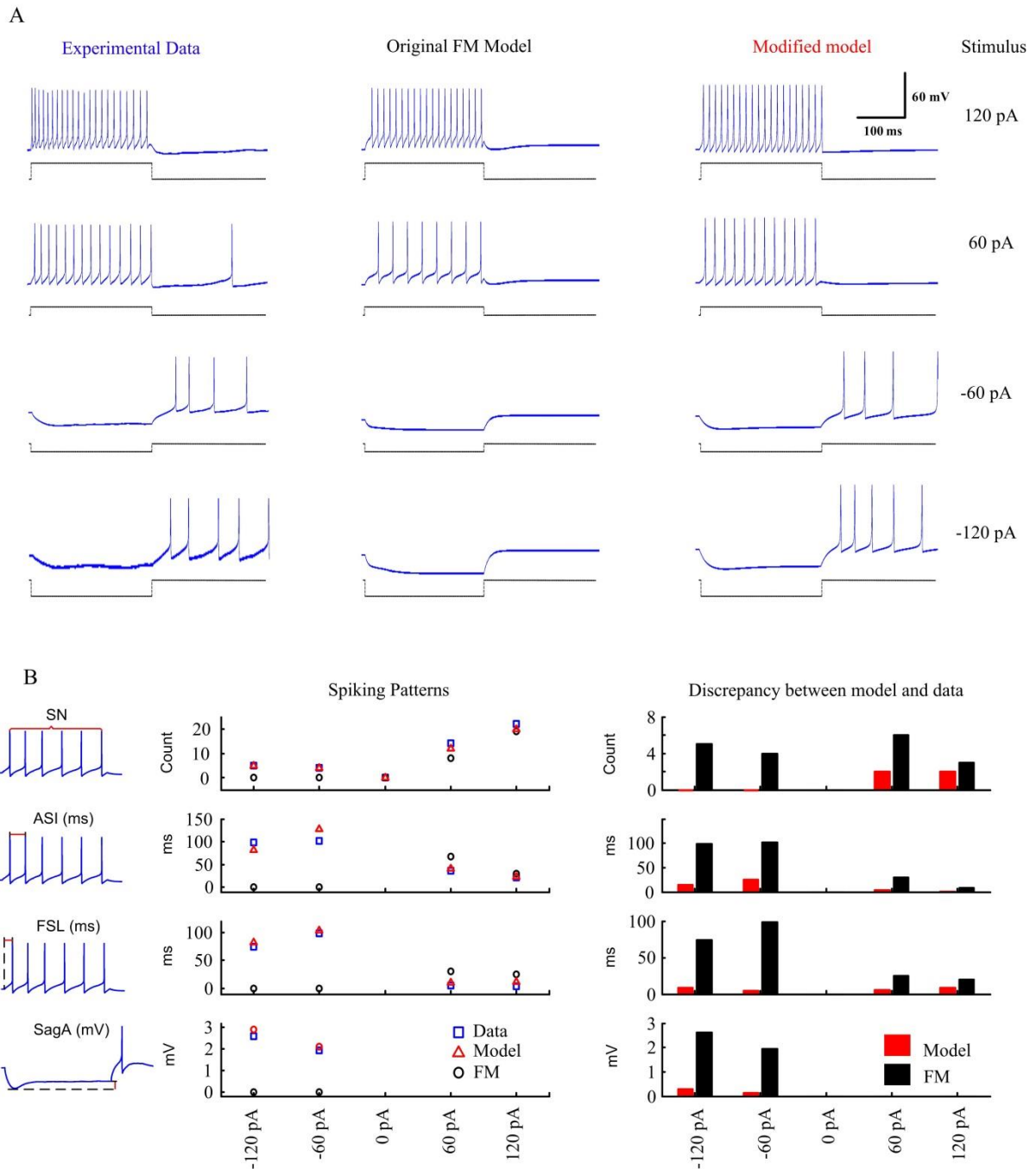


Figure 5.1 A. The original FM model could not reconstruct the RGC responses to hyperpolarising current injections (A, middle column, lower two rows). After the model was modified by adding J_h , the modified model (right column) was able to closely match the experimental data in the leftmost column, including the slow depolarising “sag” on hyperpolarisation below the resting membrane potential, as well as the rebound spiking activity after hyperpolarisation. B. Left: Comparison of experimental data (blue), FM model (black) and optimised model (red) performance in terms of total spiking number (SN), averaged inter-spike interval (ASI), first spike latency (FSL) and sag amplitude (SagA). Right: Comparison of modified model (red) and FM model (black) performance in terms of discrepancy between model outputs and data

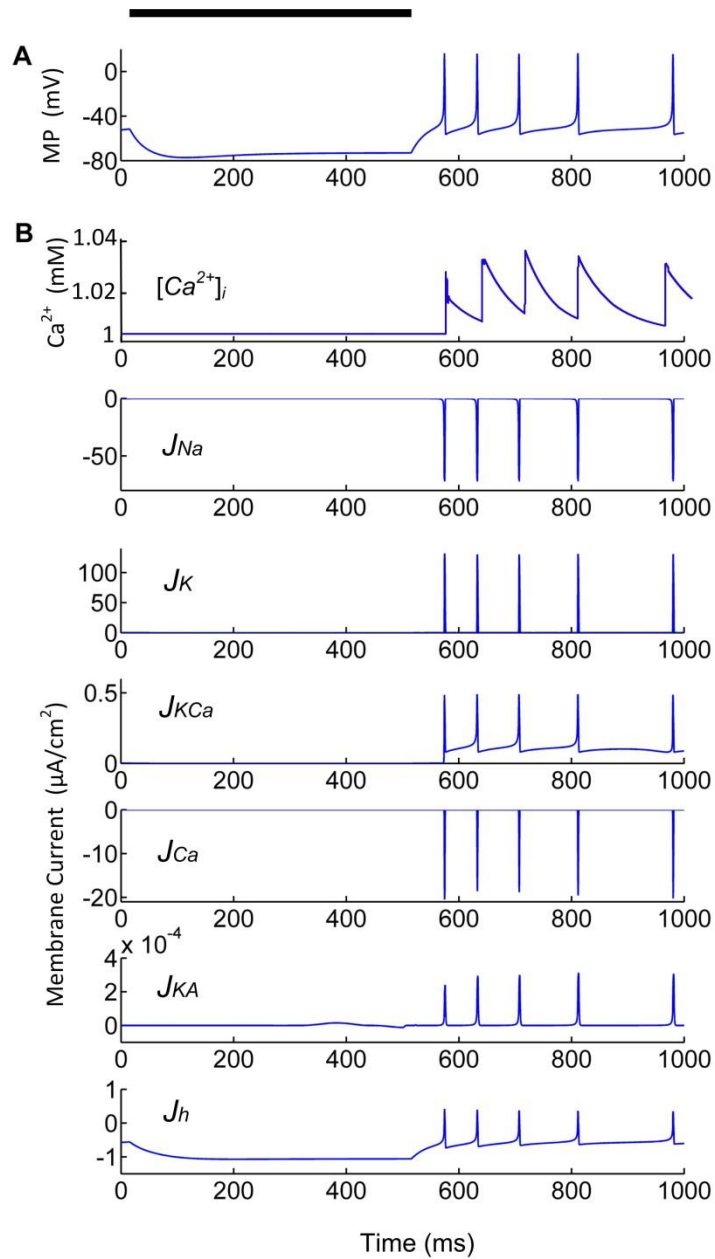


Figure 5.2 Model-generated membrane potential (A) and corresponding ionic currents and calcium concentration (B) in response to a 120 pA hyperpolarising stimulus shown by the bar in the top panel.

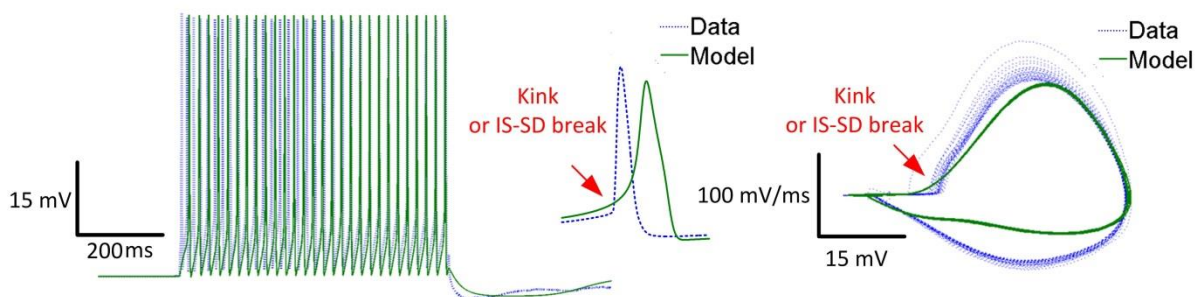


Figure 5.3 Single-compartment model could not fit certain neuronal behaviours such as the fast rate of rise of action potentials at spike onset (the kink), also known as IS-SD break in the 2-D phase plot of rate vs membrane potential (right panel), as indicated by the red arrows.

TABLE 5.1
Parameter values for the generic RGC model

Channel		
J_{Na}	$J_{Na} = \bar{g}_{Na} m^3 h (V_m - 90.99)$	
	$\alpha_m = -0.6(V_m + 30)/(e^{-0.1(V_m+30)} - 1)$	$\beta_m = 20e^{-0.0556(V_m+55)}$
	$\alpha_h = 0.4e^{-0.05(V_m+50)}$	$\beta_h = 6/(1 + e^{-0.1(V_m+20)})$
J_{Ca}	$J_{Ca} = \bar{g}_{Ca} c^3 (V_m - V_{Ca})$	
	$\frac{d[Ca^{2+}]_i}{dt} = -\left(\frac{3J_{Ca}}{2Fr} J_{Ca}\right) - \frac{[Ca^{2+}]_i - 0.0001}{50}$	$V_{Ca} = \frac{RT}{2F} \ln\left(\frac{2}{[Ca^{2+}]_i}\right)$
	$\alpha_c = -0.0052(V_m + 9.2)/(e^{-0.2584(V_m+9.2)} - 1)$	$\beta_c = 14.92e^{-0.2636(V_m+15.47)}$
J_K	$J_K = \bar{g}_K n^4 (V_m + 70.5259)$	
	$\alpha_n = -0.0943(V_m + 21.73)/(e^{-0.2584(V_m+21.73)} - 1)$	$\beta_n = 1.7565e^{-0.1913(V_m+56.71)}$
J_{KA}	$J_{KA} = \bar{g}_{KA} A^3 h_A (V_m + 70.5259)$	
	$\alpha_A = -0.0002(V_m + 54.47)/(e^{-0.2047(V_m+54.47)} - 1)$	$\beta_A = 0.0244e^{-0.2291(V_m+42)}$
	$\beta_{h_A} = 0.0028e^{-0.0118(V_m+81.77)}$	$\beta_{h_A} = 1.5821/(1 + e^{-0.4532(V_m+58.04)})$
J_{KCa}	$J_{KCa} = \bar{g}_{KCa} (V_m + 70.5259)$	
	$g_{KCa} = \bar{g}_{KCa} \left[\left(\frac{[Ca^{2+}]_i}{0.001} \right)^2 / \left(1 + \left(\frac{[Ca^{2+}]_i}{0.001} \right)^2 \right) \right]$	
J_h	$J_h = \bar{g}_h y^2 (V_m + 10.03)$	
	$\alpha_y = 0.161e^{-0.0259(V_m+97.18)}$	$\beta_y = -0.00002(V_m + 67)/(1 - e^{-0.014(V_m+67)})$
J_L	$J_L = \bar{g}_L (V_m + 32.174)$	
Maximum Conductance	$\bar{g}_{Na}: 0.8634 \text{ mS/cm}^2$	$\bar{g}_{KCa}: 0.0056 \text{ mS/cm}^2$
	$\bar{g}_K: 1.7352 \text{ mS/cm}^2$	$\bar{g}_h: 0.0124 \text{ mS/cm}^2$
	$\bar{g}_{KA}: 20.966 \text{ mS/cm}^2$	$\bar{g}_L: 0.00042 \text{ mS/cm}^2$
	$\bar{g}_{Ca}: 0.4837 \text{ mS/cm}^2$	$Ac: 0.2621 \text{ cm}^2 *$
Initial Variable Value	$V_m: -53 \text{ mV}$	$n: 0.001$
	$[Ca^{2+}]_i: 0.0001 \text{ mM}$	$A: 0.0031$
	$m: 0.0835$	$h_A: 0.0013$
	$h: 0.9995$	$y: 0.8143$
	$c: 0$	

Table 5.1 Conductance and rate parameters for single-compartment generic RGC model. All rates are in units of 1/ms, voltages in units of mV, $[Ca^{2+}]_i$ in units of mM, and membrane currents in units of $\mu\text{A/cm}^2$. m , h , c , n , A , h_A and y are voltage and time-dependent gating variables, whose dynamics are given by $\frac{dx}{dt} = \alpha_x(1 - x) - \beta_x x$, where x denotes the gating variable in question. (*) Ac represents the total RGC membrane area of the RGC. F denotes Faraday's constant and r denotes the depth of the spherical shell beneath the membrane for the inward calcium current. R denotes the gas constant, and T is the temperature, which is set to be 310 K.

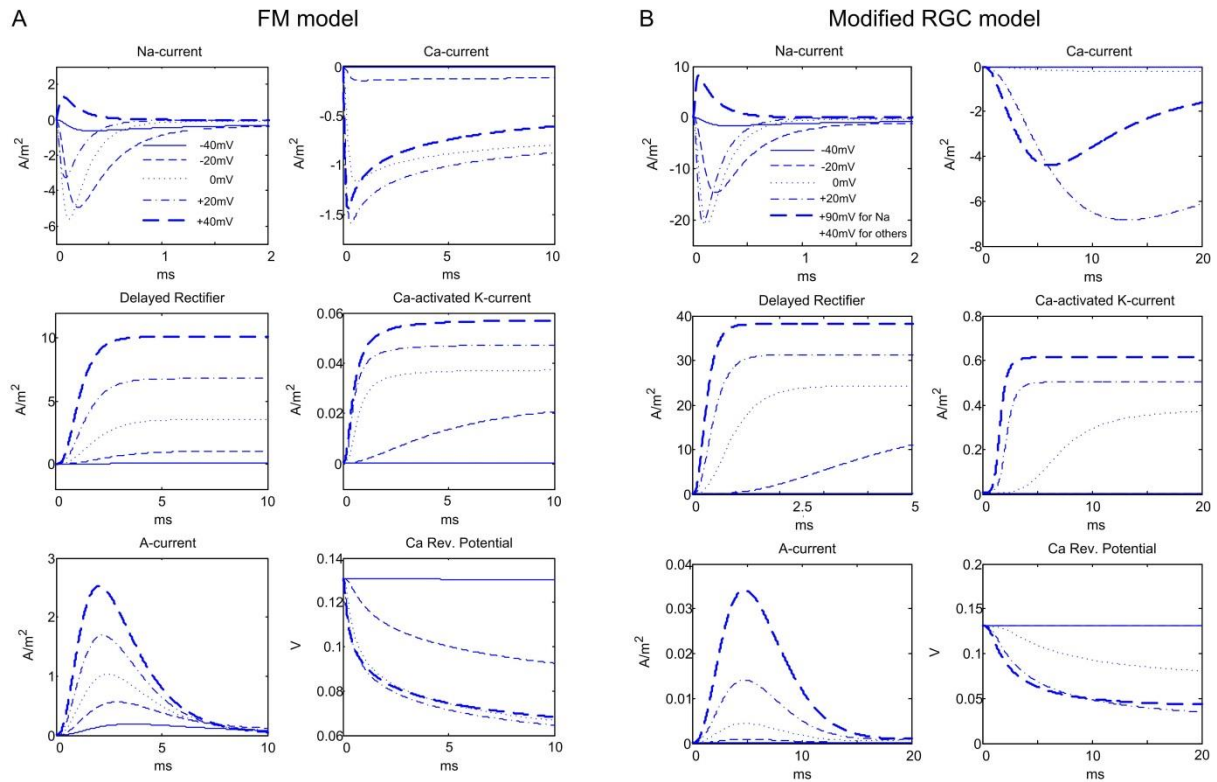


Figure 5.4 Comparison of voltage-clamp behaviours of five ion channels and Ca^{2+} Nernst potential reconstructed by the original FM model (A) and the modified RGC model (B). All simulations were carried out using the single-compartment model summarised in Fohlmeister and Miller (1997a) and Table 5.1. For the original FM model, depolarisations were initiated from a holding potential of -65 mV and included clamp steps to -40 , -20 , 0 , $+20$, and $+40$ mV. The time duration was 10 ms except for J_{Na} , which was 2 ms. For the modified RGC model, clamp steps were set to -40 , -20 , 0 , $+20$, and $+40$ mV except for J_{Na} , which was -40 , -20 , 0 , $+20$, and $+90$ mV. The time duration was 20 ms except for J_{Na} and J_{K} , which were 2 ms and 5 ms, respectively.

Figure 5.4 demonstrates voltage-clamp simulations of five ion channels and the J_{Ca} reversal potential reconstructed from the original FM model (Figure 5.4A) and the modified RGC model (Figure 5.4B). All simulations were carried out using the single-compartment models described summarised in Fohlmeister and Miller (1997a) and Table 5.1 of this chapter. For the original FM model, depolarisations were initiated from a holding potential of -65 mV and included clamp steps from -40 to $+40$ mV, in increments of 20 mV. The time duration was set to 10 ms, except for the J_{Na} simulations, which were 2 ms. For the modified RGC model, clamp steps were set from -40 to $+40$ mV in increments of 20 mV, except for the J_{Na} simulations, which were -40 , -20 , 0 , $+20$, and $+90$ mV. The time duration was 20 ms except for the J_{Na} and J_{K} simulations which were 2 ms and 5 ms, respectively. As illustrated in Figure 5.4, despite the large changes in model parameter values, the modified model was able to qualitatively reproduce the voltage-clamp behaviours and Ca^{2+} dynamics of the Fohlmeister and Miller (1997a) study, suggesting that the dynamics of each ionic current were preserved.

5.2 The Contribution of J_h in Shaping Rebound Activities

An additional set of simulation were undertaken to investigate the contribution of the hyperpolarisation-activated current to spiking activity in the modified RGC model. One parameter, g_h , the maximum membrane conductance of J_h , was gradually reduced in order to model the effect of J_h on rebound spiking in the RGC. All other model parameters were held fixed.

Figure 5.5A illustrates the model results when gradually reducing J_h . RGC spiking patterns, such as rebound FSL (or post offset FSL, was defined as the time between the stimulus offset and half-maximum amplitude of the first hyperpolarisation-induced AP), total spike number and hyperpolarisation-induced sag amplitude, were all gradually altered with lower J_h conductance, revealing its important role in shaping RGC spiking activity, particularly the RGC response to hyperpolarising current injections. In addition, as shown in Figure 5.5B, the rebound impulse in response to multiple current injections could be eliminated when J_h was partially blocked by 50%, while the depolarising voltage responses were relatively unaltered. Blockage of J_h also resulted in a slight hyperpolarising shift of resting membrane potential.

In another simulation, the performance of model J_h was reconstructed in terms of voltage and current-clamp simulations. Voltage-clamp simulations were generated with a holding potential of -65mV, while sequentially hyperpolarising the cell from -65 to -115 mV in decrements of 10 mV. Each voltage clamp step was 1 s in duration, as indicated by the horizontal bar. In Figure 5.6A1, the family of current traces due to an applied voltage-clamp exhibited an initial instantaneous ohmic current jump followed by a slow further increase in the inward current. The magnitude and apparent rate of activation of the inward current increased with higher hyperpolarising voltage commands. In Figure 5.6B1, the RGC model was increasingly hyperpolarised below the resting potential with sequential injections of negative current-clamp steps of 3 s in duration (from 0 to -300 pA in decrements of 50 pA). The RGC model revealed a time dependent “sag” in its voltage response on hyperpolarisation with step currents, with increases in the amplitude and apparent rate of decay of the sag being evident with larger current injections. Figure 5.6C1 is a simulation from the same RGC model after J_h was partially blocked by 70%. The injected current steps have durations of 3 s (from 0 to -210 pA in decrements of 35 pA). Block of J_h clearly eliminated the development of the sag, with the voltage response assuming an apparently passive character and increasing in an ohmic manner with increasing injected current amplitudes. In addition, block of J_h

resulted in a hyperpolarising shift of resting membrane potential from -53 to -65 mV. Figure 5.6D1 illustrates the voltage-current (V-I) relationship from the results shown in Figure 5.6B1-C1. The steady state voltage values at the end of the 3 s pulse were measured for each current step under both control (B1, triangle) and J_h block (C1, circle) conditions, and have been plotted against the corresponding injected current amplitudes.

Figure 5.6A2, B2 and C2 illustrate corresponding *in vitro* voltage-clamp and current-clamp recordings from amphibian RGCs under similar stimulation conditions from the study of Mitra and Miller (2007a). The simulation results closely matched the experimental J_h behaviour in terms of overall waveshapes (A2, B2 and C2) and comparable reduction in steady state voltage values after J_h was blocked by 70% (Figure 5.6D2).

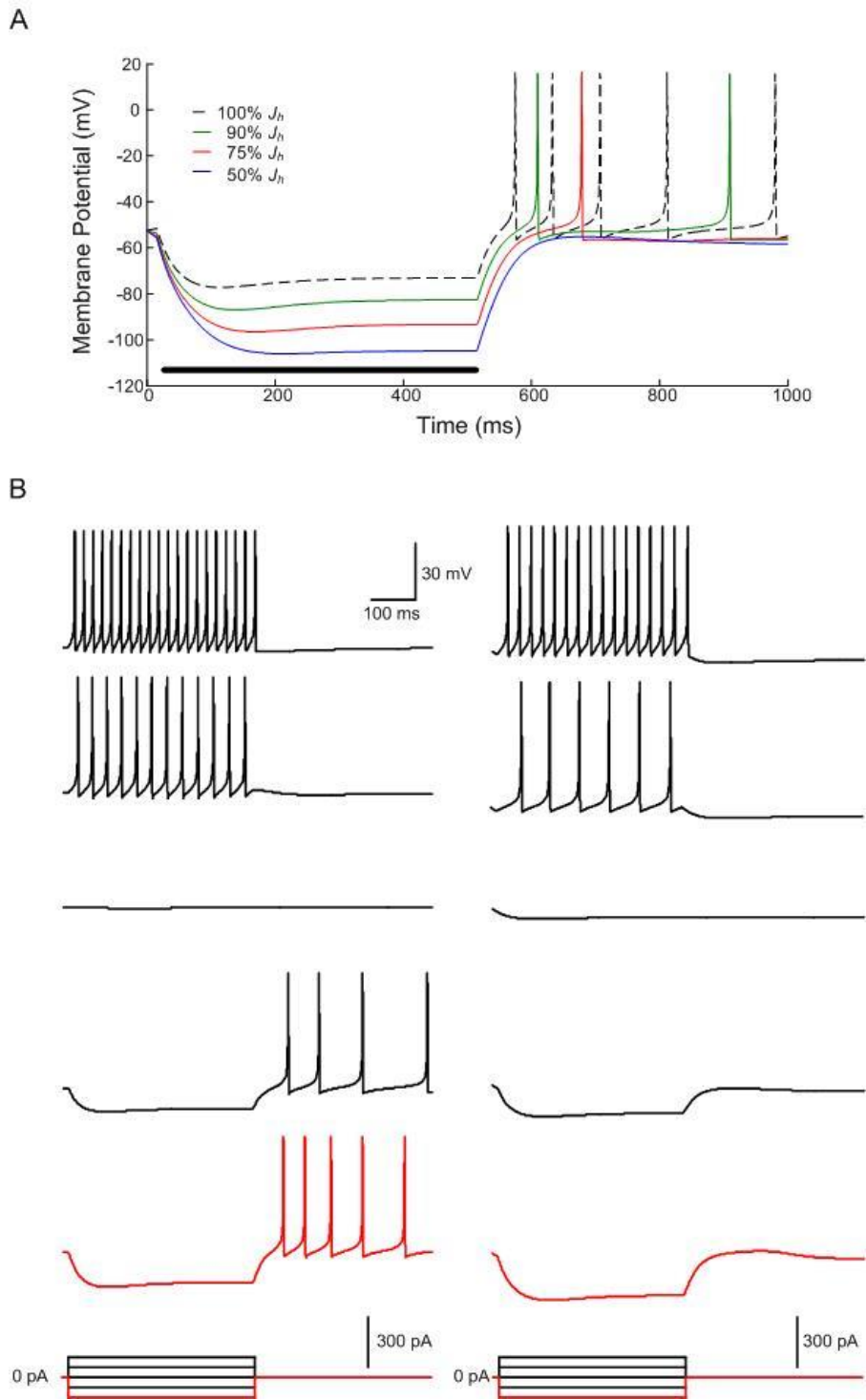


Figure 5.5 A. Model-generated membrane potentials due to partial block of J_h . B. The rebound spikes (lower three panels) were eliminated by reducing the maximum conductance of J_h by 50%, whilst the depolarising responses (upper two panels) and spontaneous (third panel) activity were relatively unaltered.

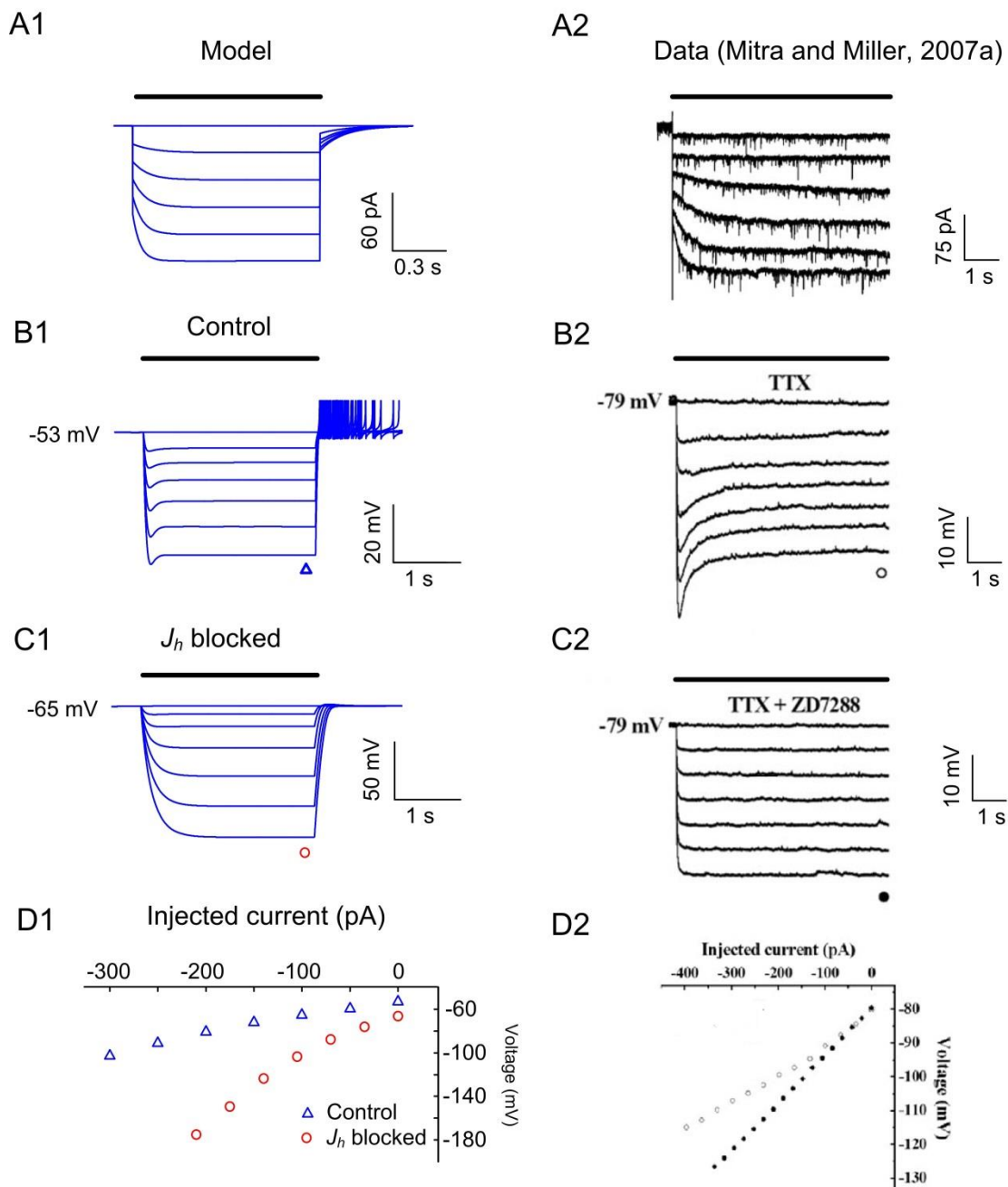


Figure 5.6 Voltage- and current-clamp simulations of J_h . A1: Family of reconstructed J_h using the voltage-clamp protocol in which the RGC was held at -65 mV and sequentially hyperpolarised from -65 mV to -115 mV in increments of 10 mV. Each step was of 1 s duration, as shown by the horizontal bar. B1: Model-reconstructed voltage responses elicited with the current clamp protocol in which the RGC was sequentially hyperpolarised below the resting membrane potential with incremental injections of negative current steps. The seven current steps were from 0 to -300 pA (in decrement of 50 pA). Each step was of 3 s duration. C1: Model-reconstructed voltage responses after J_h was partially blocked by 70% . Current steps were from 0 to -210 pA (in decrement of 35 pA). D1, Reconstructed current-voltage (I - V) relationship, where the steady state voltages measured at the end of each current step in B1 and C1 have been plotted against the magnitudes of the injected currents. A2-D2. *In vitro* voltage-clamp and current-clamp recordings from amphibian RGCs under similar stimulation conditions to A1-D1. Adapted from Mitra and Miller (2007a). Stimulus intervals were indicated by the horizontal bars.

5.3 Discussion

In this chapter, a multi-objective parameter optimisation fitting technique (see section 4.2 in Chapter 4) was used to identify the potential missing currents in the original FM ionic model. The modified model structure was dependent on the information provided by additional experimental data and multiple model outputs. For example, results from the original FM model suggested that additional ionic currents activated by hyperpolarisation, were necessary for reproducing rebound excitation (see Figure 5.1).

Since the FM formulations and parameters were based on tiger salamander RGC electrical activities, it may be necessary to modify its original parameters to reconstruct spiking responses recorded in mammalian RGCs. In this chapter, rather than only optimising parameters of the missing current, conductance and rate parameters for each current were also optimised. Model parameters across these multiple datasets were constrained to share the same values, since any action potential waveshape variation would be due to differences in the external stimulus current alone. Although model parameter values in the original FM formulations were largely modified to match multiple datasets, the resulting model still preserves the original membrane current dynamics, as indicated by the similar voltage-clamp behaviours and Ca^{2+} dynamics between the modified and original FM models (Figure 5.4).

In our results, rebound excitation can be eliminated when J_h is blocked by partially reducing its maximum conductance, revealing its contribution to the rebound excitation in RGCs. Also, our results indicated that J_h may contribute to the resting membrane properties of RGCs. Indeed, the range of resting potentials for RGCs can be within activation range of J_h (McCormick and Pape, 1990).

Model predication to non-optimised data could help in refining experimental designs for obtaining additional data, which in turn may modify the model structure (e.g. by continually incorporating additional ionic currents into the model) or parameters (e.g. by limiting or relaxing constraints on certain model parameters to reproduce new experimental information). A positive coupling between simulation and experiment can be achieved by iteratively comparing model-predicted results and subsequent experimental data. This iterative model-refinement technique is generally applicable to a range of excitable cell models. By using this technique, more accurate ionic models can be constructed semi-automatically, reducing the gap between theoretical models and real biological neurons.

Like most existing models, the modified single-compartment RGC model of this chapter has certain limitations, representing compromises necessary to achieve simplified and computationally-efficient descriptions of membrane current kinetics. One disadvantage is the isolated electrotonic structure in a single-compartment model. Disparities between the FM model and experimentally-observed behaviours cannot be eliminated by simply optimising model parameters (Fohlmeister and Miller, 1997a). Modelling studies based on realistic cell morphology have found that the existence of neuronal compartments that differ in both size and ionic channel densities of ionic channels could account for more realistic spike generation and propagation (Carras et al., 1992). More recent neuron modelling studies have suggested that a single-compartment model cannot explain certain phenomena, such as the rapid rate of rise in action potential initiation due to missing coupling currents between neighbouring cellular regions, and due to the back propagation from the axon and dendrites (Naundorf et al., 2006, McCormick et al., 2007). Therefore, rather than modelling the intrinsic properties of a single compartment, spatial anatomical information and ionic channel distributions are also required for accurate RGC modelling. In the next chapter, we have included detailed morphological information and cell-specific intrinsic properties to address these issues.

In addition, all optimised model parameters were determined based solely on their fits to the multiple-AP data. It was noticed that some resulting parameter values appeared to lie far from published values. For example, the estimated reversal potential for J_{Na} of 90.99 is greater than its 60~65 mV value in existing models (Mainen et al., 1995, Schachter et al., 2010, Fohlmeister and Miller, 1997a). The second example was the value of E_h , the reversal potential for J_h . Hyperpolarization-activated current is a mixed-cation current which is commonly carried by both Na^+ and K^+ ions (Ishida, 1995, Stradleigh et al., 2011), and its reversal potential should be between the value of E_K and E_{Na} . In this chapter, it's optimised value was -10 mV, lying outside reported physiological range of -25~-70 mV in experimental studies (Robinson, 2003, Biel et al., 2009, Lee and Ishida, 2007). Another example was the value of E_L , the leakage current equilibrium potential. It's optimised value was -32 mV, compared to its original value of -60 mV, which resulted in a reversal of the direction of this current at the resting potential of -55 mV. A final example is the cell membrane area, which appears to be larger than the reported anatomical size of the cell (Fohlmeister et al., 2010, Wong et al., 2012, O'Brien et al., 2002). However, it should be pointed out that these fits to multiple AP data were obtained using single-compartment RGC models. The fact that some

optimised parameters appeared to lie outside their normal physiological range may indicate that such single-compartment formulations are unable to adequately reproduce the required electrophysiological behaviour within the constraints of expected parameter ranges, and that it is necessary to include additional morphological complexity in the models. For example, the large value of optimised membrane area (0.261 cm^2) obtained may reflect the influence of dendritic and axonal regions. Our optimisation approach suggested that such a large cell membrane area is necessary to closely reconstruct the multiple experimental datasets. Considering that RGC dendrites have much larger overall membrane surface area compared with the soma (Fohlmeister et al., 2010, Wong et al., 2012, O'Brien et al., 2002), the optimised large membrane area obtained may reflect this property. Such morphological complexity has been incorporated into the subsequent multi-compartment models of chapters 6 and 7, where all optimised parameter values (including the E_{Na} and E_h mentioned above) are within more appropriate physiological ranges. It should also be noted that, despite the seemingly unphysiological values of some model parameters, the optimised single-compartment models of this chapter still preserve their original membrane current dynamics, as indicated by the similar voltage-clamp behaviours and Ca^{2+} dynamics between the optimised and original FM models (see Figure 5.4).

Moreover, J_h is not the only current responsible for rebound excitation. Many studies have reported that the low-threshold voltage activated (also known as T-type) calcium current and persistent sodium current can also provide a significant contribution to rebound excitation (Wang et al., 1991, Kameneva et al., 2011, McCormick and Huguenard, 1992). In the following chapters, further refinements of this work included modifying the model structure by adding other known RGC ionic currents.

Chapter 6 Morphologically-Realistic RGC Modelling

Over the last several few decades, known ionic mechanisms in RGCs continues to be updated with the identification of new ionic channel types such as the hyperpolarisation activated current (J_h) and the T-type calcium current (J_{CaT}), with further advances in *in vitro* experimental techniques (Miller et al., 2002, Tabata and Ishida, 1996, Lee and Ishida, 2007, Margolis and Detwiler, 2007, Henderson and Miller, 2003). The contribution of J_h and J_{CaT} to neuronal excitability has been reported in many experimental studies. J_h was found to have a significant effect on the subthreshold range of membrane potentials, decreasing input resistance (Magee, 1998, Surges et al., 2004), supporting spontaneous activity (McCormick and Pape, 1990), assisting dendritic summation (Abbas et al., 2013), controlling rebound spike timing and frequency (Engbers et al., 2011), as well as controlling the resting membrane potential (McCormick and Pape, 1990). J_{CaT} has been reported to contribute to bursting firing (Destexhe et al., 1998), as well as assisting J_h to fire rebound spikes following a hyperpolarising stimulus (Engbers et al., 2011). The properties of these new currents and their regional distributions may significantly contribute to their overall response. However, there is still limited knowledge on the differences in ion channel expression among the identified RGC types. More importantly, the contribution of this diversity to unique responses of each RGC type is still unclear.

The large range of RGC morphologies and their contribution to shaping RGC responses has rarely been examined quantitatively in previous studies, except for a few limited modelling studies (Maturana et al., 2013, Fohlmeister and Miller, 1997b), likely due to the difficulty of isolating the pure contribution of morphology in the experiments.

Recent experimental studies have suggested that dendritic voltage-gated conductances influence neuronal behaviour under physiological conditions (Stuart et al., 2008). A more recent study also suggests that datasets from multiple locations along the soma and dendrites are necessary for constraining model parameters of an entire neuron (Keren et al., 2009). However, measuring dendritic activities in RGCs is more difficult than other classes of cortical neurons, due to the small diameter of the dendrites. At present, there is limited experimental evidence of full dendritic AP in RGCs (Sivyer and Williams, 2013, Velte and Masland, 1999).

In this chapter, a morphologically-realistic modelling approach was used to study the biophysical mechanisms underlying multiple functionally-identified RGC types. J_h and J_{CaT} were added to the original FM formulation to build a new multi-compartment ionic model structure. With optimised cell-specific model parameters and the incorporation of detailed cell morphologies, these models were able to closely reproduce multiple RGC responses in various cells. The significance of regional distribution of ionic channels and cell morphology in shaping RGC firing patterns are discussed in detail. Moreover, the optimised models were also used to reconstruct dendritic APs without expressly including relevant data in the multi-objective optimisation, to investigate the predictive ability of the optimised models.

6.1 RGC Morphology Reconstruction

Mouse and rabbit RGCs were identified by their electrophysiology, dendritic field size/structure and stratification in the inner plexiform layer (IPL), as described in Section 4.3, Chapter 4. Cell morphologies and physical parameters can be found in Figure 6.1. Mouse ON and OFF RGC morphologies were obtained from Kong et al. (2005). Rabbit ON and OFF parasol RGC morphologies were reconstructed by Dr. David Tsai in the Graduate School of Biomedical Engineering, UNSW. Each RGC was filled with neurobiotin and digitally reconstructed using a confocal microscope with a 20×0.7 NA air and a 40×1.1 numerical aperture (NA) oil immersion objective lens, in conjunction with Imaris (Bitplane AG) and Fiji (National Institute of Health, USA) image analysis and processing software. Morphological data were digitized and subsequently imported into NEURON computational software (Hines and Carnevale, 1997), which approximated the eq. (3.2) into a multi-compartmental representation of the neuron, equivalent to a finite-difference approximation of the second spatial derivative. The model included the soma, axon initial segment (AIS), axon hillock, axon and dendrites. Depending on the complexity of cell morphology, about 300~1000 morphological segments were chosen to ensure accurate spatial resolution (see Figure 6.2).

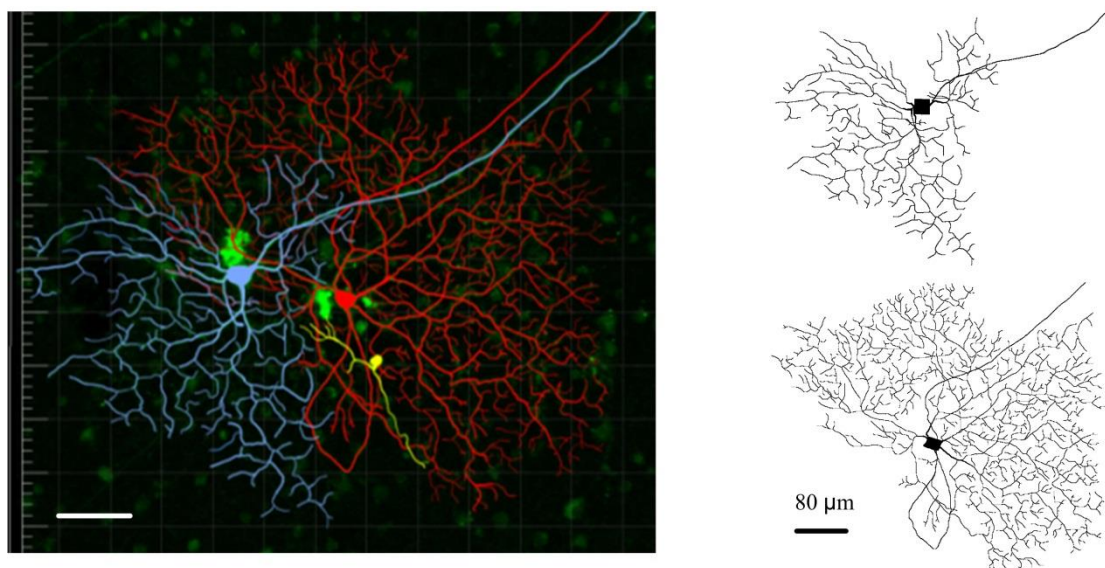


Figure 6.1 Example of RGC morphology reconstruction. Left. Rabbit ON (red) and OFF P (blue) RGC morphology visualised in Imaris software, scale bar: 80 μm . Right. Computer-reconstructed RGC morphology in NEURON software. The soma was reconstructed using an equivalent cylinder representation sharing the same somatic cell membrane area as the real cell. These two RGCs were reconstructed by Dr. David Tsai in the Graduate School of Biomedical Engineering, UNSW.

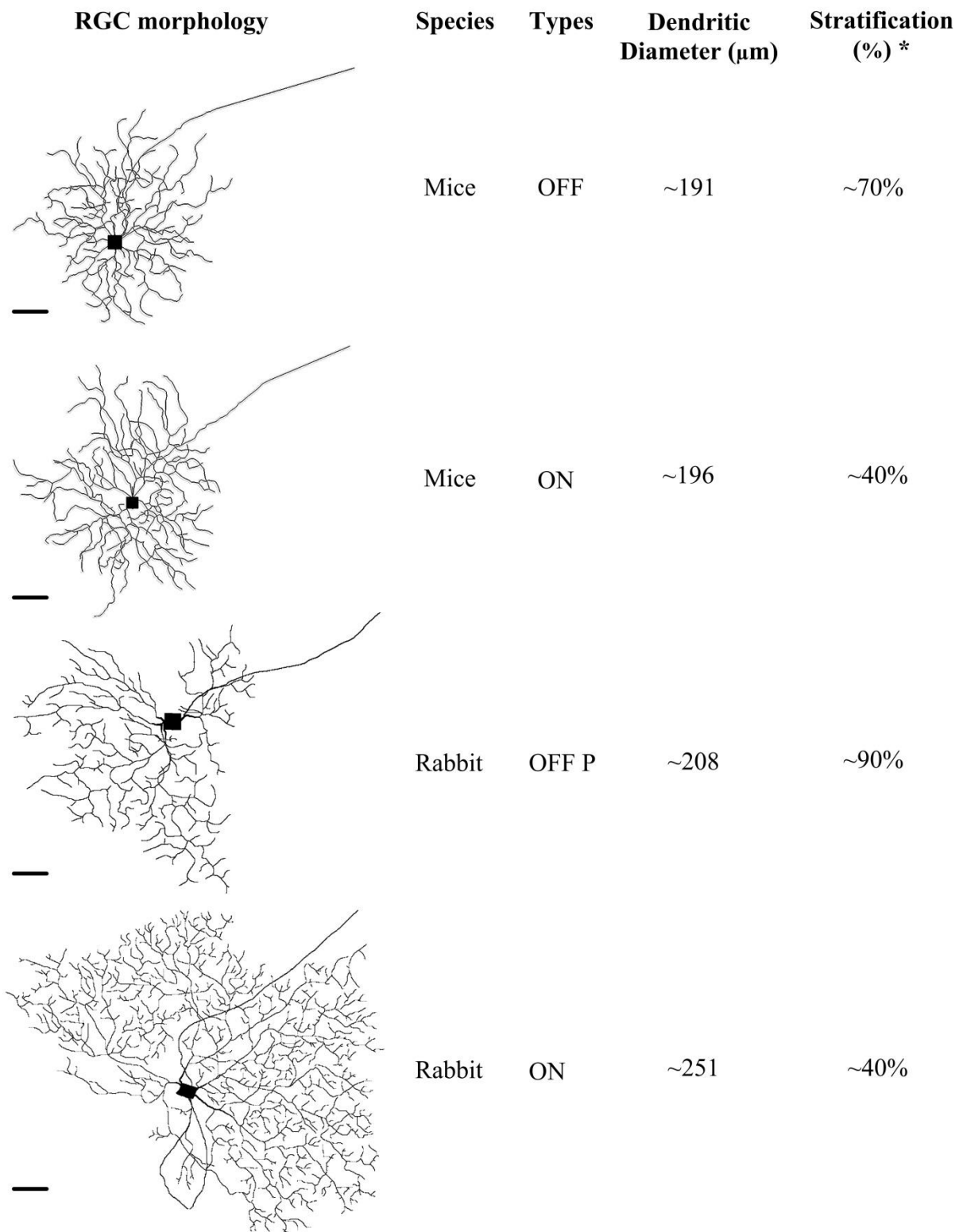


Figure 6.2 RGC morphological reconstruction using NEURON software. Two mouse RGCs (Kong et al., 2005) and two rabbit RGCs were used. RGC types were identified by their electrophysiological and physical properties. The scale bar at the left of each figure denotes 40 μm . * The inner (i.e. vitreal) edge of the ganglion cell layer was defined as 0%.

6.2 Cell-Specific RGC Modelling with Shared Kinetic Parameters

In this section, three models based on realistic representations of three RGC morphologies were used to investigate the contribution of neuron spatial structure and membrane ion channel properties to RGC electrical activity. In all simulations, RGC models shared common ionic channel kinetics, differing only in their regional ionic channel distributions (i.e. maximal membrane conductance values) and cell morphology. Since a synaptic blocker (see Section 4.3 in Chapter 4) was applied during the *in vitro* recording, the influence from the retinal network was not a factor in distinguishing different RGC types.

In cellular morphological models, the membrane potential can be described by the cable equation:

$$\frac{\partial}{\partial s} \left(\sigma_i \frac{\partial V_m}{\partial s} \right) = \beta \left(C_m \frac{\partial V_m}{\partial t} + J_{ion} - J_{stim} \right) \quad (6.1)$$

where s is the arc-length along the neuron, σ_i is the intracellular conductivity, β is the local surface to volume ratio ($\beta=2/r$ for a circular cylinder neuron of radius r), J_{stim} is the somatic current injection and J_{ion} represents the total membrane current density (amperes per unit membrane area). Other than the original FM formulations, two additional ionic currents, hyperpolarisation-activated current (J_h) and T-type calcium current (J_{CaT}) were added to simulate mechanisms underlying rebound spiking.

The RGC models were simultaneously fitted to three groups of AP datasets recorded from ON, OFF and OFF Parasol (OFF P) cells. All maximum conductance as well as specific gating rate kinetic parameters describing J_h and J_{CaT} were chosen to be optimised (see tables 6.1 and 6.2). The intrinsic properties of the three RGC models were reconstructed using identical optimised values of kinetic parameters but cell-specific optimised maximum membrane conductance (\bar{g}_j) parameters. Each group included twelve RGC voltage responses recorded during depolarising and hyperpolarising somatic current injections (500 ms duration, -210 to 120 pA in 30 pA steps). It was assumed that spiking pattern variations were due to the differential distribution of ion channels and cell morphologies among the three RGC types. As such, kinetic parameter values were shared between each RGC type, and the maximum membrane conductance parameters were set to be cell-specific. In all simulations, models were run for 500 ms before stimulation onset, in order to ensure that steady-state had been reached prior to stimulus delivery.

Resting potentials were set to -62, -65 and -60 mV for ON, OFF and OFF P models, respectively. Depolarising current injections with amplitudes of 100, 120 and 140 pA were used for the soma in all cells. Hyperpolarising current injections with amplitudes of 120, 140 and 160 pA were used for OFF, OFF P cells and 120, 200, 300 pA were used for the ON cell. Stimulation durations were set to be 500 ms. Membrane potentials were recorded in response to multiple depolarising (red) and hyperpolarising (blue) somatic current injections in each RGC.

As shown in Figure 6.3, three RGC models with identical ionic channel kinetic parameters showed robust spiking behaviours with different combinations of RGC morphologies (Figure 6.3B) and non-uniformly distributed ionic channel conductances (Figure 6.3A and E). In particular, OFF and OFF P cells demonstrated marked excitation in response to hyperpolarising stimuli, including a large time-dependent depolarising “sag” (~17 and ~11 mV respectively) during hyperpolarisation. They also exhibited different levels of rebound spike rate following termination of the hyperpolarising stimulus (see blue traces in Figure 6.3C). The ON cell only showed a relative small sag (~3 mV). After the current step was terminated, the ON cell did not show any rebound spiking activities, despite having a much higher hyperpolarising amplitude (300 pA compared with 160 pA in the OFF cells). Furthermore, these three cell types exhibited different spiking frequency and latency in response to the same levels of stimuli (highlighted in the red and blue traces of Figure 6.3C). The rate of membrane voltage change (Figure 6.3D) also differed between each cell type. It should be noted that each model demonstrated marked initial segment-soma dendritic (IS-SD) break, as shown by the rate of voltage change (phase plot). This IS-SD break was absent in our single-compartment model (Figure 5.3), due to the absent the back propagation from axonal and dendritic compartments. Red and blue traces in Figure 6.3 highlight individual depolarised and hyperpolarised responses corresponding to the step commands of the same colour.

The maximum conductance parameters of all membrane ionic channels were set to be region-specific, in order to reflect the relative proportion of ion channels in specific regions (i.e. soma, hillock, AIS, axon and dendrites) in each RGC. Resulting maximum membrane conductance values per region in each cell are also listed in Table 6.1. Figure 5.3E indicated the estimated ionic channel distributions in each neuronal compartment, defined as maximum conductance ratio between each RGC region and the soma ($\bar{g}_j, x/\bar{g}_j, \text{soma}$). In particular, the

cells included a tenfold ratio of AIS to somatic Na⁺ channel density (red bar), and a fivefold ratio of AIS to somatic T-type Ca²⁺ channel density (light blue bar).

All of these simulation results qualitatively matched the experimental recordings from biological RGC types (see Figure 4.4 in Chapter 4). Each model was able to reproduce realistic firing properties to both hyperpolarising and depolarising stimuli, including the patterns of depolarising sag, frequency adaptation, FSL, as well as the spiking property variations caused by different stimulus amplitudes.

An additional simulation was undertaken to investigate the contribution of the hyperpolarisation-activated and T-type calcium currents to spiking behaviour using the OFF RGC model. Two specific parameters, the maximum membrane conductances of J_h and J_{CaT} , were gradually reduced in order to model the effect of these two currents on rebound excitation. All other model parameters were held fixed. As shown in Figure 6.4A, blocking J_h has a stronger influence on rebound activity than J_{CaT} , particularly in terms of rebound FSL. In addition, block of J_h resulted in reduction of hyperpolarised-induced sag amplitude and shift of resting membrane potential (Figure 6.4B), whilst block J_{CaT} did not influence these two properties.

Despite the successful reconstruction of spiking activities, each RGC model was optimised against time-series AP data only. However, other information such as AP waveshape (2-D phase plot) has also been reported to carry important neuronal information (Fohlmeister and Miller, 1997b), and may therefore, also contribute to RGC identification. The ability of these models to accurately reconstruct cell-specific AP waveforms was still unclear. In addition, ON and OFF RGC model presented in this chapter are reconstructed based on cell morphologies and data from these different species, limiting the accuracy and utility of these models. These issues were addressed in the next section.

TABLE 6.1.
Ionic Channel Distributions

Channel	Regional Maximum Membrane Conductances (mS/cm ²)				
	Soma	Axon	AIS	Hillock	Dendrites
ON					
J_{Na}	51	51	510	51	19.1
J_K	13.1	13.1	13.1	13.1	8.73
J_{KA}	39.4	-	39.4	39.4	26.27
J_{Ca}	1.1	-	1.1	1.1	1.47
J_{KCa}	0.047	0.047	0.047	0.047	7.23e-4
J_h	0.11	0.11	0.11	0.11	0.11
J_{CaT}	0.029	0.029	0.029	0.029	0.145
J_L	0.147	0.147	0.147	0.147	0.147
OFF					
J_{Na}	45.9	45.9	459	45.9	17.2
J_K	13.1	13.1	13.1	13.1	8.73
J_{KA}	39.4	-	39.4	39.4	26.27
J_{Ca}	1.1	-	1.1	1.1	1.47
J_{KCa}	0.47	0.47	0.47	0.47	7.23e-4
J_h	0.383	0.383	0.383	0.383	0.383
J_{CaT}	0.052	0.052	0.052	0.052	0.26
J_L	0.147	0.147	0.147	0.147	0.147
OFF P					
J_{Na}	48	48	480	48	18
J_K	25.2	25.2	25.2	25.2	16.8
J_{KA}	18.9	-	18.9	18.9	12.6
J_{Ca}	2.2	-	2.2	2.2	2.94
J_{KCa}	0.047	0.047	0.047	0.047	7.23e-4
J_h	0.132	0.132	0.132	0.132	0.132
J_{CaT}	0.017	0.017	0.017	0.017	0.085
J_L	0.07	0.07	0.07	0.07	0.07

Table 6.1 Regional ionic channel distributions in ON, OFF and OFF P RGC models. Ionic channel maximum conductances were set to be compartment-specific, in order to reflect the proportion of ion channels in specific regions of each RGC.

TABLE 6.2.
Optimized ionic current formulations for ON, OFF and OFF P RGC models.

Channel		
J_{Na}	$J_{Na} = \bar{g}_{Na} m^3 h (V_m - 35)$	
	$\alpha_m = -0.6(V_m + 30)/(e^{-0.1(V_m+30)} - 1)$	$\beta_m = 20e^{-(V_m+55)/18}$
	$\alpha_h = 0.4e^{-(V_m+50)/20}$	$\beta_h = 6/(1 + e^{-0.1(V_m+20)})$
J_{Ca}	$J_{Ca} = \bar{g}_{Ca} c^3 (V_m - V_{Ca})$	
	$\frac{d[Ca^{2+}]_i}{dt} = -\left(\frac{3}{2F\tau} J_{Ca}\right) - \frac{[Ca^{2+}]_i - 0.0001}{50}$	$V_{Ca} = \frac{RT}{2F} \ln\left(\frac{1.8}{[Ca^{2+}]_i}\right)$
	$\alpha_c = -0.3(V_m + 13)/(e^{-0.1(V_m+13)} - 1)$	$\beta_c = 10e^{-(V_m+38)/18}$
J_K	$J_K = \bar{g}_K n^4 (V_m + 75)$	
	$\alpha_n = -0.02(V_m + 40)/(e^{-0.1(V_m+40)} - 1)$	$\beta_n = 0.4e^{-(V_m+50)/80}$
J_{KA}	$J_{KA} = \bar{g}_{KA} A^3 h_A (V_m + 75)$	
	$\alpha_A = -0.006(V_m + 90)/(e^{-0.1(V_m+90)} - 1)$	$\beta_A = 0.1e^{-(V_m+30)/10}$
	$\beta_{hA} = 0.04e^{-(V_m+70)/20}$	$\beta_{hA} = 0.6/(1 + e^{-0.1(V_m+40)})$
J_{KCa}	$J_{KCa} = g_{KCa} (V_m + 75)$	
	$g_{KCa} = \bar{g}_{KCa} \left[\left(\frac{[Ca^{2+}]_i}{0.001} \right)^2 / (1 + \left(\frac{[Ca^{2+}]_i}{0.001} \right)^2) \right]$	
J_h	$J_h = \bar{g}_h y (V_m + 26.8)$	
	$y_\infty = 1/(1 + e^{(V_m+75)/5.5})$	$\tau_y = 561.2 e^{0.01(V_m+20)} / (1 + e^{0.2(V_m+20)})$
J_{CaT}	$J_{CaT} = \bar{g}_{CaT} m_T^3 h_T (V_m - V_{Ca})$	
	$\alpha_{mT} = \frac{0.91}{1 + e^{-0.17(V_m+61.5)}}$	$\beta_{mT} = \frac{0.64}{1 + e^{-0.03(V_m+10)}} + \frac{0.64}{1 + e^{0.2(V_m+89.4)}}$
	$\alpha_{hT} = 0.013e^{0.022(V_m+131.1)}$	$\beta_{hT} = \frac{0.9}{1 + e^{-0.02(V_m+42.9)}}$
J_L	$J_L = \bar{g}_L (V_m + 75)$	

Table 6.2 Ionic channel kinetic parameters were shared among ON, OFF and OFF P RGC models. All rates are in units of 1/ms, voltages in units of mV, $[Ca^{2+}]_i$ in units of mM, time constants in units of ms, and membrane currents in units of mA/cm². Parameters highlighted in red (i.e. maximal membrane conductances) were allowed to vary between different RGCs and in different morphological compartments. Kinetic parameters optimized are shown in blue. These parameters were held fixed for all neural compartments. Simulated temperature was set to be 308 K.

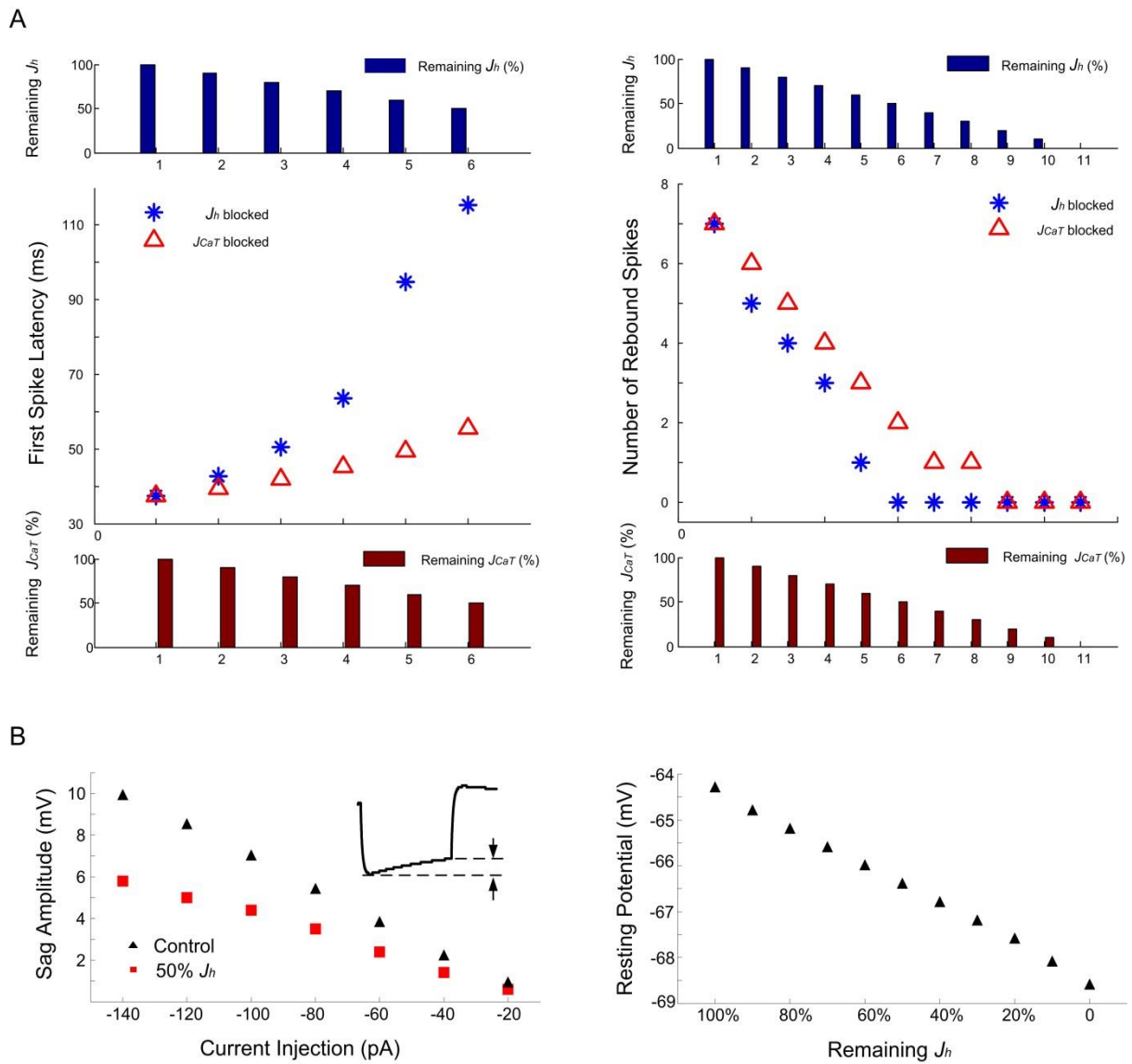


Figure 6.4 A. Model-generated FSL and rebound spike number after J_h and J_{CaT} were progressively blocked by reducing their maximum conductance parameters. Rebound excitation was significantly reduced in terms of rebound FSL (left) and spiking number (right) by blocking J_h , whilst block of J_{CaT} was less effective in reducing rebound spiking number and influencing FSL. B. The depolarising sag (measured as peak-to-steady state potential difference during hyperpolarising stimulation) in response to multiple hyperpolarising currents was significantly attenuated when J_h was blocked by 50% (left panel). There was a linear hyperpolarising shift in resting membrane potential with increasing levels of J_h block (right panel).

6.3 Accurate Reconstruction of RGC Electrical Activities with Multi-Objective Optimisation

In this section, the ON and OFF P RGC models based on realistic morphologies were simultaneously fitted to time-series action potential (AP) datasets and phase plot datasets (time derivative of membrane potential versus membrane potential), recorded from each cell type. In total, twelve AP datasets plus twelve phase plot datasets were used to optimise each RGC model. In addition to the AP and phase plot datasets, our objective function also included quantitative data relating to spiking patterns such as FSL, total spike number, average ISI during depolarisation, and “sag” amplitude in response to hyperpolarising injections (see the definition of each spiking property in Table 4.1 in section 4.2.4).

During parameter optimisation, the values of most gating rate kinetic parameters were shared between the ON and OFF P cell models. A subset gating rate kinetic parameters along with all maximum membrane conductance (\bar{g}_j) parameters (indicators of ion channel densities), were optimised and set to be cell-specific to reflect the intrinsic properties of each cell type (see Tables 6.3-6.5). In addition, the somatic current magnitudes were also fitted to ensure the accurate reconstruction of multiple spiking patterns against a range of stimulus amplitudes (see Figure 6.5D and Figure 6.6D). In all simulations, a model was run for 500 ms prior to stimulation onset, in order to reach steady state.

”

6.3.1 Morphologically and Functionally-Accurate ON and OFF RGC Model

Experimental data for optimising each model was recorded from the same RGC used for morphology reconstruction (see Figure 6.1). Each data group included twelve RGC voltage responses recorded during depolarising and hyperpolarising somatic current injections (500 ms duration, -120 ~ 210 pA)

Figure 6.5 and Figure 6.6 show fitted AP results for an ON and OFF P cell following multi-dataset optimisation. The OFF P model demonstrated rebound excitation in response to hyperpolarising stimuli, including pronounced depolarising “sag” (~5 mV) during hyperpolarisation (Figure 6.6C) owing to the activation of J_h . In contrast, the ON model shown in 6.5C only revealed a relatively small sag (~3 mV), despite having a much higher hyperpolarising stimulus (140 pA compared with 50 pA in the OFF P model). ON and OFF model reconstructions (red traces) closely matched the experimental data (blue traces) recorded from the same RGC used for morphology reconstruction. However, when original FM formulations (Fohlmeister and Miller, 1997b) were used on the same RGC morphologies shown in Figure 6.5D and 6.6D, a hyperpolarisation current injection caused the membrane to hyperpolarise along an approximately exponential time course governed by the passive membrane time constant. When the current injection was terminated, the membrane voltage smoothly decayed back to its original resting potential (see black traces in Figure 6.5C and 6.6C).

The ON and OFF P RGC models also exhibited significantly different ionic channel distributions in their neuronal compartments (Figure 6.5E and 6.6E) which contributed to the cell-specific spiking patterns and AP waveshapes in response to multiple somatic injections. In particular, the ON cell exhibited an ~sevenfold ratio of AIS to somatic J_{Na} density versus a corresponding ~fourfold ratio in the OFF P cell. In addition, a high dendritic J_h ratio (twofold AIS to that in soma) and J_{CaT} (fivefold AIS to that in soma) were obtained in the OFF P cell, whilst the ON cell only exhibited relatively low J_h (dendrite-to-somatic J_h ratio was 1.3:1) and J_{CaT} (dendrite-to-somatic J_h ratio was 1:1). The optimised maximum membrane conductance values in each cellular region for the ON and OFF P models are also listed in Table 6.3.

Moreover, the rate of membrane voltage change (i.e. 2-D phase plot) also differed between the two optimised model neurons. In particular, the model ON cell exhibited lower rates of depolarising/repolarising phases, higher overshoot and more obvious initial segment-soma dendritic (IS-SD) break than the OFF P cell. All of these simulation results closely matched

the recorded rate of membrane voltage change (blue) from real RGCs. In contrast, the phase plots reconstructed by the original FM model (black) were generally far from the experimental data.

Figure 6.7 shows the quantitative comparison between the optimised model and the original FM model performance in terms of their reconstructed response to a range of stimulation amplitudes. Hyperpolarising somatic injections (H1~H4) were set to be -26, -70, -110, 140 pA for the ON cell, and -20, -30, -38, -50 pA for the OFF P cell. The depolarising injections (D1~D7) were set to 17, 60, 97, 116, 131, 150 and 160 pA for the ON cell and 30, 46, 61, 74, 87, 103, 120 pA for the OFF cell. In the upper panels of Figure 6.7A, B and C, the optimised ON and OFF P models (red) each exhibited unique spiking patterns, including FSL, interspike interval and total spike number for different stimulus amplitudes. The optimised model demonstrated an obvious advantage over the original FM model, as indicated by the residual bars between model-reconstructed and experimental spiking patterns shown in the lower panels. The black circles in Figure 6.7A and B indicate non-existent data. Panels D and E of Figure 6.7 showed model-reconstructed (red), and experimental (blue) sag amplitude and post offset FSL under multiple hyperpolarizing injections. The original FM model could not reproduce ‘sag’ during hyperpolarizing injections, or rebound spiking activity, indicating the importance of the added membrane currents (i.e. J_h and J_{CaT}) in shaping firing patterns. Black triangles in panels D and E indicate the data that original FM model failed to reproduce. Panel F of Figure 6.7 shows a quantitative comparison between optimised model (red) and FM model (black) rate of membrane voltage change using a normalised 2D RMS (for details, see section 4.2.4). The residual bars in the lower panel indicate that the optimised model demonstrates far higher accuracy in reconstructing the rate of membrane voltage change.

To further explore the predictive ability of the models, we also examined the membrane potential at the AIS, soma and distal dendrite for the ON and OFF P RGC models used throughout this chapter (Figure 6.8B and A). When a stimulus of 100 pA was applied to the soma, different AP and Na^+ channel density waveforms were observed in each cellular region between the ON (panel B) and OFF P (panel A) models. Recording sites in the AIS, soma and dendrite were indicated by the blue, red and green cones respectively. In a more recent experimental study (Sivyer and Williams, 2013), simultaneous whole-cell current-clamp recordings were made from the soma and the parent dendrites of rabbit RGCs under both light and electrical stimulation. As shown in Figure 6.8C, a 200 pA somatic current injection evoked a somatic AP (black AP recorded by gray electrode), which rapidly back-propagated

to dendritic recording sites (red AP by red electrode) with little amplitude decrement. Interestingly, although experimental dendritic AP data was not available to include in our optimisation, our model-reconstructed dendritic APs (Figure 6.8A) closely matched recent recordings obtained from RGC dendrites in terms of overall waveshape and comparable reduction in AP amplitude compared to that of the soma (see Figure 6.8C).

Figure 6.9 demonstrates the normalised current-voltage (I-V) curve for J_h and J_{CaT} , generated by the OFF P model, compared to experimental voltage-clamp data recorded from the actual OFF P cell used to optimise model parameters. J_h voltage-clamp simulations were generated using a holding potential of -55mV, while sequentially hyperpolarising the cell from -55 to -105 mV in decrements of 10 mV. Each voltage clamp step was of duration 500 ms. In the right panel of Figure 6.9A, the family of current traces exhibited a slow increase in the inward current. The magnitude and rate of activation of this inward current increased with higher hyperpolarising commands. The left and middle panels of Figure 6.9A show the experimental and reconstructed normalised current-voltage (I-V) J_h relationship. The steady state J_h values at the end of the 500 ms pulse were measured for each current step and have been plotted against the corresponding injected current amplitudes. In another simulation, J_{CaT} voltage-clamp behaviours were reconstructed with a holding potential of -100mV, while sequentially depolarising the cell from -80 to -35 mV in increments of 5 mV. In the left panel of Figure 6.9B, the family of current traces exhibited a fast activation component which is followed by a relatively slow inactivation component. The left and middle panels of Figure 6.9B show the experimental and reconstructed normalised I-V relationship for J_{CaT} using the peak J_{CaT} amplitudes versus the corresponding injected current amplitudes. Both experimental and simulated currents were obtained from the soma. As can be seen from the figure, the model (Figure 6.9A and B, right panel) closely matched the actual J_h and J_{CaT} dynamics observed (Figure 6.9A and B, left panel).

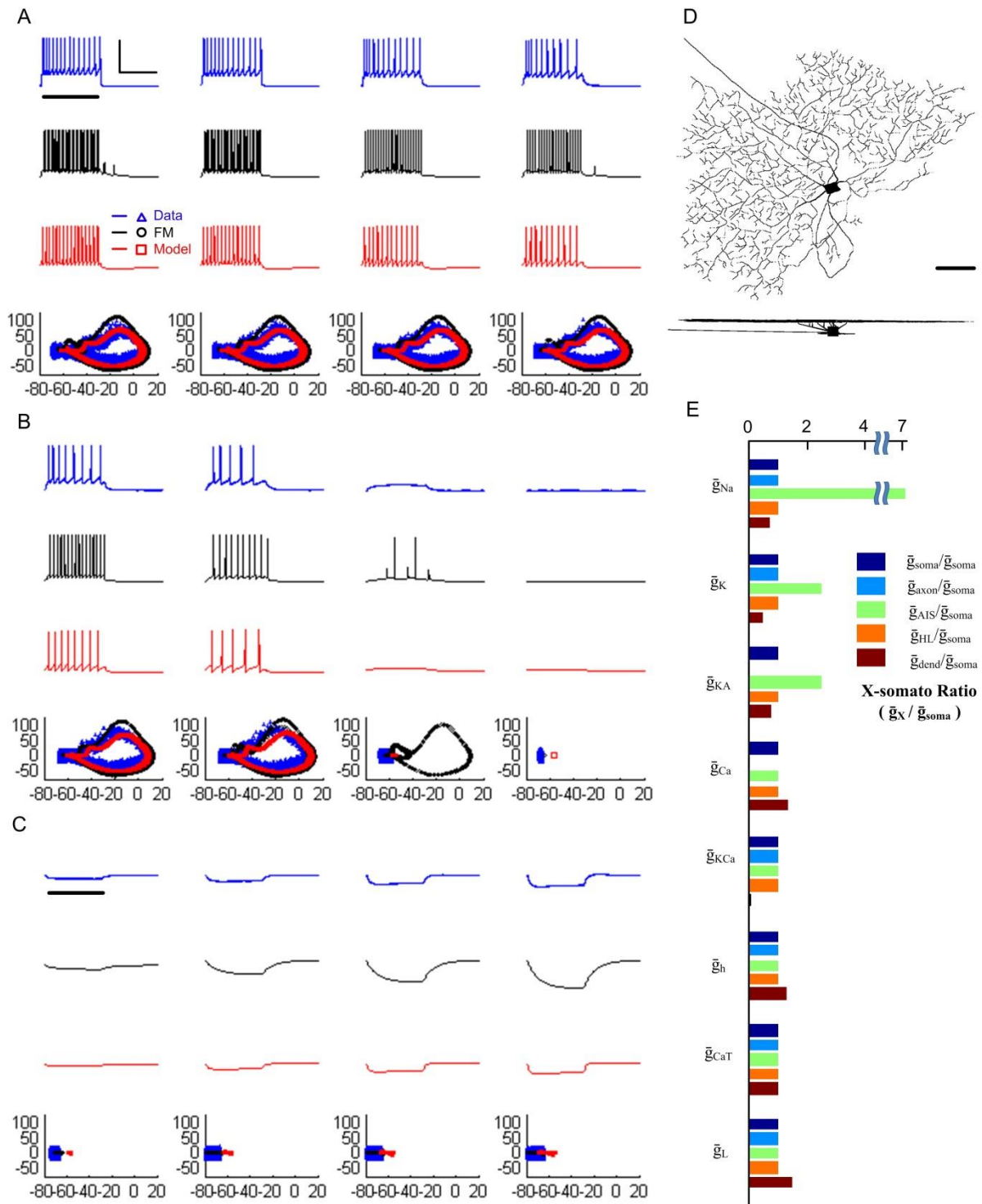


Figure 6.5 Comparison of ON RGC optimised model (red), original FM model (black) outputs and experimental data (blue) in response to multiple somatic injections of 120~210 pA (panel A), 0~90 pA (panel B) and -120~-30 pA (panel C). A, B and C. Upper: Experimentally recorded membrane potential (blue) from ON RGC. Middle: optimised (red) and FM (black) model-generated membrane potentials in response to a family of somatic current pulses shown by the thick horizontal line in the top left trace of panel A. Lower: Phase plot (dV_m/dt versus V_m) of experimentally-recorded (blue), optimised (red) and FM (black) model-generated membrane potential responses to multiple somatic injections. D. Reconstructed ON RGC morphology. Horizontal bar: 40 μ m. E. Ionic channel distribution ratio between each RGC region and the soma (defined as $\bar{g}_j / \bar{g}_{j, soma}$) in ON model.

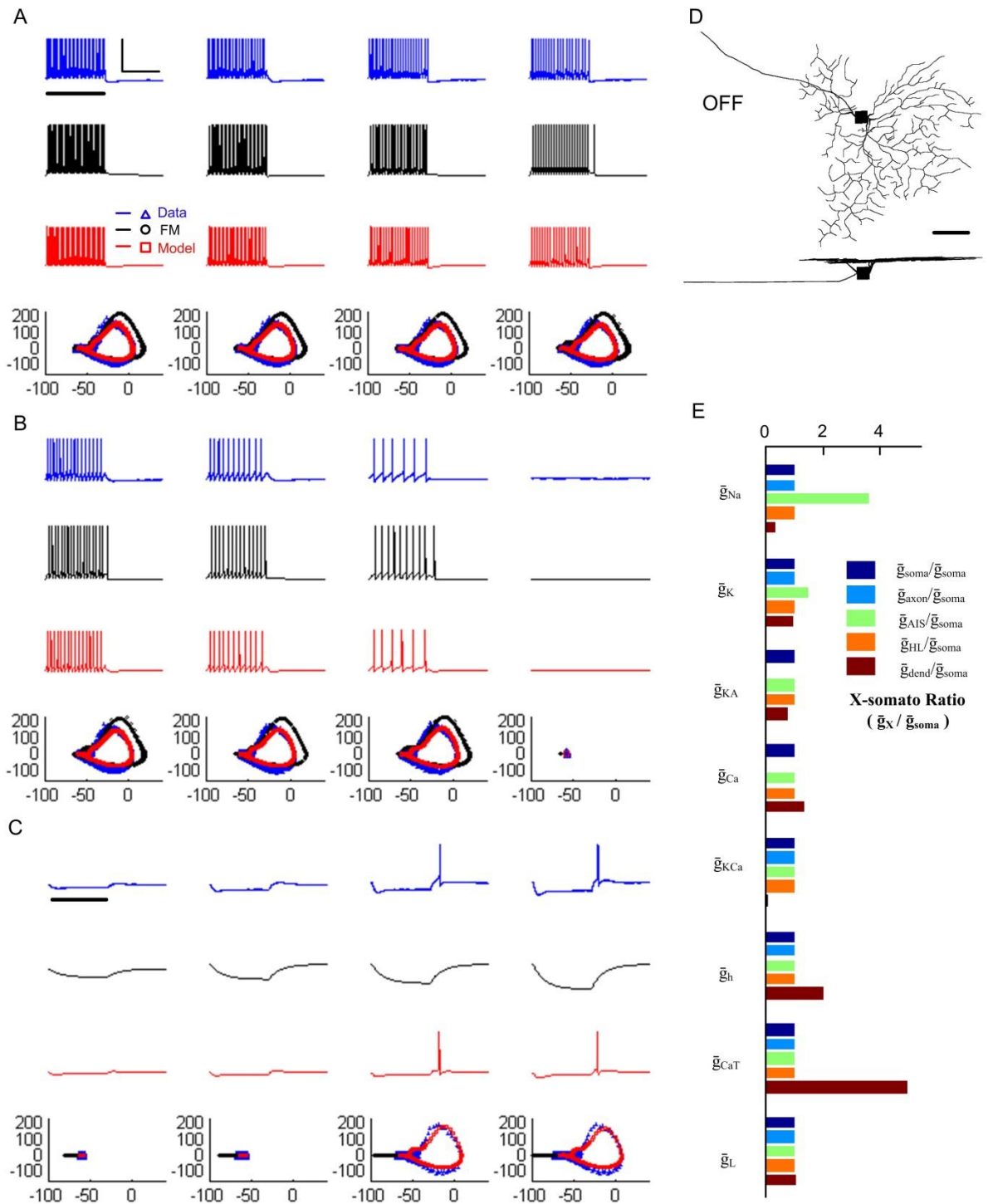


Figure 6.6 Comparison of OFF P RGC optimised model (red), original FM model (black) outputs and experimental data (blue) in response to multiple somatic injections of 120~210 pA (panel A), 0~90 pA (panel B) and -120~-30 pA (panel C). A, B and C. Upper: Experimental membrane potentials obtained in OFF RGC. Middle: optimised (red) and FM (black) model-reconstructed membrane potentials in response to a family of somatic current pulses. Lower: Phase plots of experimentally recorded (blue), optimized (red) and FM (black) model-generated membrane potential responses to multiple somatic injections. D. Reconstructed OFF P RGC morphology. Horizontal bar: 40 μ m. E. Ionic channel distribution ratio between each RGC region and the soma (defined as $\bar{g}_i, x / \bar{g}_i, soma$) for the OFF P model.

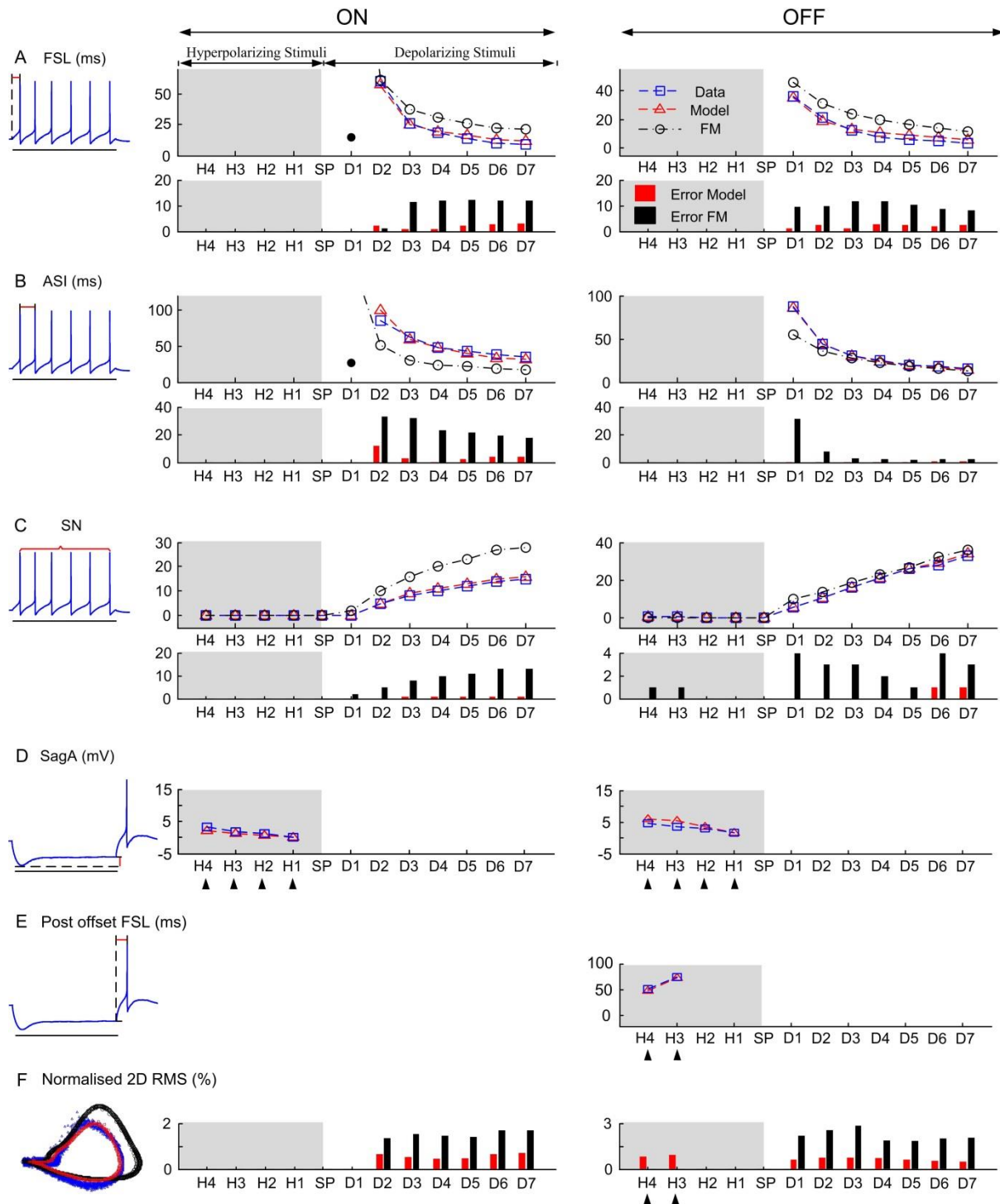


Figure 6.7 Comparison of optimised model (red) and original FM model (black) performance against experimental data (blue) using a range of stimulation amplitudes. A, B and C. Upper, model-reconstructed (red), FM model-reconstructed (black) and experimental (blue) spiking patterns in response to multiple somatic injections. Black circles in A and B indicate non-existent data. Lower, Comparison of optimised model (red) and FM model (black) performance in terms of discrepancy between models and data. H1-H4: hyperpolarizing injections, D1-D7: depolarizing injections, SP: no injection. D and E. Model-reconstructed (red), and experimental (blue) sag amplitude and post offset FSL under multiple hyperpolarizing injections. Note that the original FM model was not able to reproduce the characteristic ‘sag’ during hyperpolarizing injections, nor could it reproduce rebound spiking activity. F. Comparison of optimised model (red) and FM model (black) reconstructed phase plots in terms of normalised 2D RMS. Black triangles in D, E and F indicate experimental data that original FM model failed to reconstruct.

TABLE 6.5.
Optimized ionic current formulations for OFF RGC model.

Channel		
J_{Na}	$J_{Na} = \bar{g}_{Na} m^3 h (V_m - 35)$	
	$\alpha_m = -0.6(V_m + 30)/(e^{-0.1(V_m+30)} - 1)$	$\beta_m = 20e^{-(V_m+55)/18}$
	$\alpha_h = 0.4e^{-(V_m+50)/20}$	$\beta_h = 6/(1 + e^{-0.1(V_m+20)})$
J_{Ca}	$J_{Ca} = \bar{g}_{Ca} c^3 (V_m - V_{Ca})$	
	$\frac{d[Ca^{2+}]_i}{dt} = -\left(\frac{3}{2F\tau} J_{Ca}\right) - \frac{[Ca^{2+}]_i - 0.0001}{55}$	$V_{Ca} = \frac{RT}{2F} \ln\left(\frac{1.8}{[Ca^{2+}]_i}\right)$
	$\alpha_c = -0.15(V_m + 13)/(e^{-0.1(V_m+13)} - 1)$	$\beta_c = 10e^{-(V_m+38)/18}$
J_K	$J_K = \bar{g}_K n^4 (V_m + 68)$	
	$\alpha_n = -0.02(V_m + 40)/(e^{-0.1(V_m+40)} - 1)$	$\beta_n = 0.4e^{-(V_m+50)/80}$
J_{KA}	$J_{KA} = \bar{g}_{KA} A^3 h_A (V_m + 68)$	
	$\alpha_A = -0.003(V_m + 90)/(e^{-0.1(V_m+90)} - 1)$	$\beta_A = 0.1e^{-(V_m+30)/10}$
	$\beta_{hA} = 0.04e^{-(V_m+70)/20}$	$\beta_{hA} = 0.6/(1 + e^{-0.1(V_m+40)})$
J_{KCa}	$J_{KCa} = \bar{g}_{KCa} (V_m + 68)$	
	$g_{KCa} = \bar{g}_{KCa} \left[\left(\frac{[Ca^{2+}]_i}{0.001} \right)^2 / \left(1 + \left(\frac{[Ca^{2+}]_i}{0.001} \right)^2 \right) \right]$	
J_h	$J_h = \bar{g}_h y (V_m + 26.8)$	
	$y_\infty = 1/(1 + e^{(V_m+75)/5.5})$	$\tau_y = 588.2 e^{0.01(V_m+10)} / (1 + e^{0.2(V_m+10)})$
J_{CaT}	$J_{CaT} = \bar{g}_T m_T^3 h_T (V_m - V_{Ca})$	
	$\alpha_{mT} = 1/(1.7 + e^{-(V_m+28.8)/13.5})$	$\beta_{mT} = \left(1 + e^{-\frac{V_m+63}{7.8}} \right) / \left(1.7 + e^{-\frac{V_m+28.8}{13.5}} \right)$
	$\alpha_{hT} = e^{-(V_m+160.3)/17.8}$	$\beta_{hT} = \alpha_{hT} \left(\sqrt{0.25 + e^{\frac{V_m+83.5}{6.3}}} - 0.5 \right)$
	$\alpha_d = \left(1 + e^{\frac{V_m+37.4}{30}} \right) / \left(240 \left(0.5 + \sqrt{0.25 + e^{\frac{V_m+83.5}{6.3}}} \right) \right)$	$\beta_d = \alpha_d \sqrt{0.25 + e^{\frac{V_m+83.5}{6.3}}}$
J_L	$J_L = \bar{g}_L (V_m + 70.5)$	

Table 6.5 Specific ionic channel kinetics parameters for ON RGC model, all the other parameters were shared between ON and OFF P models. All rates are in units of 1/ms, voltages in units of mV, $[Ca^{2+}]_i$ in units of mM, time constant in units of ms, and membrane currents in units of mA/cm². Parameters highlighted in red (i.e. maximal membrane conductances) were allowed to vary between the ON and OFF P cells, as well as vary in different morphological compartments (see Table 6.3). Kinetic parameters optimized are shown in blue. These parameters were held fixed for all neural compartments. Simulated temperature was set to be 308 K.

6.3.2 RGC Dendritic Activation

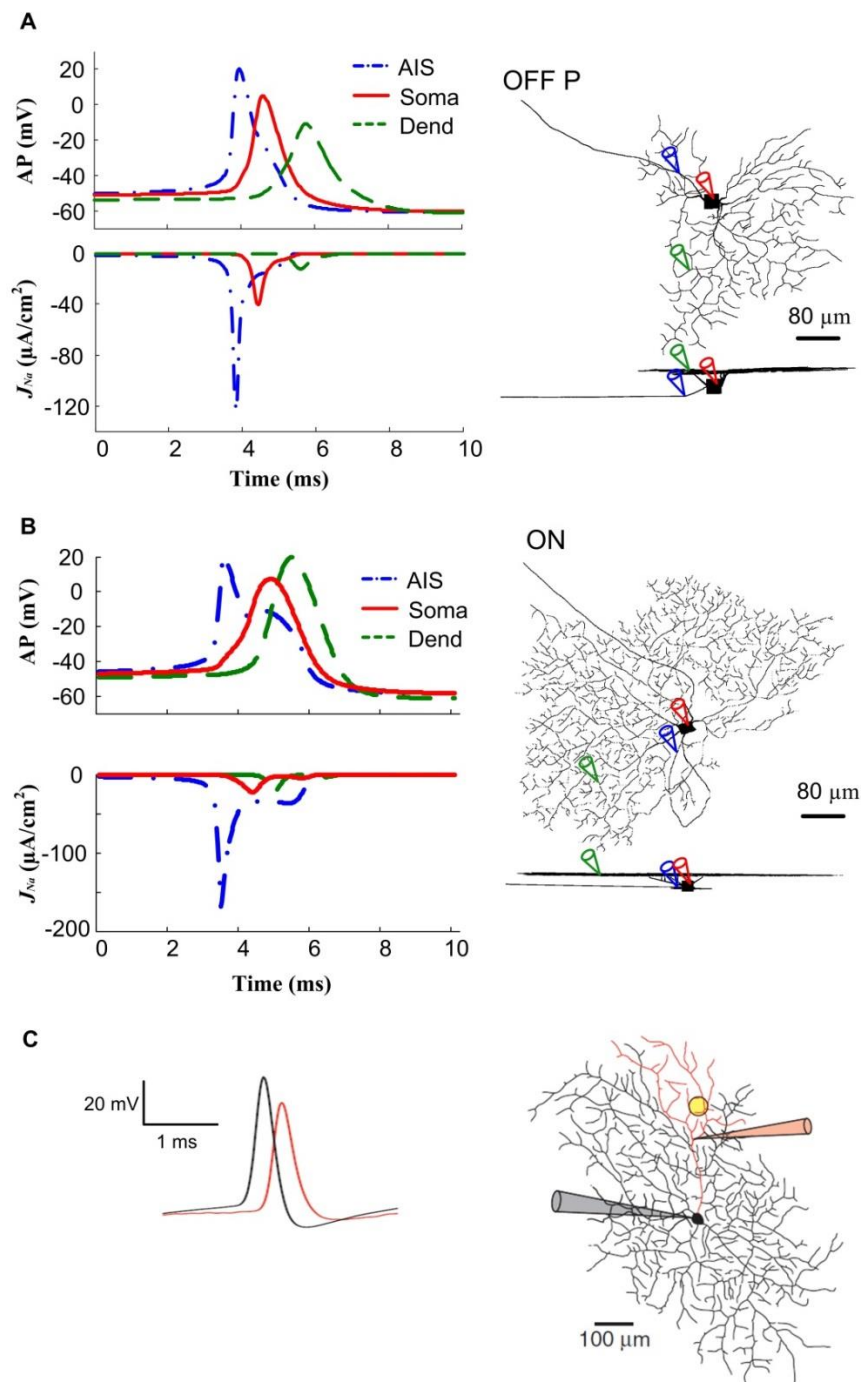


Figure 6.8 Cell-specific APs in dendrites and the AIS. A. Upper: Model-reconstructed AP in AIS (blue), soma (red) and dendritic tree (green). Lower: Model-reconstructed Na^+ current from axon initial segment (blue), soma (red) and dendritic tree (green). Right: Location of AIS, somatic and dendritic APs in OFF P cell morphology. B. Upper: Model-reconstructed APs in AIS (blue), soma (red) and dendritic tree (green). Lower: Model-reconstructed Na^+ current from AIS (blue), soma (red) and dendritic tree (green). Right: Location of AIS, somatic and dendritic APs in ON cell morphology. C. Experimental data from Sivyer and Williams (2013). This study suggested that a full AP can be evoked by both a flashing-spot light stimulus and direct somatic current injection. Left: Experimental RGC somatic (black) and dendritic (red) AP in response to a 0.2 nA somatic current injection. Right: Reconstructed rabbit RGC. Yellow circle shows flashing-spot light stimulus location. The red coloured portion indicates the recorded dendritic sub-tree.

6.3.3 Role of J_h and J_{CaT} in RGC Spiking

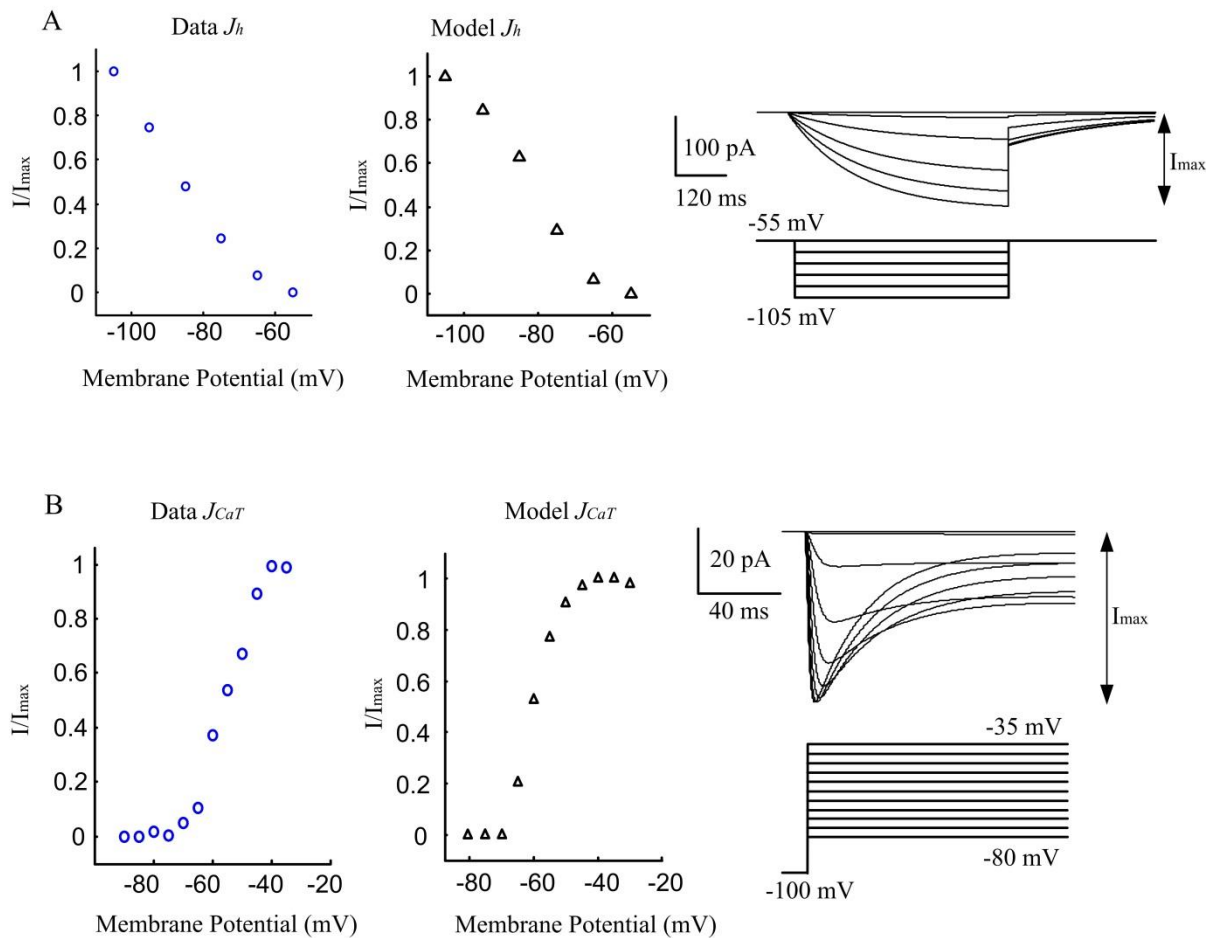


Figure 6.9 Simulated and experimental voltage-clamp behaviour of J_h and J_{CaT} . Experimental voltage-clamp currents were obtained from the same OFF P cell used throughout this chapter. A. Left: Experimental normalised current-voltage (I-V) J_h relationship from the amplitude of steady-state membrane hyperpolarisation-activated current obtained in RGCs (from a holding potential of -55 mV, in 10 mV steps). Middle: Simulated normalised I-V relationship for J_h . Right: Voltage-clamp simulation of J_h in the OFF P RGC model. Simulated somatic current injection: 500 ms duration, from a holding potential of -55 mV, in 10 mV steps. Membrane current shown is for the soma. B. Left: Experimental normalised I-V relationship for J_{CaT} calculated from peak amplitude (from a holding potential of -100 mV, in 5 mV steps). Middle: Simulated normalised I-V J_{CaT} relationship. Right: Voltage-clamp simulation for J_{CaT} in the OFF P RGC model. Simulated somatic current injection: 120 ms duration, from a holding potential of -100 mV, in 5 mV steps. Membrane current shown is for the soma.

To investigate the contribution of J_h and J_{CaT} to spiking activity in the OFF P RGC model, we set the somato-dendritic channel distribution ratio of J_h and J_{CaT} (defined by $\vartheta_j = \bar{g}_{j,den}/\bar{g}_{j,soma}$) as indicators of RGC rebound firing properties, where $\bar{g}_{j,den}$ and $\bar{g}_{j,soma}$ represent the maximum membrane conductance of the corresponding ionic current in the soma and dendrites respectively. These two membrane currents were chosen because of their absence in the original FM model and importantly, their contribution during hyperpolarising stimuli. The two ratios, $\bar{g}_{h,den}/\bar{g}_{h,soma}$ and $\bar{g}_{T,den}/\bar{g}_{T,soma}$, were varied over the ranges 0~6 and 0~12, respectively. Five RGC properties were determined from the model: rebound spike number;

rebound FSL; rebound ISI, depolarising sag amplitude and input resistance (Figure 6.10A-E). Analysis was undertaken at the soma to characterise RGC activities in response to a hyperpolarising somatic injection (500 ms duration, 50 pA amplitude).

The results suggested significant correlations between certain spiking properties. For example, rebound spike number (Figure 6.10A) and average ISI (Figure 6.10D) showed similar patterns of “wave crests” and “troughs” in parameter space. These “waves” or oscillations in parameter space occurred where spiking properties altered dramatically with slight changes in conductance, typically the region around the boundary between two different spiking states. Moreover, we found that the intrinsic activity of the neuron was more sensitive to changes in conductance in certain directions (across wave crests) and relatively insensitive to changes in other directions (along the “troughs”), as indicated in the ISI (Figure 6.10D) and FSL (Figure 6.10B) maps.

In Figure 6.10C, the membrane resistance was defined as the ratio of membrane voltage displacement to injected current using a 120 pA hyperpolarising somatic current injection. This resistance gradually decreased with increasing dendritic J_h , indicating its role in the integration of neuronal inputs. It should be noted that individual membrane response properties may not provide enough information on how ionic channel distribution can influence the global behaviour of the RGC model. For example, the sag amplitude (Figure 6.10E) and input resistance (Figure 6.10C) maps cannot indicate the parameter regions which affect RGC spiking behaviours, whilst the ISI (Figure 6.10D) and spike number (Figure 6.10A) maps can suggest how to regulate J_h and J_{CaT} channel densities without largely influencing overall RGC responses. In addition, ISIs were almost absent in the region $\vartheta_T < 10 - 2\vartheta_h$ as indicated by the white region in Figure 6.10D, where the FSL (Figure 6.10B) maps become more useful, since the latter property was present over most of the parameter space investigated.

RGC post-offset activity states (Figure 6.10E) were classified as 1) passive (no rebound spiking after termination of hyperpolarising injection), 2) rebound, 3) spontaneous activity (excited before stimulus onset), and 4) sub-threshold oscillation (refer to a sub-threshold V_m fluctuation during hyperpolarising injection). It should be noticed that the sub-threshold oscillations were always combined with rebound or spontaneous activity.

In another set of simulations, the influence of J_h and J_{CaT} over a large stimulation range (hyperpolarisation stimulus amplitude 50-150 pA, with duration of 0-500 ms) was examined.

Figure 6.11A shows the simulated rebound spiking properties reconstructed for various combinations of J_h and J_{CaT} . The plots of the figure compare the 1) spike number (SN), 2) first spike latency (FSL), 3) rebound average ISI, as well as 4) the ratio of FSL and ISI between models for various hyperpolarising depths and durations. As the hyperpolarisation stimulus amplitude and duration increase, the full model indicated a progressively increasing SN, decreasing FSL and ISI, and greater FSL/ISI ratio. Partially blocking J_{CaT} altered the FSL/ISI ratio without largely affecting FSL, whilst partially blocking J_h substantially altered FSL and FSL/ISI ratio.

However, despite their significant influence on rebound spiking patterns, J_h and J_{CaT} did not have a significant influence on shaping the rebound AP waveforms. As Figure 6.11B indicates, the AP phase plots were nearly identical after the J_h and J_{CaT} conductances were substantially altered.

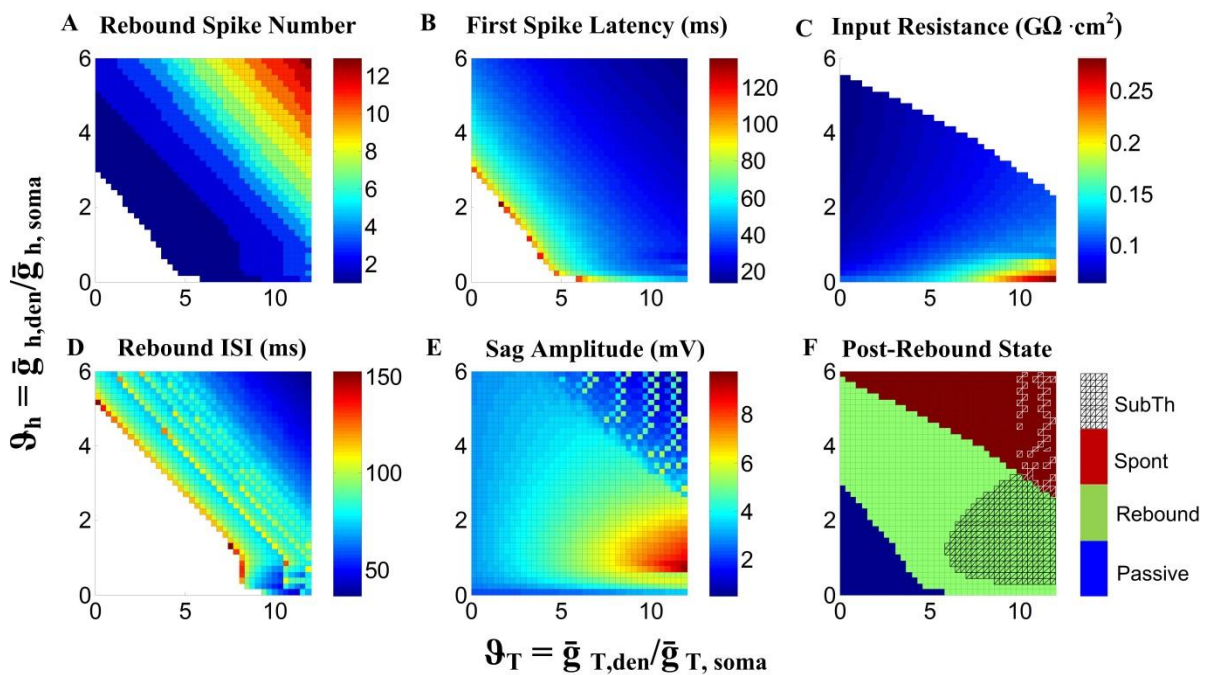


Figure 6.10 Dependency of post-offset activities on somato-dendritic distribution of J_h and J_{CaT} ($\vartheta_h = \bar{g}_{h,den}/\bar{g}_{h,soma}$ and $\vartheta_T = \bar{g}_{T,den}/\bar{g}_{T,soma}$). All simulations were undertaken using a hyperpolarising somatic current injection (500 ms duration, -50 pA amplitude). A. Rebound spike number. B. First spike latency (measured as the time between the stimulus offset and half-maximum amplitude of the first somatic AP). The empty pixels (white) represent regions without a somatic AP. C. Input resistance (measured as the ratio of membrane voltage displacement and injected current to a hyperpolarising somatic current injection of -120 pA). Empty pixels represent regions where strong oscillation occurred during hyperpolarisation and the input resistance could not be determined. D. Averaged ISI. The empty pixels represent regions with less than two spikes. E. Sag amplitude (measured as peak to steady-state potential difference) during hyperpolarising stimulation. The pixels located in the northeast corner represent regions of strong oscillation where the sag amplitude could not be determined. F. Post-offset activity state. Blue: passive response. Green: rebound response. Red: spontaneous response. Hashed-net: sub-threshold oscillations.

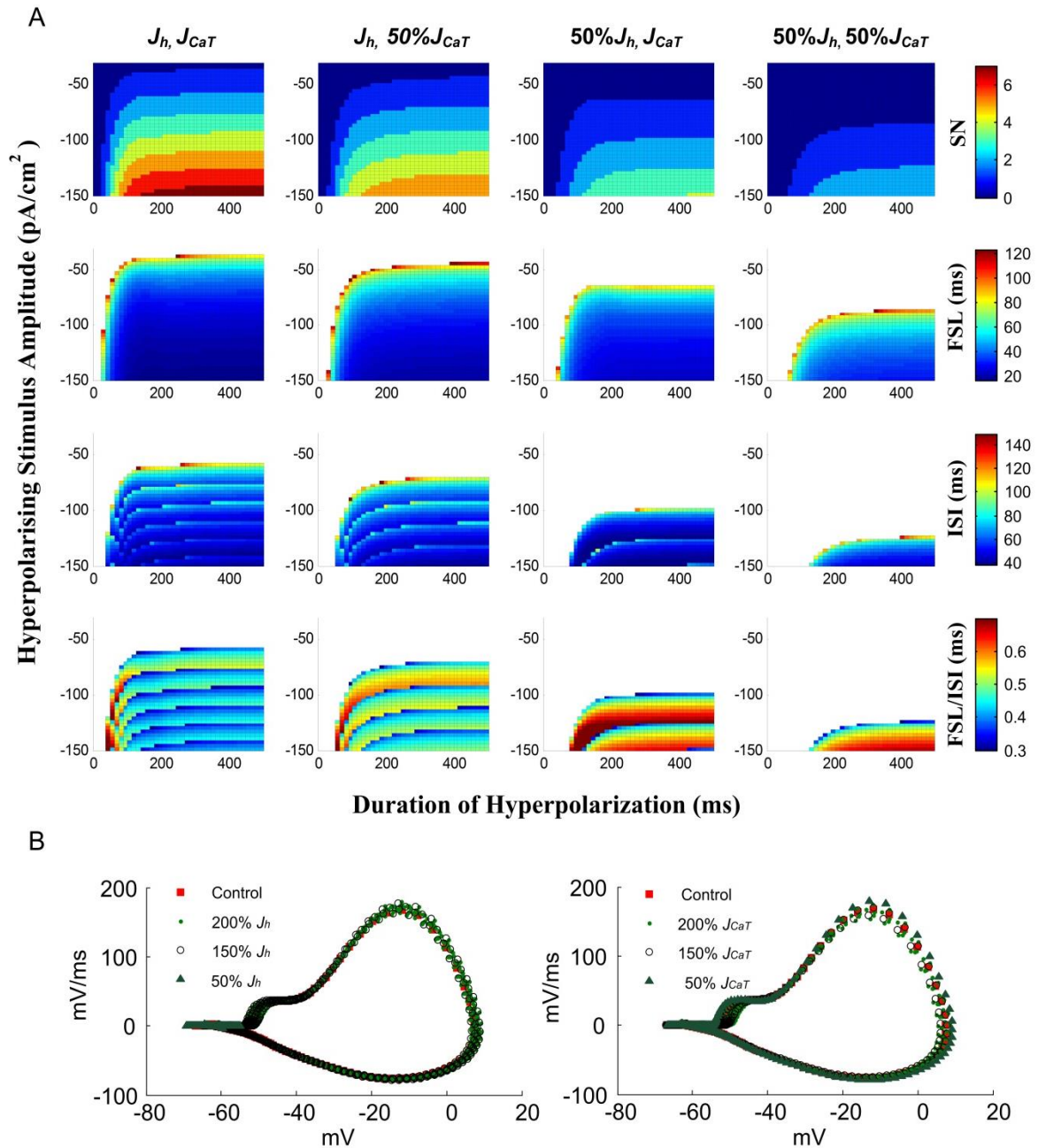


Figure 6.11 The roles of J_h and J_{CaT} on simulated rebound activity over a larger stimulation range. A. Rebound spiking properties reconstructed by different combinations of J_h and J_{CaT} . From left to right, the plots compare the 1) spike number (SN), 2) FSL, 3) averaged ISI, and 4) the ratio of FSL and ISI between models for various hyperpolarising stimulus amplitudes and durations. B. The first AP phase plots during rebound. J_h and J_{CaT} do not appear to have a significant influence on AP waveshapes.

6.4 Influence of Cell Morphology on RGC Firing Patterns

The behaviours of these cells are a result of their biophysical properties, network connectivity, as well as the geometry of their neuronal processes. Since neuronal morphology has been reported to play a vital role in shaping response properties and integration of neuronal inputs in many cell types throughout the central nervous system (CNS) (Vetter et al., 2001a, Spruston, 2008), we hypothesise that cell morphology also plays a role in shaping the response of RGCs. The modelling approach developed in this chapter allowed us to quantitatively control the cellular properties, allowing the effects of morphology on firing properties to be cleanly isolated. In section 6.4.1, the results suggested that in addition to their intrinsic biophysical properties, morphological differences in RGCs classes can also largely differentiate their functional response.

Morphologically-detailed modelling can be also used to study how APs propagate through the complex RGC structure following intracellular stimulation. In section 6.4.2 and 6.4.3, the RGC models reconstructed AP propagation along the dendritic tree, and importantly, how dendritic structure with active ionic channels influences the local signal propagation. Simulation results shown in section 6.4 suggest that the physical properties of the dendritic tree facilitate dendritic signal processing, whilst dendritic active conductances further regulate spiking properties through the interaction between dendrites and the soma-axon compartments.

6.4.1 Morphologically-Specific Responses of ON and OFF RGCs

To understand how morphology shapes the RGC responses, we developed a morphology-specific model using the ON and OFF RGC morphological data shown in Figure 6.3. Model parameters were estimated to ensure reasonable RGC behaviours in response to multiple stimuli. To isolate the contribution of morphology to cellular responses, ON and OFF RGC models shared identical biophysical model parameters and differed only in their physical structure. As shown in Figure 6.12, voltage responses from two mouse RGC models were recorded during multiple depolarising (80, 100 and 120 pA for ON cell; 60, 80 and 100 pA for OFF cell) and hyperpolarising (-120, -140 and -160 pA) somatic current injections.

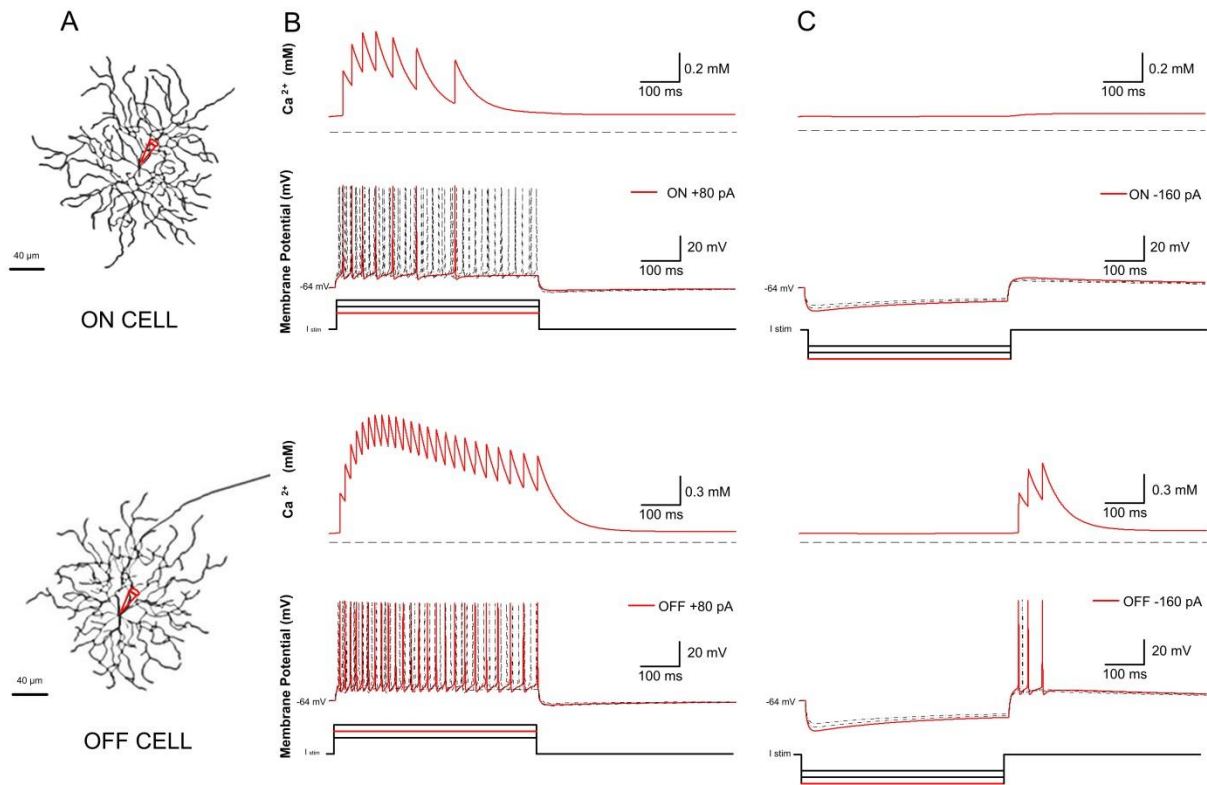


Figure 6.12 A. Computer-reconstructed geometry for ON and OFF RGC types. In this set of simulations, identical ion channel parameters and distributions were implemented in both cells. B and C. Multiple model-generated membrane potentials and somatic intracellular calcium concentration while injecting a family of current pulses at the soma. The model reproduced both normal (B) and rebound (C) RGC spikes. The somatically injected depolarizing currents were of 500 ms duration with amplitudes 80, 100 and 120 pA for the ON cell and 60, 80 and 100 pA for the OFF cell. The hyperpolarizing current steps were -120, -140 and -160 pA. Red traces highlight an individual response with its corresponding stimulus trace denoted by the red step below.

Figure 6.12 illustrates the unique responses in the two RGC types due to their different morphology. The OFF cell demonstrated excitation in response to hyperpolarising stimuli, including a slow depolarising “sag” on hyperpolarisation, as well as a significant rebound burst at termination of the hyperpolarising stimulus. Notably, the ON cell only showed a small passive response under the same condition. In addition, these two cell types exhibited different spiking frequency, response latency and Ca^{2+} dynamics in response to the same levels of stimuli (as highlighted in the red traces). Finally, it should be noted that simulated responses reasonably matched recent experimental observations from ON and OFF RGCs (Margolis et al., 2010).

These simulations suggested that morphological variations between ON and OFF RGCs are able to produce substantial differences in spiking behaviour, indicating that morphology plays an important role in shaping RGC spiking activity. In these models, all biophysical parameters describing voltage-gated channel kinetics and the membrane conductances in each region shared the same values. Hence the individual responses of the ON and OFF cells in

Figure 6.12 were solely dependent on cell morphology. It should be noted however, that in addition to morphology, the intrinsic electrophysiological properties of ON and OFF cells also shape spiking activity. For example, the absence and presence of rebound excitations in ON and OFF RGCs could be a result of their differently distributed ionic channels (Margolis and Detwiler, 2007).

6.4.2 Influence of Dendritic Bifurcations on Action Potential Propagation

In another set of simulations, we examined the influence of the dendritic tree structure on AP propagation along the dendrites. The daughter branches were disconnected from the primary dendrite in the computer-reconstructed RGC geometry (see Figure 6.13A1-A2). Simulated APs were then obtained at each position along the dendrite in response to a somatic depolarization step (100 pA amplitude, 500 ms duration).

Figure 6.13 shows the effects of removing daughter branches from the primary dendrite. In both the control and dendritic pruning cases, AP trains initiate in the soma of the RGC and propagate out into the distal dendrite in response to somatic current injection (Figure 6.13C1-C2, upper panel). However, branch removal resulted in considerable changes in AP characteristics, as follows:

- **AP waveform geometry:** Following previous studies, AP phase plot was used to analyse AP waveshape (Izhikevich, 2007, Fohlmeister and Miller, 1997b). In our simulations, the “full model” and “pruned model” indicated a clear difference in AP waveshape Figure 6.13C1-C2, lower panel). After peripheral branches were removed variations in dendritic AP waveshape (i.e. AP peak value, AP duration, rise and fall time) along the dendrites were largely eliminated (also see middle panel, Figure 6.13D).
- **Spike timing:** First spike latency (FSL), defined as the time difference between the stimulus offset and half-maximum amplitude of the first dendritic AP, was used to calculate AP occurrence time in the dendrites (see left panel, Figure 6.13D). As shown in the FSL curve, the higher propagation speed in the “pruned” dendritic tree ensures nearly simultaneous AP occurrence from soma to distal dendrites, within less than 1 ms (AP duration is 1-2 ms). In contrast, the model with full dendritic tree experienced a ~3 ms latency between somatic and distal dendritic APs.

- AP upstroke: The spike threshold, defined as the membrane potential at which dV/dt of the AP crossed 5-20 mV/ms, is an important parameter for analysing the site of AP initiation (Yu et al., 2008, Naundorf et al., 2006). Figure 6.13D (right panel) revealed that the monotonic decrease of threshold voltage along the dendrite was weakened by removing the surrounding daughter branches.

The dramatic change of AP characteristics along the dendrite could be attributed to current loading with a large number of bifurcation points in RGC dendrites. At a proximal branching point, the orthodromic AP from the soma was distributed among multiple daughter branches, which could weaken the propagating AP by splitting the current from the primary dendrite. As the AP propagated towards the distal branches, there were progressively less branching points, and eventually a sealed end. In this condition, the AP size might increase as a result. Removing dendritic branches in the model resulted in less AP characteristic alterations and promoted a stronger AP propagation. Recent modelling studies of CA1 pyramidal neuron also suggested that removal of dendritic branches could convert a weak propagating neuron to a strong propagating neuron (Golding et al., 2001). Interestingly, the somatic and dendritic AP waveforms simulated in the pruned model closely agree with the published dendritic AP recordings in rabbit RGCs (Velte and Masland, 1999), which only exhibit minimal branching points.

In addition, the slowing and broadening in kinetics of the dendritic AP in our simulation (Figure 6.13D) is consistent with lower densities of sodium and potassium current in dendrites. Strong AP propagation in the dendritic tree was impossible without active dendritic processes in our model. The critical roles of active dendrites and corresponding ionic channel distribution in shaping RGC firing patterns are discussed in the next section.

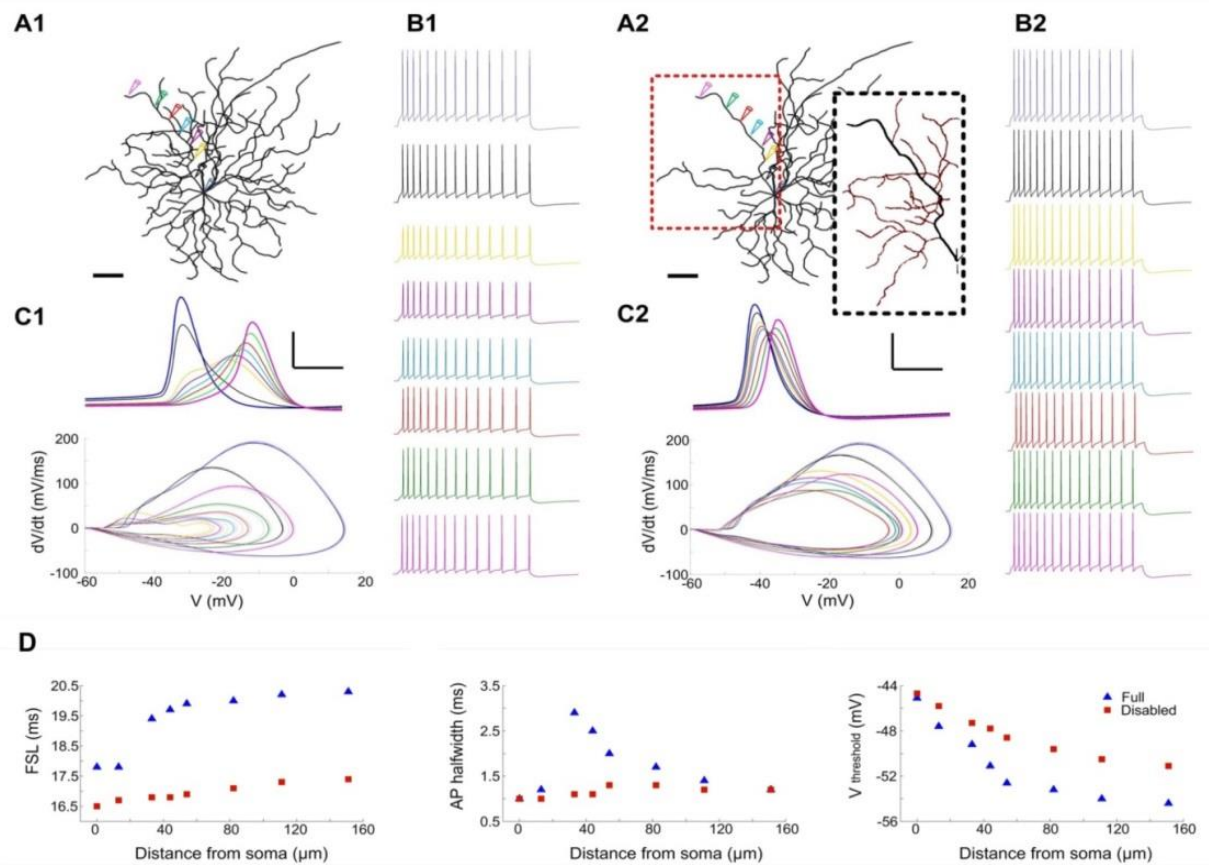


Figure 6.13 Influence of dendritic branches on AP propagation. A1-A2. Reconstructed OFF RGC morphology containing an intact dendritic arbour (A1) or with surrounding daughter branches removed (A2) from the primary dendrite. A2 Inset: pruned branches are labelled in red. Scale bar: 40μm. B1-B2. Simulated APs obtained from the soma and dendrite. Coloured traces correspond to the same-coloured electrode in A1 and A2. C1-C2. Upper. Plot of first AP in each spike train. Scale bar: 20 mV and 2 ms. Lower. Phase plot of dV/dt versus membrane potential (V) for somatic and dendritic spikes. D. Comparison of model behaviours before (▲) and after (■) daughter branches were pruned. Left. First spike latency in the dendrite as a function of distance. Middle. Dendritic AP duration (the width of the AP at half-amplitude) as a function of distance. Right. Dendritic spike threshold (the membrane potential at which dV/dt crossed 5-20 mV/ms) as a function of distance. In both cases, spike thresholds revealed a monotonic decrease with distance from the soma.

6.4.3 Influence of Active Dendritic Density on RGC Firing Patterns

To further examine the influence of active dendritic morphology in shaping RGC spiking responses, active dendritic branches were successively removed from the full computer-reconstructed RGC geometry (Figure 6.14A). Somatic membrane potentials were then obtained in response to both depolarizing and hyperpolarizing somatic current injections. The simulation results indicated increasing spiking frequency and a reduction in FSL with reduced dendritic branching (Figure 6.14B), revealing the temporal low-pass filtering properties of the dendritic structure (Rose and Fortune, 1999, Rose and Call, 1993). Considering that dendrites have larger overall membrane surface area (i.e. large capacitance) and lower active membrane conductances compared with the soma, a neuron can be approximated using a first order low-pass RC filter in which the fast ionic currents (e.g. Na^+) are filtered. In our simulations, the reduced capacitance obtained by removing dendritic branches likely accounts for their weakened low-pass filtering characteristic.

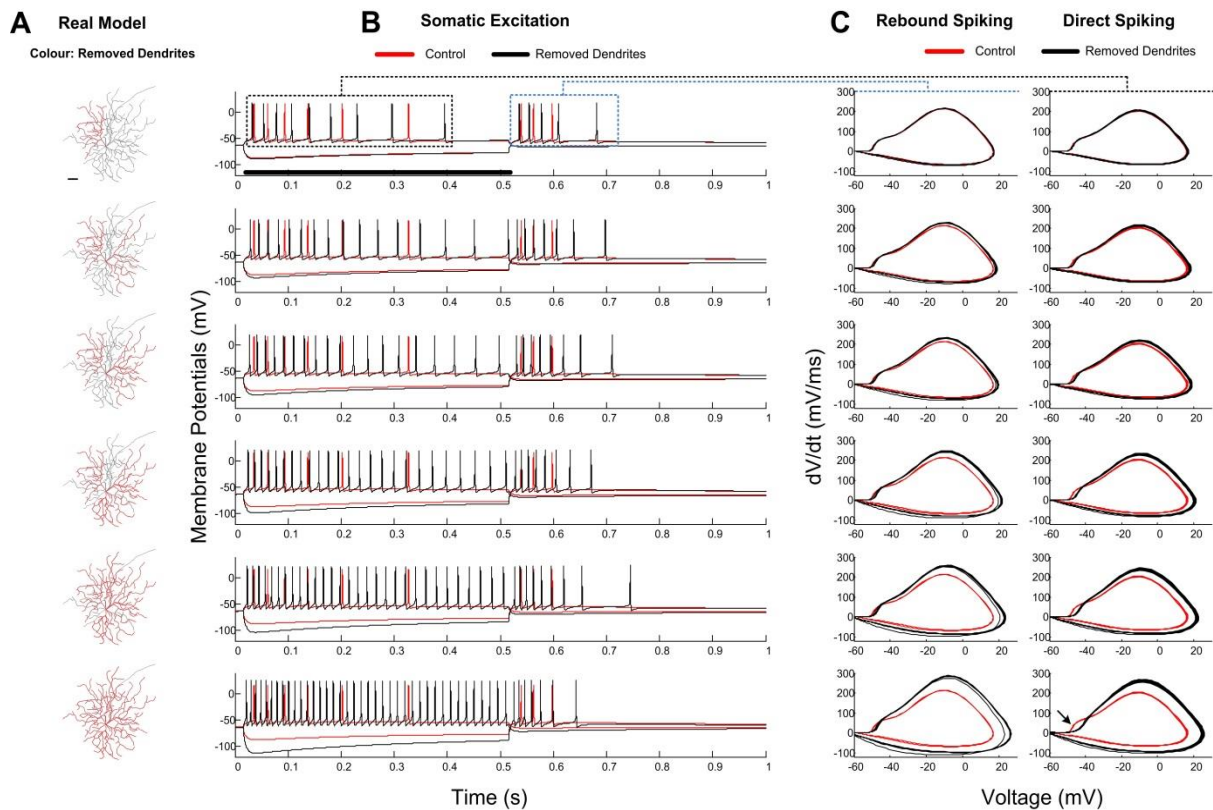


Figure 6.14 Distinct firing patterns in the RGC model with identical biophysics but different active dendritic densities. A. RGC morphologies. Removed dendritic branches were labelled by corresponding colours. B. Membrane potentials in response to various somatic current injections before (red) and after (black) the removal of dendrites. Note the presence of both normal and rebound RGC spikes. External somatic current injection: 500 ms duration (horizontal bar) with amplitudes of 60 pA for depolarising and -160 pA for hyperpolarising injections. C. Phase plot (dV/dt versus V) of the somatic direct (right) and rebound (left) action potential triggered by depolarising and hyperpolarising simulation respectively. The elimination of initial segment soma dendritic break is indicated by the arrow.

In addition, both direct and rebound AP waveshapes (Figure 6.14C), as shown by the rate of voltage change (phase plot), were affected. These included increasing rates of rising/falling phases, and increases in AP overshoot. In particular, the IS-SD break in the phase plot (labelled by the arrow in Figure 6.14C) was progressively eliminated as more active dendritic branches were removed. Marked increase in the rising and falling phase of the phase plot can be explained by the presence of higher somatic Na^+ and K^+ currents with less active dendrites. The existence of IS-SD break, explained by the presence of high Na^+ channel density in the AIS, corresponds to spike initiation. The reduction of IS-SD break with less active dendrites revealed the moving location of AP initiation.

6.5 Discussion

This chapter presented a significant improvement over existing modelling approaches (Tsai et al., 2012, Fohlmeister et al., 2010, Kameneva et al., 2011) in that multiple RGC spiking responses were accurately reconstructed in different functionally-identified RGCs using cell-specific ion channel distributions and morphologies. These models were able to predict experimental information not used in model optimisation, including dendritic AP waveform (Figure 6.8), as well as the influence of the dendritic tree on AP wavelshape and spiking behaviour (Figures 6.13-6.14). The multi-objective optimisation approach presented provides a promising platform for realistic modelling of cellular electrical activity in the entire RGC population.

6.5.1 Accurate RGC Electrical Activity Reconstruction

The optimisations of this chapter were performed on a large range of model parameters, rather than only maximum membrane conductances. Estimating only membrane conductances while fixing ion channel kinetic parameters will excessively limit the parameter search space, reducing the accuracy of model fits, particularly when optimising against multiple datasets. In this chapter, all models were optimised to closely reproduce action potential waveforms recorded under multiple current injections, which would not be possible if only a few membrane conductance parameters were available to be optimised.

We found that introducing additional datasets with extra information (e.g. AP phase plot and spiking patterns) will bring more fitting challenges, prolonging the optimising time, particularly with stringent constraints on parameters. However, the credibility of a model is enhanced by its ability to simultaneously reconstruct experimental data which includes more information on system behaviours. The inherent advantage of optimisation against multiple datasets was discussed in (Guo et al., 2013). Other than the time-series AP datasets and AP phase plots, the RGC models were able to accurately reconstruct multiple spiking features including spike number, latency and interval. Accurate spiking pattern reconstruction is necessary for RGC modelling, since spiking patterns carry information in terms of the neural code, transferring key information to downstream neurons.

Compared to previous multi-compartment RGC models, morphologies reconstructed in this study were from the same cells used for data recording. Since their physical properties also

influence their neuronal behaviours, these models, incorporating both accurate physical and ionic mechanisms, represent an important advance over previous modelling studies. The predictive ability of these models in reconstructing RGC responses to extracellular stimulation, will be investigated in the Chapter 7.

6.5.2 Cell-Specific Ionic Channel Expression

Limited experimental information on ionic channel kinetics and distribution in functionally-identified RGCs makes assigning model parameters a difficult task. Ionic channel distribution and kinetic parameters in our models were fully dependent on the multiple data obtained. Importantly, the resulting model parameters obtained are all supported by relevant experimental evidence:

1. The presence of rebound activities is related to higher J_h and J_{CaT} somato-dendritic ratios in the OFF cell compared to the ON cell model. Recent experimental evidence in RGCs also suggest the presence of higher J_{CaT} density in dendrites (Miller et al., 2002). Despite the limited experimental information on J_h distribution in RGCs, it was also reported to have higher density in CA1 pyramidal neuron dendrites (Magee, 1998).
2. The large range of threshold variations as well as the different IS-SD break in the AP phase plots between ON and OFF cells can be explained by their J_{Na} kinetics and regional distributions. Experimentally, J_{Na} has been reported to demonstrate appreciably different kinetics among different RGC types (Kaneda and Kaneko, 1991, Lipton and Tauck, 1987). Although AP phase plots are not typically used for neuron identification, the simulations of this chapter suggest that differences in AP waveforms among RGC types can be an effective indicator of cell-specific ionic channel distributions.
3. The ON and OFF RGC model behaviours also demonstrated significant differences in J_h kinetics, as suggested by their unique depolarizing sag amplitude and time constant in the data. Experimentally, it has been reported that different neuron types (Pape, 1996, Magee, 1998) including RGCs (Lee and Ishida, 2007) demonstrate variable kinetics of J_h activation and inactivation.

6.5.3 Contribution of J_h and J_{CaT} to RGC Function

Rather than analysing absolute channel distributions in a given functional region, we considered that the distribution ratios provide more information on the interaction between soma and active dendrites. The firing pattern sensitivity to dendritic J_h and J_{CaT} (Figure 6.10) provided a continuous spectrum of RGC firing properties in response to hyperpolarising inputs. RGC activities are a result of the interaction between all membrane current present, and not only a result of J_h and J_{CaT} . However, these two currents were both absent from the original FM model, and both channels are responsible for neuron activities in response to hyperpolarising stimuli. Thus, at the very least, our sensitivity analysis provides information on how the presence of these new membrane currents contributes to RGC behaviours. In future studies, we intend to extend our method to include more membrane conductances to explore the even higher dimensional RGC parameter space.

Three dimensional plots of model behaviours in response to various channel distributions can also provide a clear global map of activity states of the RGC. Similar activities can be reproduced by different combinations of dendritic J_h and J_{CaT} conductances. On the other hand, it was found that model behaviours can be highly sensitive to parameter tweaking, especially in the region near the boundary between different activity states. Interestingly, some experimental evidence has suggested the presence of large channel density variations in the same functionally-identified neuron types (Golowasch et al., 1999), while other studies have found that neuron activities are very sensitive to small variations in channel expression (Goldman et al., 2001).

The contribution of J_h and J_{CaT} to neuronal excitability has been reported in many experimental studies (see introduction section of this chapter). These experimental findings are consistent with the simulations of this chapter. For example, it was found that multiple response properties can be eliminated by tweaking the regional density of J_h and J_{CaT} , revealing their contribution to rebound excitation in RGCs. Interestingly, although the OFF RGC data and model did not reveal any spontaneous or sub-threshold oscillations, as suggested by previous studies, the post-rebound activity state map (Figure 6.10F) revealed that these often-observed behaviours can be explained by higher dendritic J_h and J_{CaT} densities.

In summary, differences in ionic channel properties between RGC types raise the possibility that each type may exhibit markedly preferential firing patterns in response to identical inputs. On the other hand, neuronal morphologies also influence the flow of intracellular currents between neighbouring compartments through their specific membrane area and intracellular resistivity. These two important factors contribute to the unique electrical activities of ON and OFF RGCs. Realistic modelling approaches, which aim to accurately reproduce membrane ionic mechanisms and morphology, can offer important information on the mechanisms underlying neural coding, improving our understanding of the differential activation of ON and OFF RGCs to various stimuli.

Chapter 7 Differential RGC Responses to High-Frequency Extracellular Stimulation

Existing retinal visual prosthetic devices are limited in their ability to selectively or differentially stimulate retinal neurons, as reported in multiple experimental studies using artificial electric stimulation (Sekirnjak et al., 2008, Margalit and Thoreson, 2006, Tsai et al., 2009, Freeman et al., 2011). Other studies have suggested the possibility of preferentially activating individual RGC types using particular stimulus profiles (Jensen and Rizzo, 2005, Jensen and Rizzo, 2006).

Recent studies have given more attention to high-frequency electrical stimulation (HFS), suggesting the possibility of targeting functionally-distinct RGC types by optimising the stimulation frequency. HFS has been explored in cochlear prosthetics (Litvak et al., 2001, Litvak et al., 2003). It has also been used to induce selective conduction block in peripheral axon fibres (Joseph and Butera, 2011), underlying the possibility of selectively activating different retinal neuron types with HFS. The *in vitro* study of Cai et al. (2011) suggested that not all stimulus pulses were able to trigger full somatic APs when RGCs were stimulated with a wide range of stimulation frequencies (from 100 to 700 Hz). They also found that the percentage of pulses eliciting full somatic APs was further reduced with increasing stimulation frequency. A more recent *in vitro* study of Twyford et al. (2014) suggested the possibility of employing 2 kHz HFS to maximise the difference in responses between ON and OFF RGC types. These studies indicate that stimulation frequency could be the key stimulus parameter to modulate the differential activation of RGCs. The findings of these studies formed the basis of the modelling work in this chapter.

In a new set of simulations, the optimised ON and OFF RGC models of the previous chapter were used to gain insights into the mechanisms underlying selective responses to 2 kHz extracellular electrical stimulation. With optimised model parameters and detailed cell morphologies, these RGC models were able to closely replicate published experimental ON and OFF RGC responses to epiretinal electrical stimulation.

More importantly, a novel modelling approach was also developed to find the correlation between RGC response patterns and dendritic structure/ionic channel distributions, in order to shed light on the likely mechanisms underlying the non-monotonic response profile to high-frequency extracellular electrical stimulation.

7.1 Response to Constant Amplitude Stimulation

The cable formulation of neural activation (see eq. (6.1)) was extended to simulate cell responses to extracellular electrical stimulation. Membrane potential was calculated from the difference between intracellular potential V_i and extracellular potential V_e :

$$V_m = V_i - V_e \quad (7.1)$$

where V_i is derived from,

$$\frac{\partial}{\partial s} \left(\sigma_i \frac{\partial V_i}{\partial s} \right) = \beta \left(C_m \frac{\partial V_m}{\partial t} + J_{ion} \right) \quad (7.2)$$

The extracellular voltage distribution was simulated using a disk electrode source (Greenberg et al., 1999, Tsai et al., 2012, Jeng et al., 2011),

$$V_e = \frac{2I_s R_s}{\pi} \sin^{-1} \left(\frac{2R}{\sqrt{(a-R)^2 + z^2} + \sqrt{(a+R)^2 + z^2}} \right) \quad (7.3)$$

where I_s is the stimulation current, a and z are the radial and axial distance respectively from the center of the disk for $z \neq 0$, R is the radius of the disk ($R=15 \mu\text{m}$), and R_s is the electrode transfer resistance. The epiretinal stimulation electrode fixed at a $5\text{-}\mu\text{m}$ distance from the centre of AIS. All ionic model parameter values were listed in Tables 6.3-6.5 in Chapter 6.

We simulated the response with extracellular high-frequency stimulation (HFS) using 2 kHz Lilly-type (Lilly et al., 1955) biphasic current pulses (shown in Figure 7.1) in ON and OFF cells. The amplitude of the stimulus train remained constant within a given trial, but varied across trials ranging from 0 to $90 \mu\text{A}$. Figure 7.2B shows distinct non-monotonic spike-stimulus profiles for the ON and OFF RGC models. Reconstructed RGC responses were measured at axon. At low stimulus magnitudes, the axonal spiking number typically increased with stimulus amplitude. However, as the amplitude increased further, the number of elicited spikes decreased substantially, creating a non-monotonic response profile. This observation is consistent with the recent *in vitro* studies (Twyford et al., 2014). The total number of axonal spikes elicited over the 250 ms pulse train was plotted as a function of stimulus amplitude for both ON and OFF cells. Total Spike number were determined from both the full AP (Figure 7.2E) and current (Figure 7.2F) spikes. Direct visualisation of the elicited APs was possible with no confusion from the high-frequency artefact (Figure 7.2E). The stimulus-response profiles demonstrated a distinct onset, width and amplitude, which indicated the differential response of the ON and OFF cells to electrical stimulation. It was

also observed that the RGC model reproduced similar somatic and axonal response patterns (see Figure 7.2D), and this similarity was also found in the other simulations in this chapter (results not shown). The difference in excitability between model ON and OFF RGCs was also indicated by their response to intracellular current injection (Figure 7.2C)

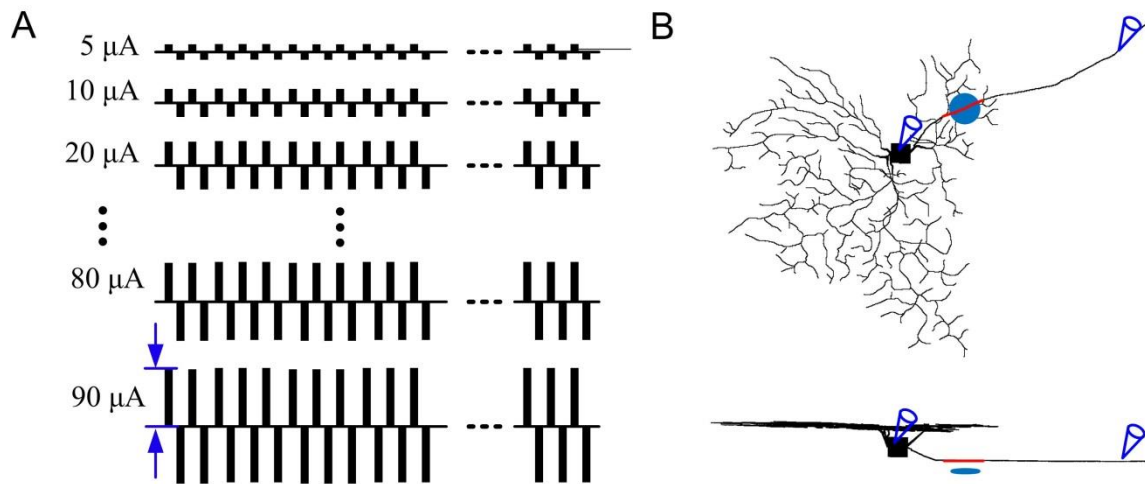


Figure 7.1 The applied 2-kHz extracellular stimulus waveforms consisted of biphasic constant-current pulses with a pulse width of 100 μs per phase, a cathodal-anodal inter-phase interval of 160 μs and an anodal-cathodal inter-phase interval of 140 μs. A. Constant-amplitude stimulation. B. Stimulating and “measuring” locations in the model OFF RGC. The epiretinal stimulation electrode (shown as a flat disk) was applied at a 5-μm distance from the centre of AIS (red compartment), and spiking responses were obtained in the soma and axon, shown by the cone-shaped electrodes.

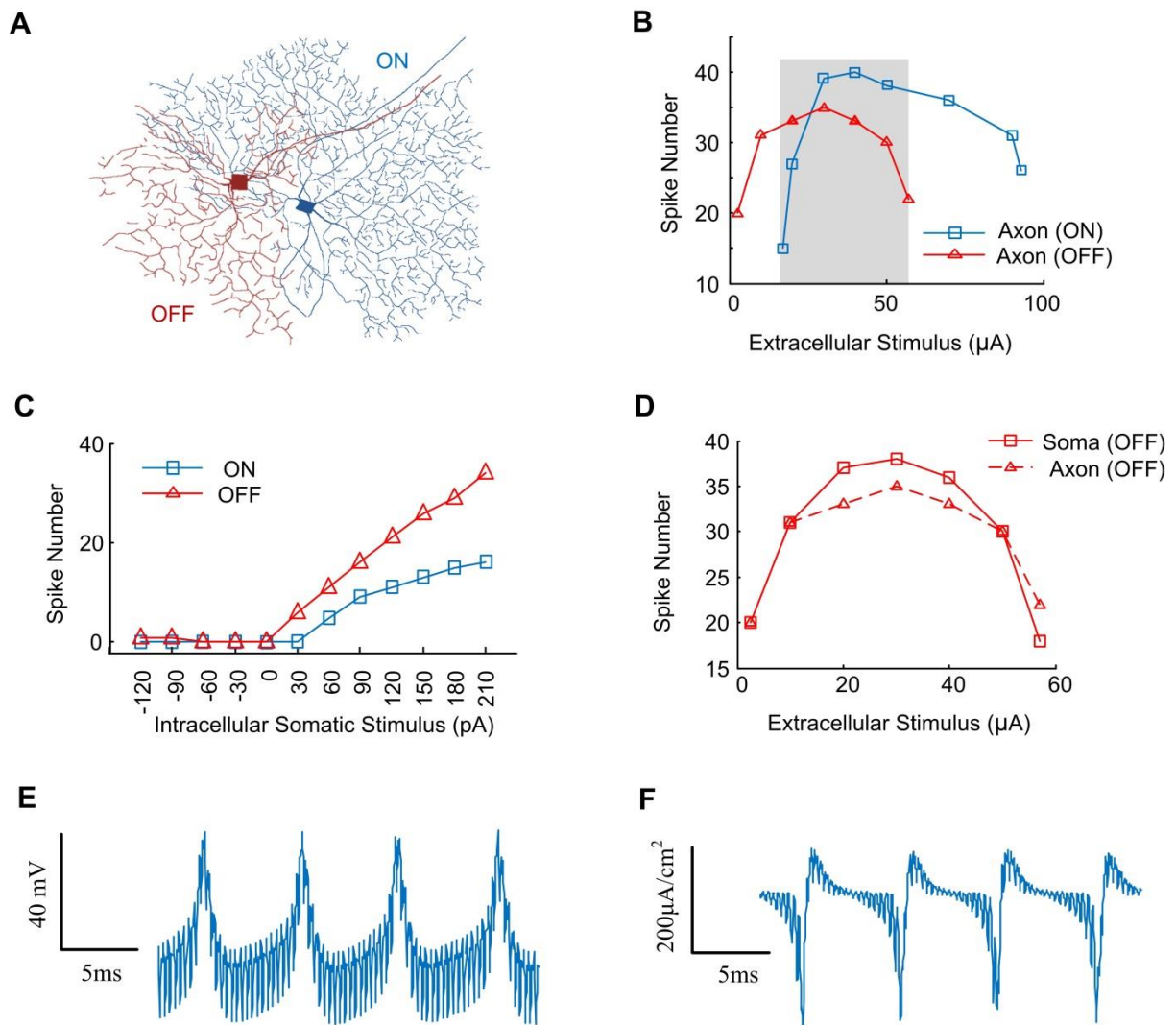


Figure 7.2 Simulated selective activation of ON and OFF RGCs to 2 kHz HFS. **A.** ON and OFF RGC model morphologies. **B.** Evoked axonal spiking numbers in ON and OFF RGC models with constant-amplitude 2 kHz HFS (250 ms duration, 0–90 μA). In the shadow region, the ON cell (blue) became progressively more excitable with stronger stimulation while the OFF cell excitation was progressively inhibited (red). It should be noticed that the shadow region can be used to adjust the extracellular stimulus range to selectively activate ON and OFF RGCs. **C.** Difference in excitability between ON and OFF RGC models in response to intracellular somatic current injection. **D.** Somatic and axonal response simulated in OFF RGC. **E** and **F.** Somatic membrane potential and total membrane ionic current trains. The 2 kHz stimulus artefact can be seen embedded within the membrane potential and current traces.

7.1.1 Possible Mechanisms Underlying the Non-Monotonic Extracellular Response

To investigate possible mechanisms underlying the non-monotonic extracellular response properties, three sets of simulations were undertaken to investigate the influence of RGC morphology and ionic channel expressions. The stimulation setting in this section were as same as those in section 7.1

1. We simulated the spiking response using OFF cell model parameters (ionic channel expressions and distributions) with the ON cell morphology, as well as using ON cell parameters with OFF cell morphology. Using this approach, we could relatively isolate the contribution of morphology and ionic channel expression in shaping the cell response patterns. Figure 7.3 shows that the non-monotonic stimulus response profile can be altered in terms of onset, height and width, when employing model parameters with the different cell morphology – revealing the potential contribution of both ionic and physical properties in the spiking pattern response to HFS.

2. In another set of simulations, we progressively removed the dendritic tree by disconnecting dendritic branches from the full reconstructed RGC geometry (see Figure 7.4), examining the somatic spiking in response to a range of HFS stimulation amplitudes. The simulation results indicated that the soma became more excitable with fewer dendrites. As a result, the non-monotonic response profile changed into monotonic with largely reduced dendritic branching. This suggested that the physical structure of the dendritic tree is a significant contributor to the non-monotonic nature of HFS-based RGC responses.

3. In a final set of simulations, the dendritic active properties were adjusted by progressively changing the J_{Na} distribution within the dendritic tree (see Figure 7.5). The default dendritic maximal sodium conductance value (i.e. 21.68 mS/cm²) was represented by δ . The simulation results indicated that the non-monotonic response was progressively eliminated when dendritic maximal sodium conductance value was increased to around $2\delta\sim 4\delta$. The simulation results indicated that the non-monotonic response was progressively eliminated with increased dendritic sodium channel density. Furthermore, the width of the non-monotonic response curve decreased with reduced dendritic sodium channel density, whereas the height of the curve was relatively unaltered. We also found that changing other ionic channel densities (e.g. J_{Ca} , J_K , J_h , or J_{CaT}) in the dendrites did not significantly alter the non-monotonic response profile, indicating the importance of dendritic sodium channels in shaping the non-monotonic RGC extracellular stimulus-response curve.

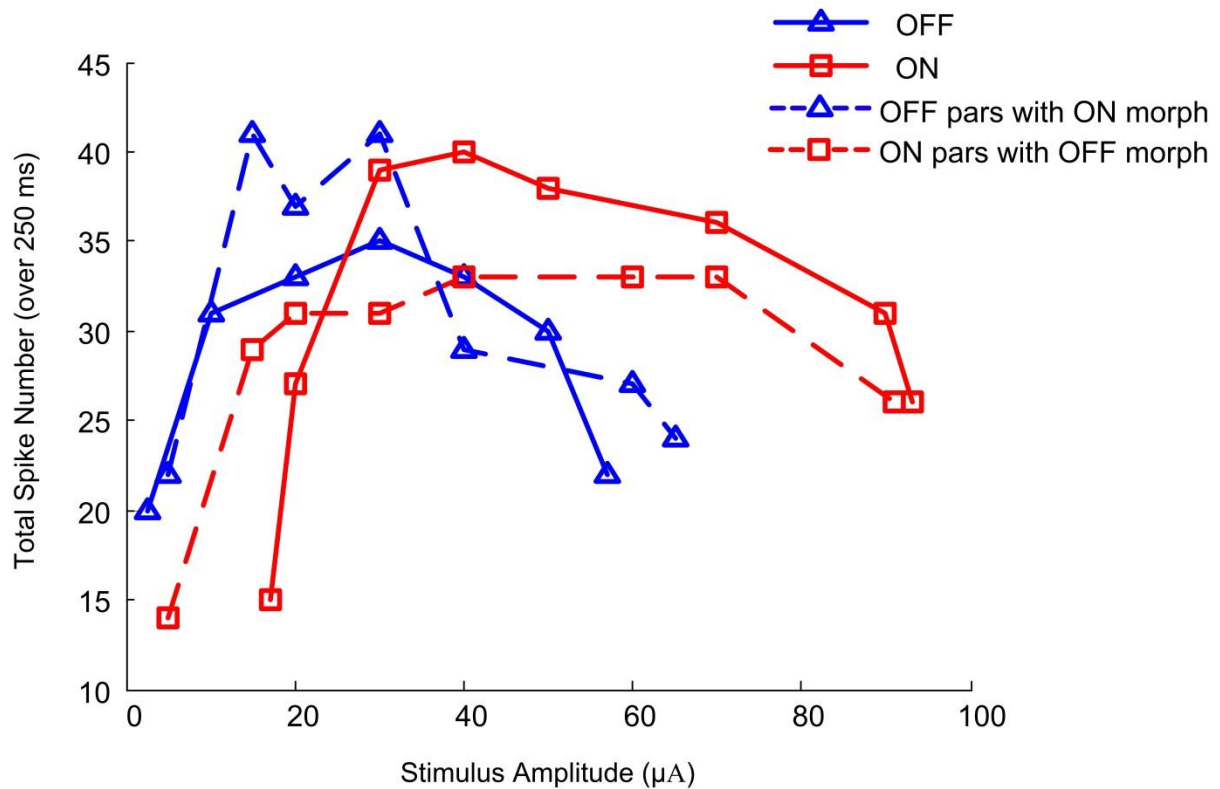


Figure 7.3 Stimulus-response profiles on interchanging ionic parameters and cell morphology in ON and OFF RGCs. Blue and red solid lines indicate ON and OFF RGC response patterns to 2 kHz HFS using default parameters and morphology. Blue and red dashed lines indicate the spiking patterns on interchanging the intrinsic and physical properties of the two cell types.

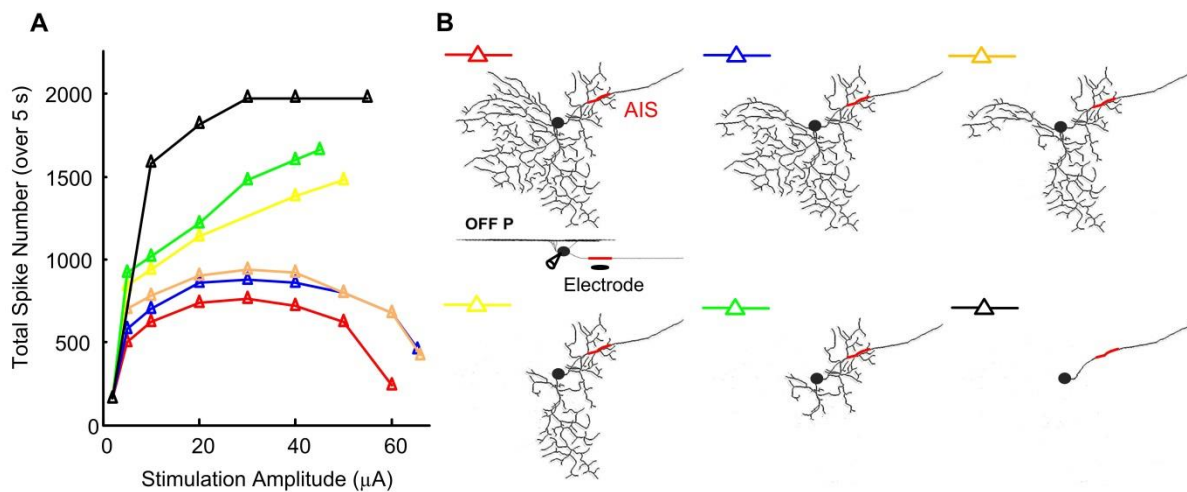


Figure 7.4 Non-monotonic RGC spiking response profile was altered by progressively removing active dendrites. A. Simulated total spike numbers over a 5-second train of 2 kHz stimulation as a function of stimulus amplitude before (red) and after the removal of corresponding dendrites. B. Cellular morphologies. Colours correspond to the spiking profiles in (A).

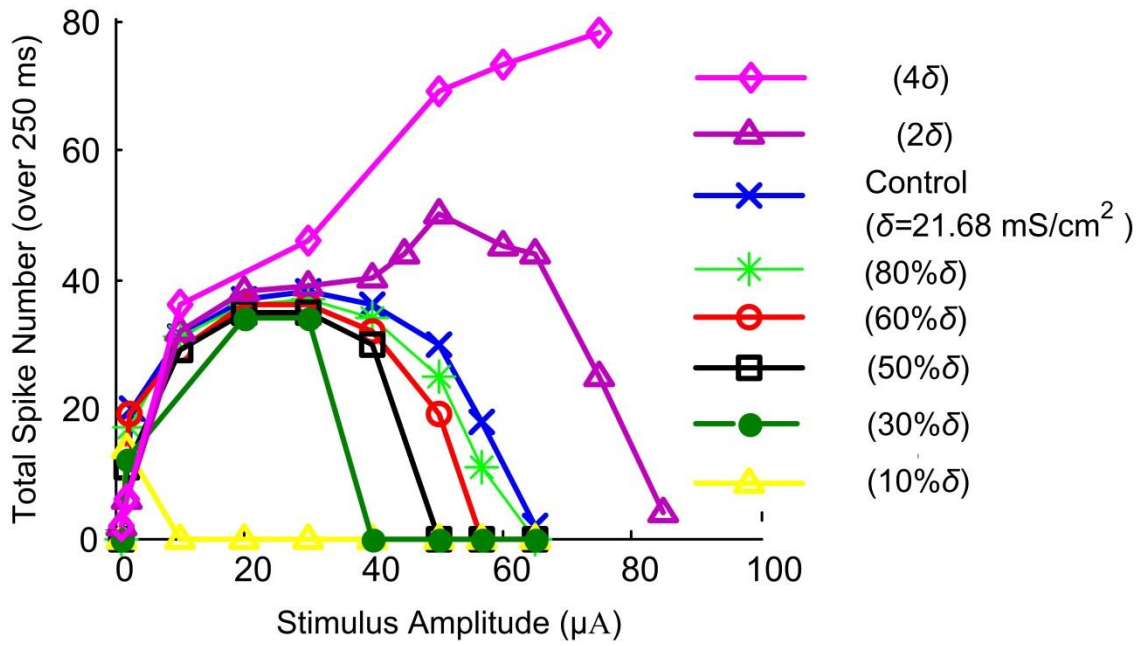


Figure 7.5 Non-monotonic RGC spiking response pattern was altered by progressively changing the dendritic sodium channel density (i.e. maximal sodium conductance, δ) in the dendrites. Note that the spiking profile became monotonic with higher dendritic sodium channel density (4δ).

7.1.2 Effect of Electrode Location and Stimulus Frequency on Extracellular Stimulus-Response Profile

In order to investigate the effect of electrode position on the non-monotonic response properties, we placed the stimulus electrode at different dendritic locations (electrode locations were shown in Figure 7.6B) at a fixed vertical distance of 5 μm from the ganglion cell. The stimulus duration was 250 ms. Figure 7.6A illustrates the non-monotonic response profiles observed at the soma in OFF P model. Changing the electrode position also altered other spiking response properties such as onset, offset and peak spike number.

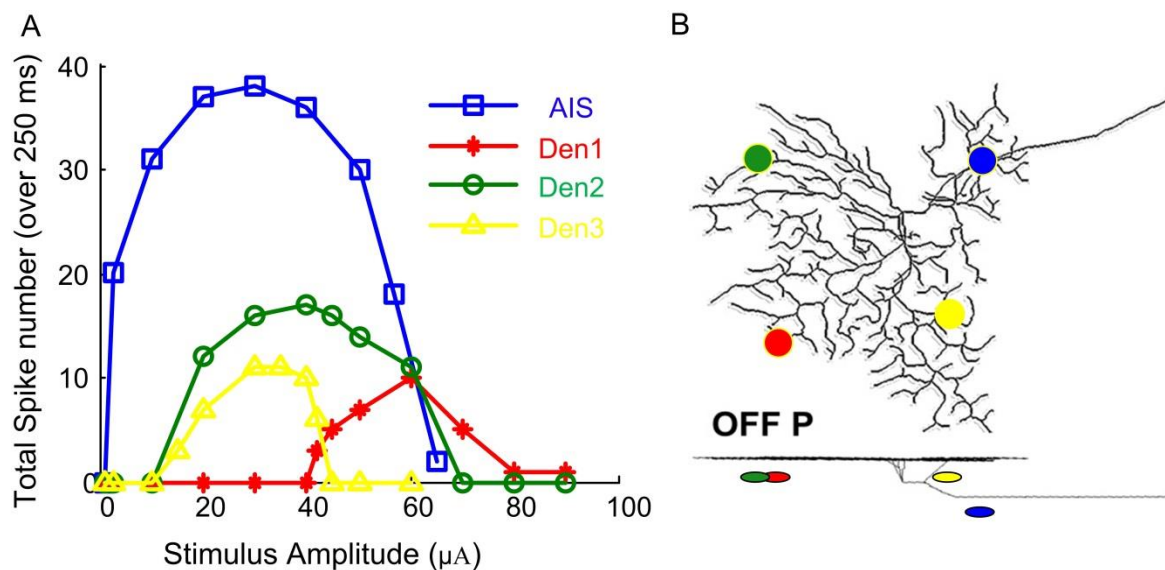


Figure 7.6 Non-monotonic spiking response with respect to different stimulus locations. Different colours correspond to the various spiking pattern curves (A) corresponding to locations of electrodes (B). In each case the electrodes were 5 μm from the RGC.

We also investigated the response of the RGC model to a wide range of stimulation frequencies spanning 50-1500 pulses per second (PPS). Stimulus waveforms were set to biphasic with a pulse width of 100 μs per phase, a cathodal-anodal inter-phase interval of 160 μs , and a rate-specific anodal-cathodal inter-phase interval. The stimulation duration was fixed at 250 ms, and RGC response was observed at soma.

Figure 7.7A illustrates that the response profiles became monotonic at lower stimulus rates. The relationship between pulse amplitude and the percentage of pulses eliciting somatic varied considerably with stimulus frequency. The RGC model was able to reliably follow all pulse trains (one to one response) at rates up to 100PPS, whereas it failed to follow trains at rates higher than 300PPS. Increasing the rate further had little effect on the total number of spikes elicited. Figure 7.7B shows somatic APs in response to 200PPS stimulation. The results indicated that AIS-elicited APs propagated to the soma, but not all were able to trigger

somatic APs (see the sub-threshold pulses indicated by the red arrows). This “many-to-one” response between low-frequency stimuli and cell responses have been observed experimentally in many RGC types (Cai et al., 2011).

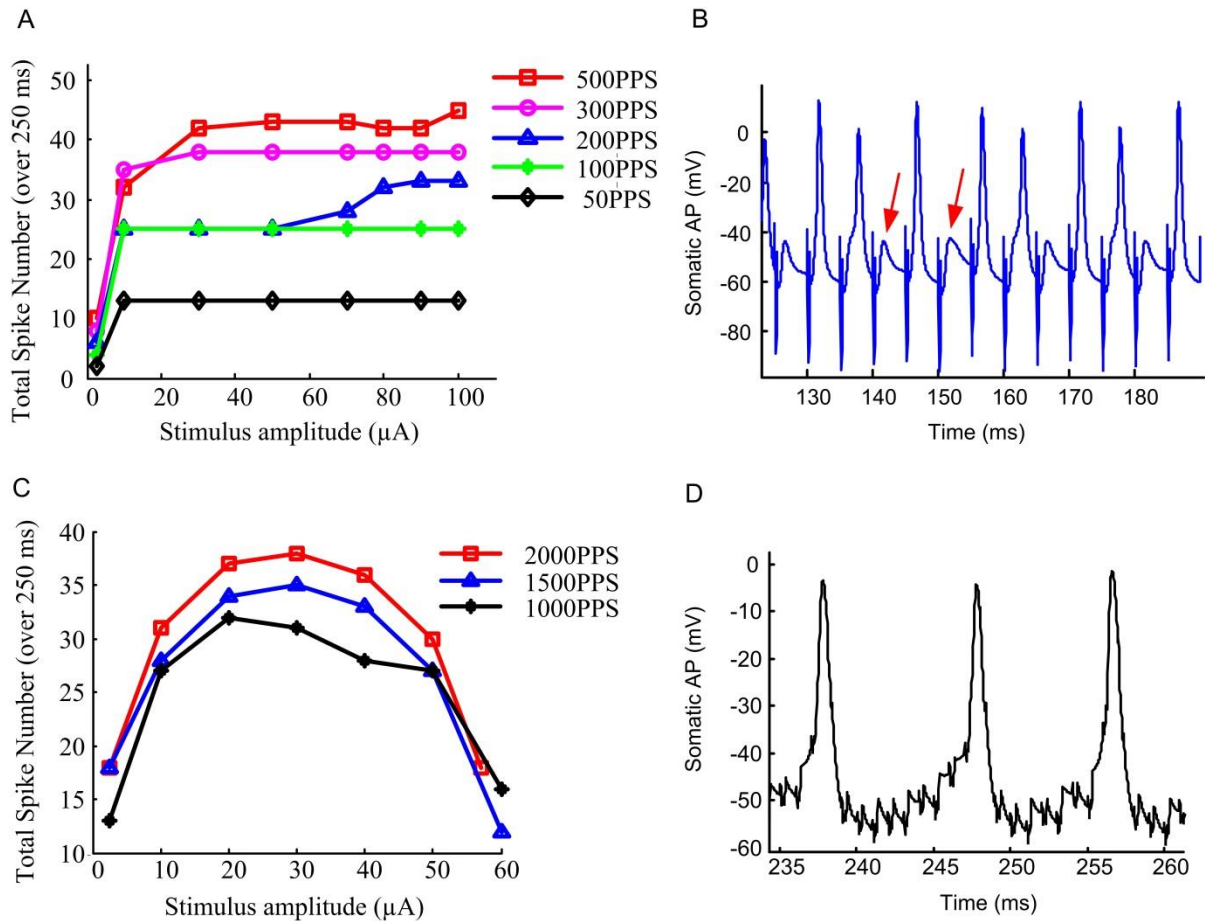


Figure 7.7 RGC response to extracellular stimulation at various frequencies. A. Total number of spikes elicited by trains of 50, 100, 200, 300 and 500 PPS plotted as a function of pulse amplitude. For pulse rates higher than 100 PPS, the model RGC could not generate a “one to one” somatic spike in response to each pulse. B. Somatic APs in response to 200 PPS stimulation. The AIS-elicited APs propagated to the soma, but not all were able to trigger somatic APs (sub-threshold pulses are indicated by red arrows). C. Total number of spikes elicited by trains of 1000, 1500 and 2000PPS. The model RGC was still able to generate non-monotonic spiking response profiles at rates higher than 1000PPS. D. Somatic APs in response to 1000PPS stimulation.

7.2 Response to Amplitude-Modulated Stimulation

Changes to instantaneous stimulus amplitude (as was the case for the 250 ms duration biphasic stimulus described earlier) may not accurately simulate natural visual input to the retina, since natural luminance changes generally occur more gradually and smoothly over time rather than sudden step changes (Twyford et al., 2014, Puchalla et al., 2005, Felsen and Dan, 2005). Therefore, we were also interested in how our RGC models respond to gradual or transient changes in stimulus amplitude rather than large instantaneous changes. We simulated the ON and OFF model axonal responses to two types of non-zero baseline amplitude modulation, as shown in Figure 7.8A. Stimulation waveforms were reconstructed using constant-amplitude stimulation and a 300-millisecond-wide amplitude modulation “diamond” with symmetric rise and fall phases.

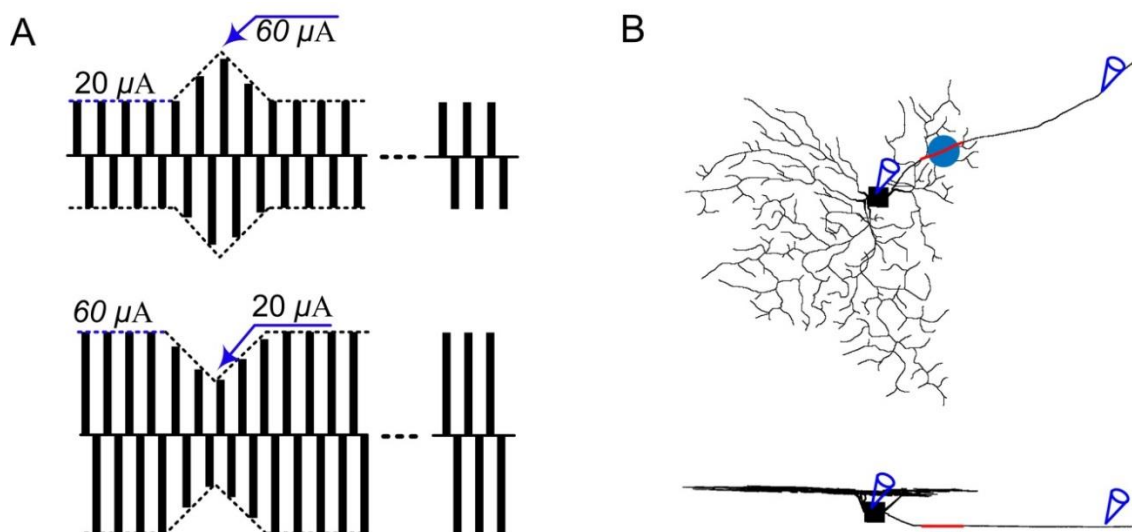


Figure 7.8 Applied 2 kHz amplitude-modulated stimulation. A. Upper: Positive baseline amplitude modulation. Stimulation waveforms were reconstructed from a constant-amplitude stimulation in (A) with a 300-millisecond-wide amplitude modulation “diamond” with symmetric rise and fall phases. The baseline amplitude was 20 μA and the peak amplitude of the “diamond” was 60 μA . Lower: Negative baseline amplitude modulation, with the baseline at 60 μA and the minimum amplitude at the diamond “notch” at 20 μA . B. Simulated stimulus and “measuring” locations in the model OFF RGC. The epiretinal stimulation electrode (shown as a flat disk) was applied at a 5- μm distance from the centre of AIS (red compartment), and spiking responses were obtained in the soma and axon, shown by the cone-shaped electrodes.

Figure 7.9B illustrates the simulated distinct ON and OFF cell responses. The stimulus baseline was fixed at 20 μA and the peak level was 60 μA (Figure 7.8A upper panel). The ON cell response demonstrated an increased spiking rate during the diamond-shaped modulation, returning to resting level as soon as the modulation was complete. The OFF cell showed an opposite response profile to that of the ON cell.

In another set of simulations, we reversed the amplitude levels of the baseline and the modulation peak. The baseline was fixed at 60 μA and the minimum “notch” level was 20 μA (Figure 7.8A lower panel). The inverted stimulus elicited the opposite response: there was a decrease in ON cell activity and an increase in OFF cell spikes during the diamond-shaped modulation (see Figure 7.9B, lower panel). All of these simulation results closely matched experimentally-observed RGC responses (Figure 7.9A) recorded under similar stimulation conditions in Twyford et al. (2014), in which the investigators utilised a 40- μA baseline with a 60- μA peak and a 60- μA baseline with a 40- μA minimum “notch”.

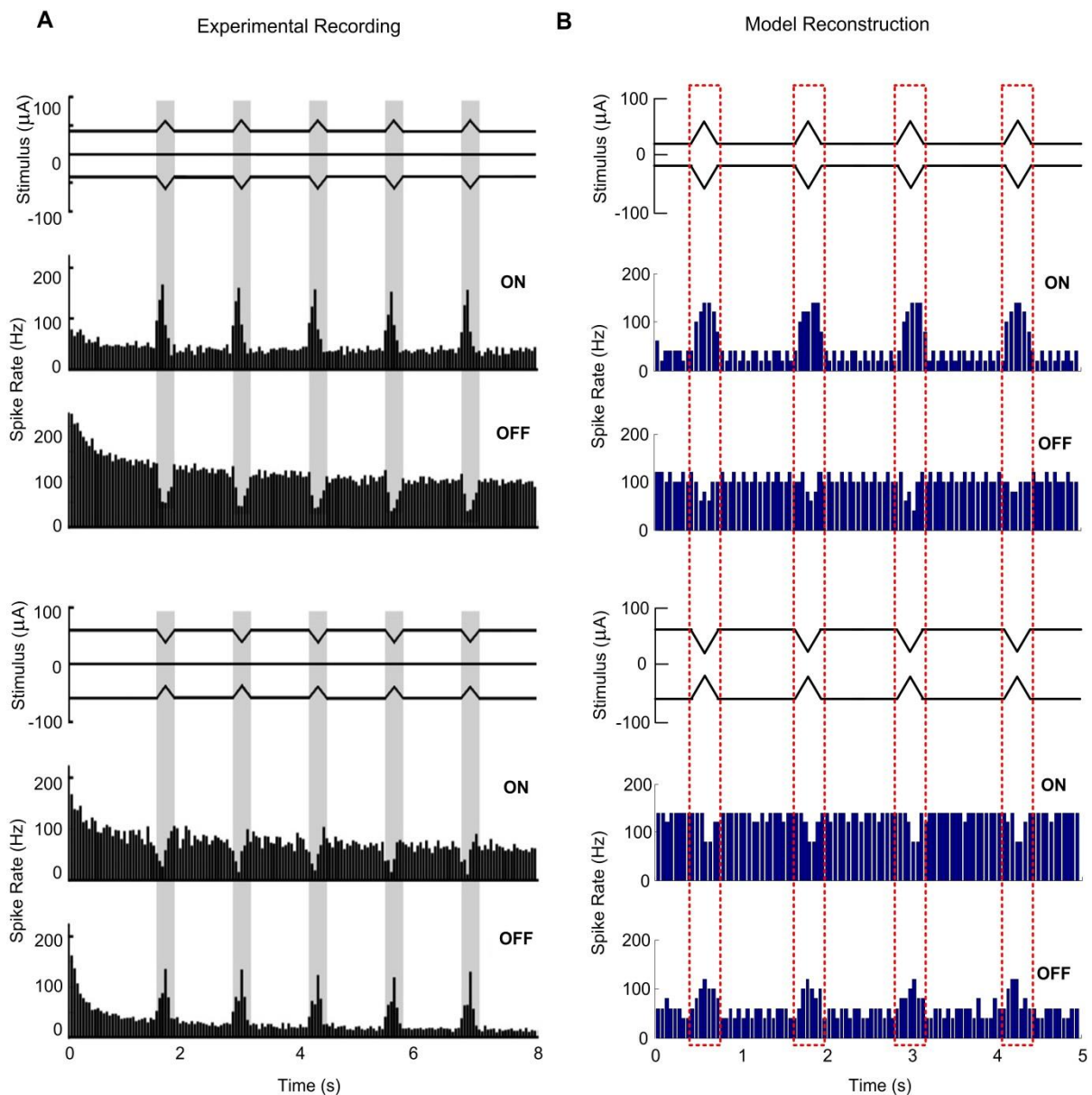


Figure 7.9 A. *In vitro* preferential ON and OFF RGC recruitment under HFS from Twyford et al. (2014). Average spiking rates for ON ($n=7$) and OFF ($n=7$) cells in response to stimulus waveform shown at the top of each panel (Upper panel: 40- μA baseline with 60- μA peak. Lower panel: 60- μA baseline with 40- μA minimum “notch”). B. Simulation results using realistic ON and OFF RGC models.

7.3 Threshold Maps

Simulated threshold maps for the ON and OFF RGC models were constructed by determining the stimulus threshold to biphasic pulses (with pulse width of 100 μs per phase, and a cathodal-anodal inter-phase interval of 160 μs) in the region around each cell. The vertical distance of the epiretinal stimulation electrode from the cell was fixed at 5 μm , and the spiking responses were obtained from the soma. Direct visualisation of full APs was readily obtained, with no confusion from the stimulus artefact. A bisection search method (Pal, 2009) was adopted to locate the threshold between given upper and lower limits of the stimulus amplitude. The upper stimulus limit was set to be the highest threshold value measured at the boundary of the map, and the lower limit was 0 μA . On each iteration of the bisection method, stimulus amplitude was set to the mid-point value between the upper and lower limits and new upper/lower limits were updated accordingly from the new trial stimulus tested. The termination condition was set to be 1 μA between the upper and lower limits, thereby controlling the resolution of the threshold value. After the threshold at one spatial location was determined, the stimulation electrode was moved to a neighbouring location (by 10 μm) and the above searching process was repeated. The new initial search value was set to the threshold value found in the previous location. Since the threshold difference between neighbouring locations should be minimised, the “dynamic” initial setting allowed less searching iterations.

Figure 7.10 demonstrates threshold maps for the ON and OFF RGC models in response to identical extracellular electrical stimulation profiles. Threshold differences between the cells were mostly due to their cell-specific ionic channel expressions and distributions. Overlaying the threshold map with the relevant RGC morphology revealed that both RGC types showed their highest sensitivity to electrical stimulation around the proximal axonal (i.e. AIS) region. More importantly, the OFF RGC model demonstrated a larger low-threshold field and higher sensitivity to stimulations near the proximal axon/soma regions. This is because the OFF RGC incorporated a higher sodium channel density in the AIS. On the other hand, the ON RGC model exhibited a larger excitable dendritic field due to its higher dendritic J_{Na} . This differentiation of RGC excitability can facilitate the explanation for different onsets of the non-monotonic RGC response profiles to HFS in Figure 7.2B.

Jeng et al. (2011) and Fried et al. (2009) retinal studies suggested that the low-threshold field (i.e. placement of the stimulating electrode near this region results in the lowest thresholds.)

was aligned with the dense band of sodium channels (named AIS in this thesis) within the proximal axon, using immunochemical staining technique. In their studies, low-threshold regions were spatially distinct from the soma and proximal axon, and a central region of low threshold which was surrounded by concentric field of increasing threshold, was found to be above AIS. Interestingly, our simulation results were found to be in agreement with these published *in vitro* data in terms of overall size and location of the low-threshold field.

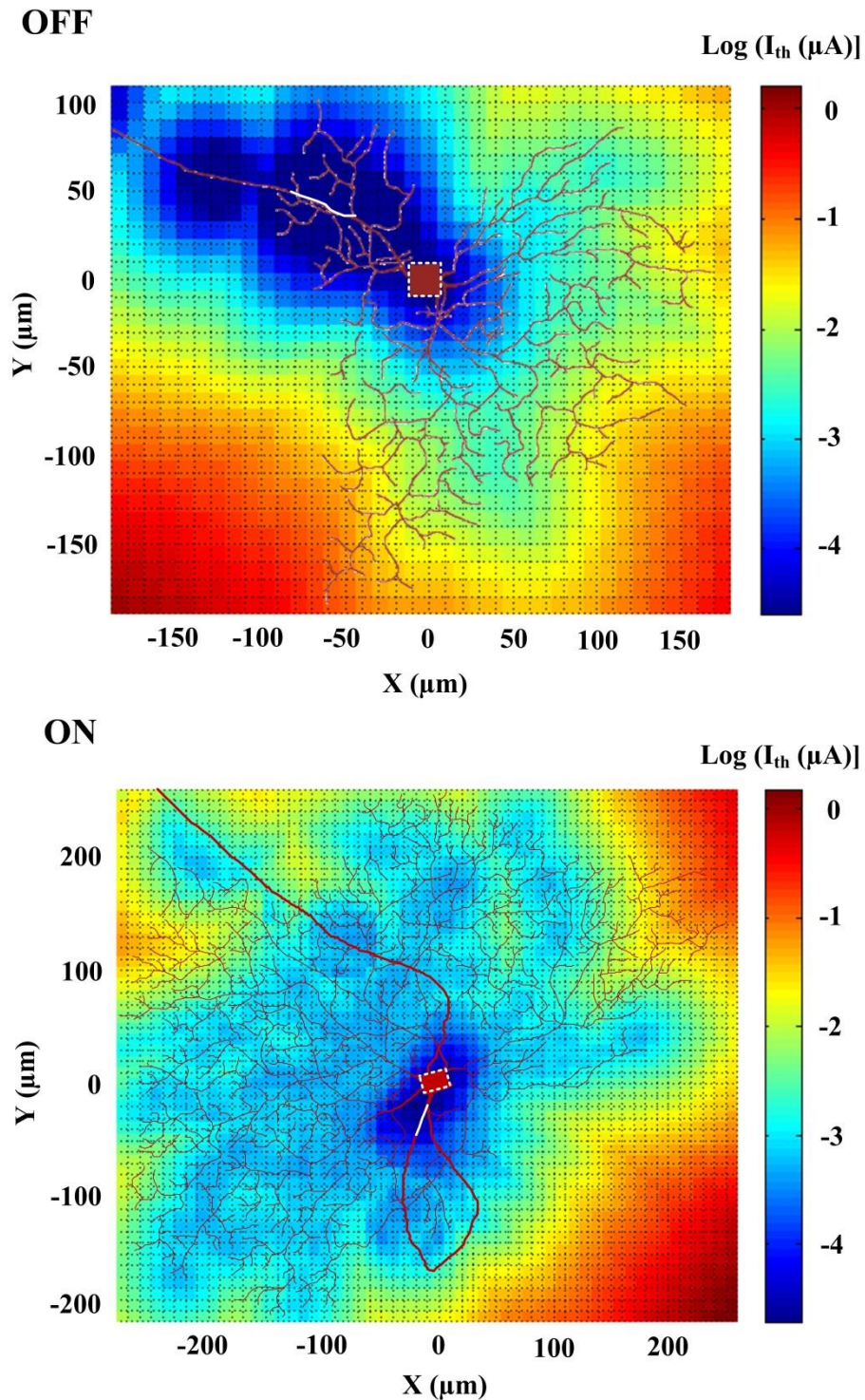


Figure 7.10 Simulated threshold maps overlaid with RGC morphology. Each pixel denotes the threshold obtained from the soma, in response to epiretinal biphasic pulses at that X–Y location. The pixel spacing is set to be $10 \mu m$. The colour bar indicates the logarithm of the threshold stimulus amplitude in μA . The soma was labelled as the red square surrounded with white dashed boundary and the axon was highlighted with a thick line. Overlaying the threshold map with RGC morphology revealed that the region of lowest threshold was aligned with the AIS (labelled by the white line). Differences were observed between ON and OFF cell in terms of size and location of the low-threshold region.

7.4 Influence of RGC Morphology on Stimulus-Response Profile

RGC stimulus-response profiles are a result of their biophysical properties, network connectivity, and importantly, the physical geometry of their neuronal processes. Neuronal morphology has been reported to play a vital role in shaping the response properties as well as the integration of neuronal inputs in many cell types throughout the central nervous system (CNS) (Vetter et al., 2001b, Spruston, 2008). It is therefore likely that similar morphological-dependence is also present in RGCs.

To facilitate analysis of the contribution of dendritic structure to RGC spiking, we developed a random RGC morphological generator, adapted from an existing neuronal morphology generation approach (Cuntz et al., 2010).

The soma was initially defined as a point at the origin O . With the soma as the centre, a number of (N) random *carrier* points, which would serve as the basis of dendritic growth, were distributed within a circular planar region of radius r , as shown in Figure 7.11A. Here, N can be regarded as the number of dendritic branches. The vertical positioning of these carrier points was later added in as a normal distribution, with an average distance of H from the origin O .

The algorithm, based on the minimum spanning tree algorithm (Prim, 1957), generated one-by-one dendritic branches by connecting unconnected carrier points to *node* points of the tree. At each step, a sweep through all nodes starting from the soma was undertaken to find the carrier point closest to the tree. A cost function, adapted from Cuntz et al. (2010), was used to calculate the weighted distance \tilde{d} between a carrier point to a node in the tree, as follows:

$$\tilde{d} = d_e \cdot (1 - bf) + d_p \cdot bf \quad (7.1)$$

where d_e is the Euclidean distance between a carrier point and a node in the tree; d_p is the length of the path along the corresponding branch from the soma to the carrier point, which is the sum of d_e and the length of the branch from the soma to the corresponding node; and bf is a balance factor, which weighs d_e and d_p against each other in the cost function. The carrier point with the shortest \tilde{d} was chosen as the *candidate* point to be connected to the corresponding node. This process is illustrated in Figure 7.11B.

However, before the connection was performed, an additional constraint was implemented. If d_e was smaller than a threshold length d_{seg} , the candidate point was added to the tree; but if d_e

was greater than d_{seg} , a *jitter* point was generated near the node, a jitter point was generated near the node, along the projected direction from the node to the candidate point. The jitter point was subsequently added to the tree, and subsequently added to the tree, and the candidate point sent back to the group of unconnected carrier points for the next iterative step. The iterations continued until all carriers points had been added to the tree.

Following generation of the dendritic tree, the soma was then extended into a 10 μm segment. A 50 μm long axonal hillock and a 1000 μm long axon were later added after the soma. The vertical distance between the axon and the soma was set to 10 μm , and the first 50 μm segment of the axon was defined as the axonal initial segment (AIS).

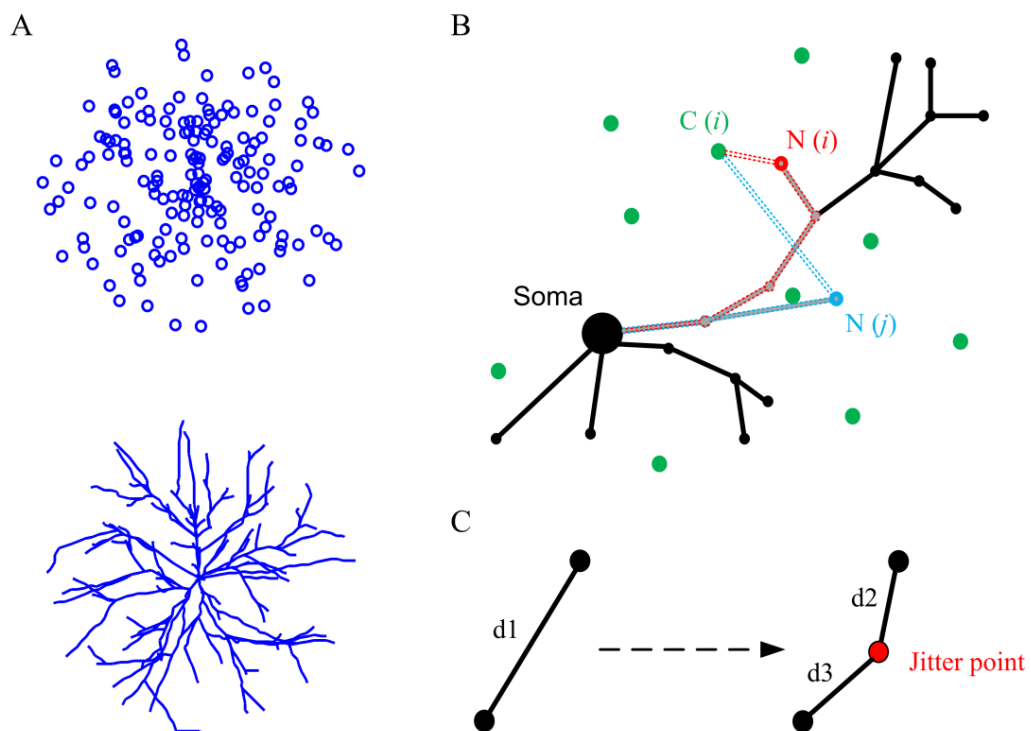


Figure 7.11 Illustration of the RGC dendritic morphology generator. (A) Upper: homogeneously distributed random carrier points in a circle starting from a root (soma) located at its centre. Lower: an example of the dendritic tree grown on carrier points. (B) The growth is described by an extended minimum spanning tree algorithm: unconnected *carrier* points (green) are to be connected one by one to the *nodes* of the dendritic tree (black). Red and blue hollowed dashed lines indicate two sample Euclidean distances (d_e) to the nodes $N(i)$ and $N(j)$ of the tree from the sample carrier point $C(i)$. d_p is the sum of d_e and the length of the branch from the soma to the corresponding node (solid dashed lines). The carrier point with the lowest cost function (see text) is then chosen as the *candidate* point to be connected to the corresponding node. (C) A jitter point (red) was generated near the node (black), when d_1 was greater than d_{seg} .

In these models, all biophysical parameters describing voltage-gated channel kinetics and ionic distributions shared the same values. Thus, the different spiking response of each RGC was solely dependent on its own morphology. When a variety of morphologies were simulated, distinct firing patterns were recorded. Response patterns were strongly correlated to the two morphological parameters: the number of dendritic branches (N) and the radius of the dendritic field (r).

To isolate the contributions of these two morphological parameters in shaping RGC spiking behaviours, three groups of simulations based on different assumptions were performed:

1. Dendritic branch number was held fixed ($N = 500$) and the spiking response profile to HFS was simulated with different dendritic field radii r as shown in Figure 7.13A2. Ten RGC morphologies were randomly generated at each level, and the spike response curves were plotted showing averaged spike numbers with standard error. The results indicated that the somatic spiking response was eliminated by decreasing the dendritic size (Figure 7.13A1), and the peak spike number could be approximated by a sigmoidal function of the dendritic field radius (Figure 7.13A3).
2. Dendritic field radius value was held fixed ($r = 150 \mu\text{m}$) and the spiking response profile to HFS was simulated with different dendritic branch numbers N as shown in Figure 7.13B2. We found that the somatic spiking response was eliminated by increasing the dendritic density (Figure 7.13B1). Furthermore, the peak spike number with the same RGC size could be approximated by a decaying exponential function of the dendritic branch number (Figure 7.13B3).
3. Since cell surface area has also been reported to correlate strongly to neuronal functions (Mainen and Sejnowski, 1996), simulations using different RGC morphologies with similar total membrane area were also performed. Figure 7.12A demonstrates an empirical relationship between dendritic cell membrane area A_d and morphological parameters N and r . We found the relationship between these three parameters can be well-estimated by the following equation:

$$A_d(N, r) = 0.2465 \cdot r \cdot N^{0.6721}, \quad (7.2)$$

where r is in units of μm and A_d in units of μm^2 . Based on eq. (7.2), we were able to reproduce different RGC morphologies with nearly identical cell membrane area, and therefore isolate the contribution of A_d in shaping spiking response.

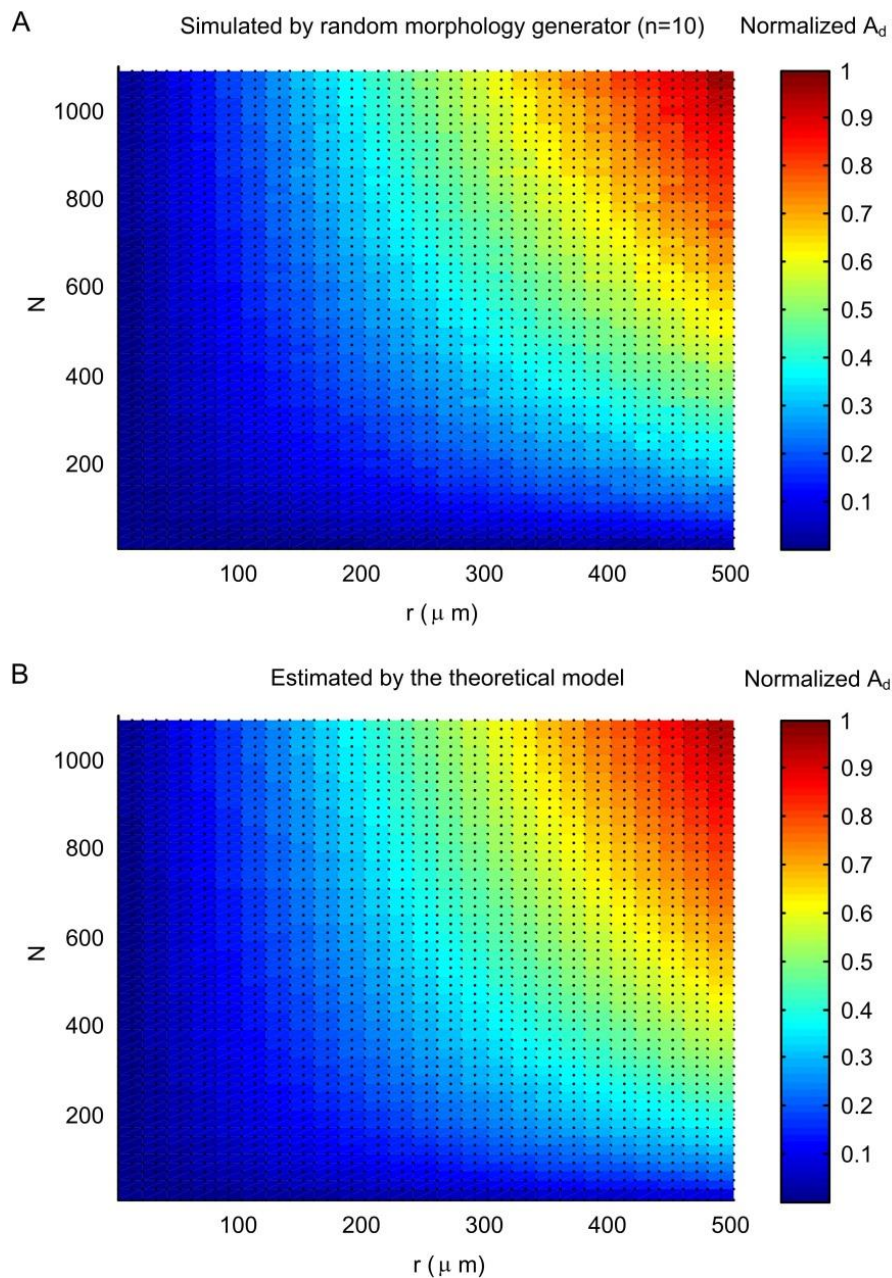


Figure 7.12 (A) Normalised dendritic cell membrane area (A_d) plotted as a function of dendritic density (N) and dendritic field radius (r) reproduced by the random morphology generator. (B) Dendritic cell membrane area using numerical estimation based on a regression equation (see text).

Spike response profiles were then investigated in these RGC models with near-constant dendritic cell membrane area ($A_d = 8200 \pm 200 \mu\text{m}^2$) and different dendritic numbers/dendritic field radii (see Figure 7.13C2). With identical cell membrane area, the peak total spike number was found to be linearly dependent on dendritic branch number (Figure 7.13C3).

In all stimulations, each morphological level was randomly generated 10 times, and standard errors were calculated. The results demonstrated robust non-monotonic response profiles, as indicated by the small standard error bars shown in Figure 7.13A1, B1 and C1

To test the sensitivity of RGC firing patterns to dendritic morphology over a large range of morphological parameters, we set peak spike numbers of the non-monotonic response profiles as indicators of RGC firing properties. The two morphological parameters, N and r , were varied across the ranges of 20~1000 and 50~350 μm , respectively. These ranges were set to lie within published RGC morphological data (Wong et al., 2012, O'Brien et al., 2002). Analysis was undertaken at the soma to characterise RGC activity in response to HFS at 300 ms duration.

Simulation results, as shown in Figure 7.14A, suggested a continuous spectrum of peak spike numbers with respect to a large range of systematic morphological variations. It should be noted that the “noise” present in the 2D plot was due to the stochastic process of morphology generation.

We found the correlation between peak spike number and morphological parameters can be numerically estimated by the following empirical equation derived from Figure 7.13A3 and Figure 7.13B3,

$$SN(N, r) = 55 \cdot \left(0.75 + \frac{0.38}{1 + e^{-0.025(r-130)}} \right) (1 + e^{-0.002N}), \quad (7.3)$$

where SN is total spike number and r is in units of μm . As shown in Figure 7.14B, the empirical profile reconstructed by eq. (7.3) was in good agreement with the simulated results using the random morphology generator. Root mean square (RMS) error between the simulation result and the empirical model was 7 spikes.

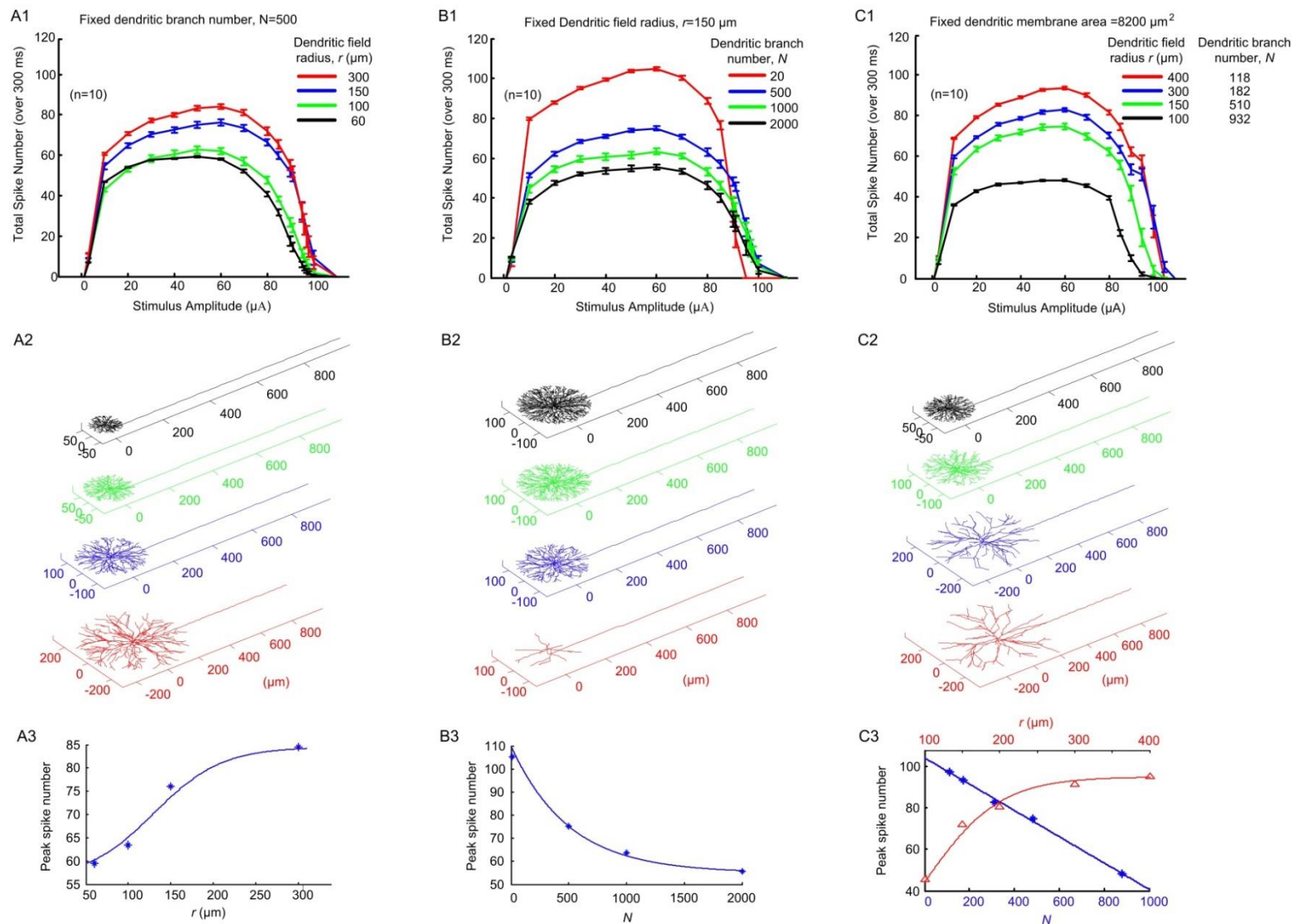


Figure 7.13 Influence of RGC morphology on spiking pattern in response to 2000 PPS HFS. Panel A: Spiking pattern with fixed dendritic branch number ($N = 500$) and different dendritic field radii r as shown in A2. Each morphological level was randomly generated 10 times. Peak spike number could be approximated by a sigmoidal function of r (A3). Error bars represent standard errors. Panel B: Spiking pattern with fixed dendritic field radius ($r = 150 \mu\text{m}$) and different dendritic branch numbers N . Peak spike number could be approximated by a decaying exponential function of N (B3). Panel C: Spiking pattern with fixed dendritic cell membrane area ($A_d = 8200 \mu\text{m}^2$). With identical cell membrane area, peak spike number was linearly dependent on N .

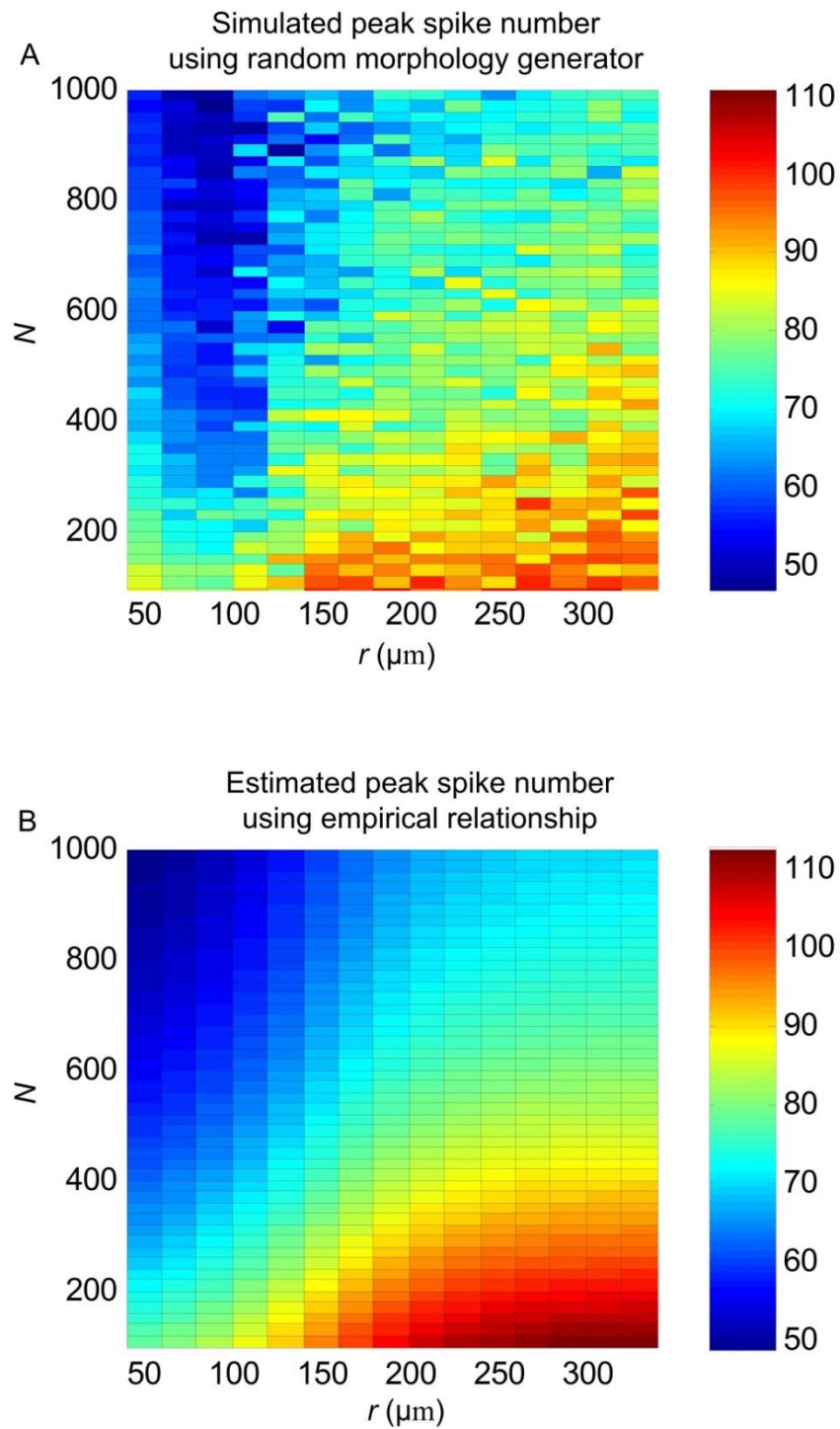


Figure 7.14 Peak total spikes plotted as a function of dendritic branch number N and dendritic field radius r . A. Simulated results using the random RGC generator. B. Empirical estimate based on nonlinear regression equations derived from Fig. 7.12 A3 and B3.

7.5 Discussion

7.5.1 Selective Activation and Possible Mechanisms

In this thesis, we define “selective” to mean targeted activation of one neuron type in preference to another neuron type. i.e. ON instead of OFF RGCs, or *vice versa*.

The results shown in this chapter are built based on the recent *in vitro* study suggesting the possibility of employing 2 kHz HFS to maximize the difference in responses between ON and OFF RGC types (Twyford et al., 2014). Although 2 kHz is not considered “high frequency” in other neural stimulation applications (Joseph and Butera, 2011, Litvak et al., 2003, Litvak et al., 2001, Schiller and Bankirer, 2007), it is the highest frequency that has been used in regards to current visual prosthetic stimulation strategies.

In this chapter, we used morphologically-generated RGC models to gain insights into the mechanisms underlying selective responses to extracellular electrical stimulation. With the optimised ionic channel distributions in each neuronal compartment obtained from Chapter 6, and incorporating detailed cell morphologies, we were able to reproduce the patterns of preferential excitation observed experimentally, when varying the extracellular stimulus amplitude across a wide range of values. It should be noticed that our model parameters were not optimised to fit *in vitro* experimental RGC responses to extracellular stimulation in this chapter. Therefore, the modelling results showed a different stimulation range (20-60 μA) compared to experimental range (40-60 μA) in Twyford et al. study. However, our models are able to exactly fit the published stimulation range by optimising model parameters if this is necessary.

To our knowledge, very little has been published on modelling selective activation of functionally-distinct RGCs. One reason may be that existing RGC models do not consider the functional significance of cellular morphology and membrane channel properties in each cellular region. For example, as shown in Figure 7.15, the existing FM model (Fohlmeister and Miller, 1997b) parameters (ionic channel expressions and distributions) were used in the ON and OFF RGC morphologies shown in the left panel. Compared to the optimised model performance in the upper panel, the FM ON (blue) and FM OFF (red) RGCs in the lower panel do not show a clear differential stimulus response profile in terms of onset, height and width, revealing improved model performance with the optimised ON/OFF parameters of

chapter 6. Moreover, most RGC models have only been validated against experiment data using simple, parametric stimulus sets with instantaneous amplitude change (e.g. a long rectangular profile), far from the real-life retinal input. Our RGC models, however, were validated by *in vitro* datasets closer to natural retinal stimuli (Twyford et al., 2014).

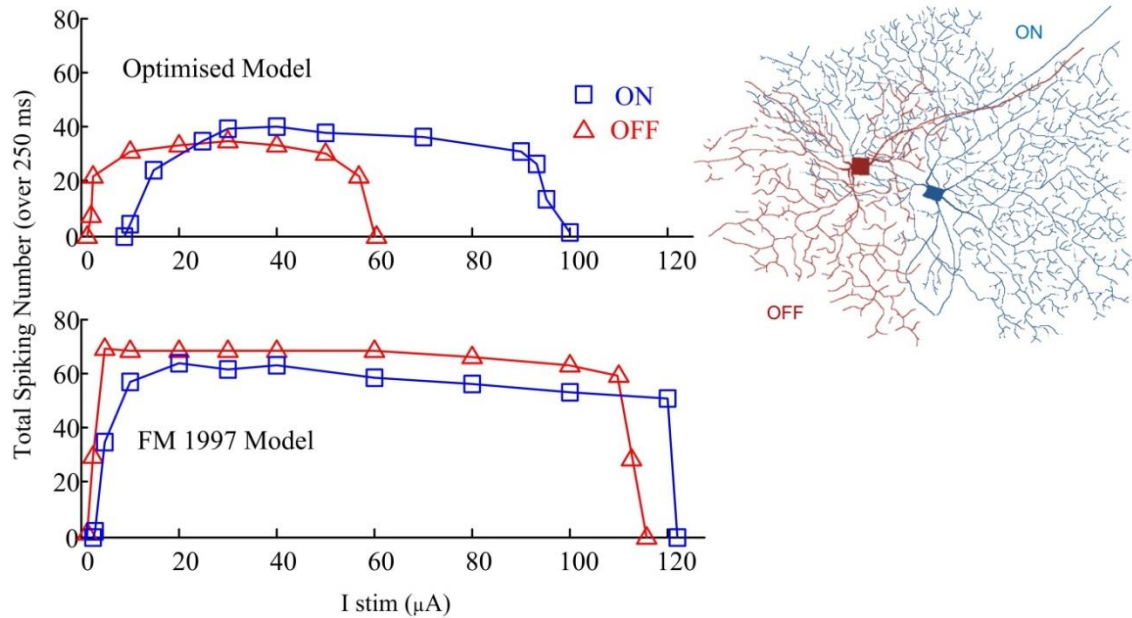


Figure 7.15 Comparison of optimised to Fohlmeister and Miller 1997 model performance against the ON and OFF RGC models of this chapter, in response to 2kHz epiretinal electrical stimulation. Upper panel: Blue and red lines indicate ON and OFF RGC response patterns to 2 kHz HFS using optimised parameters (see Tables 6.3-6.5) with corresponding RGC morphology shown in the right panel. Lower panel: Blue and red lines indicate ON and OFF RGC response patterns using the original FM model parameters under identical stimulation conditions.

More importantly, we also used computational models to shed light on the likely mechanisms underlying the non-monotonic stimulus response profile, namely the “up and down” spike number response as a function of stimulus amplitude. We also examined how this profile was affected by cell morphology and active membrane channel properties. The differential activation (Figure 7.9B) between simulated ON and OFF RGCs in response to amplitude-modulated HFS pulse trains was due to differences in the onset, peak and width of their characteristic non-monotonic response (Figure 7.2B). These differences in turn were most likely to due to their unique ionic channel expressions and cell-specific morphologies. Indeed, differences in ionic channel properties between RGC types, as well as differences in their dendritic morphology, raise the possibility that each type may exhibit markedly differential firing patterns in response to identical stimulus input. We found three important

characteristics of the spiking pattern profile that can be controlled by changing cellular properties:

1. **Peak spiking number (height) is dependent on the dendritic density:** Under simulations of dendritic pruning (Figure 7.4), the stimulus-response profile could be altered by progressively removing the active RGC dendritic structure, indicating that the non-monotonic response likely results from active somato-dendritic interactions. Higher dendritic loading can inhibit somatic excitation, and therefore, may contribute to the reduction in peak spike number (height) of the non-monotonic response.
2. **Width is mainly controlled by dendritic active conductance:** The non-monotonic stimulus-response profile could be also altered by progressively changing the dendritic sodium channel distribution (Figure 7.5). Activate dendrites mainly influence the width of the non-monotonic response profiles.
3. **Stimulus threshold (onset) is due to AIS properties:** The simulated threshold maps (Figure 7.10) indicated marked differential sensitivity to electrical stimulation between the two RGC types, especially in the proximal axon region. The stimulus threshold difference could be due to differences in the size and/or location of the AIS, as well as ionic channel density and kinetics within the AIS. The OFF model incorporated a larger AIS compartment and higher sodium channel density in the AIS region than that of the ON model, explaining the lower onset of its non-monotonic response profile. In addition, the different sodium and potassium channel kinetics within the AIS can also contribute to the differential RGC sensitivity to electrical stimulation.

Modelling studies of nerve conduction block in axons indicated that the suppression of neuronal response is due either to the voltage-gated potassium channel (Liu et al., 2009) or sodium channel properties (Kilgore and Bhadra, 2004). In this thesis, however, the RGC response suppression at higher stimulus amplitudes (i.e. the “decreasing” part of non-monotonic stimulus-response profile) may align with overall RGC properties rather than particular local factors. At higher amplitudes, the somatic RGC response is inhibited by hyperpolarising currents back-propagating from the multiple dendritic branches. This inhibition becomes stronger with increasing stimulus amplitudes, until the response is totally abolished. Further understanding the detailed contribution of these RGC properties in the observed suppression may help predict which potential RGC types can be targeted by HFS.

7.5.2 The Site of AP Initiation in RGCs

The simulated threshold map results suggested that the low-threshold region of RGCs was in the proximal axon, close to the AIS. Multiple anatomical landmarks have previously been reported to be the site of lowest-threshold (presumably the site of AP initiation) in RGCs; for example, soma (Greenberg et al., 1999), sodium channel band (Jeng et al., 2011, Fried et al., 2009, Werginz et al., 2014), thin segment/sodium channel band (Carras et al., 1992, Sheasby and Fohlmeister, 1999), axon bend (Schiefer and Grill, 2006) and AIS (Sekirnjak et al., 2008). Although not all these anatomical landmarks were included in the current model structure, our results supported the hypothesis that the proximal axon region of a RGC had the highest sensitivity to electrical stimulation, and that the anatomical/biophysical properties of this neuronal region were likely to modulate the RGC response to electrical stimulation. In addition, our models indicated that one or more anatomical features of the proximal axon such as the axonal bend, sodium-channel band, as well as AIS, may align with the low-threshold region.

7.5.3 Continuous Spectrum of Spiking Patterns with Morphological Variations

In a more “generalised” set of simulations based on the random morphology generator (Figure 7.13), the results suggested a continuous spectrum of spiking patterns with systematic morphological variations. Although this particular set of simulations did not include the contribution of variation in channel expressions and other physiological factors, it supports the idea that functional differentiation in RGC spiking behaviour is also due to dendritic morphology. RGC morphology has rarely been examined quantitatively in previous studies, except for a few limited modelling studies (Maturana et al., 2013, Fohlmeister and Miller, 1997b), likely due to the difficulty of isolating the contribution of morphology in experiments. Computational studies hence provide a promising platform for understanding how the physical characteristics of RGCs influence their behaviour. To our knowledge, the simulations of this chapter are the first to systematically study the contribution of dendritic morphology to RGC responses to extracellular electrical stimulation. Since there is a wide anatomical variety of RGC morphologies (Wong et al., 2012, O'Brien et al., 2002, Rockhill et al., 2002), this study can serve as the basis for population-based RGC modelling.

Compared to using only a morphology generator (Cuntz et al., 2010), our modelling approach involves representing the neuron with both accurate morphology and an optimised ionic model. In addition, existing modelling studies (Maturana et al., 2013, Mainen and Sejnowski, 1996) have been largely limited to investigating the influence of cell structure on cell response to intracellular current injections. To our knowledge, the simulations of this chapter are the first to systematically study the contribution of dendritic morphology to RGC responses due to extracellular electrical stimulation.

In summary, our modelling studies suggest that the cell-specific non-monotonic response (i.e. the base of selective excitation) to 2 kHz electrical extracellular stimulation results from a complex balance between intrinsic and physical RGC properties. Intrinsic cellular properties including ionic channel expressions and distributions contributed to the threshold/onset and width of non-monotonic response profile, and physical properties such as dendritic loading and field size controlled the height of the stimulus response curve. All of these cellular properties combined produce a distinct stimulus range for each RGC excitation, suggesting the intriguing possibility of selectively activating different RGC classes using a suitably-designed electrical stimulation strategy. This approach can be used to design electrical stimulus profiles capable of cell-specific activation, and is broadly applicable for the development of sophisticated stimulation strategies for visual prostheses.

Chapter 8 Conclusions

8.1 Thesis Contributions

This thesis aimed to develop a series of biophysically-accurate computational neuronal models to assist in the understanding of mechanisms underlying RGC activities in response to electrical stimulation, both intracellular and extracellular. The results outlined in Chapters 5, 6, and 7 have three major contributions to existing RGC studies and current retinal prosthesis development.

8.1.1 A generic neuron model optimisation approach

The multi-objective optimisation approach developed in this thesis can provide a practical means of reconstructing hidden information underlying multiple biological RGC responses. Previous neuronal modelling and optimisation studies indicate that the limited information in a single dataset may result in non-unique reconstruction of membrane currents, some of which may not be accurate from a known physiological viewpoint. However, the multi-objective optimisation technique described in this thesis appears to provide stringent constraints on the dynamics of underlying membrane currents, yielding reconstructed AP waveforms and spiking patterns in agreement with experimental studies.

In addition, the results suggest that optimisation with well-defined objective functions can improve the predictive power of the models, particularly when the additional datasets includes information not initially present. Our multi-dataset optimised parameters yielded good predictions to non-optimised data under different experimental conditions, namely *in vitro* selective RGC responses to extracellular high-frequency stimulations. It is likely that this high degree of model prediction will be generally hard to achieve with only single-objective optimisation.

This multi-objective optimisation approach provides a valuable tool in elucidating the ionic mechanisms underlying RGC electrical activities. This approach is generally applicable to other excitable cell models including cardiac myocytes and non-RGC neurons. By using this technique, more accurate neural ionic models can be constructed automatically, reducing the gap between theoretical models and real neurons.

8.1.2 Accurate ON and OFF RGC simulations

In Chapter 6, two major classes of RGC were reconstructed - ON and OFF - using realistic 3D morphologies obtained from images of rabbit RGCs, whose electrical responses were also obtained using whole-cell patch clamp recording. The models incorporated biophysically-accurate formulations of ionic channels present in the membrane, taking into account differences in various functional cellular regions including the soma, hillock, axon, dendrites and AIS. Unlike previous RGC models, parameters of these multi-compartment models were fitted to multiple actual electrical activities recorded.

With anatomical information and cell-specific ionic channel expression, the models could accurately reproduce the differential AP waveforms and spiking patterns in ON and OFF RGC classes. This approach represented a major step forward in accurately reconstructing electrical activities in functionally-distinct RGCs, and will help advance our understanding of ionic mechanisms underlying RGC activation.

8.1.3 Selective activation of ON and OFF RGC types

In Chapter 7, the simulation results using accurate ON and OFF RGC formulations revealed that it is possible to selectively or preferentially activate either cell-type using high-frequency electrical stimulation. These results were also confirmed by *in vitro* studies in rabbit retinas. It should be noticed that the morphologically-realistic models were not optimised to reproduce RGC responses to extracellular stimulation. Nevertheless, predictive ability of the models was confirmed by their close match to *in vitro* ON and OFF RGC activities recorded under totally different experimental conditions. Since human vision is thought to be mediated primarily by two major classes of RGCs - ON and OFF, the ability to selectively activate either or both of these cell types using artificial electrical stimulation will lead to dramatic improvements in the quality of elicited vision.

Rather than passively reconstructing the measured RGC response patterns, the modelling approach detailed in Chapter 7 can provide likely mechanisms underlying the response profile to extracellular high-frequency stimulation. This was achieved by controlling the cell morphological and biophysical properties, revealing advantages of computational modelling over difficult to do experimental measurements. Since the major challenge of present prosthetic vision devices is to understand the factors that shape the response of a single

retinal neuron to electrical stimulation (Jeng et al., 2011), the model presented in this thesis has the potential to be used to develop a wide range of intracellular and extracellular stimulation strategies. Armed with such computational models, it is possible to form a tight-loop investigation cycle, consisting of computational predictions on potentially beneficial stimulation strategies and experimental validations. These data-driven models can then provide a promising approach to rapidly probe the responses of identified RGCs to a broad range of novel stimulus configurations, as well as formulate theories of selective RGC encoding.

8.2 Future Work

An important next step following the results of this thesis is to determine if knowledge of the resulting RGC mechanisms can be used for practical stimulation strategy design for a vision prosthesis. Future studies should expand the analysis to additional RGC types, in order to build comprehensive models of the electrical responses of the entire RGC population and further contribute to the understanding of retinal encoding and visual information processing. About twenty types of mammalian RGCs have been functionally-identified thus far. Once the biophysical/physical properties of all RGC types are well understood by this cell-specific modelling approach, the relative response to a wide range of stimulation schemes can be clearly predicted using a population-based computational model.

An improved understanding of the population-based RGC activation process will enable accurate computational evaluation of retinal stimulation, so that a wide range of stimulus waveforms and parameters can readily be tested. In particular, stimulus strategies allowing selective activation of functionally-distinct RGCs will result in major improvements in the quality of artificial vision, and will form an important component of further visual prosthetic stimulation systems.

Publications Arising from This Thesis

- GUO, T., TSAI, D., Bai, S, MORLEY, J. W., SUANING, G. J., LOVELL, N. H. & DOKOS, S. "Understanding the retina: a review of computational models of the retina from the single-cell to network level," *Critical Reviews in Biomedical Engineering*. Vol. 42(5), pp 491-436, 2014. doi: 10.1615/CritRevBiomedEng.2014011732
- GUO, T., LOVELL, N. H., TSAI, D., TWYFORD, P., FRIED, S., MORLEY, J. W., SUANING, G. J. & DOKOS, S. Selective activation of ON and OFF retinal Ganglion Cells to high-frequency electrical stimulation: A modeling study, *the 36th Annual International Conference of the IEEE Engineering in Medicine and Biology Society*. Chicago, US: IEEE Press (Student paper competition, Asian-Pacific finalist).
- GUO, T., TSAI, D., MORLEY, J. W., SUANING, G. J., LOVELL, N. H. & DOKOS, S. 2014b Unique characteristics of ON and OFF retinal ganglion cells: A modeling study. *the 36th Annual International Conference of the IEEE Engineering in Medicine and Biology Society*. Chicago, US: IEEE Press.
- GUO, T., TSAI, D., MORLEY, J. W., SUANING, G. J., LOVELL, N. H. & DOKOS, S. 2013b. Cell-specific modeling of retinal ganglion cell electrical activity. *the 35th Annual International Conference of the IEEE Engineering in Medicine and Biology Society*. Osaka, Japan: IEEE Press (Student paper competition, Asian-Pacific finalist).
- GUO, T., TSAI, D., MORLEY, J. W., SUANING, G. J., LOVELL, N. H. & DOKOS, S. 2013c. Influence of cell morphology in a computational model of ON and OFF retinal ganglion cells. *the 35th Annual International Conference of the IEEE Engineering in Medicine and Biology Society*. Osaka, Japan: IEEE press.
- GUO, T., TSAI, D., SOVILJ, S., MORLEY, J. W., SUANING, G. J., LOVELL, N. H. & DOKOS, S. 2013d. Influence of active dendrites on firing patterns in a retinal ganglion cell model. *the 35th Annual International Conference of the IEEE Engineering in Medicine and Biology Society*. Osaka, Japan: IEEE Press.
- GUO, T., TSAI, D., SUANING, G. J., LOVELL, N. H. & DOKOS, S. 2012. Modeling normal and rebound excitation in mammalian retinal ganglion cells. *the 34th Annual International Conference of the IEEE Engineering in Medicine and Biology Society*. San Diego, US: IEEE press.
- GUO, T., LOVELL, N. H., TSAI, D., TWYFORD, P., FRIED, S., MORLEY, J. W., SUANING, G. J. & DOKOS, S. Optimizing retinal ganglion cell responses to high-frequency electrical stimulation strategies for preferential neuronal excitation, *the 7th International Conference of the IEEE Engineering in Medicine and Biology Society on Neural Engineering*. Montpellier, France: IEEE press.
- BAI, S., GUO, T., TSAI, D., MORLEY, J. W., SUANING, G. J. LOVELL, N. H., & DOKOS, S. Influence of Dendritic Morphology on the Dynamic Properties of Retinal Ganglion Cells: A Computational Study, *Engineering in Medicine and Biology Society (EMBC), the 7th International Conference of the IEEE Engineering in Medicine and Biology Society on Neural Engineering*. Montpellier, France: IEEE press.

Bibliography

- ABBAS, S. Y., HAMADE, K. C., YANG, E. J., NAWY, S., SMITH, R. G. & PETTIT, D. L. 2013. Directional summation in non-direction selective retinal ganglion cells. *PLoS Comput Biol*, 9, e1002969.
- ABRAMIAN, M., LOVELL, N. H., HABIB, A., MORLEY, J. W., SUANING, G. J. & DOKOS, S. 2014. Quasi-monopolar electrical stimulation of the retina: A computational modelling study. *J Neural Eng*, 11, 025002.
- ABRAMIAN, M., LOVELL, N. H., MORLEY, J. W., SUANING, G. J. & DOKOS, S. 2011. Activation of retinal ganglion cells following epiretinal electrical stimulation with hexagonally arranged bipolar electrodes. *J Neural Eng*, 8, 035004.
- ACHARD, P. & DE SCHUTTER, E. 2006. Complex parameter landscape for a complex neuron model. *Plos Comput Biol*, 2, 794-804.
- AHNELT, P. & KOLB, H. 1994a. Horizontal cells and cone photoreceptors in human retina - a golgi-electron microscopic study of spectral connectivity. *J Comp Neurol*, 343, 406-427.
- AHNELT, P. & KOLB, H. 1994b. Horizontal cells and cone photoreceptors in primate retina - a golgi-light microscopic study of spectral connectivity. *J Comp Neurol*, 343, 387-405.
- AHUJA, A. K., BEHREND, M. R., KURODA, M., HUMAYUN, M. S. & WEILAND, J. D. 2008. An in vitro model of a retinal prosthesis. *IEEE Trans Bio-Med Eng*, 55, 1744-1753.
- AHUJA, A. K., DORN, J. D., CASPI, A., MCMAHON, M. J., DAGNELIE, G., DACRUZ, L., STANGA, P., HUMAYUN, M. S., GREENBERG, R. J. & GRP, A. I. S. 2011. Blind subjects implanted with the argus ii retinal prosthesis are able to improve performance in a spatial-motor task. *Brit J Ophthalmol*, 95, 539-543.
- AIDLEY, D. J. 1979. *The physiology of excitable cells* Cambridge Cambridge University Press.
- AL ABED, A., GUO, T., LOVELL, N. H. & DOKOS, S. 2013a. Optimisation of ionic models to fit tissue action potentials: Application to 3d atrial modelling. *Comput Math Methods Med*, 2013, 951234.
- AL ABED, A., LOVELL, N. H., SUANING, G. J. & DOKOS, S. 2013b. A continuum neuronal tissue model based on a two-compartmental representation of cells. *the 35th Annual International Conference of the IEEE Engineering in Medicine and Biology Society*. Osaka, Japan: IEEE press.
- AL ABED, A., YIN, S., SUANING, G. J., LOVELL, N. H. & DOKOS, S. 2012. A convolution based method for calculating inputs from dendritic fields in a continuum model of the retina. *the 34th Annual International Conference of the IEEE Engineering in Medicine and Biology Society*. San Diego, US: IEEE Press.
- ALTMAN, K. W. & PLONSEY, R. 1990. Point-source nerve bundle stimulation - effects of fiber diameter and depth on simulated excitation. *IEEE Trans Bio-Med Eng*, 37, 688-698.
- AMTHOR, F. R., TAKAHASHI, E. S. & OYSTER, C. W. 1989. Morphologies of rabbit retinal ganglion-cells with concentric receptive-fields. *J Comp Neurol*, 280, 72-96.
- AOYAMA, T., KAMIYAMA, Y. & USUI, S. 2005. Simulation analysis of receptive-field size of retinal horizontal cells by ionic current model. *Visual Neurosci*, 22, 65-78.
- AOYAMA, T., KAMIYAMA, Y., USUI, S., BLANCO, R., VAQUERO, C. F. & DE LA VILLA, P. 2000. Ionic current model of rabbit retinal horizontal cell. *Neurosci Res*, 37, 141-151.

- ARGUELLO, E., SILVA, R., HUERTA, M. & CASTILLO, C. 2013. New trends in computational modeling: A neuroid-based retina model. *the 35th Annual International Conference of the IEEE Engineering in Medicine and Biology Society*. Osaka, Japan: IEEE Press.
- AYOUB, G. S. & COPENHAGEN, D. R. 1991. Application of a fluorometric method to measure glutamate release from single retinal photoreceptors. *J Neurosci Meth*, 37, 7-14.
- BACCUS, S. A., OLVECZKY, B. P., MANU, M. & MEISTER, M. 2008. A retinal circuit that computes object motion. *J Neurosci*, 28, 6807-6817.
- BARANAUSKAS, G. & MARTINA, M. 2006. Sodium currents activate without a hodgkin and huxley-type delay in central mammalian neurons. *J Neurosci*, 26, 671-684.
- BAYLOR, D. A., HODGKIN, A. L. & LAMB, T. D. 1974. Reconstruction of the electrical responses of turtle cones to flashes and steps of light. *J Physiol.*, 242, 759-91.
- BEELER, G. W. & REUTER, H. 1977. Reconstruction of action potential of ventricular myocardial fibers. *J Physiol-London*, 268, 177-210.
- BERRY, M. J., 2ND, BRIVANLOU, I. H., JORDAN, T. A. & MEISTER, M. 1999. Anticipation of moving stimuli by the retina. *Nature*, 398, 334-8.
- BEVERIDGE, G. & SCHECHTER, R. 1970. *Optimisation: Theory and practice*, New York, US, McGraw-Hill.
- BHALLA, U. S. & BOWER, J. M. 1993. Exploring parameter space in detailed single neuron models - simulations of the mitral and granule cells of the olfactory-bulb. *J Neurophysiol*, 69, 1948-1965.
- BIEL, M., WAHL-SCHOTT, C., MICHALAKIS, S. & ZONG, X. 2009. Hyperpolarization-activated cation channels: From genes to function. *Physiological reviews*, 89, 847-85.
- BOINAGROV, D., LOUDIN, J. & PALANKER, D. 2010. Strength-duration relationship for extracellular neural stimulation: Numerical and analytical models. *J Neurophysiol.*, 104, 2236-48.
- BOMASH, I., ROUDI, Y. & NIRENBERG, S. 2013. A virtual retina for studying population coding. *Plos One*, 8, e53363.
- BORG-GRAHAM, L. J. 2001. The computation of directional selectivity in the retina occurs presynaptic to the ganglion cell. *Nat Neurosci.*, 4, 176-83.
- BORST, A., FLANAGIN, V. L. & SOMPOLINSKY, H. 2005. Adaptation without parameter change: Dynamic gain control in motion detection. *P Natl Acad Sci USA*, 102, 6172-6176.
- BOYCOTT, B. B. & WASSLE, H. 1991. Morphological classification of bipolar cells of the primate retina. *Eur J Neurosci*, 3, 1069-1088.
- BRINDLEY, G. S. 1956. The passive electrical properties of the frog's retina, choroid and sclera for radial fields and currents. *J Physiol*, 134, 339-52.
- BUCHHOLTZ, F., GOLOWASCH, J., EPSTEIN, I. R. & MARDER, E. 1992. Mathematical model of an identified stomatogastric ganglion neuron. *J Neurophysiol*, 67, 332-40.
- BUSH, K., KNIGHT, J. & ANDERSON, C. 2005. Optimizing conductance parameters of cortical neural models via electrotonic partitions. *Neural Networks*, 18, 488-496.
- CAI, C. F., LIANG, P. J. & ZHANG, P. M. 2007. A simulation study on the encoding mechanism of retinal ganglion cell. *Lect N Bioinformat*, 4689, 470-479.
- CAI, C. S., REN, Q. S., DESAI, N. J., RIZZO, J. F. & FRIED, S. I. 2011. Response variability to high rates of electric stimulation in retinal ganglion cells. *J Neurophysiol*, 106, 153-162.
- CARRAS, P. L., COLEMAN, P. A. & MILLER, R. F. 1992. Site of action potential initiation in amphibian retinal ganglion cells. *J Neurophysiol.*, 67, 292-304.

- CONNAUGHTON, V. P., GRAHAM, D. & NELSON, R. 2004. Identification and morphological classification of horizontal, bipolar, and amacrine cells within the zebrafish retina. *J Comp Neurol*, 477, 371-385.
- CONNOR, J. A., WALTER, D. & MCKOWN, R. 1977. Neural repetitive firing - modifications of hodgkin-huxley axon suggested by experimental results from crustacean axons. *Biophys J*, 18, 81-102.
- COTTARIS, N. P., ELFAR, S. D., IEZZI, R. & ABRAMS, G. W. 2005. How the retinal network reacts to epiretinal stimulation to form the prosthetic visual input to the cortex: Computational modeling of a degenerated retina. *Invest Ophth Vis Sci*, 46, S74-90.
- CUNTZ, H., FORSTNER, F., BORST, A. & HAUSSER, M. 2010. One rule to grow them all: A general theory of neuronal branching and its practical application. *Plos Comput Biol*, 6, e1000877.
- CURLANDER, J. C. & MARMARELIS, V. Z. 1987. A linear spatiotemporal model of the light-to-bipolar cell system and its response characteristics to moving bars. *Biol Cybern.*, 57, 357-363.
- DAGUANNO, A., BARDAKJIAN, B. L. & CARLEN, P. L. 1986. Passive neuronal membrane parameters - comparison of optimization and peeling methods. *Ieee Trans Bio-Med Eng*, 33, 1188-1196.
- DASTGHEIB, Z. S., AZEMI, A., KHADEMI, M., SHAJIEE, M., ARVANEH, M., GHOLIZADEH, H. & SABZEVARI, V. R. 2009. Identification of ionic conductances in a reentry model of ventricular myocardium cells. *J Applied Sci*, 9, 555-560.
- DAYAN, P. & ABBOTT, L. F. 2001. *Theoretical neuroscience*, Cambridge, US, MIT Press.
- DE BALTHASAR, C., PATEL, S., ROY, A., FREDI, R., GREENWALD, S., HORSAGER, A., MAHADEVAPPA, M., YANAI, D., MCMAHON, M. J., HUMAYUN, M. S., GREENBERG, R. J., WEILAND, J. D. & FINE, I. 2008. Factors affecting perceptual thresholds in epiretinal prostheses. *Invest Ophth Vis Sci*, 49, 2303-2314.
- DESCHUTTER, E. & BOWER, J. M. 1994. An active membrane model of the cerebellar purkinje-cell .2. Simulation of synaptic responses. *J Neurophysiol*, 71, 401-419.
- DESTEXHE, A., NEUBIG, M., ULRICH, D. & HUGUENARD, J. 1998. Dendritic low-threshold calcium currents in thalamic relay cells. *J Neurosci*, 18, 3574-88.
- DOKOS, S. 2014. Computational models of neural retina. In: DIETER, J. & RANU, J. (eds.) *Encyclopedia of computational neuroscience*. Springer.
- DOKOS, S. & LOVELL, N. H. 2003. A curvilinear gradient path method for optimization of biological systems models. *Modelling and Control in Biomedical Systems 2003 (Including Biological Systems)*.
- DOKOS, S. & LOVELL, N. H. 2004. Parameter estimation in cardiac ionic models. *Prog Biophys Mol Bio*, 85, 407-431.
- DOKOS, S., SUANING, G. J. & LOVELL, N. H. 2005. A bidomain model of epiretinal stimulation. *IEEE Trans Neural Syst Rehabil Eng*, 13, 137-46.
- DOWLING, J. 2005. Artificial human vision. *Expert Rev Med Devices*, 2, 73-85.
- DREOSTI, E., ESPOSTI, F., BADEN, T. & LAGNADO, L. 2011. In vivo evidence that retinal bipolar cells generate spikes modulated by light. *Nat Neurosci*, 14, 951-952.
- DRUCKMANN, S., BANITT, Y., GIDON, A., SCHURMANN, F., MARKRAM, H. & SEGEV, I. 2007. A novel multiple objective optimization framework for constraining conductance-based neuron models by experimental data. *Front Neurosci*, 1, 7-18.
- DRUCKMANN, S., BERGER, T. K., HILL, S., SCHURMANN, F., MARKRAM, H. & SEGEV, I. 2008. Evaluating automated parameter constraining procedures of neuron models by experimental and surrogate data. *Biol Cybern*, 99, 371-9.

- ELBELTAGI, E., HEGAZY, T. & GRIERSON, D. 2005. Comparison among five evolutionary-based optimization algorithms. *Adv Eng Inform*, 19, 43-53.
- ENCISO, G., REMPE, M., DMITRIEV, A. V., GAVRIKOV, K. E., TERMAN, D. & MANGEL, S. C. 2010. A model of direction selectivity in the starburst amacrine cell network. *J Comput Neurosci.*, 28, 567-578.
- ENGBERS, J. D., ANDERSON, D., TADAYONNEJAD, R., MEHAFFEY, W. H., MOLINEUX, M. L. & TURNER, R. W. 2011. Distinct roles for i(t) and i(h) in controlling the frequency and timing of rebound spike responses. *J Physiol*, 589, 5391-5413.
- ENROTH-CUGELL, C. & FREEMAN, A. W. 1987. The receptive-field spatial structure of cat retinal y cells. *J Physiol*, 384, 49-79.
- EULER, T. & WASSLE, H. 1995. Immunocytochemical identification of cone bipolar cells in the rat retina. *J Comp Neurol*, 361, 461-78.
- FELSEN, G. & DAN, Y. 2005. A natural approach to studying vision. *Nat Neurosci*, 8, 1643-1646.
- FINK, M. & NOBLE, D. 2009. Markov models for ion channels: Versatility versus identifiability and speed. *Philos T R Soc A*, 367, 2161-2179.
- FOHLMMEISTER, J. F. 2009. A nerve model of greatly increased energy-efficiency and encoding flexibility over the hodgkin-huxley model. *Brain Res*, 1296, 225-33.
- FOHLMMEISTER, J. F., COHEN, E. D. & NEWMAN, E. A. 2010. Mechanisms and distribution of ion channels in retinal ganglion cells: Using temperature as an independent variable. *J Neurophysiol*, 103, 1357-1374.
- FOHLMMEISTER, J. F., COLEMAN, P. A. & MILLER, R. F. 1990. Modeling the repetitive firing of retinal ganglion cells. *Brain Res.*, 510, 343-5.
- FOHLMMEISTER, J. F. & MILLER, R. F. 1997a. Impulse encoding mechanisms of ganglion cells in the tiger salamander retina. *J Neurophysiol*, 78, 1935-1947.
- FOHLMMEISTER, J. F. & MILLER, R. F. 1997b. Mechanisms by which cell geometry controls repetitive impulse firing in retinal ganglion cells. *J Neurophysiol*, 78, 1948-1964.
- FOSTER, W. R., UNGAR, L. H. & SCHWABER, J. S. 1993. Significance of conductances in hodgkin-huxley models. *J Neurophysiol*, 70, 2502-2518.
- FOUTZ, T. J. & MCINTYRE, C. C. 2010. Evaluation of novel stimulus waveforms for deep brain stimulation. *J Neural Eng*, 7, 066008.
- FREED, M. 2001. Parallel cone bipolar pathways to a ganglion cell use different rates and amplitudes of quantal excitations. *Invest Ophth Vis Sci*, 42, S519-S519.
- FREED, M. A. 2000. Parallel cone bipolar pathways to a ganglion cell use different rates and amplitudes of quantal excitation. *J Neurosci*, 20, 3956-3963.
- FREED, M. A., SMITH, R. G. & STERLING, P. 1992. Computational model of the on-alpha ganglion-cell receptive-field based on bipolar cell circuitry. *P Natl Acad Sci USA*, 89, 236-240.
- FREEMAN, D. K., EDDINGTON, D. K., RIZZO, J. F. & FRIED, S. I. 2010a. Selective activation of neuronal targets with sinusoidal electric stimulation. *J Neurophysiol*, 104, 2778-2791.
- FREEMAN, D. K., RIZZO, J. F. & FRIED, S. I. 2010b. Electric stimulation with sinusoids and white noise for neural prostheses. *Front Neurosci*, 4, 28.
- FREEMAN, D. K., RIZZO, J. F. & FRIED, S. I. 2011. Encoding visual information in retinal ganglion cells with prosthetic stimulation. *J Neural Eng*, 8.
- FRIED, S. I., LASKER, A. C. W., DESAI, N. J., EDDINGTON, D. K. & RIZZO, J. F. 2009. Axonal sodium-channel bands shape the response to electric stimulation in retinal ganglion cells. *J Neurophysiol*, 101, 1972-1987.

- FRIED, S. I., MUNCH, T. A. & WERBLIN, F. S. 2002. Mechanisms and circuitry underlying directional selectivity in the retina. *Nature*, 420, 411-4.
- FUJIKADO, T., MORIMOTO, T., KANDA, H., KUSAKA, S., NAKAUCHI, K., OZAWA, M., MATSUSHITA, K., SAKAGUCHI, H., IKUNO, Y., KAMEI, M. & TANO, Y. 2007. Evaluation of phosphenes elicited by extraocular stimulation in normals and by suprachoroidal-transretinal stimulation in patients with retinitis pigmentosa. *Graef Arch Clin Exp*, 245, 1411-1419.
- GERDING, H. 2007. A new approach towards a minimal invasive retina implant. *J Neural Eng*, 4, S30-S37.
- GOLD, C., HENZE, D. A. & KOCH, C. 2007. Using extracellular action potential recordings to constrain compartmental models. *J Comput Neurosci*, 23, 39-58.
- GOLD, C., HENZE, D. A., KOCH, C. & BUZSAKI, G. 2006. On the origin of the extracellular action potential waveform: A modeling study. *J Neurophysiol*, 95, 3113-3128.
- GOLDBERG, D. E. 1989. *Genetic algorithms in search, optimisation and machine learning*, Boston, US, Addison Wesley.
- GOLDING, N. L., KATH, W. L. & SPRUSTON, N. 2001. Dichotomy of action-potential backpropagation in cal pyramidal neuron dendrites. *J Neurophysiol*, 86, 2998-3010.
- GOLDMAN, M. S., GOLOWASCH, J., MARDER, E. & ABBOTT, L. F. 2001. Global structure, robustness, and modulation of neuronal models. *J Neurosci*, 21, 5229-5238.
- GOLLISCH, T. & MEISTER, M. 2010. Eye smarter than scientists believed: Neural computations in circuits of the retina. *Neuron*, 65, 150-64.
- GOLOWASCH, J., ABBOTT, L. F. & MARDER, E. 1999. Activity-dependent regulation of potassium currents in an identified neuron of the stomatogastric ganglion of the crab cancer borealis. *J Neurosci*, 19, RC33.
- GREENBERG, R. J., VELTE, T. J., HUMAYUN, M. S., SCARLATIS, G. N. & DE JUAN, E., JR. 1999. A computational model of electrical stimulation of the retinal ganglion cell. *IEEE Trans Biomed Eng.*, 46, 505-14.
- GUENTHER, T., LOVELL, N. H. & SUANING, G. J. 2012. Bionic vision: System architectures - a review. *Expert Rev Med Devic*, 9, 33-48.
- GUNAY, C., EDGERTON, J. R. & JAEGER, D. 2008. Channel density distributions explain spiking variability in the globus pallidus: A combined physiology and computer simulation database approach. *J Neurosci*, 28, 7476-7491.
- GUO, T., AL ABED, A., LOVELL, N. H. & DOKOS, S. 2013. Optimisation of a generic ionic model of cardiac myocyte electrical activity. *Comput Math Methods Med*, 2013, 706195.
- GURKIEWICZ, M. & KORNGREEN, A. 2007. A numerical approach to ion channel modelling using whole-cell voltage-clamp recordings and a genetic algorithm. *Plos Comput Biol*, 3, 1633-1647.
- HADELER, K. P. & KUHN, D. 1987. Stationary states of the hartline-ratliff model. *Biol Cybern.*, 56, 411-417.
- HAMER, R. D., NICHOLAS, S. C., TRANCHINA, D., LAMB, T. D. & JARVINEN, J. L. P. 2005. Toward a unified model of vertebrate rod phototransduction. *Visual Neurosci*, 22, 417-436.
- HARTLINE, H. K. 1938. The response of single optic nerve fibers of the vertebrate eye to illumination of the retina. *Am J Physiol*, 121, 400-415.
- HAYES, R. D., BYRNE, J. H., COX, S. J. & BAXTER, D. A. 2005. Estimation of single-neuron model parameters from spike train data. *Neurocomputing*, 65, 517-529.

- HENDERSON, D. & MILLER, R. F. 2003. Evidence for low-voltage-activated (I_{va}) calcium currents in the dendrites of tiger salamander retinal ganglion cells. *Vis Neurosci*, 20, 141-52.
- HENNIG, M. H., FUNKE, K. & WORGOTTER, F. 2002. The influence of different retinal subcircuits on the nonlinearity of ganglion cell behavior. *J Neurosci.*, 22, 8726-38.
- HENNIG, M. H. & WORGOTTER, F. 2007. Effects of fixational eye movements on retinal ganglion cell responses: A modelling study. *Front Comput Neurosc*, 1, Doi: 10.3389/Neuro.10/002.2007.
- HENRIQUEZ, C. S. 1993. Simulating the electrical behavior of cardiac tissue using the bidomain model. *Crit Rev Biomed Eng*, 21, 1-77.
- HERRMANN, R., HEFLIN, S. J., HAMMOND, T., LEE, B., WANG, J., GAINETDINOV, R. R., CARON, M. G., EGGERS, E. D., FRISHMAN, L. J., MCCALL, M. A. & ARSHAVSKY, V. Y. 2011. Rod vision is controlled by dopamine-dependent sensitization of rod bipolar cells by GABA. *Neuron*, 72, 101-110.
- HERZ, A. V. M., GOLLISCH, T., MACHENS, C. K. & JAEGER, D. 2006. Modeling single-neuron dynamics and computations: A balance of detail and abstraction. *Science*, 314, 80-85.
- HESSE, L., SCHANZE, T., WILMS, M. & EGER, M. 2000. Implantation of retina stimulation electrodes and recording of electrical stimulation responses in the visual cortex of the cat. *Graef Arch Clin Exp*, 238, 840-845.
- HINES, M. L. & CARNEVALE, N. T. 1997. The neuron simulation environment. *Neural computation*, 9, 1179-1209.
- HODGKIN, A. L. & HUXLEY, A. F. 1952. A quantitative description of membrane current and its application to conduction and excitation in nerve. *J Physiol.*, 117, 500-44.
- HOFER, H., CARROLL, J., NEITZ, J., NEITZ, M. & WILLIAMS, D. R. 2005. Organization of the human trichromatic cone mosaic. *J Neurosci*, 25, 9669-79.
- HOOD, D. C., SHADY, S. & BIRCH, D. G. 1993. Heterogeneity in retinal disease and the computational model of the human-rod response. *J Opt Soc Am A.*, 10, 1624-30.
- HOSOYA, T., BACCUS, S. A. & MEISTER, M. 2005. Dynamic predictive coding by the retina. *Nature*, 436, 71-7.
- HUYS, Q. J. M., AHRENS, M. B. & PANINSKI, L. 2006. Efficient estimation of detailed single-neuron models. *J Neurophysiol*, 96, 872-890.
- ISHIDA, A. T. 1995. Ion channel components of retinal ganglion cells. *Prog Retin Eye Res*, 15, 261-280.
- IZHIKEVICH, E. M. 2007. *Dynamical systems in neuroscience: The geometry of excitability and bursting*, London, England, The MIT Press.
- JACKMAN, S. L., BABAI, N., CHAMBERS, J. J., THORESON, W. B. & KRAMER, R. H. 2011. A positive feedback synapse from retinal horizontal cells to cone photoreceptors. *Plos Biol*, 9.
- JENG, J., TANG, S., MOLNAR, A., DESAI, N. J. & FRIED, S. I. 2011. The sodium channel band shapes the response to electric stimulation in retinal ganglion cells. *J Neural Eng*, 8, 036022.
- JENSEN, R. J. & RIZZO, J. F. 2005. Responses of rabbit retinal ganglion cells to electrical stimulation with a subretinal electrode. *Invest Ophthalm Vis Sci*, 46.
- JENSEN, R. J. & RIZZO, J. F. 2006. Thresholds for activation of rabbit retinal ganglion cells with a subretinal electrode. *Exp Eye Res*, 83, 367-373.
- JENSEN, R. J. & RIZZO, J. F. 2008. Activation of retinal ganglion cells in wild-type and rd1 mice through electrical stimulation of the retinal neural network. *Vision Res*, 48, 1562-1568.

- JENSEN, R. J., ZIV, O. R. & RIZZO, J. F. 2005. Thresholds for activation of rabbit retinal ganglion cells with relatively large, extracellular microelectrodes. *Invest Ophth Vis Sci*, 46, 1486-1496.
- JOARDER, S. A., ABRAMIAN, M., SUANING, G. J., LOVELL, N. H. & DOKOS, S. 2011. A continuum model of retinal electrical stimulation. *J Neural Eng*, 8, 066006.
- JOLIVET, R., LEWIS, T. J. & GERSTNER, W. 2004. Generalized integrate-and-fire models of neuronal activity approximate spike trains of a detailed model to a high degree of accuracy. *J Neurophysiol*, 92, 959-976.
- JOSEPH, L. & BUTERA, R. J. 2011. High-frequency stimulation selectively blocks different types of fibers in frog sciatic nerve. *IEEE Trans Neural Syst Rehabil Eng*, 19, 550-7.
- JUNG, L. H., SHANY, N., EMPERLE, A., LEHMANN, T., BYRNES-PRESTON, P., LOVELL, N. H. & SUANING, G. J. 2013. Design of safe two-wire interface-driven chip-scale neurostimulator for visual prosthesis. *Ieee J Solid-St Circ*, 48, 2217-2229.
- JUUSOLA, M., WECKSTROM, M., UUSITALO, R. O., KORENBERG, M. J. & FRENCH, A. S. 1995. Nonlinear models of the first synapse in the light-adapted fly retina. *J Neurophysiol*, 74, 2538-2547.
- KAMENEVA, T., MEFFIN, H. & BURKITT, A. N. 2011. Modelling intrinsic electrophysiological properties of on and off retinal ganglion cells. *J Comput Neurosci*, 31, 547-561.
- KAMIYAMA, Y., OGURA, T. & USUI, S. 1996. Ionic current model of the vertebrate rod photoreceptor. *Vision Res*, 36, 4059-4068.
- KANEDA, M. & KANEKO, A. 1991. Voltage-gated sodium currents in isolated retinal ganglion cells of the cat: Relation between the inactivation kinetics and the cell type. *Neurosci Res*, 11, 261-75.
- KEAT, J., REINAGEL, P., REID, R. C. & MEISTER, M. 2001. Predicting every spike: A model for the responses of visual neurons. *Neuron*, 30, 803-17.
- KEPLER, T. B., ABBOTT, L. F. & MARDER, E. 1992. Reduction of conductance-based neuron models. *Biol Cybern*, 66, 381-7.
- KEREN, N., BAR-YEHUDA, D. & KORNGREEN, A. 2009. Experimentally guided modelling of dendritic excitability in rat neocortical pyramidal neurones. *J Physiol-London*, 587, 1413-1437.
- KEREN, N., PELED, N. & KORNGREEN, A. 2005. Constraining compartmental models using multiple voltage recordings and genetic algorithms. *J Neurophysiol*, 94, 3730-3742.
- KILGORE, K. L. & BHADRA, N. 2004. Nerve conduction block utilising high-frequency alternating current. *Med Biol Eng Comput*, 42, 394-406.
- KLAASSEN, L. J., SUN, Z. Y., STEIJAERT, M. N., BOLTE, P., FAHRENFORT, I., SJOERDSMA, T., KLOOSTER, J., CLAASSEN, Y., SHIELDS, C. R., TEN EIKELDER, H. M. M., JANSSEN-BIENHOLD, U., ZOIDL, G., MCMAHON, D. G. & KAMERMANS, M. 2011. Synaptic transmission from horizontal cells to cones is impaired by loss of connexin hemichannels. *Plos Biol*, 9.
- KLAUKE, S., GOERTZ, M., REIN, S., HOEHL, D., THOMAS, U., ECKHORN, R., BREMMER, F. & WACHTLER, T. 2011. Stimulation with a wireless intraocular epiretinal implant elicits visual percepts in blind humans. *Invest Ophth Vis Sci*, 52, 449-455.
- KOCH, C. & SEGEV, I. 1997. *Methods in neuronal modeling*, Cambridge, US, MIT Press.
- KOLB, H. 1974. Connections between horizontal cells and photoreceptors in retina of cat - electron-microscopy of golgi preparations. *J Comp Neurol*, 155, 1-14.
- KOLB, H., NELSON, R. & MARIANI, A. 1981. Amacrine cells, bipolar cells and ganglion-cells of the cat retina - a golgi-study. *Vision Res*, 21, 1081-1114.

- KONG, J. H., FISH, D. R., ROCKHILL, R. L. & MASLAND, R. H. 2005. Diversity of ganglion cells in the mouse retina: Unsupervised morphological classification and its limits. *The Journal of comparative neurology*, 489, 293-310.
- KOURENNYI, D. E., LIU, X. D., HART, J., MAHMUD, F., BALDRIDGE, W. H. & BARNES, S. 2004. Reciprocal modulation of calcium dynamics at rod and cone photoreceptor synapses by nitric oxide. *J Neurophysiol*, 92, 477-483.
- KUCHENBECKER, J. A., SAHAY, M., TAIT, D. M., NEITZ, M. & NEITZ, J. 2008. Topography of the long- to middle-wavelength sensitive cone ratio in the human retina assessed with a wide-field color multifocal electroretinogram. *Vis Neurosci*, 25, 301-6.
- KUFFLER, S. W. 1953. Discharge patterns and functional organization of mammalian retina. *J Neurophysiol*, 16, 37-68.
- LAMB, T. D. & PUGH, E. N., JR. 1992. A quantitative account of the activation steps involved in phototransduction in amphibian photoreceptors. *J Physiol.*, 449, 719-58.
- LANGILLE, M., GONZALEZ-CUETO, J. A. & SUNDAR, S. 2008. Analysis of the selective nature of sensory nerve stimulation using different sinusoidal frequencies. *Int J Neurosci*, 118, 1131-1144.
- LEE, S. C. & ISHIDA, A. T. 2007. Ih without kir in adult rat retinal ganglion cells. *J Neurophysiol*, 97, 3790-3799.
- LI, W. & DEVRIES, S. H. 2006. Bipolar cell pathways for color and luminance vision in a dichromatic mammalian retina. *Nat Neurosci*, 9, 669-675.
- LILLY, J. C., HUGHES, J. R., ALVORD, E. C. & GALKIN, T. W. 1955. Brief, noninjurious electric waveform for stimulation of the brain. *Science*, 121, 468-469.
- LIPTON, S. A. & TAUCK, D. L. 1987. Voltage-dependent conductances of solitary ganglion cells dissociated from the rat retina. *J Physiol*, 385, 361-91.
- LITVAK, L., DELGUTTE, B. & EDDINGTON, D. 2001. Auditory nerve fiber responses to electric stimulation: Modulated and unmodulated pulse trains. *J Acoust Soc Am*, 110, 368-79.
- LITVAK, L. M., SMITH, Z. M., DELGUTTE, B. & EDDINGTON, D. K. 2003. Desynchronization of electrically evoked auditory-nerve activity by high-frequency pulse trains of long duration. *J Acoust Soc Am*, 114, 2066-78.
- LIU, H. L., ROPPOLO, J. R., DE GROAT, W. C. & TAI, C. F. 2009. The role of slow potassium current in nerve conduction block induced by high-frequency biphasic electrical current. *Ieee T Bio-Med Eng*, 56, 137-146.
- LIU, Z., GOLOWASCH, J., MARDER, E. & ABBOTT, L. F. 1998. A model neuron with activity-dependent conductances regulated by multiple calcium sensors. *J Neurosci*, 18, 2309-2320.
- LOVELL, N. H., CLOHERTY, S. L., CELLER, B. G. & DOKOS, S. 2004. A gradient model of cardiac pacemaker myocytes. *Prog Biophys Mol Bio*, 85, 301-323.
- LU, Y., MAHAUT-SMITH, M. P., VARGHESE, A., HUANG, C. L. H., KEMP, P. R. & VANDENBERG, J. I. 2001. Effects of premature stimulation on hERG K⁺ channels. *J Physiol-London*, 537, 843-851.
- LUO, C. H. & RUDY, Y. 1991. A model of the ventricular cardiac action-potential - depolarization, repolarization, and their interaction. *Circ Res*, 68, 1501-1526.
- LUO, Y. H. & DA CRUZ, L. 2014. A review and update on the current status of retinal prostheses (bionic eye). *Br Med Bull.*, 109, 31-44.
- MACNEIL, M. A. & MASLAND, R. H. 1998. Extreme diversity among amacrine cells: Implications for function. *Neuron*, 20, 971-982.
- MAGEE, J. C. 1998. Dendritic hyperpolarization-activated currents modify the integrative properties of hippocampal CA1 pyramidal neurons. *J Neurosci*, 18, 7613-7624.

- MAINEN, Z. F., JOERGES, J., HUGUENARD, J. R. & SEJNOWSKI, T. J. 1995. A model of spike initiation in neocortical pyramidal neurons. *Neuron*, 15, 1427-1439.
- MAINEN, Z. F. & SEJNOWSKI, T. J. 1996. Influence of dendritic structure on firing pattern in model neocortical neurons. *Nature*, 382, 363-6.
- MARC, R. E., JONES, B. W., WATT, C. B. & STRETTOI, E. 2003. Neural remodeling in retinal degeneration. *Prog Retin Eye Res*, 22, 607-655.
- MARGALIT, E. & THORESON, W. B. 2006. Inner retinal mechanisms engaged by retinal electrical stimulation. *Invest Ophth Vis Sci*, 47, 2606-2612.
- MARGOLIS, D. J. & DETWILER, P. B. 2007. Different mechanisms generate maintained activity in on and off retinal ganglion cells. *J Neurosci*, 27, 5994-6005.
- MARGOLIS, D. J., GARTLAND, A. J., EULER, T. & DETWILER, P. B. 2010. Dendritic calcium signaling in on and off mouse retinal ganglion cells. *J Neurosci*, 30, 7127-7138.
- MARQUARDT, D. W. 1963. An algorithm for least-squares estimation of nonlinear parameters. *J Soc Ind Appl Math*, 11, 431-441.
- MARTINEK, J., STICKLER, Y., REICHEL, M., MAYR, W. & RATTAY, F. 2008. A novel approach to simulate hodgkin-huxley-like excitation with comsol multiphysics. *Artif Organs*, 32, 614-619.
- MASLAND, R. H. 2001. The fundamental plan of the retina. *Nat Neurosci*, 4, 877-886.
- MASLAND, R. H. 2012. The neuronal organization of the retina. *Neuron*, 76, 266-80.
- MATTEUCCI, P. B., CHEN, S. C., TSAI, D., DODDS, C. W. D., DOKOS, S., MORLEY, J. W., LOVELL, N. H. & SUANING, G. J. 2013. Current steering in retinal stimulation via a quasimonopolar stimulation paradigm. *Invest Ophth Vis Sci*, 54, 4307-4320.
- MATURANA, M. I., KAMENEVA, T., BURKITT, A. N., MEFFIN, H. & GRAYDEN, D. B. 2013. The effect of morphology upon electrophysiological responses of retinal ganglion cells: Simulation results. *J Comput Neurosci.*, DOI: 10.1007/s10827-013-0463-7.
- MCCORMICK, D. A. & HUGUENARD, J. R. 1992. A model of the electrophysiological properties of thalamocortical relay neurons. *J Neurophysiol*, 68, 1384-400.
- MCCORMICK, D. A. & PAPE, H. C. 1990. Properties of a hyperpolarization-activated cation current and its role in rhythmic oscillation in thalamic relay neurones. *J Physiol*, 431, 291-318.
- MCCORMICK, D. A., SHU, Y. & YU, Y. 2007. Neurophysiology: Hodgkin and huxley model--still standing? *Nature*, 445, 1060-1063.
- MENNERICK, S., ZENISEK, D. & MATTHEWS, G. 1997. Static and dynamic membrane properties of large-terminal bipolar cells from goldfish retina: Experimental test of a compartment model. *J Neurophysiol*, 78, 51-62.
- MENSI, S., NAUD, R., POZZORINI, C., AVERMANN, M., PETERSEN, C. C. H. & GERSTNER, W. 2012. Parameter extraction and classification of three cortical neuron types reveals two distinct adaptation mechanisms. *J Neurophysiol*, 107, 1756-1775.
- MILLER, R. F., STAFF, N. P. & VELTE, T. J. 2006. Form and function of on-off amacrine cells in the amphibian retina. *J Neurophysiol*, 95, 3171-3190.
- MILLER, R. F., STENBACK, K., HENDERSON, D. & SIKORA, M. 2002. How voltage-gated ion channels alter the functional properties of ganglion and amacrine cell dendrites. *Arch Ital Biol*, 140, 347-359.
- MITRA, A., MANITIUS, A. & SAUER, T. 2012. Prediction of single neuron spiking activity using an optimized nonlinear dynamic model. *34th Annual International Conference of the Ieee Engineering in Medicine and Biology Society*. San Disgo, US: IEEE Press.

- MITRA, P. & MILLER, R. F. 2007a. Mechanism underlying rebound excitation in retinal ganglion cells. *Visual neuroscience*, 24, 709-31.
- MITRA, P. & MILLER, R. F. 2007b. Normal and rebound impulse firing in retinal ganglion cells. *Vis Neurosci*, 24, 79-90.
- MOMIN, A., CADIOU, H., MASON, A. & MCNAUGHTON, P. A. 2008. Role of the hyperpolarization-activated current *ih* in somatosensory neurons. *J Physiol*, 586, 5911-29.
- MOOSMANG, S., STIEBER, J., ZONG, X., BIEL, M., HOFMANN, F. & LUDWIG, A. 2001. Cellular expression and functional characterization of four hyperpolarization-activated pacemaker channels in cardiac and neuronal tissues. *Eur J Biochem*, 268, 1646-52.
- MORITOH, S., KOMATSU, Y., YAMAMORI, T. & KOIZUMI, A. 2013. Diversity of retinal ganglion cells identified by transient gfp transfection in organotypic tissue culture of adult marmoset monkey retina. *Plos One*, 8.
- MOSCATO, P. 1989. On evolution, search, optimization, genetic algorithms and martial arts: Towards memetic algorithms. *Caltech Concurrent Computation Program*
- MURPHEY, C. R., MOORE, L. E. & BUCHANAN, J. T. 1995. Quantitative-analysis of electrotonic structure and membrane-properties of nmda-activated lamprey spinal neurons. *Neural Comput*, 7, 486-506.
- NAUNDORF, B., WOLF, F. & VOLGUSHEV, M. 2006. Unique features of action potential initiation in cortical neurons. *Nature*, 440, 1060-1063.
- NELSON, R., FAMIGLIETTI, E. V. & KOLB, H. 1978. Intracellular staining reveals different levels of stratification for on-center and off-center ganglion-cells in cat retina. *J Neurophysiol*, 41, 472-483.
- NOLTE, J. 2009. *The human brain: An introduction to its functional anatomy*, Mosby/Elsevier.
- NOWOTNY, T., LEVI, R. & SELVERSTON, A. I. 2008. Probing the dynamics of identified neurons with a data-driven modeling approach. *Plos One*, 3.
- NYGREN, A., FISET, C., FIREK, L., CLARK, J. W., LINDBLAD, D. S., CLARK, R. B. & GILES, W. R. 1998. Mathematical model of an adult human atrial cell - the role of k^+ currents in repolarization. *Circ Res*, 82, 63-81.
- O'BRIEN, B. J., ISAYAMA, T., RICHARDSON, R. & BERSON, D. M. 2002. Intrinsic physiological properties of cat retinal ganglion cells. *J Physiol*, 538, 787-802.
- OESCH, N., EULER, T. & TAYLOR, W. R. 2005. Direction-selective dendritic action potentials in rabbit retina. *Neuron*, 47, 739-50.
- OGURA, T., SATOH, T. O., USUI, S. & YAMADA, M. 2003. A simulation analysis on mechanisms of damped oscillation in retinal rod photoreceptor cells. *Vision Res*, 43, 2019-2028.
- PAL, S. 2009. *Numerical methods: Principles, analyses, and algorithms*, Oxford University Press.
- PANINSKI, L., PILLOW, J. W. & SIMONCELLI, E. P. 2004. Maximum likelihood estimation of a stochastic integrate-and-fire neural encoding model. *Neural Comput*, 16, 2533-2561.
- PAPE, H. C. 1996. Queer current and pacemaker: The hyperpolarization-activated cation current in neurons. *Annu Rev Physiol*, 58, 299-327.
- PEICHL, L., WASSLE, H., BOYCOTT, B. B. & PEICHL, L. 1981. Morphological identification of on-center and off-center brisk transient (y) cells in the cat retina. *Proc R Soc Ser B-Bio*, 212, 139-+.

- PILLOW, J. W., PANINSKI, L., UZZELL, V. J., SIMONCELLI, E. P. & CHICHILNISKY, E. J. 2005. Prediction and decoding of retinal ganglion cell responses with a probabilistic spiking model. *J Neurosci*, 25, 11003-11013.
- PILLOW, J. W., SHLENS, J., PANINSKI, L., SHER, A., LITKE, A. M., CHICHILNISKY, E. J. & SIMONCELLI, E. P. 2008. Spatio-temporal correlations and visual signalling in a complete neuronal population. *Nature*, 454, 995-U37.
- PINSKY, P. F. & RINZEL, J. 1995. Intrinsic and network rhythmogenesis in a reduced traub model for ca3 neurons (vol 1, pg 59, 1994). *J Comput Neurosci*, 2, 275-275.
- POZNANSKI, R. R. 1992. Modelling the electrotonic structure of starburst amacrine cells in the rabbit retina: A functional interpretation of dendritic morphology. *Bulletin of mathematical biology*, 54, 905-28.
- PRIM, R. C. 1957. Shortest connection networks and some generalizations. *At&T Tech J*, 36, 1389-1401.
- PRINZ, A. A., BILLIMORIA, C. P. & MARDER, E. 2003a. Alternative to hand-tuning conductance-based models: Construction and analysis of databases of model neurons. *J Neurophysiol*, 90, 3998-4015.
- PRINZ, A. A., THIRUMALAI, V. & MARDER, E. 2003b. The functional consequences of changes in the strength and duration of synaptic inputs to oscillatory neurons. *J Neurosci*, 23, 943-954.
- PUBLIO, R., CEBALLOS, C. C. & ROQUE, A. C. 2012. Dynamic range of vertebrate retina ganglion cells: Importance of active dendrites and coupling by electrical synapses. *PLoS One*, 7, e48517.
- PUBLIO, R., OLIVEIRA, R. F. & ROQUE, A. C. 2009. A computational study on the role of gap junctions and rod i-h conductance in the enhancement of the dynamic range of the retina. *PLoS One*, 4, e6970.
- PUBLIO, R., OLIVEIRA, R. F. & ROQUEA, A. C. 2006. A realistic model of rod photoreceptor for use in a retina network model. *Neurocomputing*, 69, 1020-1024.
- PUCHALLA, J. L., SCHNEIDMAN, E., HARRIS, R. A. & BERRY, M. J. 2005. Redundancy in the population code of the retina. *Neuron*, 46, 493-504.
- RALL, W. 1959. Branching dendritic trees and motoneuron membrane resistivity. *Exp Neurol*, 1, 491-527.
- RALL, W. 1977. Core conductor theory and cable properties of neurons. In: KANDEL, E. R., BROOKHART, J. M. & MOUNTCASTLE, V. B. (eds.) *Handbook of physiology - the nervous system*. Bethesda, US: American Physiological Society.
- RATEAU, Y. & ROPERT, N. 2006. Expression of a functional hyperpolarization-activated current (ih) in the mouse nucleus reticularis thalami. *J Neurophysiol*, 95, 3073-85.
- RATTAY, F. & RESATZ, S. 2004. Effective electrode configuration for selective stimulation with inner eye prostheses. *IEEE Trans Biomed Eng*, 51, 1659-64.
- RATTAY, F., RESATZ, S., LUTTER, P., MINASSIAN, K., JILGE, B. & DIMITRIJEVIC, M. R. 2003. Mechanisms of electrical stimulation with neural prostheses. *Neuromodulation*, 6, 42-56.
- RAUCH, A., LA CAMERA, G., LUSCHER, H. R., SENN, W. & FUSI, S. 2003. Neocortical pyramidal cells respond as integrate-and-fire neurons to in vivo-like input currents. *J Neurophysiol*, 90, 1598-1612.
- REKECZKY, C., ROSKA, B., NEMETH, E. & WERBLIN, F. S. 2001. The network behind spatio-temporal patterns: Building low-complexity retinal models in cnn based on morphology, pharmacology and physiology. *Int J Circ Theor App*, 29, 197-239.
- RESATZ, S. & RATTAY, F. 2004. A model for the electrically stimulated retina. *Math Comp Model Dyn*, 10, 93-106.

- RISTANOVIC, D., MILOSEVIC, N. T., JELINEK, H. F. & STEFANOVIC, I. B. 2009. Mathematical modelling of neuronal dendritic branching patterns in two dimensions: Application to retinal ganglion cells in the cat and rat. *Biol Cybern.*, 100, 97-108.
- ROBINSON, R. B. 2003. Hyperpolarization-activated cation currents: From molecules to physiological function. *Annu Rev Physiol*, 65, 453-480.
- ROBSON, J. G. & FRISHMAN, L. J. 1995. Response linearity and kinetics of the cat retina: The bipolar cell component of the dark-adapted electroretinogram. *Visual Neurosci.*, 12, 837-50.
- ROBSON, J. G. & FRISHMAN, L. J. 1996. Photoreceptor and bipolar-cell contributions to the cat electroretinogram: A kinetic model for the early part of the flash response. *J Opt Soc Am A.*, 13, 613-622.
- ROCKHILL, R. L., DALY, F. J., MACNEIL, M. A., BROWN, S. P. & MASLAND, R. H. 2002. The diversity of ganglion cells in a mammalian retina. *J Neurosci*, 22, 3831-3843.
- ROSE, G. J. & CALL, S. J. 1993. Temporal filtering properties of midbrain neurons in an electric fish: Implications for the function of dendritic spines. *J Neurosci*, 13, 1178-89.
- ROSE, G. J. & FORTUNE, E. S. 1999. Mechanisms for generating temporal filters in the electrosensory system. *J Exp Biol*, 202, 1281-9.
- ROSKA, B. & MEISTER, M. 2014. The retina dissects visual scenes into distinct features *In*: WERNER, J. S. & CHALUPA, L. M. (eds.) *The new visual neurosciences*. London: MIT Press.
- ROTH, B. J. & WIKSWO, J. P. 1994. Electrical-stimulation of cardiac tissue - a bidomain model with active membrane-properties. *IEEE Trans Bio-Med Eng*, 41, 232-240.
- ROUSER, G., NELSON, G. J., FLEISCHER, S. & SIMON, C. 1968. Lipid composition of animal cell membranes, organelles, and organs. *Biological membranes*. New York, US: Academic Press.
- SACHS, H. G. & GABEL, V. P. 2004. Retinal replacement--the development of microelectronic retinal prostheses--experience with subretinal implants and new aspects. *Graefes Arch Clin Exp Ophthalmol*, 242, 717-23.
- SAGLAM, M., HAYASHIDA, Y. & MURAYAMA, N. 2009. A retinal circuit model accounting for wide-field amacrine cells. *Cogn Neurodynamics*, 3, 25-32.
- SARKAR, A. X. & SOBIE, E. A. 2010. Regression analysis for constraining free parameters in electrophysiological models of cardiac cells. *Plos Comput Biol*, 6.
- SCHACHTER, M. J., OESCH, N., SMITH, R. G. & TAYLOR, W. R. 2010. Dendritic spikes amplify the synaptic signal to enhance detection of motion in a simulation of the direction-selective ganglion cell. *PLoS Comput Biol*, 6, e1000899.
- SCHIEFER, M. A. & GRILL, W. M. 2006. Sites of neuronal excitation by epiretinal electrical stimulation. *IEEE Trans Neur Sys Reh*, 14, 5-13.
- SCHILLER, Y. & BANKIRER, Y. 2007. Cellular mechanisms underlying antiepileptic effects of low- and high-frequency electrical stimulation in acute epilepsy in neocortical brain slices in vitro. *J Neurophysiol*, 97, 1887-1902.
- SEKIRNJAK, C., HOTTOWY, P., SHER, A., DABROWSKI, W., LITKE, A. M. & CHICHILNISKY, E. J. 2006. Electrical stimulation of mammalian retinal ganglion cells with multielectrode arrays. *J Neurophysiol*, 95, 3311-3327.
- SEKIRNJAK, C., HOTTOWY, P., SHER, A., DABROWSKI, W., LITKE, A. M. & CHICHILNISKY, E. J. 2008. High-resolution electrical stimulation of primate retina for epiretinal implant design. *J Neurosci*, 28, 4446-4456.
- SEKIRNJAK, C., HULSE, C., JEPSON, L. H., HOTTOWY, P., SHER, A., DABROWSKI, W., LITKE, A. M. & CHICHILNISKY, E. J. 2009. Loss of responses to visual but

- not electrical stimulation in ganglion cells of rats with severe photoreceptor degeneration. *J Neurophysiol*, 102, 3260-3269.
- SHAH, S. & LEVINE, M. D. 1996a. Visual information processing in primate cone pathways. I. A model. *IEEE Trans Syst Man Cybern B Cybern.*, 26, 259-74.
- SHAH, S. & LEVINE, M. D. 1996b. Visual information processing in primate cone pathways. II. Experiments. *IEEE Trans Syst Man Cybern B Cybern.*, 26, 275-89.
- SHEASBY, B. W. & FOHLMEISTER, J. F. 1999. Impulse encoding across the dendritic morphologies of retinal ganglion cells. *J Neurophysiol*, 81, 1685-98.
- SHIRAHATA, T. 2008. Simulation of rabbit a-type retinal horizontal cell that generates repetitive action potentials. *Neurosci Lett*, 439, 116-118.
- SHIRAHATA, T. 2011. The effect of variations in sodium conductances on pacemaking in a dopaminergic retinal neuron model. *Acta Biol Hung*, 62, 211-214.
- SHIVDASANI, M. N., LUU, C. D., CICIONE, R., FALLON, J. B., ALLEN, P. J., LEUENBERGER, J., SUANING, G. J., LOVELL, N. H., SHEPHERD, R. K. & WILLIAMS, C. E. 2010. Evaluation of stimulus parameters and electrode geometry for an effective suprachoroidal retinal prosthesis. *J Neural Eng*, 7.
- SIVYER, B. & VANEY, D. I. 2010. Dendritic morphology and tracer-coupling pattern of physiologically identified transient uniformity detector ganglion cells in rabbit retina. *Visual Neurosci*, 27, 159-170.
- SIVYER, B. & WILLIAMS, S. R. 2013. Direction selectivity is computed by active dendritic integration in retinal ganglion cells. *Nat Neurosci*, 16, 1848-1856.
- SMITH, R. G. 1995. Simulation of an anatomically defined local circuit: The cone-horizontal cell network in cat retina. *Vis Neurosci*, 12, 545-61.
- SMITH, R. G., FREED, M. A. & STERLING, P. 1986. Microcircuitry of the dark-adapted cat retina - functional architecture of the rod cone network. *J Neurosci*, 6, 3505-3517.
- SMITH, R. G. & VARDI, N. 1995. Simulation of the aii amacrine cell of mammalian retina - functional consequences of electrical coupling and regenerative membrane-properties. *Visual Neurosci*, 12, 851-860.
- SPRUSTON, N. 2008. Pyramidal neurons: Dendritic structure and synaptic integration. *Nat Rev Neurosci*, 9, 206-221.
- STARR, C., EVERS, C. & STARR, L. 2010. *Biology: Concepts and applications*, Cengage Learning.
- STEFFEN, M. A., SEAY, C. A., AMINI, B., CAI, Y. D., FEIGENSPAN, A., BAXTER, D. A. & MARSHAK, D. W. 2003. Spontaneous activity of dopaminergic retinal neurons. *Biophys J*, 85, 2158-2169.
- STEINBERG, R. H., FISHER, S. K. & ANDERSON, D. H. 1980. Disc morphogenesis in vertebrate photoreceptors. *J Comp Neurol*, 190, 501-8.
- STERLING, P., FREED, M. A. & SMITH, R. G. 1988. Architecture of rod and cone circuits to the on-beta ganglion cell. *J Neurosci*, 8, 623-42.
- STETT, A., BARTH, W., WEISS, S., HAEMMERLE, H. & ZRENNER, E. 2000. Electrical multisite stimulation of the isolated chicken retina. *Vision Res*, 40, 1785-1795.
- STRADLEIGH, T. W., OGATA, G., PARTIDA, G. J., OI, H., GREENBERG, K. P., KREMPELY, K. S. & ISHIDA, A. T. 2011. Colocalization of hyperpolarization-activated, cyclic nucleotide-gated channel subunits in rat retinal ganglion cells. *The Journal of comparative neurology*, 519, 2546-73.
- STUART, G., SPRUSTON, N. & HAUSSER, M. 2008. *Dendrites*, New York, US, Oxford University Press.
- SUN, W. Z., LI, N. & HE, S. G. 2002. Large-scale morphological survey of mouse retinal ganglion cells. *J Comp Neurol*, 451, 115-126.

- SURGES, R., FREIMAN, T. M. & FEUERSTEIN, T. J. 2004. Input resistance is voltage dependent due to activation of i-h channels in rat cal pyramidal cells. *J Neurosci Res*, 76, 475-480.
- SYED, Z., VIGMOND, E., NATTEL, S. & LEON, L. J. 2005. Atrial cell action potential parameter fitting using genetic algorithms. *Med Biol Eng Comput*, 43, 561-571.
- SZEKELY, D., VANDENBERG, J. I., DOKOS, S. & HILL, A. P. 2011. An improved curvilinear gradient method for parameter optimization in complex biological models. *Med Biol Eng Comput*, 49, 289-96.
- TABAK, J., MURPHEY, C. R. & MOORE, L. E. 2000. Parameter estimation methods for single neuron models. *J Comput Neurosci*, 9, 215-236.
- TABATA, T. & ISHIDA, A. T. 1996. Transient and sustained depolarization of retinal ganglion cells by ih. *J Neurophysiol*, 75, 1932-43.
- TAYLOR, G. C., COLES, J. A. & EILBECK, J. C. 1995. Mathematical-modeling of weakly nonlinear pulses in a retinal neuron. *Chaos Soliton Fract*, 5, 407-413.
- TEETERS, J., JACOBS, A. & WERBLIN, F. 1997. How neural interactions form neural responses in the salamander retina. *J Comput Neurosci*, 4, 5-27.
- TORRE, V., FORTI, S., MENINI, A. & CAMPANI, M. 1990. Model of phototransduction in retinal rods. *Cold Sh Q B*, 55, 563-573.
- TRAUB, R. D., BUHL, E. H., GLOVELI, T. & WHITTINGTON, M. A. 2003. Fast rhythmic bursting can be induced in layer 2/3 cortical neurons by enhancing persistent na+ conductance or by blocking bk channels. *J Neurophysiol*, 89, 909-21.
- TRAUB, R. D., CONTRERAS, D., CUNNINGHAM, M. O., MURRAY, H., LEBEAU, F. E., ROOPUN, A., BIBBIG, A., WILENT, W. B., HIGLEY, M. J. & WHITTINGTON, M. A. 2005. Single-column thalamocortical network model exhibiting gamma oscillations, sleep spindles, and epileptogenic bursts. *J Neurophysiol.*, 93, 2194-232.
- TSAI, D., CHEN, S., PROTTI, D. A., MORLEY, J. W., SUANING, G. J. & LOVELL, N. H. 2012. Responses of retinal ganglion cells to extracellular electrical stimulation, from single cell to population: Model-based analysis. *PLoS One*, 7, e53357.
- TSAI, D., MORLEY, J. W., SUANING, G. J. & LOVELL, N. H. 2009. Direct activation and temporal response properties of rabbit retinal ganglion cells following subretinal stimulation. *J Neurophysiol*, 102, 2982-2993.
- TSAI, D., MORLEY, J. W., SUANING, G. J. & LOVELL, N. H. 2011. Frequency-dependent reduction of voltage-gated sodium current modulates retinal ganglion cell response rate to electrical stimulation. *J Neural Eng*, 8, 066007.
- TUKKER, J. J., TAYLOR, W. R. & SMITH, R. G. 2004. Direction selectivity in a model of the starburst amacrine cell. *Visual Neurosci*, 21, 611-625.
- TWYFORD, P., CAI, C. & FRIED, S. 2014. Differential responses to high-frequency electrical stimulation in on and off retinal ganglion cells. *J Neural Eng*, 11, 025001.
- USUI, S., ISHIHARA, A., KAMIYAMA, Y. & ISHII, H. 1996a. Ionic current model of bipolar cells in the lower vertebrate retina. *Vision Res*, 36, 4069-76.
- USUI, S., KAMIYAMA, Y., ISHII, H. & IKENO, H. 1996b. Reconstruction of retinal horizontal cell responses by the ionic current model. *Vision Res*, 36, 1711-1719.
- USUI, S., MITARAI, G. & SAKAKIBARA, M. 1983. Discrete nonlinear reduction model for horizontal cell response in the carp retina. *Vision research*, 23, 413-20.
- VALLERGA, S., COVACCI, R. & POTTALA, E. W. 1980. Artificial cone responses - a computer-driven hardware model. *Vision Res*, 20, 453-457.
- VAN ELBURG, R. A. & VAN OUYEN, A. 2010. Impact of dendritic size and dendritic topology on burst firing in pyramidal cells. *PLoS Comput Biol.*, 6, e1000781.
- VAN HATEREN, J. H. & SNIPPE, H. P. 2007. Simulating human cones from mid-mesopic up to high-photopic luminances. *J Vision*, 7, 1-11.

- VAN HOOK, M. J. & BERSON, D. M. 2010. Hyperpolarization-activated current (i(h)) in ganglion-cell photoreceptors. *PLoS one*, 5, e15344.
- VAN ROSSUM, M. C. W., O'BRIEN, B. J. & SMITH, R. G. 2003. Effects of noise on the spike timing precision of retinal ganglion cells. *J Neurophysiol*, 89, 2406-2419.
- VAN WELIE, I., REMME, M. W., VAN HOOFT, J. A. & WADMAN, W. J. 2006. Different levels of ih determine distinct temporal integration in bursting and regular-spiking neurons in rat subiculum. *J Physiol*, 576, 203-14.
- VANIER, M. C. & BOWER, J. M. 1999. A comparative survey of automated parameter-search methods for compartmental neural models. *J Comput Neurosci*, 7, 149-171.
- VELTE, T. J. & MASLAND, R. H. 1999. Action potentials in the dendrites of retinal ganglion cells. *J Neurophysiol*, 81, 1412-1417.
- VELTE, T. J. & MILLER, R. F. 1995. Dendritic integration in ganglion cells of the mudpuppy retina. *Visual Neurosci*, 12, 165-75.
- VELTE, T. J. & MILLER, R. F. 1997. Spiking and nonspiking models of starburst amacrine cells in the rabbit retina. *Visual Neurosci.*, 14, 1073-1088.
- VETTER, P., ROTH, A. & HAUSSER, M. 2001a. Propagation of action potentials in dendrites depends on dendritic morphology. *Journal of neurophysiology*, 85, 926-937.
- VETTER, P., ROTH, A. & HAUSSER, M. 2001b. Propagation of action potentials in dendrites depends on dendritic morphology. *Journal of neurophysiology*, 85, 926-937.
- VICTOR, J. D. 1987. The dynamics of the cat retinal x-cell center. *J Physiol-London*, 386, 219-246.
- VICTOR, J. D. 1988. The dynamics of the cat retinal y-cell subunit. *J Physiol-London*, 405, 289-320.
- VIGH, J., BANVOLGYI, T. & WILHELM, M. 2000. Amacrine cells of the anuran retina: Morphology, chemical neuroanatomy, and physiology. *Microsc Res Tech.*, 50, 373-83.
- VOLKER, M., SHINODA, K., SACHS, H., GMEINER, H., SCHWARZ, T., KOHLER, K., INHOFFEN, W., BARTZ-SCHMIDT, K. U., ZRENNER, E. & GEKELER, F. 2004. In vivo assessment of subretinally implanted microphotodiode arrays in cats by optical coherence tomography and fluorescein angiography. *Graef Arch Clin Exp*, 242, 792-799.
- WANG, L., LIU, S. Q. & OU, S. X. 2011. Numerical simulation of neuronal spike patterns in a retinal network model. *Neural Regen Res*, 6, 1254-1260.
- WANG, X. J., RINZEL, J. & ROGAWSKI, M. A. 1991. A model of the t-type calcium current and the low-threshold spike in thalamic neurons. *J Neurophysiol*, 66, 839-50.
- WASSLE, H. 2004. Parallel processing in the mammalian retina. *Nature reviews. Neuroscience*, 5, 747-57.
- WASSLE, H. & BOYCOTT, B. B. 1991. Functional architecture of the mammalian retina. *Physiol Rev*, 71, 447-480.
- WEILAND, J. D., LIU, W. & HUMAYUN, M. S. 2005. Retinal prosthesis. *Annu Rev Biomed Eng*, 7, 361-401.
- WERGINZ, P., FRIED, S. I. & RATTAY, F. 2014. Influence of the sodium channel band on retinal ganglion cell excitation during electric stimulation - a modeling study. *Neurosci.*, 266, 162-177.
- WHITE, J. A., MANIS, P. B. & YOUNG, E. D. 1992. The parameter-identification problem for the somatic shunt model. *Biol Cybern*, 66, 307-318.
- WILKE, R., GABEL, V. P., SACHS, H., SCHMIDT, K. U. B., GEKELER, F., BESCH, D., SZURMAN, P., STETT, A., WILHELM, B., PETERS, T., HARSCHER, A., GREPPMAIER, U., KIBBEL, S., BENAVIDES, H., BRUCKMANN, A., STINGL, K., KUSNYERIK, A. & ZRENNER, E. 2011. Spatial resolution and perception of

- patterns mediated by a subretinal 16-electrode array in patients blinded by hereditary retinal dystrophies. *Invest Ophth Vis Sci*, 52, 5995-6003.
- WILLMS, A. R., BARO, D. J., HARRIS-WARRICK, R. M. & GUCKENHEIMER, J. 1999. An improved parameter estimation method for hodgkin-huxley models. *J Comput Neurosci*, 6, 145-68.
- WOHRER, A. & KORNPORST, P. 2009. Virtual retina: A biological retina model and simulator, with contrast gain control. *J Comput Neurosci.*, 26, 219-49.
- WONG, R. C., CLOHERTY, S. L., IBBOTSON, M. R. & O'BRIEN, B. J. 2012. Intrinsic physiological properties of rat retinal ganglion cells with a comparative analysis. *J Neurophysiol*, 108, 2008-2023.
- WONG, Y. T., CHEN, S. C., SEO, J. M., MORLEY, J. W., LOVELL, N. H. & SUANING, G. J. 2009. Focal activation of the feline retina via a suprachoroidal electrode array. *Vision Res*, 49, 825-833.
- YAMAUCHI, S., KIM, H. & SHINOMOTO, S. 2011. Elemental spiking neuron model for reproducing diverse firing patterns and predicting precise firing times. *Front Comput Neurosci*, 5.
- YANG, C. Y., LUKASIEWICZ, P., MAGUIRE, G., WERBLIN, F. S. & YAZULLA, S. 1991. Amacrine cells in the tiger salamander retina: Morphology, physiology, and neurotransmitter identification. *J Comp Neurol.*, 312, 19-32.
- YIN, S., DOKOS, S. & LOVELL, N. H. 2013. Bidomain modeling of neural tissue. In: HE, B. (ed.) *Neural engineering*. Springer US.
- YIN, S., LOVELL, N. H., SUANING, G. J. & DOKOS, S. 2010. A continuum model of the retinal network and its response to electrical stimulation. *the 32th Annual International Conference of the IEEE Engineering in Medicine and Biology Society*. 2010/11/26 ed. Buenos Aires, Argentina: IEEE Press.
- YIN, S., LOVELL, N. H., SUANING, G. J. & DOKOS, S. 2011. Continuum model of light response in the retina. *the 33th Annual International Conference of the IEEE Engineering in Medicine and Biology Society*. Boston, US: IEEE press.
- YU, Y., SHU, Y. & MCCORMICK, D. A. 2008. Cortical action potential backpropagation explains spike threshold variability and rapid-onset kinetics. *J Neurosci*, 28, 7260-7272.
- ZHANG, Y. F., KIM, I. J., SANES, J. R. & MEISTER, M. 2012. The most numerous ganglion cell type of the mouse retina is a selective feature detector. *P Natl Acad Sci USA*, 109, E2391-E2398.
- ZHOU, J. A., WOO, S. J., PARK, S. I., KIM, E. T., SEO, J. M., CHUNG, H. & KIM, S. J. 2008. A suprachoroidal electrical retinal stimulator design for long-term animal experiments and in vivo assessment of its feasibility and biocompatibility in rabbits. *J Biomed Biotechnol*.
- ZRENNER, E., BARTZ-SCHMIDT, K. U., BENAÏ, H., BESCH, D., BRUCKMANN, A., GABEL, V. P., GEKELER, F., GREPPMAIER, U., HARSCHER, A., KIBBEL, S., KOCH, J., KUSNYERIK, A., PETERS, T., STINGL, K., SACHS, H., STETT, A., SZURMAN, P., WILHELM, B. & WILKE, R. 2011. Subretinal electronic chips allow blind patients to read letters and combine them to words. *P Roy Soc B-Biol Sci*, 278, 1489-1497.